Università degli Studi di Padova
Centro Ricerche Fusione

Ghent University

JOINT RESEARCH DOCTORATE IN FUSION SCIENCE AND ENGINEERING
Cycle XXXIV

BEAM PHYSICS VIA TOMOGRAPHIC DIAGNOSTICS

Coordinator: Prof. Fabio Villone

Supervisor at Università degli Studi di Padova (Home University):
Dr. Gianluigi Serianni

Co-Supervisors at Università degli Studi di Padova (Home University):
Prof. Emanuele Sartori
Dr. Matteo Agostini

Supervisor at Ghent University (Host University): Prof. Geert Verdoolaege

Ph.D. student: Margherita Ugoletti

Padova, January 2022

A Chiara

Abstract

The goal of this thesis work is the study of the beam physics of the negative ion beam for ITER HNB. A new diagnostics is installed on SPIDER, the full-size prototype of ITER negative ion source: the visible tomography. It is composed of a set of visible cameras which measure the light emitted by the beam particles when they interact with the background gas. An algorithm to reconstruct through tomographic inversion the two-dimensional pattern of the beam emission is developed, and the reconstructed profiles are adopted to study the homogeneity of the beam current, also with the support of a model to directly correlate the beamlet emission with the beamlet current density. Thanks to the masking of most of the apertures composing SPIDER multi-beamlets negative ion beam, the single-beamlet divergence is estimated through the Gaussian fit of the 1D beam profiles.
The results obtained by this new technique are utilized to investigate the beam features as a function of the main source and accelerator parameters, integrating the information provided by all the other diagnostics available. A strong correlation between the beam properties and the plasma features is found, thus a deep investigation of the source plasma is carried out. The beam homogeneity depends on the uniformity of both electrons and negative ions at the extraction region, in order to obtain identical beamlet optics at all the apertures and to avoid localised heating of the extraction grid due to the co-extracted electrons. The estimation of the single-beamlet current density is exploited to better interpret the spectroscopic measurements both close to the grid system (together with the electrostatic probes data), and inside the drivers. This experience is fundamental for the future operation at full performances, when the characterization of the single beamlet will be more challenging. The various operational regimes explored, both with and without caesium evaporation, are investigated to improve the understanding of the physics behind the generation and extraction of a large negative ion beams, when the principal source and accelerator control parameters are varied. This is the first comprehensive analysis of the experimental data measured during the experimental campaign of SPIDER experiment, and the performances achieved in term of beam divergence and homogeneity, as well as beamlet current density and co-extracted electrons currents are presented.

Abstract (Italiano)

L'obiettivo di questo lavoro di tesi è lo studio della fisica del fascio di ioni negativi per l'iniettore di particelle neutre di ITER. Una nuova diagnostica è stata installata su SPIDER, il prototipo a grandezza naturale della sorgente di ioni negativi di ITER: la tomografia visibile. È composta da una serie di telecamere visibili che misurano la luce emessa dalle particelle del fascio quando interagiscono con il gas di fondo. Eśtato sviluppato un algoritmo per ricostruire tramite inversione tomografica il pattern bidimensionale dell'emissione del fascio, e i profili ricostruiti sono stati utilizzati per studiare l'omogeneità della corrente del fascio, anche con il supporto di un modello per correlare direttamente l'emissione di un beamlet con la sua densità di corrente. Grazie al mascheramento della maggior parte delle aperture che compongono il fascio di ioni negativi di SPIDER, si è stimata la divergenza del singolo beamlet attraverso il fit gaussiano dei profili 1D del fascio.
I risultati ottenuti da questa nuova tecnica sono stati utilizzati per studiare le caratteristiche del fascio in funzione dei principali parametri della sorgente e dell'acceleratore, integrando le informazioni fornite da tutte le altre diagnostiche disponibili. Poichè si è trovata una forte correlazione tra le proprietà del fascio e le caratteristiche del plasma, si è studiato nel dettaglio anche il plasma della sorgente. L'omogeneità del fascio dipende dall'uniformità sia degli elettroni che degli ioni negativi nella regione di estrazione, al fine di ottenere la stessa ottica per tutti i beamlet ed evitare il riscaldamento localizzato della griglia di estrazione a causa degli elettroni co-estratti. La stima della densità di corrente del singolo beamlet viene sfruttata per interpretare meglio le misure spettroscopiche sia vicino alle griglie (insieme ai dati delle sonde elettrostatiche), sia all'interno dei driver. Questa esperienza è fondamentale per il futuro funzionamento di SPIDER a pieno regime, quando la caratterizzazione del singolo beamlet sarà più difficile da ottenere. I vari regimi operativi esplorati, sia con che senza evaporazione del cesio, sono stati analizzati per migliorare la comprensione della fisica della generazione e l'estrazione di un grande fascio di ioni negativi, quando vengono variati i principali parametri di controllo della sorgente e dell'acceleratore. Questa è la prima analisi completa dei dati raccolti durante la campagna sperimentale dell'esperimento SPIDER, e sono presentate le prestazioni ottenute in termini di divergenza e omogeneità del fascio, così come la densità di corrente del beamlet e le correnti di elettroni co-estratti.

Abstract (Dutch)

Het doel van dit proefschrift is de studie van de bundelfysica van de negatieve ionenbundel voor ITER HNB. Een nieuwe diagnostiek werd geïnstalleerd op SPIDER, het prototype op ware grootte van de negatieve ionenbron op ITER: de zichtbare tomografie. Deze bestaat uit een reeks zichtbare camera's die het licht meten dat wordt uitgezonden door de bundeldeeltjes wanneer zij interageren met het achtergrondgas. Er werd een algoritme ontwikkeld om door middel van tomografische inversie het tweedimensionale patroon van de bundelemissie te reconstrueren, en de gereconstrueerde profielen werden gebruikt om de homogeniteit van de bundelstroom te bestuderen, mede met behulp van een model om de emissie van de deelbundels direct te correleren met hun stroomdichtheid. Door het grootste deel van de aperturen af te dekkenvan SPIDERs negatieve ionenbundel met meerdere deelbundel, werd de divergentie van elke deelbundel geschat via een Gaussiaanse fit van de 1D-bundelprofielen.
De met deze nieuwe techniek verkregen resultaten werden gebruikt om de bundeleigenschappen te onderzoeken als functie van de belangrijkste bron- en versnellerparameters, waarbij de door alle andere beschikbare diagnostieken verstrekte informatie werd geïntegreerd. Er werd een sterke correlatie gevonden tussen de eigenschappen van de bundel en die van het plasma. Daarom werd, een diepgaand onderzoek van het bronplasma gevoerd. De bundelhomogeniteit hangt af van de uniformiteit van zowel elektronen als negatieve ionen in het extractiegebied, om identieke optische karakteristieken van de deelbundels te bekomen bij elke apertuur en om plaatselijke verhitting van het extractierooster door de meegeëxtraheerde elektronen te voorkomen. De schatting van de stroomdichtheid van de afzonderlijke deelbundels werd benut om de spectroscopische metingen beter te kunnen interpreteren, zowel dicht bij het rastersysteem (samen met de gegevens van de elektrostatische sondes), als binnenin de drivers. De hierbij verworven ervaring is van fundamenteel belang voor de toekomstige operatie bij volle performantie, wanneer de karakterisering van de afzonderlijke deelbundels een grotere uitdaging zal vormen. De verschillende onderzochte operationele regimes, zowel met als zonder cesiumverdamping, werden onderzocht om een beter inzicht te krijgen in de fysica achter het genereren en extraheren van een grote negatieve ionenbundel, wanneer de belangrijkste bron- en versnellerparameters worden gevarieerd. Dit is de eerste uitgebreide analyse van de experimentele gegevens die zijn gemeten tijdens de experimentele campagne van het SPIDER-experiment. De bereikte prestaties in termen van bundeldivergentie en -homogeniteit, alsmede de stroomdichtheid van de deelbundels en mede-geëxtraheerde elektronenstromen, worden in dit werk gepresenteerd.

List of Acronyms

HNB	Heating Neutral Beam
NI-NBI	Negative Ion - Neutral Beam Injector
SPIDER	Source for the Production of Ions of Deuterium Extracted from a Radio-frequency plasma
MITICA	Megavolt ITER Injector and Concept Advancement
NIO1	Negative Ion Optimization phase 1
BUG	BAvarian Test Machine for Negative Ion Upgrade
NIFS-RNIS	National Institute for Fusion Science - Research Negative Ion Source
LPGP	Laboratoire de Physique des Gaz ed des Plasmas, University Paris-Saclay
RFEA	Retarding Field Energy Analyser
CFC	Carbon Fiber Composite
LP	Langmuir Probe
BES	Beam Emission Spectroscopy
STRIKE	Short-Time Rectractable Instrumental Kalorimeter Experiment
SART	Simultaneous Algebraic Reconstruction Technique
LoS	Line-of-Sight
RMS	Root Mean Square
PG	Plasma Grid
EG	Extraction Grid
GG	Grounded Grid
BP	Bias Plate
CESM	Co-extracted Electrons Suppression Magnet
ADCM	Alternate Deflection Compensation Magnet
P, P_0	Perveance, normalized perveance
G1-G4	Group1-Group4. From top to bottom, they indicate the 4 beamlet groups into which SPIDER beam is divided.
S1-S4	Segment1-Segment4. From top to bottom, they indicate the 4 segments into which SPIDER source is divided. Each segment corresponds to a beamlet group.
B1-B28	Beamlet1-Beamlet28. They indicate the 28 open beamlets composing SPIDER beam during experimental operations with a limited number of extracted beamlets.
ISBI	Current flowing to bias the Plasma Grid
ISBP	Current flowing to bias the Bias Plate
V_{PG}	Plasma Grid potential
V_{BP}	Bias Plate potential

EGPS	Extraction Grid Power Supply
$\boldsymbol{U_{extr}}$	Extraction voltage
AGPS	Acceleration Grid Power Supply
$\boldsymbol{U_{acc}}$	Acceleration voltage
R	Acceleration to Extraction voltage ratio
$\boldsymbol{I_{filter}}$	Current flowing through the Plasma Grid to generate the magnetic filter field
SF	Standard Filter. Standard direction of the magnetic filter field current (from top to bottom of the PG).
RF	Reversed Filter. Reversed direction of the magnetic filter field current (from bottom to top of the PG). When specified, it indicates the radio-frequency power.
PL	Plasma Light

Contents

Summary

The world energy consumption is continuously augmenting, not only because of the population growth but also because of the more energy consuming life style of the world population. To satisfy this thirst for energy, fossil fuel consumption is increasing dramatically, starting a relentless global warming process which is causing the climate to change. In this scenario, new sources of energy with zero environmental impact play a crucial role. Among these, nuclear fusion is one of the most attractive because of several advantages.
ITER, latin word for *the way*, is an international project aiming at realizing a nuclear fusion reactor capable of producing energy based on fusion reactions between light nuclei. Located in southern France, it will be the world's largest *tokamak* aiming at producing 500 MW of fusion power from 50 MW of input power and at demonstrating the successful control of the plasma and the fusion reactions.
One of the main requirements for achieving fusion is to heat the plasma at very high temperature, in the order of tens of keV. Neutral beam heating is now the most important method for plasma heating in almost all fusion experiments. High energy neutral particles when are injected in the plasma vessel are unaffected by the magnetic fields, and travel along straight-line trajectories until they are ionized by the background plasma, with consequent transfer of energy during the collisions. The neutral beam energy required to heat the core of the tokamak plasma is proportional to the plasma minor radius and to the density: in the case of ITER, about 1 MeV is required.
Neutral beam injection from negative ions (NI-NBI), mainly H^- and D^-, is much more efficient in producing high energy neutral beams than positive ions, even if their production presents harder issues with respect to the production of positive ions.
The ITER Neutral Beam Test Facility is hosted in Padova, at Consorzio RFX, and includes the two experiments SPIDER and MITICA. Respectively, they aim at developing and testing the full-size ITER negative ion source and the full-size heating neutral beam injectors. In particular, ITER will initially be equipped with two heating neutral beam injectors designed to deliver a total of 33.3 MW of either 1 MeV D or 0.87 MeV H to the ITER plasma for up 3600 s in D, 1000 s in H.
SPIDER test facility is in operation since 2018. It is a full-size prototype of ITER NBI negative ion source. It can operate both with hydrogen and deuterium plasma, produced inside four pairs of drivers, aiming to provide particles with an energy of 110 keV using an accelerator composed by three grids (the Plasma Grid, facing the plasma, the

Extraction Grid, from which the negative ions are extracted and the Grounded Grid, which accelerates the ions up to the energy required), with a beam duration up to 3600 s. Once generated inside the drivers, the plasma expands in the expansion region, where the electron temperature is decreased thanks to a magnetic filter field, thus decreasing the destruction probability of the negative ions. The beam is subdivided into 1280 beamlets, most of which were masked due to pumping system limitations during the entire SPIDER experimental operation. SPIDER goals are to demonstrate the ITER requirements for the negative ion and co-extracted electron current densities, for pulses up to one hour, together with the beam optimization in terms of divergence and homogeneity, imposed by the required operation of the 1 MeV beam necessary for ITER beam sources. Furthermore, another SPIDER's goal is to prove the capability of completely characterizing the negative ion source and beam through a set of diagnostics as complete as possible. The plasma in the source is studied both inside the drivers and next to the Plasma Grid, in the region where negative ions are produced and then extracted, while optical, electrical and calorimetrical diagnostics are used to characterize the beam properties.

The goal of this thesis is the development of the visible tomography as a new diagnostic to characterize the large size negative ion beam of SPIDER, in terms of beam divergence and homogeneity of the beam current. The results obtained by this technique are then exploited to integrate the information supplied by the other diagnostics already available, aiming at better understanding the physics behind the production and the extraction of high energy negative ion beams. Being the beam strictly dependent on the plasma from which it is extracted, a deep investigation of the plasma properties inside the source is carried out, and the beam features are interpreted and explained starting from the analysis of the plasma itself.

SPIDER visible tomography is composed by 15 visible cameras looking perpendicularly at the beam through viewports all around the vacuum vessel. It is used for the first time to reconstruct the 2D beam pattern, through a tomographic inversion of line-integrated measurements of the visible radiation, originating from the interaction of the beam with the background gas. Tested at first on the negative ion beam of the source NIO1, this technique demonstrated its capability in reconstructing a small negative ion beam (composed of a matrix of 3x3 beamlets). A robust calibration of the set of line-integrated measurements is mandatory, both to compare relatively the data collected by the various cameras, and to know exactly where each sensor is looking at. The calibration of the 15 cameras composing SPIDER tomography diagnostic, both in laboratory and on-site is tested for the first time and validated. The calibrated signals are then used to reconstruct the emission pattern of the beamlets composing SPIDER beam during the entire experimental campaign. The algorithm chosen is the Simultaneous Algebraic Reconstruction Technique (SART), which is based on an error correcting procedure and on the pixel method: the beam emission pattern is subdivided in pixels, in which the emissivity ϵ_i of each pixel is unknown. Different number and sizes of pixels were tested,

and the limit and the resolution of the technique was studied. The reconstruction of both NIO1 and SPIDER beams demonstrated a good agreement between the experimental and the inverted profiles. Furthermore, a model was developed to directly correlate the beam emissivity to the beam current density, by taking into account both the energy of the beam particles and density of the the background gas in which they propagate, as well as the different species composing the beam at the position observed by visible cameras. When the beamlets composing a negative ion beam are isolated and distinguishable (as in the case of NIO1 and of SPIDER with most of the beamlets masked), this diagnostic allows also to estimate the single beamlet divergence, through the Gaussian fit of the 1D profile of the beamlets.
All these methods are validated by comparing the results obtained by the other beam diagnostics available on SPIDER, demonstrating for the first time the possibility of studying both the homogeneity and divergence of a large negative ion beam with this diagnostic.

A detailed study of SPIDER beam and source was then carried out. Low beam divergence is necessary to obtain an optimal transmission efficiency, reducing the heat loads on the NBI components, sputtering damages and secondary emission currents. The beam divergence is defined during the ion extraction and acceleration, starting with the extraction of ion beamlets from a plasma through multi-apertures electrodes. The shape of the *meniscus* (which is the boundary between the plasma and the negative ion beam), gives a first major contribution to the divergence, imposing with its curvature the initial focal length of the beamlets being extracted. It depends both on the plasma density and collisionality and on the electrostatic field generated by the extraction voltage. It is convenient to define the beamlet *perveance* at the meniscus surface (in analogy with diodes with curved emitters) and for direct comparison with beam simulation codes, so that it is correlated to the beam space charge at the meniscus. Along the beam acceleration, at the apertures of each electrode after the meniscus (i.e. for SPIDER triode accelerator, they are at the Extraction Grid and Grounded Grid apertures) an electrostatic lens is formed, which influences the beamlet focal distance, depending on the electric field strength of the opposite sides of the electrodes. In SPIDER, the ratio between the acceleration and extraction voltages determines the focal length which focuses the beam, thus characterizing what happens in the second accelerator gap. Furthermore, the energy distribution of negative ions at the meniscus plays a key role too in determining the beamlet divergence. All these parameters affecting the beam optics are analysed and discussed, both in surface and volume operation, starting from experimental measurements. The optimum ratio of the acceleration and extraction voltages is found to be between 9.5 and 10, as expected from simulations. The optimum beam divergence in volume is ~ 20 mrad, which decreases to ~ 12 mrad after caesium evaporation in the source, in the range of parameters that could be explored. A similar divergence has been also measured on NIO1 and BUG experiment (Garching IPP), two other existing radio-frequency driven negative ion sources. This value is still large with respect to the required one, and also from the value estimated through numerical simulations, when no transverse energy of negative

ions is assumed. In the design of SPIDER and MITICA, the contribution on the beam divergence of negative ion temperature was neglected, since a good benchmark between the experimental and simulated divergence was found in the existing arc-based sources of negative ions, even without including the negative ion temperature in the simulation codes. In this source type, the negative ion temperature measured is of few eV, and the beam divergence is lower than the required 7 mrad for ITER HNB. A significant spread in the energy distribution can result in a larger beam divergence, and this was measured experimentally both in an arc (NIFS-RNIS) and radio-frequency RF (SPIDER) negative ion source by the Retarding Field Energy Analyser probe. The results obtained when the source parameters were varied were compared, showing a wider energy distribution in the radio-frequency source with respect to the one in the arc source. In SPIDER, the dependence of the beam optics on the radio-frequency power, source pressure and magnetic filter field was studied, since all of them modify the plasma density in front of the extraction region. The extraction voltage was varied together with the acceleration voltage, with ratio fixed to 9.5 (optimum of beam optics), performing perveance scans in which the beam optics was determined by its space charge. The temperature of the PG was varied as well, and the comparison between the H and D beam was studied, to evaluate the isotope effect on the beam optics. From all these analyses, an important result is found: beamlets in different vertical position, as well as in diverse locations inside the beamlet group, behave differently. This highlights a beam dis-homogeneity which must be studied in detail.

To operate at the large current density and power required for ITER HNB, a beam non-homogeneity within 10 % is necessary, to avoid uneven heat load on the acceleration system, in particular by guaranteeing a uniform co-extracted electron current on the Extraction Grid. To develop a comprehensive idea of the origin of this beam dis-homogeneity experimentally found, a characterization of the plasma in the source was performed, starting from spectroscopic and electrostatic measurements. From the drivers to the extraction region, the plasma parameters are measured, to characterize the dis-homogeneity and to study where it originates from. Some main sources of dis-homogeneity are discovered. From the drivers to the extraction region, both the magnetic filter field and the polarization of the Bias Plate (BP) and Plasma Grid have an important role in determining the properties of the plasma. The magnetic filter field is necessary to reduce the electron temperature close to the extraction region, by increasing the survival probability of negative ions. It limits the flux of electrons from the drivers to the extraction region, also improving the plasma confinement inside the driver. It also induces cross-B drift on vertical direction, modifying the profile of the plasma in the expansion region. To further reduce the electron density in the extraction region, the PG can be positively polarized with respect to the source body, together with a dedicated Bias Plate, installed 20 mm away from the grid itself. They aim at reducing the co-extracted electron amount, but they also improve the plasma generation inside the driver.

In order to clarify the origins of the beam non uniformities that were identified, the region where the plasma is generated was investigated. Since the plasma is produced in

eight independent radio-frequency drivers, it must be verified whether dis-homogeneities can to be traced back to uneven plasma generation. From the measurements of the plasma light (H_α emission) in the drivers, a top-bottom and a left-right dis-homogeneity is found, both of them depending on the strength and direction of the filter field, as well as on the BP and PG polarization. When the filter field is in the *standard direction*, meaning that the current flows from the top to the bottom of the PG, a less dense plasma is measured in the drivers at the bottom of the source, the opposite occurs when the direction of the filter field is reversed. This top-bottom asymmetry depends also on the polarization of the BP and PG: as their polarization is increased, a larger plasma light is measured especially in the drivers affected the most by the filter field (at the bottom with standard field, at the top with reversed field). A left-right asymmetry of the plasma light collected in the pairs of driver of each segment in the standard filter configuration is also measured, in particular for the drivers at the bottom of the source, for which the left-right difference strongly increases with the filter field. When the filter direction is reversed, instead, a left/right ratio of the plasma light for each pair of drivers close to one is measured in all the segments, except in the segment at the top of the source; however, also in this case, the left-right asymmetry is reduced with respect to the standard field configuration. The plasma vertical profile is then studied in the expansion region, from line-integrated spectroscopic measurements, one for each pair of drivers, parallelly to the grid, and from the electrostatic data of the Langmuir probes installed both on the BP and on the PG. Different features of the plasma, in front of the BP and in front of the PG are found, thus confirming the relevance of the first in modifying the plasma profile and in producing different properties of the plasma close to the extraction region. The various operation regimes explored during the campaign without and with caesium are studied, to figure out how the plasma properties evolve when the main source parameters are varied. All the information gathered is then used to understand the beam features.
Both in volume and surface operation, a tight correlation between the beam behaviour and the plasma in the source is found. Due to the physics peculiarities which govern the two different ways of producing negative ions, the two regimes were analysed separately. The beam homogeneity was studied through the tomographic reconstruction of the 2D beam pattern, using the single beamlet emissivity as an estimation of the beam current density. With the extremely reduced number of beamlets used during that experimental campaign, the single-beamlet current is a direct measurement of the negative ion density sampled at the (80 and 28) open apertures. A lower beam emissivity at the bottom (top) of the beam in the standard (reversed) direction of the filter field is found, as observed in the plasma light in the drivers. This top-bottom difference is slightly reduced in volume operation as the BP and PG biases are increased, in both configurations of magnetic filter field. Since the beam properties are mostly studied with reduced radio-frequency power in surface operation, the effect of the bias is found to be stronger and in the opposite direction: it increases the top/bottom beam dis-homogeneity. The increment in the beamlet current density with caesium evaporation results in a further source of difficulty for the estimation of the uniformity of negative ion extraction: as the applicable

acceleration voltage was limited (45 kV), it was not possible to operate the extraction at perveance match while maintaining sufficient optimum voltage ratio (R=9.5-10), so that the beamlet transmission throughout the accelerator was not identical for all beamlets. This resulted in different fractions of negative ion loss, so that the beamlet current at full acceleration cannot directly be related to the extracted current density at the meniscus. Indeed, as suggested by the spectroscopic measurements, a larger negative ion density is found at the top of the source, in the standard field configuration, resulting in a non optimal transmission of the extracted beamlets through the accelerator (beamlet scraping on the extraction grid), for low extraction voltage. Furthermore, both with and without caesium evaporation, a bell-shaped profile of the beamlet current density inside each beamlet group is measured, which is enhanced as the filter field is increased. This could be related to the more peaked plasma density profile inside the drivers, when the filter field is increased.

More in detail, in Chapter 1, the motivations behind the development of nuclear fusion as a new source of green energy are described, together with ITER experiments and the Neutral Beam Injection. The physics behind the production and extraction of negative ions is described in Chapter 2. In Chapter 3, the diagnostics used to study SPIDER source and beam are presented and in Chapter 4 beam emission tomography is described in detail. The beam divergence is studied in Chapter 5 while in Chapters 6 and 7, the plasma and beam homogeneity is discussed.

Chapter 1

Controlled nuclear fusion and Neutral Beam Injectors

The worldwide thirst of energy is continuously increasing, because of the population growth and of the more energy consuming world life style. The Human Development Index (HDI), which defines the growth of a country in terms of human development, i.e. a long and healthy life, being knowledgeable and have a decent standard of living, is strictly tied to the energy consumption [1]. A continuously increasing quantity of energy is required by developed and under development countries, which corresponds to a larger CO2 emission per year per capita. The dramatic increase in fossil fuel consumption has started a relentless global warming process which is causing the climate change. This increment from 1965 to 2020 is reported in Fig.1.1: even if developed countries are locally decreasing their fossil fuel consumption, it remains a necessary tool for developing countries, resulting in a continuous growth of demand. All the nations are collaborating

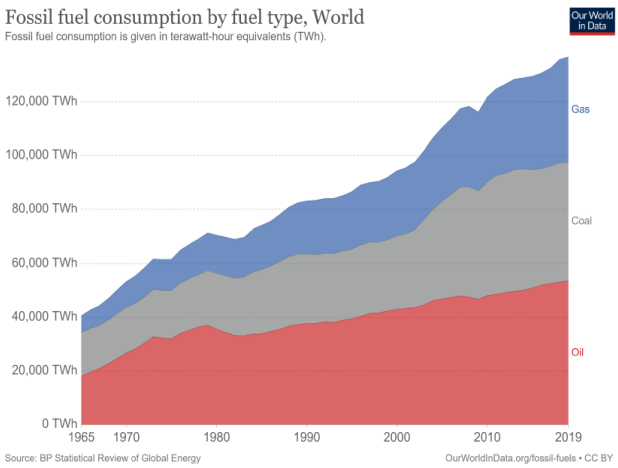

Figure 1.1: *Worldwide fossil fuel consumption by fuel time from 1965 to 2020.*

to contain the temperature increase within 2° C with respect the pre-industrial era, making mandatory the development of alternative energy sources to reduce the use of fossil fuel. International agreements, such as the Kyoto protocol in 1997 and the Paris agreement in 2016 [2], testify these joint efforts. In this scenario, renewable energies play a crucial role. Among these, the nuclear fusion is one of the most attractive because of several advantages as it will be described in next section.

1.1 Nuclear fusion as a new source of energy

Nuclear fusion is the inverse process of nuclear fission, by which two or more atomic nuclei join together, or "fuse", to form a single heavier nucleus. In this process, some of the mass of the fusing nuclei is converted into the energy released. A fusion reaction occurs when two atomic nuclei are close enough to overcome the Coulomb barrier and to assemble in generating a heavier one. Part of the nuclear binding energy is converted into kinetic energy of the products, if the nuclear fusion process ends in a more stable final atomic configuration (lower total binding energy per nucleon). This is one of the most basic form of energy production in the Universe: thermonuclear fusion reactions happen continuously into the Sun and all other stars. With few exceptions, nuclear fusion reactions involving elements lighter than Iron are exo-energetic. There are extreme astrophysical events that can lead to short periods of fusion with heavier nuclei: this is the process that gives rise to nucleosynthesis, the creation of the heavy elements during events such as supernovae [3].
The nuclear fusion as a new source of energy is attracting because of several advantages. At first, it will release no atmospheric pollution: the most studied fusion reaction produces helium, which is an inert gas, and tritium, which has an half life of 12 years (much smaller than typical radioactive wastes produced by nuclear fission). The only relatively long-term radioactivity is in the fusion reactor structural components, as a consequence of the neutron collisions, with a lifetime shorter than 100 years. Its fuel, composed by deuterium and tritium, is equally available in all locations of the Earth at a lower price than those of fissionable isotopes. Deuterium is present in the oceans water in a concentration of 33 g per ton, while tritium can be obtained exploiting nuclear reactions occurring directly inside the reactor. It exhibits an inherently safe system: even the worst conceivable accident would not have repercussions on the surrounding environment and, due to the hardness of achieving nuclear fusion reactions, small perturbations in reactor conditions will terminate them. Furthermore, its power yield per mass is larger than the other sources: burning 1kg of DT mixture would lead to an energy release of $3.4 \cdot 10^{14}$ J, which corresponds to 3.9 GW during a period of 24 hours [4].
The first step towards nuclear fusion was made in 1932 by Mark Oliphant, who discovered heavy hydrogen isotopes, starting from Ernest Rutherford's earlier experiments on nuclear transmutations. In the 40s, in the framework of the Manhattan Project, military purposes prompted efforts to achieve nuclear fusion, which it was not obtained until 1951. On November 1, 1952, the Ivy Mike Hydrogen bomb test signed the first large

scale explosion from nuclear fusion reactions [5]. The idea of an international collaboration to achieve the control of nuclear fusion energy for civil application was born in the 1980s, and became reality on 21 November 2006 by way of an international agreement signed in Paris to establish "The ITER international Fusion Energy Organization for the Joint Implementation of the ITER Project" [6], which will be described in details in next sections.

1.1.1 Basis of nuclear fusion

The stability of a nucleus is determined by its binding energy, defined as the energy required to disassemble a nucleus into the free, unbound neutrons and protons it is composed of. It corresponds to the equivalent energy of the mass defect, i.e. the difference between the mass number of a nucleus and its measured mass. The larger the binding energy per nucleon in the atom, the greater its stability. Fusing two nuclei of very small mass, such as hydrogen, will create a more massive nucleus and the process releases energy. In Fig.1.2, the binding energy as a function of the mass number is shown. As it

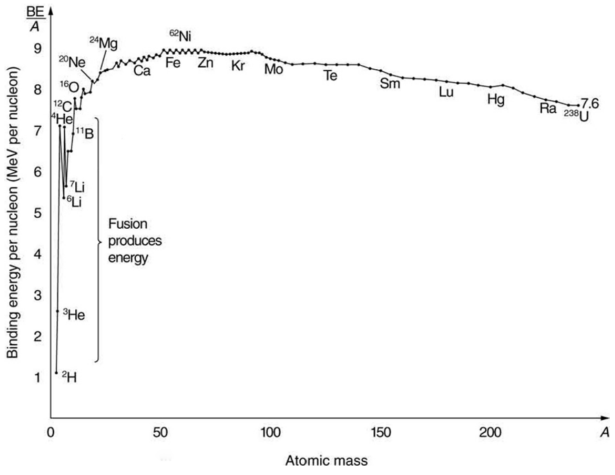

Figure 1.2: *Average binding energy per nucleon as a function of the mass number A.*

can be noticed, the curve steeply increases at low mass number, reaches a peak at A=56 (Fe), and then slowly decreases, up to A=238 (U). This shows how fusion reactions are energetically convenient for lighter nuclei, with $A < 56$, while fission is more convenient for heavier nuclei, with $A > 56$. The largest gain of energy is between the He and H atoms (largest binding energy difference); it is therefore of interest to pursue a fusion reaction that will have this atom as product. For a fusion reaction between two nuclei to occur, as for instance between deuterium (D) and tritium (T) which are both isotopes of hydrogen (H), they have to be close enough to overcome electromagnetic interaction by strong interaction ($\sim 10^{-15}$ m). In fact, for larger distances, the positive charge of the nuclei repels each other; once the Coulomb barrier, i.e. the repelling electrostatic force, is overcame, the fusion reaction can take place (see Fig.1.3). This means that,

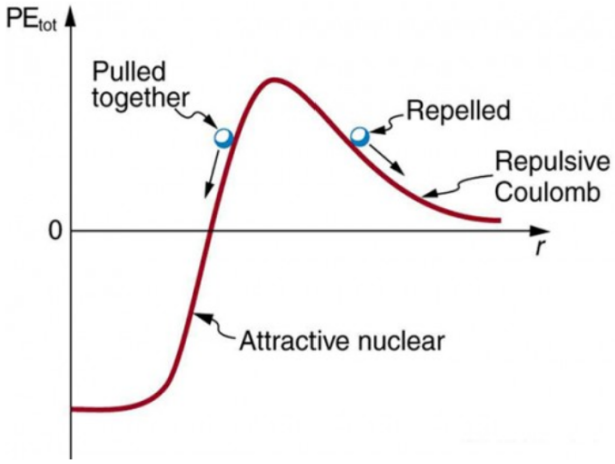

Figure 1.3: *Schematic representation of the potential energy of a Deuterium-Tritium reaction as a function of their relative distance.*

in order for a reaction to occur, the nuclei must have a large initial energy, such that they can approach each other closely and overcome the barrier. The whole problem of fusion research becomes the generation and sustainment of the conditions under which a sufficient amount of fusion reactions occurs. The most promising fusion reactions are ones which include H and its isotopes and He, and they are

$$\begin{aligned} {}^2_1D + {}^3_1T &\longrightarrow {}^4_2He + {}^1_0n + 17.6\ MeV \\ {}^2_1D + {}^2_1D &\longrightarrow {}^3_2He + {}^1_0n + 3.3\ MeV \\ {}^2_1D + {}^2_1D &\longrightarrow {}^3_1T + {}^1_1H + 4.03\ MeV \\ {}^2_1D + {}^3_2He &\longrightarrow {}^4_2He + {}^1_1H + 18.3\ MeV \end{aligned} \tag{1.1}$$

The energy released depends on the mass difference between the product and resulting nuclei [7]. The probability of a fusion reaction to occur can be described in terms of reactivity $< \sigma v >$, which is the probability of reaction per unit time and per unit density of target nuclei; σ is the reaction cross section, v the velocity of the particles and the operator $<>$ integrates over the particle velocity distribution function. Figure 1.4 shows how the reaction between D and T is the one with the highest probability at lower energy and, for this reason, it is the one of major interest. The ideal energy at which future fusion reactors will operate is between the energy with the largest particle density, assuming a Maxwell distribution of the particles, and the one for which the cross section is largest. They are supposed to achieve an energy comprises between 5 and 12 keV, which corresponds to a temperature of roughly 100 million kelvin. The matter at these temperatures is fully ionized and it is in the state of plasma. Thermonuclear fusion reactors necessitate thus to find a way to prevent the rapid loss of particles which is in the order of μs for a typical reactor size of 10 m, by considering the thermal velocity of

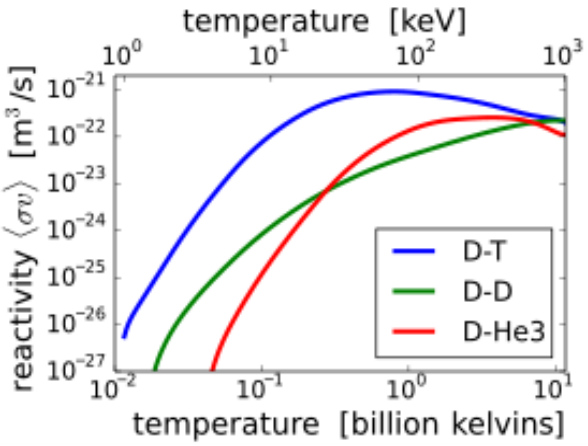

Figure 1.4: *Reactivity of the reactions listed in Eq. 1.1 as a function of the ion temperature.*

D ions and electrons at 10 keV, respectively equal to 10^6 and $6 \cdot 10^7$ m/s.
One way to confine the particles is through the magnetic confinement.

1.1.2 Magnetic confinement

Magnetic confinement exploits magnetic fields to confine the plasma. Charged particles inside a magnetic field, in fact, are affected by the Lorentz force which forces them to gyrate around the magnetic field lines, in a orbit characterized by the Larmor radius

$$\rho = \frac{m v_{th}}{ZeB} \tag{1.2}$$

This radius depends on the particles mass m, thermal velocity v_{th} and charge Z and on the magnetic field strength. For a magnetic field of 5 Tesla and a temperature of 10 keV, the Larmor radius is 4 mm for the deuterium ions and 0.07 mm for the electrons. Sources of complication are the fact that the particles are free to move along the magnetic field lines and that the currents in the plasma influence the topology of the magnetic field. Since this method of confinement works only for charged particles, the neutrons produced by the fusion reactions are free to leave the plasma on a time-scale of microseconds, resulting in a large flux on the material walls. Fusion reactors will convert this heat flux in deliverable energy.
In order to be economically sustainable, the energy delivered to a fusion reactors to keep the reactions going must to be lower than the energy released by fusion reactions themselves. Its threshold is defined by the Lawson criterion, which links the plasma density and confinement time τ, i.e. the time in which the particles are confined within the plasma [8]. It can be expressed as

$$nT\tau > 5 \times 10^{21} m^{-3}\ keVs \tag{1.3}$$

and it is used as a figure of merit to compare the performances of various existing fusion devices throughout the years, by comparing their technological advancements [9]. The reactor efficiency is defined by the ratio $Q = P_{fusion}/P_{heat}$ where P_{heat} is the power brought to the plasma by external heating systems and P_{fusion} the power released by fusion reactions.

Tokamak

The most promising magnetic configuration is the *tokamak*: invented in the 1950s by Soviet physicists Igor Tamm and Andrei Sakharov, it was inspired by an original idea of Oleg Lavrentiev [10]. In this configuration, charged particles are confined inside a torus-

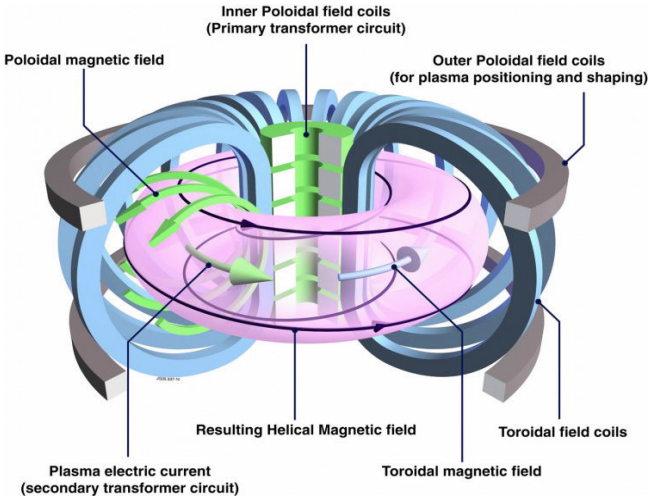

Figure 1.5: *Schematic representation of a tomakak device.*

shape vessel, by a combination of magnetic fields, with rotational symmetry around the vertical axis. A schematic representation of them is shown in Fig.1.5. In a tokamak, three superimposed magnetic fields enclose the plasma: a ring-shaped field produced by plane external coils, the field produced by the current flowing in the plasma and a vertical field which fixes the position of the current in the plasma. The field lines of the first two combined field run helicoidally around the torus centre. To lowest order, the particles gyrate around the field lines while moving freely along the field, ignoring the drift motion due to the inhomogeneous magnetic field. Because of the divergence-free nature of the magnetic field, it can be proven that such a configuration is the simplest possible topology in which a field line can remain in a finite volume of space. This is also possible since the product between current density and the magnetic field $j \times B$ balances the kinetic pressure.

1.2 ITER project

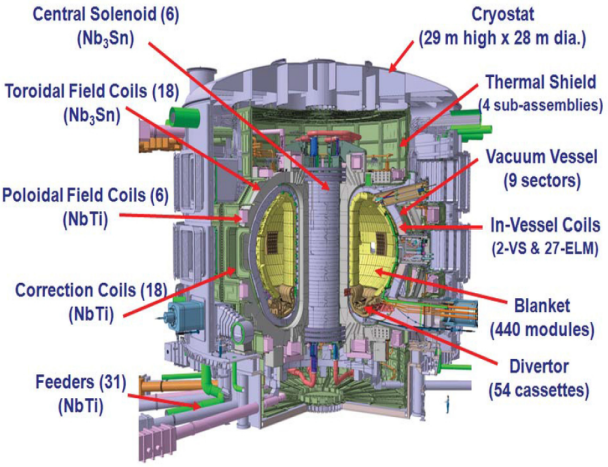

Figure 1.6: *ITER principal components.*

The International Thermonuclear Experimental Reactor ITER is an international nuclear fusion research and engineering project [6]. It is a results of a collaboration born in the 80s with the International Tokamak Reactor (INTOR). A first conceptual design was agreed upon in 1990 and it was finally completed in the 2007. The construction of the experiment at Cadarache (in France) was decided in 2006 and the ITER organization was created in 2007, officializing the beginning of the project, with an international agreement signed in Paris to establish "The ITER international Fusion Energy Organization for the Joint Implementation of the ITER Project". Nowadays, 35 nations are collaborating to build the world's largest tokamak. From 50 MW of input power, the ITER machine is designed to produce 500 MW of fusion power (Q=10), the first fusion experiment to produce net energy. A computer view of ITER is given in Fig.1.6. ITER's purpose is to demonstrate the feasibility of fusion as a new source of energy, and to test the technologies that would be needed to operate a fusion power plant, including cryogenics, heating, control and diagnostics systems, plus remote maintenance. The ITER magnet system will be the largest superconducting magnetic system ever built: composed of thousand tonnes of magnets (51 GJ of stored magnetic energy), it becomes superconducting when cooled with supercritical helium at 5 Kelvin. The toroidal field is produced by eighteen "D"-shaped toroidal field coils, placed around the vacuum vessel, designed to produce a total magnetic energy of 41 GJ and a maximum magnetic field of 11.8 T. The poloidal field system instead is composed by six ring-shaped coils situated outside of the toroidal field magnet structure, aimed to shape the plasma and to contribute to its stability by keeping it away from the walls. With the largest diameter of 24 meters, these are designed to produce a total magnetic energy of 4 GJ and a maximum magnetic field of 6 T [11].

1.2.1 Additional heating system

To achieve the elevated energy necessary to ignite and sustain the fusion reactions, ITER needs to heat the plasma to tens of keV. External heating system are thus necessary to obtain these conditions. Initially, the plasma is heated by *ohmic heating*, by the plasma current induced by the central solenoid (to generate the poloidal magnetic field). Since this heating is produced by Joule effect, as the electron temperature starts to increase, the plasma resistivity η decreases by $\sim 1/T^{3/2}$, so the ohmic heating becomes irrelevant once high temperatures are reached. To increase the plasma temperature, two main technologies are employed: transfer energy to the plasma through electromagnetic waves and by collisions with high momentum neutral particles.
Electromagnetic waves with the correct frequency are capable to heat the plasma by resonating with the its natural frequencies, leading to a large absorption of power, as heat and non-inductive current. For ITER, a system composed by ion cyclotron (IC), electron cyclotron (EC) and possibly lower hybrid (LH) will provide high energy and current drive inside the vessel. Each of those are required to couple up to 20 MW heating power to the plasma [12].
The other ITER heating and current drive system will be composed by Neutral Beam Injectors (NBI), whose principle of operation is described in details in next section. The NBI heating systems transfer energy to the fusion plasma through collisions of fast hydrogen or deuterium particles: being neutrals, they are not affected by the magnetic fields and they are free to heat the confined ions through collisions. After entering the plasma the neutral beam is ionized and, consequently, confined by the magnetic field. NBI systems can thus drive a toroidal current if the beam is injected tangentially to the fusion chamber.

1.3 Neutral beam injectors

Neutral beam heating was developed in the early 1970's and it is now the most important method for plasma heating in almost all fusion experiments. A beam of high-energy (i.e. much higher than the desired plasma temperature of 15 keV) neutral particles, being without charge, are unaffected by the magnetic field and travel along straight-line trajectories until they are ionized by collisions with the background plasma. Once ionized, the beam particles are magnetically confined and they become part of the plasma, contributing to the high-energy tail of the deuterium distribution function.
The neutral beam particles H_b^0 are trapped into the plasma through the following reactions:

$$\begin{aligned} H_b^0 + H_p^+ &\longrightarrow H_b^+ + H_p^0 \ (charge\ exchange) \\ H_b^0 + H_p^+ &\longrightarrow H_b^+ + H_p^+ + e^- \ (ionization\ by\ ions) \\ H_b^0 + e^- &\longrightarrow H_b^+ + 2e^- \ (ionization\ by\ electrons) \end{aligned} \tag{1.4}$$

where the subscript b and p stand for *beam* and *plasma* [13]. Neutral beam injections with negative ions (NI-NBI), mainly H^-, are much more efficient in producing high energy neutral beams than positive ions, because of higher neutralisation efficiency at energies higher than 100 keV [14]. This is shown in Fig.1.7, where the neutralization efficiency for both positive and negative deuterium ions as a function of their energy is represented. Because of the very low affinity of the hydrogen ion H^- A=0.75 eV, ions

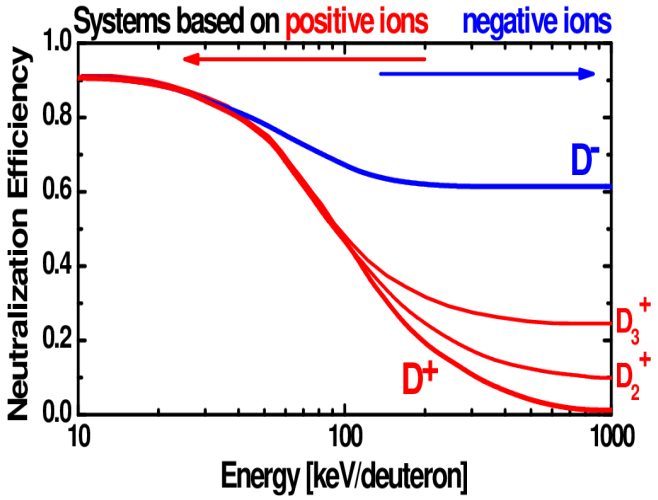

Figure 1.7: *Neutralization efficiency of positive and negative ions as a function of their energy [15].*

can easily lose the electron and become neutral. Even if there are a lot of problems in producing a high energetic beam of negative ions with respect to the positive one, NI-NBI with a beam energy of 1 MeV are required for the next generation tokamaks, like ITER. NI-NBI system consists in a beam source of negative ions, an accelerator and a neutraliser. Negative ions are produced in the plasma source. After the extraction they are accelerated to a high energy before crossing a charge exchange cell where they are neutralized. The neutralization is only partial and the remaining ions are deflected magnetically and sent to a dump. Once exiting the neutraliser, the beam will be composed for the 60% of neutral atoms, 20% of negative hydrogen ions H^- and 20% of positive hydrogen ions H^+ [16].

Negative ions based neutral beam injector (NI-NBI) is composed by four parts:

- Plasma source. The ions to be extracted and accelerated are produced into a confined plasma source. The plasma in large volume devices can be generated by hot cathodes (heated filament of bow discharge) or radio-frequency (RF) antennas (inductively coupled plasma), standing either inside or outside the discharge.

- Acceleration stage. The negative ions extracted from the source are accelerated by a voltage drop between the grids in the accelerating column. The ions exiting

from the source form a beam, or a group of smaller beams, referred to as beamlets, that are later combined to form a single larger beam.

- Neutralizer. In this region, the ion beam particles are neutralized, conserving the high kinetic energy and optimal focus. The well-focused beam of highly energetic neutral particles can then propagate through the NBI duct into the tokamak's plasma.
- Residual ion dump system. A dedicated magnetic field deflects both the non-neutralized negative ions and the positive ions, collecting them.

In the following, NI-NBI negative ions source and accelerator are described in details, highlighting both their technological and physical properties.

1.3.1 Plasma source

For fusion applications, two types of sources are developed:

- Arc driven ion sources. Electrons are emitted by thermoionic effect from heated tungsten filaments. The arc discharge is generated by negatively polarizing the tungsten filament (cathode) with respect to the walls of the plasma chamber (anode). The plasma density is directly related to the electrical power applied to the filaments, P_{arc}: filament voltage and current determine the thermoionic emission rate and intensity of the electron avalanche.
- Radio-Frequency driven ion sources. The electrons are accelerated by an oscillating field (whose field frequency is usually around 1 MHz), until their kinetic energy is large enough to ionize the atoms and to generate an inductively coupled plasma.

Both types of source have pros and cons: for the arc sources, the filaments are eroded by the plasma and can break, imposing frequent and unpredictable maintenance of the source. The radio-frequency plasma, instead, is more unstable since it is affected by the typical radio-frequency oscillations and by cross-talking of different generators, making more difficult to achieve a stable plasma. A schematic representation of both types of source is given in Fig.1.8; typical plasma parameters inside each region the plasma source is composed of are indicated. Once generated in the so-called driver, in which the electron density is $n_e \sim 5.10^{18}\ m^{-3}$ and temperature $T_e \sim 10$ eV, the plasma expands in a larger region (expansion region), where electron density and temperature are reduced typically by a factor of 10. The ions entering the expansion region have a density about 10 times lower than the electrons. In this region, the plasma is confined by permanent magnets, producing a some tenth of Tesla magnetic field at some millimetres of the plasma source edges, where they are installed; this type of structure is called *tandem* source. Once the plasma reaches the extraction area, an electrostatic field extracts negative ions (together with a large amount of unwanted electrons) through the apertures of the so-called Plasma Grid (PG). To extract the 10-50 A of negative ion current required by the large machines for fusion experiments, a current density around 100-300

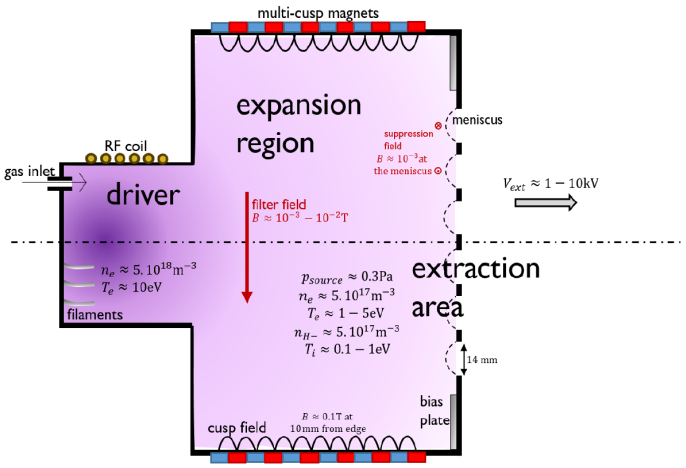

Figure 1.8: *Schematic representation of a NBI source and its components, with radio-frequency (top) or filament (bottom) driver; typical parameter of the source plasma are indicated [17].*

$H^- + e^- \rightarrow H + 2e^-$	Electron stripping
$H^- + H_x^+, Cs^+ \rightarrow H + H_x, Cs$	Mutual neutralization
$H^- + H \rightarrow e^- + H_2$	Associative detachment
$H^- + H, H_2+ \rightarrow e^- + 2H, +H + H_2$	Collisional detachment

Table 1.1: List of negative ion destruction processes.

A/m^2 is usually necessary, over an extraction area around 0.1-0.2 m^2 [18]. For nominal operations, the power transmitted to the plasma is around 10-100 kW.

1.3.2 Expansion region: magnetic filter field and biases

Due to the low binding energy (0.75 eV) of the second electron in a negative H (or D) ion, the electron can be easily stripped, i.e. removed through collisions with the background particles. In order to preserve the negative ions, collisions with the background particles and with energetic electrons must be avoided: low-pressure, low temperature plasmas are then mandatory to reduce the destruction rate of the negative ions, thus improving the efficiency of the ion source. The main processes responsible of negative ions destruction are listed in Table 1.1 [19]. For electron temperature larger than 2 eV, the most effective destruction process is the electron stripping [20]: a low electron temperature and density close to the extraction region is thus needed, not only to reduce the amount of co-extracted electrons, but also to enhance the negative ion survival probability. The rate coefficient of the mutual neutralization with positive ions is by one order of

magnitude larger than the one with atoms but, since the atomic and molecular densities are usually two orders of magnitude larger than the positive one [21], it is less relevant; typical atomic and molecular densities are $n_H \approx n_{H_2} \approx 10^{19} m^{-3}$, those of positive ions are $n_{H_x^+} \approx 10^{17} m^{-3}$.
As reported in Fig.1.8, electrons enter the expansion region with ~ 10 eV of energy and $\sim 10^{18}\ m^{-3}$ of density. To avoid negative ions destruction and to reduce the large electronic flux towards the PG, resulting in a high electron beam extracted together with the negative ion one, the electrons energy has to be reduced. The high energetic electrons are eliminated from the expansion and extraction region by generating a so-called *filter field* inside the source. It magnetizes relatively energetic electrons, resulting in a reduction of electron energy to few eV via collisions with neutral particles and Coulomb collisions with electrons, during their diffusion from the driver to the extraction region. In large sources the filter field is usually generated through a current flowing onto the PG, which induces a magnetic field inside the source, in the transverse direction with respect to the propagation of the electrons. The intensity of this field is in the order of some tenths of mT.
Together with the filter field, the co-extracted electrons are reduced by positively polarizing the PG, so that more electrons are directed towards it by electrostatic attraction. To enhance the effectiveness of the PG biasing, the source wall potential can be extended closer to the extraction apertures by means of a dedicated bias plate (BP), consisting in a metallic plate that encloses the aperture groups.

1.3.3 Accelerator system

Negative ions are extracted through the apertures of the PG by applying a positive potential to a second electrode, placed downstream and with aligned apertures, called Extraction Grid (EG); usually the source is negatively polarized with respect to the other grids, keeping the vessel grounded. The electrostatic potential thus generating repels the positive ions towards the source and extracts the negative species from the plasma. The region which is created between the plasma and the beam is called meniscus, whose shape depends on the plasma parameters, shape and size of the PG apertures and on the extraction voltage applied. The physics of the meniscus and its relation with the beam divergence is discussed in details in Chapter 2.6. Due to their negative charge, electrons are co-extracted together with negative ions and, since their density is larger, also the current is. This is one of the biggest issue that NBI has to consider, due to the elevated heat load transferred by the electrons to the accelerator system. To reduce them, together with the already explained filter field and biasing of the BP and PG, another magnetic field is usually exploited in NBI negative ion sources. It is generated by permanent magnets installed onto the EG, called Co-extracted Electrons Suppression Magnets (CESM) [22], placed with alternate polarity, in order to deflect the electrons on the EG itself, which is properly cooled. Since the mass of the ions is 1838 times larger than the electrons mass, they are affected by a deflection of few mrad, and can be extracted through the EG. Two main methods are studied to compensate this small deflection: the first exploits an additional grid, called *steering grid*, whose apertures

are slightly misaligned with respect to the other grids, thus modifying the profile of the electrostatic lens and compensating in this way the beam deflection; the second, which is the one that will be used on MITICA accelerator, uses a further set of permanent magnets installed on the EG, called Alternate Deflection Compensation Magnets (ADCM) [23].

Once extracted through the EG, negative ions are accelerated to the desired energy

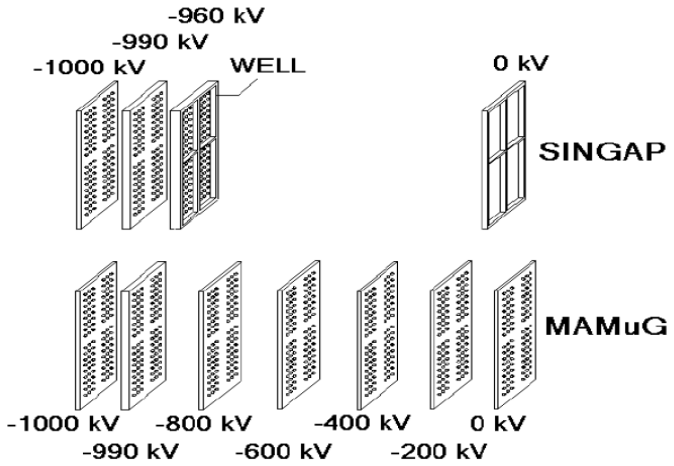

Figure 1.9: *Schematic representation of SINGAP (on top) and MAMuG (on bottom) configurations.*

by a Grounded Grid (GG), which is the last grid of the accelerator. The beamlets exiting the GG must be well aligned and without deflection. The accelerator system of ITER should accelerate negative ions to 1 MeV of energy. To achieve this goal, two designs have been proposed: Single-Aperture Single-Gap (SINGAP) configuration [24], composed only by two gaps of 40 kV and 960 kV, and the Multi-Aperture Multi-Grid (MAMuG) configuration [25], featuring a five steps gradual acceleration of 200 kV each; the two configurations are represented in Fig.1.9. Since the lower gaps reduce the energy of the co-extracted electrons, MAMuG configuration is the one chosen for MITICA accelerator.

1.3.4 PRIMA project

ITER will initially be equipped with two heating neutral beam injectors, designed to deliver 33.3 MW of either 1 Mev D or 0.87 MeV H to the ITER plasma for up 3600 s. This high energy (larger than 300 keV) is necessary to deposit the power inside the H-mode transport barrier, when ITER is in the so called *H-mode* (High Confinement Mode). The ITER Neutral Beam Test Facility, called PRIMA (Padova Research on ITER Megavolt Accelerator) is hosted in Padova, at Consorzio RFX. It includes two experiments: SPIDER (Source for the Production of Ions of Deuterium Extracted from a Radio Frequency plasma) and MITICA (Megavolt ITER Injector and Concept Advancement).

The PRIMA project's goal is to test and develop the ITER's Neutral Beam injector system. After the deployment of the two first ITER injectors, the laboratory will operate in parallel to the experiments in ITER to optimise Neutral Beam injector performance, also in view of the future fusion reactor. Future ITER NBI has to satisfy strict constrains imposed by ITER [18] and this facility aims at satisfying all of them.

- SPIDER test facility is in operation since 2018. It is a full-size prototype of ITER NBI negative ion source. It can operate both in H and D plasma, aiming to provide a total acceleration of 100 keV with a grid system composed by three grids, ith a beam duration up to 3600 s [26]. SPIDER goals are to demonstrate the ITER requirements for the negative ion and co-extracted electron current densities, for pulses up to one hour, together with the beam optimization in term of divergence and homogeneity. It will be described in details in next chapter.

- MITICA test-facility is a full-size prototype of the ITER NBI. The beginning of the operation is foreseen for 2023, and its target is to fulfill all the ITER requirements for the full beam-line. It will be used also as a test-bed, in which searching solutions to the eventual future issues connected to the achievement of ITER NBI requirements. It is composed by 5-grids accelerator, polarized from - 1 MeV to ground, as represented in Fig.1.10, where the negative ions extracted form the radio-frequency RF source (the same studied on SPIDER) are accelerated and then they enter in the neutralizer. There, an elevated gas density neutralizes the highest number of negative ions by stripping the additional electron, with a neutralization efficiency of 60%. The neutral particles are thus free to reach the calorimeter while, the negative ions not neutralized or became positive, are deflected by a magnetic field and impinge on the Residual Ion Dump [27].

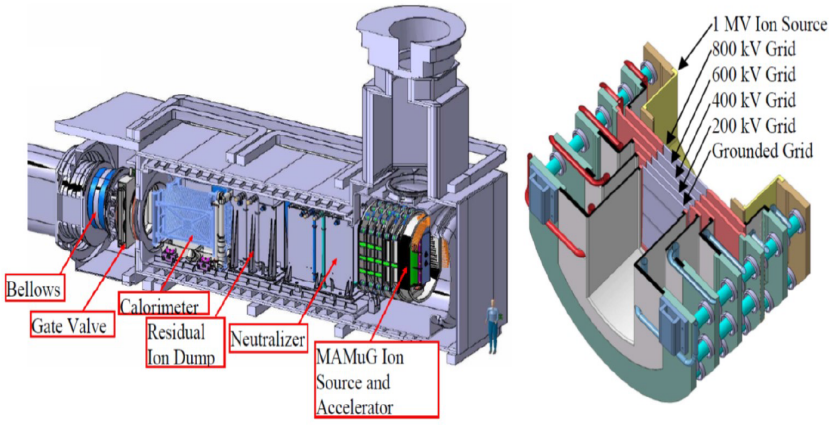

Figure 1.10: *Schematic representation of MITICA and its components (on the left) and detailed view of the 5-grids acceleration system (on the right) [28].*

1.4 SPIDER experiment

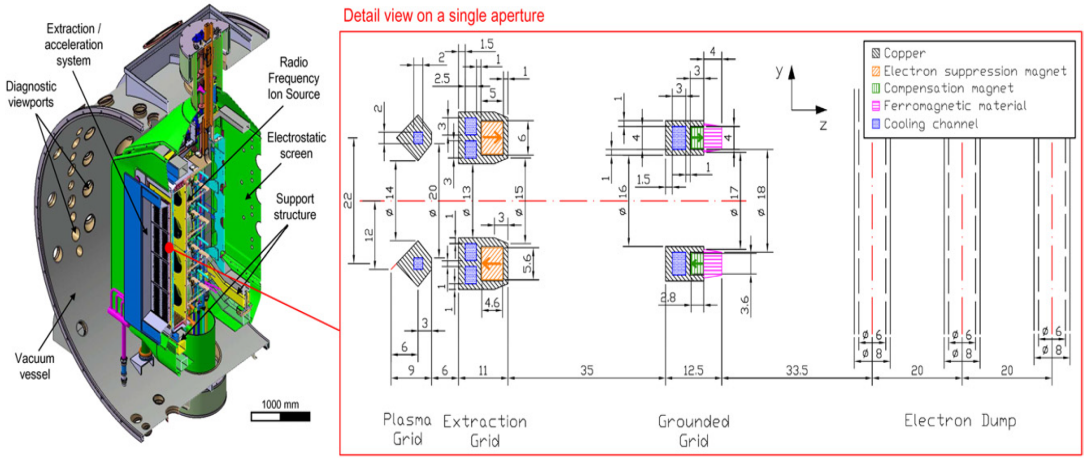

Figure 1.11: *Whole view and detailed section of the SPIDER accelerator system and electro dump. All the dimensions are in mm [29].*

SPIDER is the full-size prototype of the negative ion source for ITER Heating Neutral Beam Injector (HNB) [28] [29]. It aims at optimizing the production and extraction of negative ions, in view of MITICA operation. In particular, its goal is the validation and improvement of the ITER ion source design in terms of extracted current, electron co-extracted ratio and beam uniformity and divergence. Being one of the largest ion source in the world, twice the dimension of ELISE experiments at Garching IPP [30], whose design is as close as possible to the ITER NBI design. SPIDER aims at delivering stable current densities of 285 A/m^2 D^- for one hour and 330 A/m^2 H^- for 1000 s at a source pressure of 0.3 Pa, while the co-extracted electrons-to-ion currents ratio has to be lower than one. The beam source has a rectangular shape, 0.9 m wide and 1.9 m tall. Eight drivers (cylinders with Faraday shield of inner diameter 275 mm and 149 mm depth) generate the hydrogen or deuterium plasma at a required pressure of 0.3 Pa, through ionization by means of radio-frequency power transferred from coils wound around the drivers. The eight radio-frequency drivers are associated to four generators operating at 1 MHz (thus each pair of drivers is connected in series to the same oscillator) and capable of delivering up to 200 kW each, now limited to 100 kW per generator. Additional filaments are present in the driver, in order to facilitate plasma ignition, while a Faraday screen keeps the plasma away from the driver walls. Once generated inside the drivers, the plasma expands towards the rectangular expansion chamber, 866 mm wide, 1760 mm tall and 240 mm deep up to the plasma grid. The horizontal filter field is generated by a current flowing onto the PG (made of copper and coated with molybdenum), which ranges from 0 to 5 kA; near the PG apertures, 1.6 mT is generated for each kA of current. A detailed description of SPIDER magnetic filter field is available in

Ref.[31]. Thanks to the flexible design (no permanent magnets are involved), it is possi-

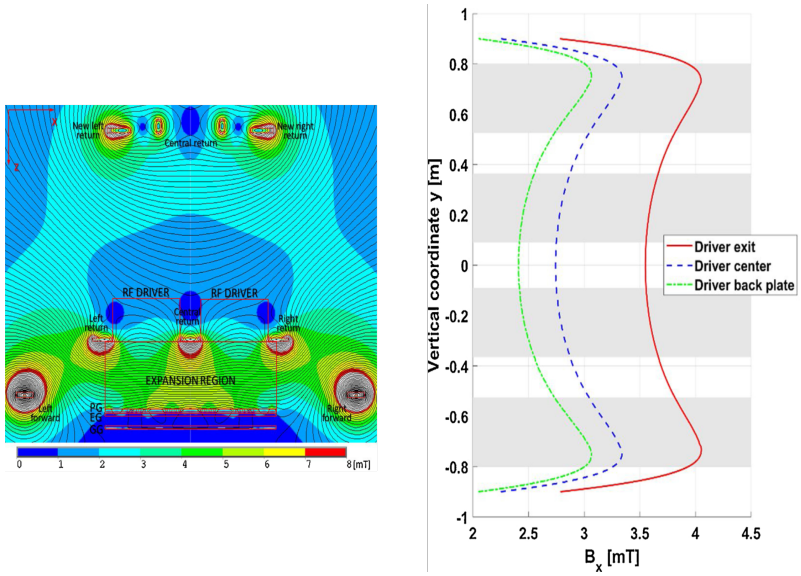

Figure 1.12: *On the left, contour plot of the absolute value of the magnetic filter field for a current of 3 kA. The drivers, expansion region, the grids and the bus-bars cross section are indicated in red. On the right, vertical profiles of the transverse horizontal B_x magnetic field at three different axial positions inside the drivers [31].*

ble to invert the direction of the filter field by reversing the current flowing through the PG and to characterize the plasma and beam behaviour in the two configurations. The magnetic filter plays a fundamental role in limiting the flux of electrons from the drivers to the extraction region, and consequently the flux of electrons to the plasma grid. The transport of the magnetized electrons across the filter is mainly due to Coulomb and elastic collisions with the background gas: the probability of both processes decreases with the electrons energy. Furthermore, the electron temperature is reduced due to additional inelastic collisions of the magnetized electrons with the background gas.
Together with the magnetic filter field, the plasma is subjected to two different external electric fields, aiming to improve the plasma generation and to remove a variable amount of electrons in the negative ion production region: the first is a potential applied between the plasma grid and the source (ISBI); the second is given by the polarization of dedicated bias plate (BP), divided into five segments, mounted 20 mm upstream the PG. Both of them are positively polarized with respect to the source.
Negative ions are then extracted and accelerated by SPIDER accelerator system. SPIDER extraction area is 0.2 m^2 which is composed by 1280 beamlets, divided in 4 groups (from the top to bottom G1, G2, G3 and G4), one for each couple of drivers, arranged in a 4x4 matrix of 16 rows with 5 beamlets each; each aperture has 14 mm diameter. To achieve the target current densities, the extracted currents are as high as 57 A D^- and 66 A H^-. The apertures of the PG feature a conical chamfers on the upstream and

downstream sides of the grid, to enhance the surface for ion production, thus increasing the ion extraction probability (see Fig.1.11). To further improve the negative ions surface generation, the PG can be heated up to 150 ° C. In order to extract and accelerate the negative ions, a maximum electric potential of 9-10 kV is generated between the PG and the EG and then a second electric field between EG and GG accelerates the particles up to an acceleration of 100 eV. Suppression magnets are embedded in the EG (CESM), to deviate the trajectories of the co-extracted electrons by dumping them on the grid surface. Different sections of the grids features diverse ways to compensate beamlet deflection: the apertures of the GG are shifted (half bottom of G2); a magnetic field is generated by permanent magnets embedded inside the GG (everywhere except G2); uncompensated section (half top of G2), to study the effectiveness of the other methods. Due to the concentrated heat load and to breakdown issues, the maximum extraction voltage used during the first experimental campaigns was 8 kV (with Cs evaporation; in volume operation was limited to 5 kV); also the acceleration voltage was restricted to 45 kV. Furthermore, since the pressure in the vacuum vessel with the present pumping system was too high to allow plasma operation with 4 generators [32], at the beginning of beam operation, 1200 of the 1280 extraction apertures were masked temporarily (June 2018 to the end of 2020) and then only 28 are left open, from beginning of 2021 to the start of the shutdown, which is started in November 2021.

1.5 Other negative ion sources

In order to meet ITER target design and operational parameters in time for ITER operations, several facilities are currently in operation all around the world. In particular, during my PhD I participated to experimental campaign in three different negative ion sources, and the results obtained in all of them are used to better understand the physics of negative ions source. In the following, the main characteristics of the experiments NIO1, BUG and NIFS-RNIS are described.

1.5.1 NIO1 at Consorzio RFX (Padua, Italy)

Negative Ion Optimization phase 1 (NIO1) is an inductively-coupled negative ion source at radio frequency (2 MHz, provided by a 2.5 kW radio-frequency generator), aimed to extract in continuous mode 130 mA of H^- in a multi-beamlet scheme, accelerating them up to an energy of 60 keV[33]. A system composed of three electrodes extracts and accelerates the negative ions: the PG held at the potential $U_{PG} \geq -60\ kV$ with respect to the ground and equipped with 9 extraction apertures arranged in a 3 x 3 matrix (radius of 3.8 mm and pitch of 14 mm); the EG, through which the negative ions are extracted with a voltage $U_{extr} \leq -10\ kV$; and the Post Acceleration (PA) grid, which is grounded, allowing the acceleration of the ions up to the final energy ($\leq 60\ keV$). After the PA, an additional grid, the Repeller (REP) grid, which is positively biased ($U_{REP} \leq 60\ V$), is present to prevent the back-streaming positive ions, produced during the beam propagation in the background gas, from being attracted into the accelerator

and dumped onto the source rear wall. A molybdenum bias plate is installed on the upstream face of the PG which can be biased up to tens of volts. CESMs magnets are mounted on the EG, to deflect the electrons on the EG itself, together with the ADCMs, necessary to compensate the residual deflection of the negative ion beam. This is the same configuration that will be used in MITICA. The current flowing through the PG (I_{PG}), together with permanent magnets installed on the PG itself, produces a magnetic filter field in the vertical direction so as to cut the higher energy tail of the electron energy distribution.

1.5.2 BUG at IPP (Garching, Germany)

BAvarian Test Machine for Negative Ions Upgrade (BUG) is a negative ion accelerator with a 1 MHz radio-frequency driver source, provided by a 150 kW generator [34]. It is a 1/8 of ITER NBI ion source, designed to run for a total beam on time of 10 s. The accelerator is a three-grids system, with -45 kV of maximum acceleration voltage and 10 kV of extraction voltage. The filter field is generated by permanent magnets displayed around the source vessel and by a current flowing through the PG. Only CESM magnets are installed, thus the beam deflection is not compensated. The beam is composed by 70 beamlets (14 mm diameter); during the experimental campaign to characterize the single beamlet, one isolated apertures was left open in the upper half of the beam, while the 35 apertures at the bottom were kept fully open.

1.5.3 NIFS-RNIS at NIFS (Toki, Japan)

The NIFS-RNIS ions source test stand is an arc discharge multi-cusp ion source [35] [36]. The plasma inside the source is ignited by six pairs of tungsten filaments heated and negatively polarized with respect to the ion source (V_{arc}), producing an arc current I_{arc}; the total power is defined as $P_{arc} = I_{arc}V_{arc}$. The expansion and extraction region are separated by magnetic filter. The arc chamber has a hexagonal cross section to avoid unnecessary connections of magnetic fields induced by the cusp and filter magnets. Cs is evaporated from the back-plate side through three lines, and then spread to the sidewalls by the end nozzles. The PG is insulated with respect to the source body, and can be polarized both positively and negatively, $V_B = V_{PG} - V_{is}$, with V_{PG} the plasma grid potential, V_{is} the ion source walls potential.

Chapter 2

Physics of the negative ion plasma and beam

In this chapter, the physics which governs the negative ion production and extraction is described.

2.1 Volume and surface negative ion production

The negative ions are produced in two different processes: by volume [37] and surface production [38].

- Volume production. In volume production one tries to maximize the production of negative ions by dissociative attachment of electrons to high vibrational states of hydrogen molecules. When the hydrogen molecules are in high vibrational states, they are prone to dissociate and attach to a low energy electron (larger cross-section). It is a two steps process. Fast electrons excite H_2 molecules with collisions (T_e about 5-10 eV) to high vibrational levels. Then the excited H_2 molecules drift to the second chamber where the lower electronic temperature (T_e about 1-2 eV) maximizes the dissociative attachment reaction rates and minimizes the neutralization probability of H^- by electronic collisions. Large amounts excited molecules and electrons are thus needed.

- Surface production. When a hydrogen atom or ion impinges on a surface, it can bounce back as a negative ion. The probability of this reaction to occur, depends on the work function ϕ of the surface, on the electron affinity A and also on the perpendicular velocity of the escaping ion:

$$\gamma(H^-, H) = exp(\frac{\phi - A}{Cv_\perp}), \tag{2.1}$$

  where C is a constant and $\phi - A$ represents the energy difference between the Fermi level of the surface and the electron affinity level.

Negative ions are produced from atoms or positive ions interacting with a low work function surface:

$$H + e^-_{surface} \rightarrow H^- \tag{2.2}$$

$$H^+ + e^-_{surface} \rightarrow H + e^-_{surface} \rightarrow H^- \tag{2.3}$$

where $e^-_{surface}$ is an electron belonging to the conduction band (i.e. with an energy close to the Fermi level) of the metallic surface where the conversion takes place. When hydrogen atom approaches to metal surface, the affinity level is lowered by image potential. The electron reaches the affinity level of a hydrogen atom located close to the surface by quantum tunneling: the hydrogen atom captures the electron and escapes as a negative ion. The lower the work function of the surface, the higher the probability of quantum tunnelling.

Typical materials used for the ion source surface have a large work function (> 4 eV), thus they are covered by alkali or alkaline earth metals, in order to reduce it; among the stable elements, caesium is chosen: it has the lowest work function, equal to 2.14 eV. Due to its low melting point (28.5° C) and its high reactivity [39], it cannot be used to construct walls or grids. Dedicated evaporations (dubbed caesium ovens) inject caesium inside the ion source [40], which is re-distributed over the source walls by the plasma itself. This operation can increase the extracted negative ion current up to a factor of 10, and yields a co-extracted electron-to-ion ratio lower than 1 [41]. One difference related to these two types of generation is that, while in volume production negative ions are generated isotropically in the entire plasma volume, in surface production they are produced only close to the PG. The energy of the resulting negative ions can thus be different, according to the process through which they are born. Volume production generates ions at plasma potential V_p, which is usually larger than the PG potential V_{PG} and can vary inside the source. In surface production, instead, the ions generated on the PG are immediately extracted, therefore their energy distribution at the meniscus is expected to be only given by their temperature (fraction of eV) [42]. A dedicated diagnostic, aiming at distinguishing the two energy distributions of negative ions, was developed and tested in the arc-based negative ion source at NIFS (RNIS); the diagnostics is described in Sect. 3.1.3, while some of the obtained results are presented in Sect. 5.4.1.

2.2 Electron drifts

As explained in the previous chapter, the magnetic filter field in negative ion source is necessary to reduce the electron temperature close to the extraction region. It is responsible of both vertical and horizontal electron drift in the expansion region, due to a combination of cross-B drift.
In the 1D approximation, i.e. assuming a uniform plasma in the direction perpendicular to the magnetic field, which means that the time derivative and the inertia terms are

neglected, as well as the pressure tensor is assumed to be diagonal and isotropic, the resulting form of the electron momentum equation can be written as

$$\partial_x(n_e k T_e) = -e n_e E - e n_e B v_y - n_e m \nu v_x \tag{2.4}$$

$$0 = e n_e B v_x - n_e m \nu v_y \tag{2.5}$$

with x the discharge axis (from the drivers to the grids) and y is the direction perpendicular to x and **B**; n_e and T_e the electron density and temperature, e the elementary charge, m and v the electron mass and velocity, k the Boltzmann constant. From which $v_y = \Omega_e/\nu, v_x = h v_x$, with $\Omega_e = qB/m$ the electron cyclotron frequency, m the electron mass, ν the electron momentum loss frequency, which includes both electron-neutral and electron-ion collisions, and $h = \Omega_e/\nu$ is the Hall parameter [43]. So the equation for the electron flux at any position between the driver and the electrode (PG) can be written as

$$\partial_x(n_e k T_e) = e n_e E + n_e m \nu v_x (1 + h^2) \tag{2.6}$$

where the two contributions are the pressure gradient term and the electrostatic force term between the electrodes. Particle-in-Cell MonteCarlo (PIC-MCC) simulations [44] show that outside the magnetic filter region, the pressure gradient term of the electron momentum completely balances the electrostatic force one, leading to the Boltzmann relation between plasma density and potential. In the magnetic field region, instead, the pressure gradient term strongly dominates the electrostatic force one. The electron current density can thus be written as

$$\boldsymbol{J_e} = \frac{q}{m(\Omega_e^2 + \nu^2)}[(q n_e \boldsymbol{E} - \boldsymbol{\nabla} p_e) \times \boldsymbol{\Omega_e} + \nu(q n_e \boldsymbol{E} - \boldsymbol{\nabla} p_e)] \tag{2.7}$$

with $p_e = n_e k T_e$ the electron pressure and $\boldsymbol{E} = -\boldsymbol{\nabla} V_p$ the electrostatic field. For B= 5 mT the electron gyro-frequency is $2\pi \times 140$ MHz, so the electrons can be assumed as magnetized and Eq.3.2 can be written as

$$\boldsymbol{J}_{e,B} = q n_e \frac{\boldsymbol{E} \times \boldsymbol{B}}{B^2} - \frac{\boldsymbol{\nabla} p_e \times \boldsymbol{B}}{B^2}, \tag{2.8}$$

neglecting the collision term due to the strong reduction of the mean electron energy once they enter the magnetic field region. The electron motion is thus dominated by the magnetic drift which is composed of a diamagnetic term $\boldsymbol{\nabla} P \times \boldsymbol{B}$ (collective effects) and a **E**x**B** term. The electric field is a combination of the Hall and the ambipolar fields. From the field direction (the magnetic field and the electric field determined by the variation of the plasma potential within the expansion region), the **E**x**B** contribution is in the opposite direction of the $\boldsymbol{\nabla} P \times \boldsymbol{B}$ drift. The plasma vertical drift is thus a combination of cross-B drifts.

The effect of these drifts on the plasma in SPIDER is studied starting from the experimental measurements. In particular, the vertical profile of the plasma in the two directions of the filter field is characterized, highlighting the relevance of the magnetic induced drifts on the vertical plasma shape in the expansion region.

2.3 Plasma sheath and virtual cathode

Since with caesium evaporation, the negative ions are mainly produced on the Plasma Grid surface, the properties of the plasma in this region play a fundamental role in determining negative ion density available to be extracted. One of the region of major interest is the so-called plasma sheath, which is formed in the region comprises between a plasma and a wall [45]. In this region, the quasi neutrality is not fulfilled and it extends for some Debye lengths from the wall. A schematic representation of the plasma-wall interaction in terms of particles density (top) and potential (bottom) profiles is given in Fig.2.1. The potential difference between the wall and the plasma is determined by the

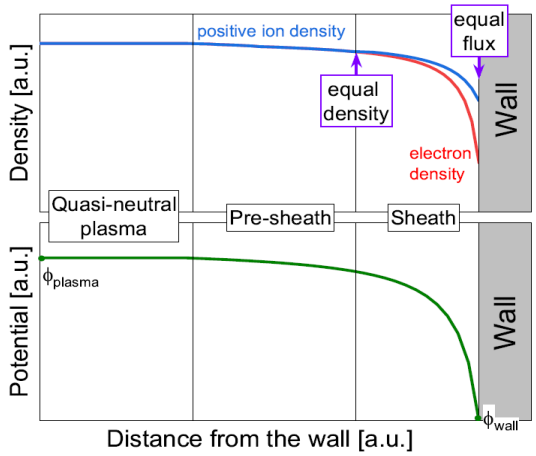

Figure 2.1: *Positive ions and electrons density (on top) and plasma potential (on bottom) profiles in the vicinity of a wall [46].*

electron temperature T_e and the mass ratio m_{ion}/m_e:

$$\phi_{plasma} - \phi_{wall} = -k_B T_e ln(\sqrt{\frac{m_{ion}}{2\pi m_e}}) \tag{2.9}$$

To preserve the plasma quasi-neutrality, an ambipolar electric field is generated, bringing to the formation of the sheath between the plasma and the wall: the electrons flux towards the wall, due to their larger mobility (lower mass), is dominant with respect to the ions flux and, as a consequence, an ambipolar electric field is settled to reduce the loss of electrons at the walls until the fluxes of the electrons and positive ions are equalized.
When a positive bias is applied to the wall, as in the case of the PG biasing in NBI negative ion source, this equilibrium is modified. Depending on the relation between the PG bias U_{bias} and the plasma potential ϕ_{plasma}, the wall can attract o repel electrons: if $U_{bias} > \phi_{plasma}$, the PG attracts electrons and the resulting electric field is towards the plasma bulk; if $U_{bias} < \phi_{plasma}$, instead, the PG repels electrons, thus attracting

positive ions, and the resulting electric field is towards the grid itself.
The physics in this region is further modified when negative ions are produced by surface generation. In fact, negative ions replace the electrons, preserving the neutrality of the plasma. When their density is large enough, the so-called *virtual cahode* forms close to the extraction region, featuring an inversion of the potential curve to equalize the fluxes of particles at the wall [47]. This structure limits the flux of negative ions from the wall towards the bulk plasma and, if the potential well is too deep with respect to the plasma potential, negative ions are not emitted any more into the plasma. In case the positive ions density in the bulk plasma is too low with respect to the negative ions one in the extraction region, the space-charge limits the negative charges density and the emission of the negative ions from the wall is prevented. This mechanism in terms of positive and negative ion densities, electron density and plasma potential is represented in Fig.2.2.

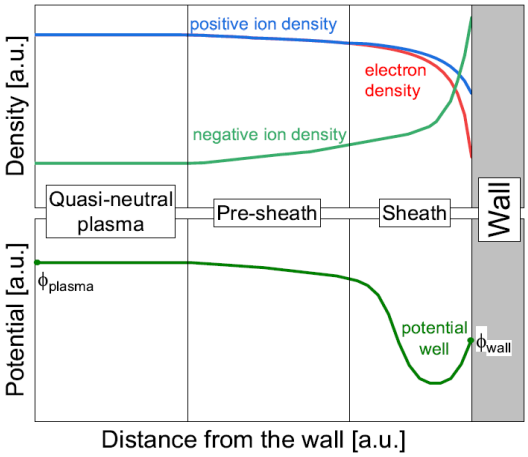

Figure 2.2: *Positive ions, negative ions and electrons density (on top) and plasma potential (on bottom) profiles in the vicinity of a wall with large negative ions density [46].*

2.4 Space charge effect

The space charge of a negative ion beam depends on the uniformity of the ion current density j_{H^-} and on the ratio R_j between the electron current density j_{e^-} and j_{H^-}; the applied voltage and electrode design play a role too. The electron-to-ion density ratio in the extraction region can be estimated by $R_n = f_R R_j (m_e/m_H)^{1/2}$, where f_R is the recirculation factor of electrons, which is slightly greater than 1 when the average electron Larmor radius r_L is larger than the extraction gap, g, whereas it becomes greater than 2 for stronger deflecting magnetic filter field B_y, while m_e and m_H are the electron and hydrogen ion masses. The electron space charge can be considered a second order correction for $R_j \gg 10$ [48], thus obtaining as upper limit for the ion emission current

density at the cathode the local Child-Langmuir law:

$$\mid j_H \mid = \frac{4\epsilon_0}{9}\sqrt{\frac{2 \mid q_H \mid}{m_H}}\frac{\mid V(d) \mid^{3/2}}{d^2} \tag{2.10}$$

with $V(d) = \phi(d) - \phi_c$, the voltage at a distance d from the *meniscus*, which is the region between the quasi-neutral plasma and the beam region, with huge electric fields and essentially a single charge species, and q_H the signed ion charge. To better express the limit of the extracted current density the concept of *perveance* is defined, $P_b = I_b/U_{extr}^{3/2}$, being I_b the beam current and U_{extr} the extraction voltage, allowing to obtain the Child perveance limit as $P_b \cong f_V^{-3/2} P_{CH}$, where $P_{CH} = k_0 A_0/g^2$, with A_0 the extraction hole area. This limitation is the reason behind the necessity of subdividing the beam for NBI injectors into multi-apertures beamlet, thus allowing to achieve the large current required; furthermore, the negative ion surface generation is only effective at low distance from the EG surface, thus limiting again the maximum aperture radius. The relation between the meniscus shape and the beam optics is described in the following.

2.5 Space charge compensation

Once left the accelerator, negative ion beam is no more focuses by the electrostatic lens of the grids and, due to their negative charge, the electrostatic force produced by the beam charges should defocalize it by mutual repulsion. Efficient transportation of a high-current ion beam requires that the space charge of the beam ions is compensated for by electric charges of opposite sign, unless external electric or magnetic field are applied. A representation of this process is shown in Fig.2.3. When the beam propagates through

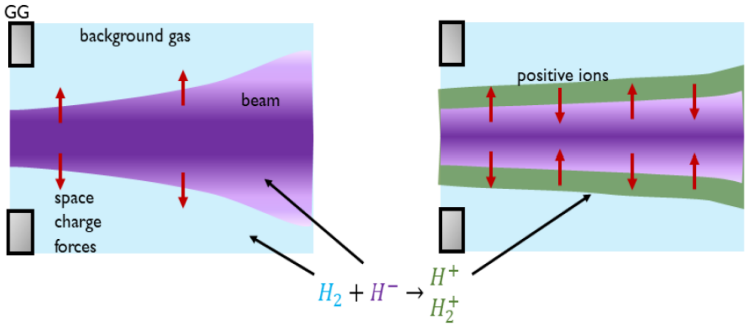

Figure 2.3: *Negative ions beam space charge compensation [17].*

a neutral gas, the beam ions neutralize in the background gas, producing also charges of the opposite sign; in the case of a negative ion beam, the compensating species are the slow positive ions, in the case of a positive ion beam, electrons are the compensating species. In the initial stage of this process, the *anti-compensating* particles are expelled from the ionization region by the radial electric field, while the compensating species

are confined in the potential well of the ion beam. Steady-state is reached when the flow of particles of both charges leaving the beam region equals the number of particles generated per unit time. These can counterbalance on the average the generation of plasma particles, namely electrons and ions, in the axial region of the beam. The space charge distribution that is established in the beam channel depends on the generation rate of plasma particle and their confinement time, and it determines the radial potential drop $\Delta\phi$ from the beam axis to the edge, and within the beam itself.
The specific features of positive and negative ion beam transport are related to the large difference in the masses of the electrons and ions, produced by ionization of the residual gas by fast heavy particle impact. The resulting system is a specific *ion-beam* plasma. In the case of a negative ion beam, when heavy positive ions act as neutralizing charge particles, two regimes of radial charged-particle fluxes can be established. These are defined by the compensation parameter $\Delta\phi$. The beam is *under-compensated* when the compensation parameter is negative and *over-compensated* the opposite. The pressure at which the compensation parameter is null is called *critical pressure*. The beam in under-compensated when the pressure is less than the critical pressure P_{CR}; it is greater than P_{CR} when it is over-compensated.
Due to the relevance of space charge compensation in governing the beam performances, very detailed numerical models are employed to describe the behaviour of the plasma in the beam drift region, applied to the investigation of this issue fir ITER HNB. Space charge compensation should be guaranteed within a short distance from the exit of the accelerator [49].

2.6 Beam optics

The beam envelope equation in the absence of external fields is defined as

$$r''(z) = K/r(z) \tag{2.11}$$

where K is the generalized perveance $K = \frac{1}{4*\pi*\epsilon_0}\sqrt{(\frac{m}{2|q|})}\frac{I_b}{V_b^{3/2}}(1-\Psi)$; the space charge compensation parameter Ψ describes the compensation degree [48]. Commonly, for negative ions, the compensation is complete in the drift region after the accelerator, even with vessel pressure of few mPa; for the fully compensated or overcompensated beam $\Psi = 1$, and the second derivative of the envelope radius is zeroed. In this condition, the beam divergence stays constant. This means that at sufficiently large distance from the accelerator, where the beam is space-charge compensated, the beam negative ions propagate in straight lines; at sufficient distance from the beamlet focal point (i.e. the point emission of the trajectories, located somewhere before the grounded grid of the accelerator) the beamlet is also laminar, and the ion trajectories do not cross each other. It is therefore convenient to describe the power density [energy flux] of each beamlet simply by its angular distribution, well approximated by superposition of two Gaussians:

$$q(\omega) = W_{beamlet}(\frac{1-F}{\pi(z\delta_c)^2}e^{-(\omega/\delta_c)^2} + \frac{F}{\pi(z\delta_h)^2}e^{-(\omega/\delta_h)^2}) \tag{2.12}$$

where ω is the beamlet aperture angle in the position z, δ_c and δ_h the divergences of the two components of the beamlet, being F the components with the wider angular aperture with respect to the total (beam halo); $W_{beamlet}$ the Gaussian amplitude. The maximum current extractable from a circular aperture of radius a, by applying a potential difference U_{extr} in between two planar electrodes at a distance d, is determined by the Child Langmuir law (space charge limit):

$$I_{max} = j_{max}\pi a^2 = \frac{4\epsilon_0}{9}\sqrt{\frac{2e}{m}}\frac{\pi a^2}{d^2}U_{extr}^{3/2} = PV^{3/2} \tag{2.13}$$

with m the ion mass and e the charge unit; I_{extr} and U_{extr} respectively the extracted current and extraction potential. This current limit is fixed by the space charge that, solving the Poisson equation, gives a space potential which limits the current density of the charges being accelerated. This equation could be extended to include the curvature of the surface from which the particles are emitted, which is often the case when an ion beam is created extracting charges from a plasma. As represented in Fig.2.4 [50], when low extraction voltage is applied, the total current extractable from a circular aperture is limited by the Child-Langmuir limit. As the voltage is increased, the extracted current saturates to a value which depends on the total charge availability (in the picture it depends on the arc current applied to the filament which generates the plasma). In radio-frequency negative ion sources, the charge availability depends on the radio-frequency power, the source pressure, the filter field applied and the goodness of the caesium coverage of the PG. The interface between the negative ion beamlet and the neutral

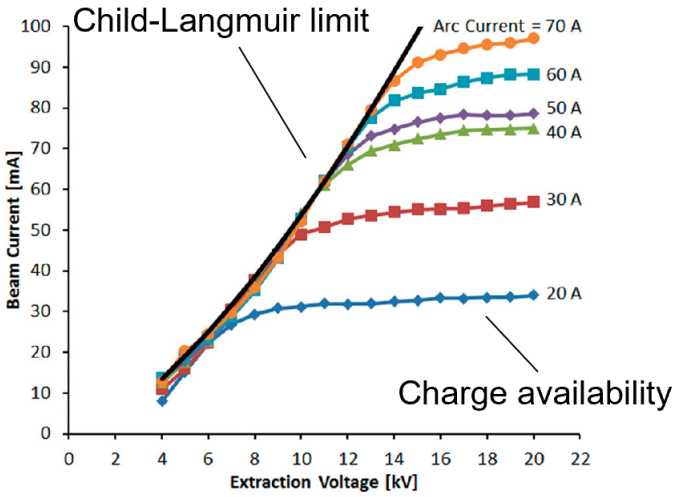

Figure 2.4: *Child-Lanmguir law for various charge availability, as a function of the extraction voltage. [50]*

plasma is called meniscus, and it plays a fundamental role in the definition of the beamlet divergence. The plasma particles which reach the meniscus are accelerated from the

plasma into the grids if they are negatively charged; positive ions are accelerated back into the plasma. The shape of the meniscus is thus defined by the available negative charges at the meniscus and the electric field generated by the extraction potential. Thus, by modifying the available negative charges at the meniscus it is possible to change the meniscus shape. The plasma pressure plays a key role in the thermal velocity of the plasma species, by changing the particle density. In the same way as the extracted current density influences the perveance, also the variation on the extraction voltage results in a modification of the perveance; and as said, for a given perveance, the meniscus position shall be the same. Second order effects include the uniformity of the current density at the meniscus, that causes local deformations of the meniscus surface and aberration of this initial electrostatic lens.
Therefore, the perveance is the relation which links the shape of the meniscus with the source macroscopic performances. Different extraction systems can be compared by introducing the normalized perveance

$$P/P_0 = \frac{\frac{I_{extr}}{U_{extr}^{3/2}}}{\frac{4N\pi\epsilon_0}{9}\sqrt{\frac{2e}{m}}(\frac{a}{d})^2} \tag{2.14}$$

where P_0 is the normalized perveance, denoting the total maximum extractable current, normalized on the N number of total apertures, calculated for infinite, planar diodes given the simplicity of the Child Langmuir formula. In negative ion sources for nuclear fusion, the normalized perveance is always lower than one: the extracted current density is usually about 30% of the maximum achievable value.
The shape of the meniscus influences the angular distribution of the extracted negative ions, providing with its curved shape a positive focal length (i.e with converging ion trajectories). The particles, in fact, cross the meniscus surface perpendicularly if their initial temperature is low enough. To minimize the angular distribution of the extracted negative ions, in order to have a parallel beam, slightly concave meniscus is desirable to compensate the 'diverging' contribution from all other effects, including the beam space charge - whose contribution rapidly decreases while increasing the ion velocity along the acceleration - and the electrostatic lenses at the following accelerator electrodes. The relation between the meniscus and the extracted beamlet shape is shown in Fig.2.5 a) (schematic representation). The meniscus shape depends on the space charge, and thus on perveance. It acts as an optical lens: the larger its curvature, the more divergent is the beam at the exit of the Plasma Grid. A too concave meniscus (first picture on the left) is obtained when the applied electric field is too strong with respect to the available negative charges at the meniscus: the meniscus deeply penetrate inside the plasma, resulting in a over-focusing of the beam before to the Extraction Grid (EG). The second image shows a too convex meniscus, when the applied electric field is not enough to compensate the space charge; in this case, most of the extracted current impinges on the EG (beamlet scraping) and the beamlet is not focused. The third image, instead, represents the optimal meniscus, which corresponds to the minimum of the beam divergence. Pictures b) and c) shows this relation between the perveance and the

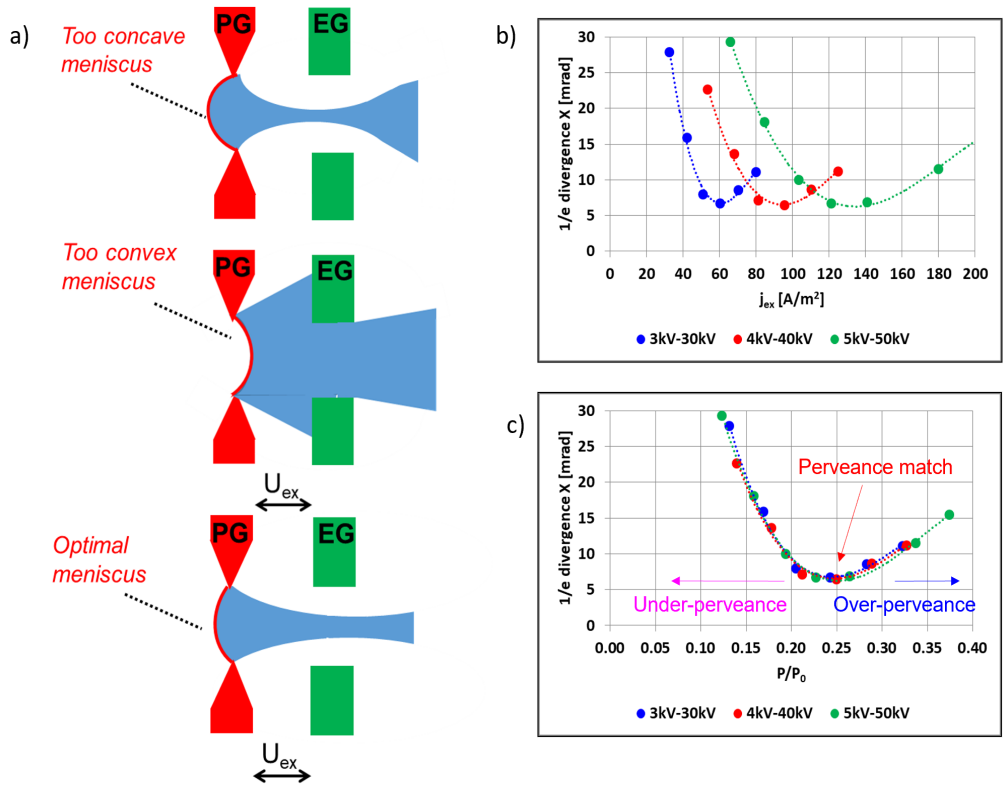

Figure 2.5: *On the left, schematic representation of the relation in between the shape of the meniscus and the beamlet divergence. On the right, three simulated curves for various pairs of acceleration and extraction voltages (ratio fixed). The width of the beamlets as a function of total current density in b) and as a function of the normalized perveance in c).*

beamlet width. In b), for three different values of extraction and acceleration voltages, the beamlet divergence as a function of the extracted current is plotted. Depending on the extraction and acceleration voltages applied, the extracted current is different but, when the three curves are plotted as a function of the normalized perveance P/P_0 (panel c)), they collapse into a single one, with the minimum of the divergence at the same value of normalized perveance, since it is uniquely determined by the geometrical structure of the extraction hole and by the beamlet extracted current. For beamlet current below the optimum value, the beamlet is under-perveant while, when it overcomes the optimum, it is over-perveant. The over-perveant regime is not always experimentally observable since the beam can be scraped on the EG (convex meniscus), cutting the angular distribution. An aperture with different electric field strength on the two sides acts like an electrostatic lens. The focal length f of such lens is defined as

$$f = \frac{4V}{E_d - E_u} \tag{2.15}$$

with V the ion energy at the lens position, E_u and E_d the upstream and downstream electric field. The focal length describing the effect of the electrode aperture combines with both the focal length caused by the meniscus, and with the divergence growth by the perveance in the PG-EG gap; the resulting focal length is obtained by summation of the reciprocal of the focal lengths by each contribution. In three-electrode acceleration systems, therefore the the voltage ratio $R = U_{acc}/U_{extr}$, in between the extraction and the acceleration gap, is the other control parameter for the beamlet divergence. The electrostatic lens at the grounded grid is always diverging (i.e. f¡0 since E_d=0 in Eq. 2.15). Another fundamental role on the beamlet divergence is played by the voltage ratio $R = U_{acc}/U_{extr}$, in between the extraction and the acceleration gap. While perveance describes the space charge at the meniscus and thus the behaviour of the beam in the PG-EG gap (first gap), R defines what happens in the second gap, between EG and AG. The total beam velocity is defined by the total voltage U_{tot} applied to the grid system and to the negative ion mass

$$v = \sqrt{\frac{2eU_{tot}}{m}} \tag{2.16}$$

Even if the initial velocity of the negative ions at the meniscus (few eV) is negligible with respect to the total energy applied by the electrostatic acceleration in the grid system, the perpendicular component of the initial ion velocity with respect to the beamlet axis causes a broadening of the beamlet divergence. The effect of negative ion temperature on the beamlet divergence is studied in details through the measurements of a dedicated RFEA an the RNIS facility (section 5.4.1).
Once in the accelerator system, the negative ions undergo collisions with the background gas. The ions which neutralize before to exit the last grid (stripping process), maintain an energy which depends on the position where the collision takes place, and even if they exit the accelerator, they would not have reached full acceleration. The stripped electrons can impinge on the grids or downstream the grid system on the tank, namely the vessel enclosing the beam. Once extracted, the negative ion beam can propagate thanks to the space charge compensation [49].

Chapter 3

Beam and source diagnostics

In this chapter, both plasma and beam diagnostics employed in this work of thesis to characterize negative ion source and beam are described. Their physical and technological characteristics are briefly introduced and their setup on SPIDER is presented. In a dedicated chapter (Chapt. 4) the visible tomography diagnostic is described in detail. The main properties of SPIDER beam, in terms of divergence and homogeneity, are discussed and correlated with the properties of the plasma which are evinced, starting from the experimental measurements of the following diagnostics. The same diagnostics are used to study plasma and beam properties on different negative ion sources, to compare their performance with SPIDER ones. In Section 3.1, the optical emission spectroscopy, the Langmuir probe and the Retarding Field Energy Analyser are described, in Section 3.2 the beam emission spectroscopy and the CFC calorimeter diagnostics.

3.1 Source diagnostics

Since the production and the destruction probability of negative ions strictly depend on the plasma properties, the characterization of plasma parameters plays a crucial role in the development and optimization of NBIs. Many aspects of the plasma have to be considered, from the magnetically induced drifts, electron density and temperature, dissociation degrees and all the energies and the concentration of both negative and positive ions. One of the main goal of SPIDER is proving essential to well diagnose the radio-frequency source, both inside the drivers and next to the plasma grid, in the region where negative ions are produced and then extracted. To satisfy the homogeneity criteria on the beam imposed by ITER (dis-uniformity within 10 %), the plasma inside the source has to be wholly characterized. To do that, plasma uniformity and surface measurements over the wide grid surface, in the back of each driver and in the expansion region are available on SPIDER [26].
In this work of thesis, the data collected by Optical Emission Spectroscopy, Langmuir Probes and Retarding Field Energy Analyser (RFEA) are analysed, interpreted and correlated with the beam properties. The RFEA was available on SPIDER only during a dedicated campaign.

3.1.1 Optical Emission Spectroscopy

Optical Emission Spectroscopy (OES) is the main diagnostic of the plasma inside SPIDER. It is a non-invasive diagnostic with a relatively simple and robust set-up. Spectra with sufficient temporal resolution can be easily recorded, whereas the spatial resolution is given by the elevated number of lines-of-sight (LoSs). The light emitted by the plasma in different regions of the source is collected by collimating lenses and optical fibres, through viewports on the vacuum vessel and 10 mm diameter holes on the nested in-vacuum source case. The large number of available LoSs allows to measure the integrated light both perpendicularly and parallelly to the grids, emitted respectively by the plasma in the drivers and in the extraction region. An absolute calibration of the optical system gives the possibility to obtain a variety of different plasma parameters: electron density and temperature, gas temperature, atomic and molecular hydrogen densities as well as caesium density, both atoms and ions. This diagnostic allows also to estimate the most interesting parameter, the negative ion density [51]. A detailed description on the OES diagnostics in SPIDER is available in Ref.[52], together with the first results is in Ref.[53]. SPIDER OES diagnostic has been commissioned during the last part of 2018 and successfully operated in the experimental campaigns since then. A schematic

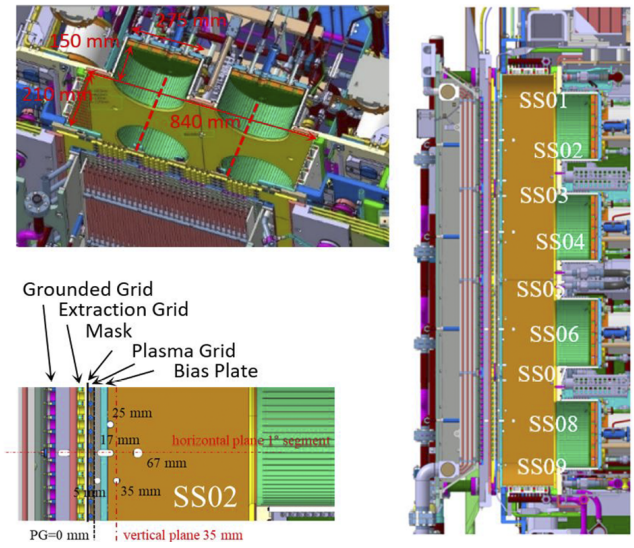

Figure 3.1: *Top-left panel: horizontal section of SPIDER source with some of the drivers (in green), the expansion chamber (in yellow) and the system of grids. Red dashed lines indicate two of the 8 LoSs which measure the plasma light in the drivers. Right panel: vertical section of SPIDER with the 9 groups of LoSs (labelled SS01-SS09). Bottom-left panel: zoom of the LoSs available inside each group of LoSs, to underline their position with respect to the PG.*

representation of the set of OES LoSs available on SPIDER is given in Fig.3.1. In the top-left panel, the location of measurements of the light emitted by the plasma in the

drivers, referred to as Plasma Light (PL), is shown (red dashed lines). This is measured by 8 silicon photodiodes with H_α filter, one for each driver, installed in vacuum, directly facing the apertures on the drivers backplate [52]. The plasma emission in the expansion region, instead, is collected using three different spectrometers (330 mm focal length Iso-Plane spectrometers [54]), with a total of 33 channels, that allow the measurement of the emission spectra in the visible range. The location of available groups of LoS is shown on the right of Fig.3.1; each group is labelled SS01-SS09.. A vertical profile of the plasma emission at 35 mm and 5 mm from the PG is used to study plasma properties. To study the properties of the plasma in this region, the group of LoSs centred on the axis of the drivers are preferred, to avoid any eventual local effect due to the interaction of the plasma with the components of the Bias Plate With these spectrometers it is possible to measure the Balmer series ($n' = 4, 5, 6, ... \rightarrow n = 3$, H and D), and the Fulcher band ($d^3\Pi_u \rightarrow a^3\Sigma_g^+$ H_2) emissions ($H_{fulcher}$), estimated as the integral of the emission from 600 to 630 nm, while checking the absence of strong Cu, O of OH lines.
From the measured spectra, the emissivity of each specific line ε_i, indicating the number of photons emitted per time, is calculated from the signal counts s_i by

$$\varepsilon_i = \frac{C_i s_i}{L t_{exp}} \tag{3.1}$$

where C_i is the specific line calibration factor, L is the length of the LoS inside the plasma and t_{exp} the exposure time.
Emission spectroscopy can be used both to control the plasma dynamics during the discharge, for example through the line identification of the species composing the plasma, and also to quantitatively correlate the collected radiation with plasma parameters, in particular particle densities. Common methods are based on the line ratio measurements and analysis of absolute intensities, supporting by population modelling [51]. The analysis of the emission of atomic hydrogen, in particular in the expansion region, is not straight-forward because many excitation reactions can occur, and the line intensities depend on several plasma parameters. In the driver, where the $T_e \sim 10$ eV and $n_e \sim 5.10^{18}$ m^{-3}, the most relevant excitation channel for atomic hydrogen emission is direct electron collision excitation from the atomic state. The molecular radiation is mainly due by direct excitation of H_2. In the expansion region, instead, the decrease in both electron temperature and density, makes relevant the recombinant processes. The emission is mainly due to the mutual neutralization of atomic and molecular positive ions with H^- and dissociative recombination.
The line radiation gives information about the population of an electronically excited state. Dedicated population models, the so-called collisional radiative (CR) models, allows to relate the excited state with the ground state, thus estimating the particle density. The population density of the excited state n(p) is obtained from the absolutely calibrated line emission

$$\varepsilon_{pk} = n(p) A_{pk} \tag{3.2}$$

where A_{pk} is the transition probability from level p to k.
In this work of thesis, the plasma homogeneity in SPIDER source is characterized using

spectroscopic measurements, both in the driver and in the expansion region. In the driver, H_α emission is used to estimate the degree of atomic excitation, thus indicative of the plasma density. In the expansion region, H_β emission is correlated with the ion saturation current measured by the Langmuir probes (described in the following section). A good agreement between the two measurements is found. This agrees with YACORA estimations, shown in Fig.3.2 [55], of the recombinant plasma present in this region, demonstrating that the emission line is dominated by dissociative recombination of $H_2^+(e^-, H_2^+ \rightarrow H(n=4), H)$. The line ratio H_α/H_β gives a qualitative estimation

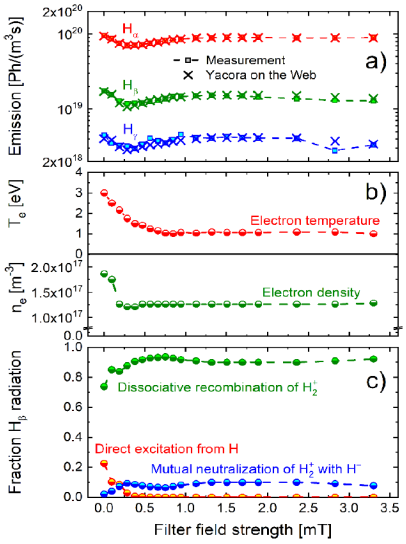

Figure 3.2: *YACORA on the Web results for the recombining plasma in the ELISE expansion region. Balmer line emissions (a)), electron temperature and density (b)) and relative relevance on the different excitation channels (c)) as a function of the filter field strength are shown [55].*

of the negative ions density, as described in [51]. The line ratio H_γ/H_2 is used to evaluate the dissociation degree. The line ratio H_β/H_γ is only used to see if there are strong modifications in these two emissions, but without correlating it with any plasma properties. All measurements carried out in the expansion region are compared with the plasma properties estimated by the Langmuir probes.

3.1.2 Langmuir probes

On SPIDER, local estimates of plasma electron density and temperature are performed with electrostatic probes installed on the Plasma Grid (PG) and on the Bias Plate (BP): they measure the ion saturation current or the full V-I characteristics, employing in this case a nearby larger floating reference electrode for radio-frequency compensation, together with passive filtering electronics installed in vacuum, as near as possible to the

probes [56]. Details of the probes design are given in Ref.[57] and both their location and

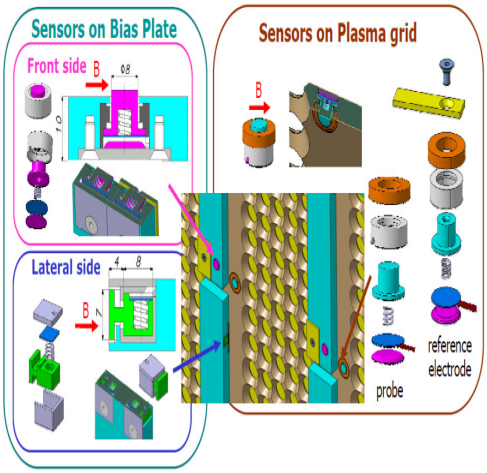

Figure 3.3: *Details of different sensors installed on the PG (right panel) and on the BP (top-left panel). For each probe design, details of the sensor and the position where they are installed are shown. [57]*

components are shown in Fig.3.3. The polarized electrode has a diameter of 8 mm and protrudes from the locking ring, which is at the same level as the supporting structure, of 1 mm, resulting in a total geometrical collection area of 75 mm^2. A total of 84 probes are installed on the PG and BP, to measure both the horizontal and the vertical plasma uniformity.
By measuring the current flowing in the circuit, the current-voltage characteristics of the plasma is obtained. Since the electron temperature T_e in ion sources is larger than the ion temperature T_i, only the first is considered in the analysis of the characteristics. By sweeping the polarization voltage V around the floating potential V_f, defined as the voltage at which the electron and ion fluxes to the probe are equal (zero net current), the V-I characteristics can be divided in three regimes:

- Ion saturation regime, for $V \ll V_f$, only positive ions are collected;
- Exponential regime, for $V_f - T_e < V < V_f + \alpha T_e$, with $\alpha \approx$ 2-3;
- Electron saturation regime, for $V \gg V_f$, when only electrons are collected.

The V-I is fitted by

$$I = I_s R(V - V_f)(exp(\frac{V - V_f}{T_e} - 1)) \tag{3.3}$$

where I_s is the ion saturation current, $R(V - V_f)$ links the effective collection area of the probe and the geometrical surface of the electrode A_{coll} [58]. The plasma electron

density is given by inverting the relation

$$I_s = hen_e\sqrt{\frac{T_e}{m_i}}A_{coll} \tag{3.4}$$

where m_i is the ion mass, e the elementary charge while h depends on probe geometry which, for a planar probe is $h = exp(-1/2) \approx 0.6$. Through the relation

$$V_s - V_f = \frac{T_e}{2e}(1 - ln(2\pi\frac{m_e}{m_i})) \tag{3.5}$$

the plasma sheath potential V_s is estimated.
In this work of thesis, the plasma properties measured by Langmuir probes are analysed. In the expansion region, the results obtained by the probes installed both on the BP and the PG are exploited to study the vertical homogeneity of the plasma, using one measurement in correspondence of each beamlet group, which corresponds to each segment in which the source is subdivided. Moreover, the plasma profile from the expansion region to the driver is characterized using the data collected during a dedicated campaign with movable probes [59].

3.1.3 Retarding Field Energy Analyser

A retarding field energy analyser is an electrostatic probe designed to measure ion energy distribution [60]. Two different designs are tested on the arc source NIFS-RNIS, to measure both negative and positive ion energy distributions, respectively the NI-RFEA and the PI-RFEA; on SPIDER, only a PI-RFEA was installed during the campaign with movable probes, very similar to the one used in RNIS arc source. More detailed descriptions of the probes are in Ref. [61] [62].

Negative Ion RFEA

The NI-RFEA is composed by 2 circular molybdenum grids (called G1 and Retarding, 400 wires/inch, 25 μm thick) and a stainless steel collector, inserted in a molybdenum case with an entrance orifice of 5.6 mm diameter and conical shape; it is in electrical contact with the Plasma Grid, aiming at reproducing one of its apertures. The probe design, with the negative ions and electrons trajectories, together with a schematic representation of the applied voltage are shown in Fig.3.4, on the left; on the right, the probe location on the PG, together with the Electron Deflection Magnets (EDM) magnetic field (bottom) are represented. The first grid, G1, can be polarized between 30 to 300 V, using an external power supply, to mimic the extraction of the negative ion, while by sweeping the potential of the Retarding grid V_{ret}, the energy of the ion is discriminated. The positive polarization of the probe attracts both negative ions and electrons, the latter are deflected after the G1 by the EDM embedded in the extraction grid. The current of the negative ions entering the probe is measured by the collector grid I_{coll}. In Fig.3.5 on the left, an example of the I_{coll} and V_{ret} timelines is shown. During the RFEA campaign, the source operated with 5 s of plasma-on time, 2 s of

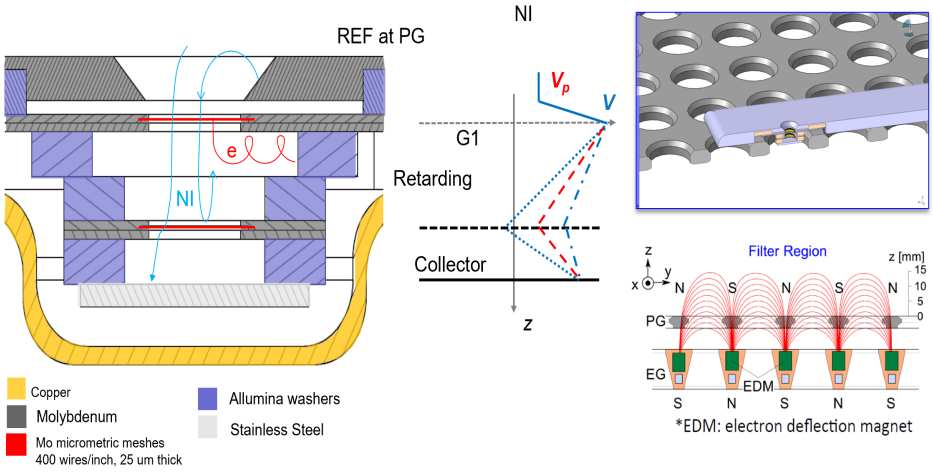

Figure 3.4: *Left: NI-RFEA design with a representation of the polarizations applied to the probe grids. Right: location of the probe on the PG and EDM magnetic field lines.*

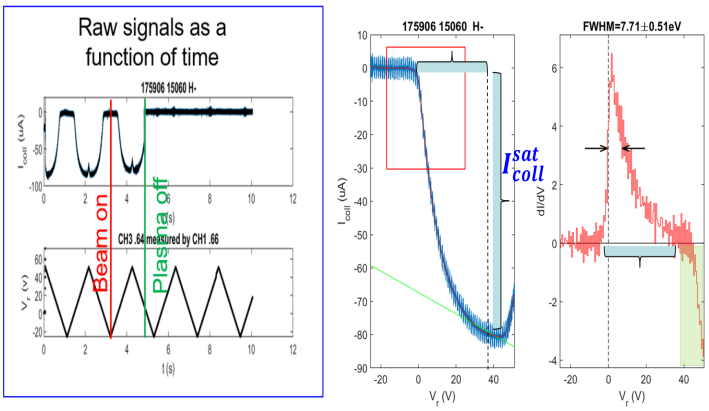

Figure 3.5: *On the left, NI-RFEA I_{coll} and V_{ret} as a function of time; on the right, I_{coll} as a function of V_{ret} and dI/dV; the regions of interest for the data analysis are highlighted.*

beam-on in the final plasma-on phase, with a pulse every few minutes. As shown in Fig.3.5 for positive values of V_{ret}, a current of few μAmps is measured by the probe, which is swept from -25 to 50 V. The I_{coll} as a function of V_{ret} is shown on the right (blue curve). To reduce the noise, the data are resampled in $\Delta V/V$ pieces which are used to derive the curve

$$\frac{dI_{coll}}{dV_i} = \frac{I_{i+1} - I_i}{V_{i+1} - V_i} \tag{3.6}$$

where the index refers to the i-th sample; the derivative obtained is also reported in Fig. 3.5.

The negative ions current density j_{H^-} is estimated by

$$j_{H^-} \approx j_{coll}^{sat} = \frac{I_{coll}^{sat}}{A_{coll} \cdot T_{tot}} \tag{3.7}$$

I_{coll}^{sat} is calculated by the difference between the current measured at V_{ret}=0 V and the value of V_{ret} for which the slope of the V-I characteristics changes, indicated by the green line in Figure. T_{tot} is the transparency of the probe (ratio between the open and the total surface); it is measured experimentally when the probe was polarized to measure positive ions, to avoid eventual contribute due to co-extracted electrons. The electron current density is measured by

$$j_{e^-} \approx j_{G1}^{sat} = \frac{I_{G1}^{mean}}{A_{G1} \cdot (1 - T_{G1})} - j_{H^-} \tag{3.8}$$

where all the quantities are measured on the first grid G1. From the Full Width at Half Maximum FWHM and the peak position of the derivative dI/dV, other information is obtained. The FWHM, indicated by the black arrows, is correlated with the axial energy component of the negative ions. The peak position, instead, by assuming that most of the ions are generated at the same potential (the PG potential through surface production) is correlated with the plasma potential. However, only an over-estimation of the negative ions velocity distribution, and thus of their temperature, is obtained by these measurements: in fact when polarized, the conical shape of the first gap reproduces a meniscus, whose shape depends on the current density and the voltage applied to the G1. The meniscus modifies the axial energy of the particles coming from the plasma and reaching the G1 grid. This behaviour is described more in details in Sect. 5.4, where the shape of the distribution is correlated with the beam divergence. The green area in Fig.3.5 highlights the part of the distribution which can be neglected, since this current is measured fot V_{ret} larger than the polarization of the collector, which was fixed at 36.5 V.

Positive Ion RFEA

The PI-RFEA design is shown in Fig.3.6, together with the dimensions and materials of which it is made and its location on the PG in the NIFS-RNIS experiment; also a schematic representation of the polarization applied to its grids is given. The probe is composed of a collector plate and four parallel nickel electrodes, hith the specification of 750 meshes/inch, thickness of 9 μm, and nominal transparency, T_{nom}=0.55. The grid electrodes and collector are insulated with ceramic rings and the whole module is contained in a copper structure, in electrical contact with the plasma grid, with an entrance aperture with 9 mm diameter. Each grid composing the probe has a different purpose:

- First grid (G1). This is the plasma facing grid, with 3.2 mm diameter. To attenuate the plasma flux entering the device, it is kept a constant negative voltage of -30 V, to repell all the negative charges allowing only the positive ions to enter. This is necessary to reduce the space charge effects [62].

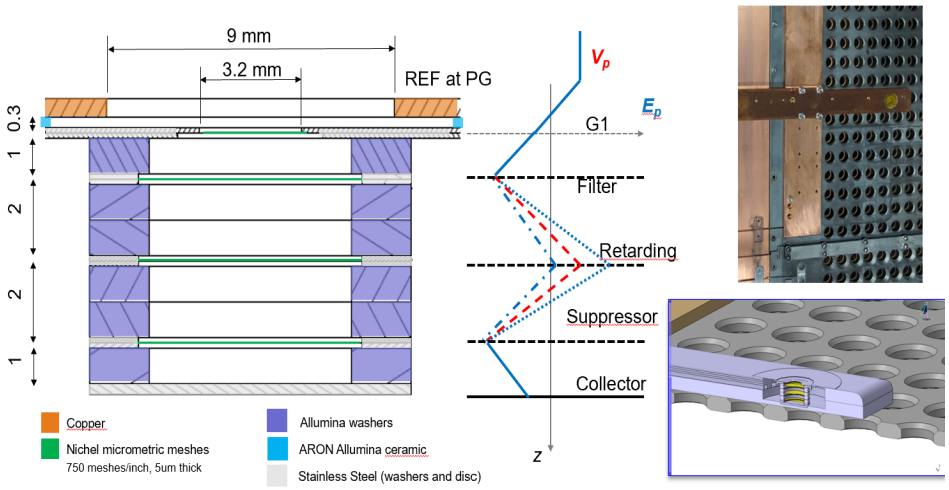

Figure 3.6: *Left: PI-RFEA design with a representation of the polarizations applied to the probe grids. Right: location of the probe on the PG.*

- Filter grid. A further grid aiming at reducing the space charge effect; its polarization is fixed to -100 V.
- Retarding grid. This grid is polarized with a swiping voltage, necessary to measure the positive ion axial energy distribution.
- Suppressor grid. The potential of this grid is fixed to -120 V, in order to repel the secondary ions emitted from the Retarding and Filter grids.
- Collector grid. Always polarized to a potential higher than the suppressor grid (to avoid secondary emission), the positive ions finally are collected by this grid.

It is demonstrated in Ref.[61] that an energy resolution lower than eV is given by this diagnostic. This value is in agreement with the expected positive ions temperature close to the PG of the NIFS-RNIS source, whose plasma potential is of few volts [63]. The data analysis is similar to the one described for the NI-RFEA in the previous section, while an example of experimental data is shown in Fig.3.7. The positive ion current density is estimated by the current measured on the first grid, while the transparency of probe is estimated from the ratio of the positive ions current measured on the G1 and on the collector; it is also corrected by considering the gas collisional transparency. Due to the high degree of electronegativity of the plasma in this region, the effective Bohm velocity u_B^* is used to estimate the positive ion density at the sheath [64], by

$$n_{H^+,s} = \frac{j_{H^+}}{eu*_B} \tag{3.9}$$

$$u_B^* = u_B \sqrt{\frac{1+\alpha_s}{1+\gamma\alpha_s}} \tag{3.10}$$

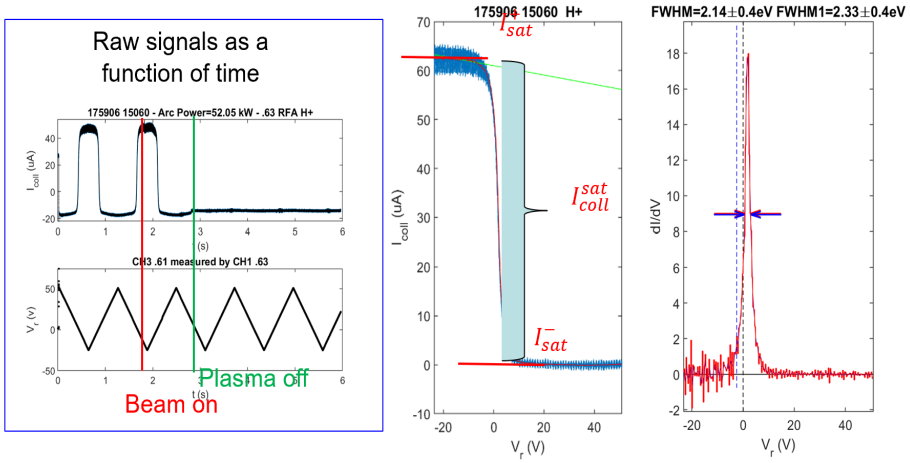

Figure 3.7: *On the left, PI-RFEA I_{coll} and V_{ret} as a function of time; on the right, I_{coll} as a function of V_{ret} and dI/dV; the regions of interest for the data analysis are highlighted.*

where $u_B = \sqrt{eT_e/m_{H^+}}$, $\alpha_s = n_{H^-,s}/n_{e_s}$ and $\gamma = T_e/T_{H^-}$.
The RFEAs used on SPIDER are very similar to the one just described, except for a slightly lower diameter to be able to pass through SPIDER accelerator apertures. The comparison between the data measured on these two different sources is given in Chapter 5.4.

3.2 Beam diagnostics

To study the uniformity of the SPIDER beam profile, as well as to estimate the beam divergence, Beam Emission Spectroscopy (BES), visible tomography and an instrumented calorimeter based on custom unidirectional carbon-fiber-composite (CFC) tiles, observed by infrared cameras, are available. Visible tomography will be described in detail in next chapter, since it is one of the main topic of this thesis work. The measurements of the beam properties carried out by BES and STRIKE calorimeter will be compared with the results obtained by visible tomography.
In the following, the operating principles of these two diagnostics and their experimental setup on SPIDER are briefly described.

3.2.1 Beam emission spectroscopy

Beam emission spectroscopy (BES) diagnostic is a non-invasive diagnostic which measures the light emitted in the collisions between the fast beam particles and the background gas in which they propagate; the background molecules are in first approximation assumed to be at room temperature. A set of collimators measure the H_α/D_α emission,

which is the most intense emitted radiation, corresponding to the transition between n=3 to n=2 levels. Many beam parameters can be inferred by measuring the integral and the width of Doppler shift of H_α/D_α. The initial design and simulation of the BES diagnostic for SPIDER are described in Ref.[65], while the first experimental measurements are in Ref.[66]. The photons produced by the de-excitation of the beam particles have a Doppler shifted wavelength λ', according to

$$\lambda' = \lambda_0 \frac{1 - \beta cos\alpha}{\sqrt{1-\beta^2}} \tag{3.11}$$

in the laboratory frame of reference; λ_0 is the unshifted H_α wavelength which corresponds to 656.2 nm. β is

$$\beta = \frac{v}{c} = \sqrt{1 - (\frac{mc^2}{mc^2 + eU_{tot}})^2} \tag{3.12}$$

where v is the beam particles speed, c the speed of light, U_{tot} the total beam particles energy, which corresponds to the total potential difference in the acceleration system. α is the angle between the beam particles' trajectory and the direction of the collected photons; it is experimentally obtained from Eq. 3.12 by fitting as a Gaussian both the full energy Doppler peak and the unshifted H_α peak (giving respectively λ' and λ_0). An example of an experimental spectrum measured on SPIDER is shown in Fig.3.8. The stripping losses are given by neutralized negative ions in the accelerator, therefore before reaching the total energy. The red curves represent the selected wavelengths interval for Gaussian fits. From the Gaussian fit of the Doppler peak the beamlet emissivity

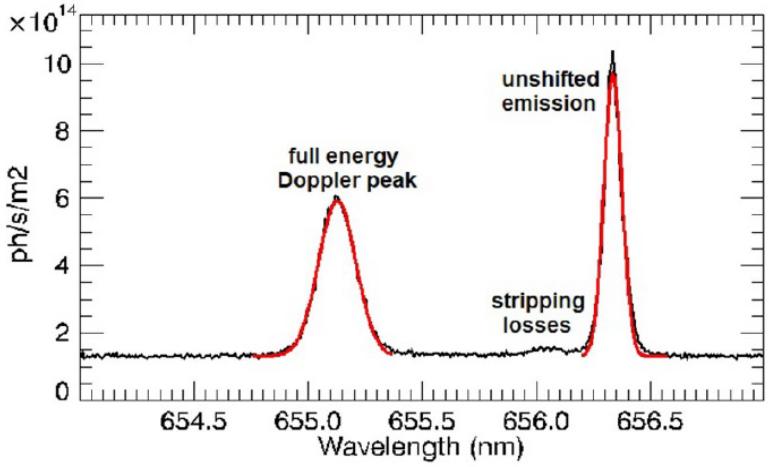

Figure 3.8: *Example of BES spectrum acquired in SPIDER.*

is obtained; since BES lines-of-sight are distributed all around the beam, they give a spatial profile of the beam intensity. Furthermore, the width of the Doppler peak allows

to estimate the beam divergence δ, according to [66]

$$\delta = \sqrt{2}(\frac{\lambda_0 \beta sin\alpha}{\sqrt{1-\beta^2}})^{-1}\sqrt{W^2 - \Delta\lambda_N^2 - \Delta\lambda_I^2 - (\frac{\lambda_0 \beta sin\alpha}{\sqrt{1-\beta^2}})^2\omega^2 - [\frac{e\lambda_0^2}{mc^2\beta}(\beta - cos\alpha)]v^2} \tag{3.13}$$

where W is the fitted width of the Doppler peak, $\Delta\lambda_N$ is the intrinsic width of the H_α/D_α line, $\Delta\lambda_I$ is broadening due to the spectrometer instrumental function, ω the angular spread introduced by the finite dimensions of the collimator optical aperture and v the ripple of the total acceleration voltage.

3.2.2 STRIKE calorimeter

The diagnostics calorimeter STRIKE (Short-Time Retractable Instrumental Kalorimeter Experiment) is made of 16 one-directional carbon-fiber-composite (CFC) tiles, mounted on two movable structures (8 per panel). The energy flux profile of the beam is observed by thermal cameras on the rear side; to guarantee the beamlet footprint on the rear side as similar as possible to the front one, the CFC is chosen since its conductivity along z is much greater (around 10 times) than in the x and y directions. A detailed description of the diagnostic is given in Ref.[67] [68], while the first experimental results on SPIDER are shown in Ref.[69]. During the experimental campaign with 80 open beamlets, only half of STRIKE calorimeter was installed, thus half of the beam hits the beam dump; an example of the footprint of the beamlets measured by the two IR cameras is shown in Fig.3.9. From the measurement of the temperature increase map at a given time, it is possible to obtain the beam energy flux by calorimetry. Thanks to the masking of most of the apertures composing SPIDER beam, the calorimetrical current of each single beamlet is measured. In addition, an electrical measurement of the total beam current impinging on each tile is available, allowing to achieve a higher time resolution with respect to the calorimetrical measurement; to recollect the electrons emitted from the surface of the tiles, due to the impact of high energy beam particles, a positive bias is applied. From the measured map of the temperature variation, the beamlet divergence and deflection are estimated. The calorimetrical beam current is obtained by

$$I_{cal} = \frac{\rho V}{U_{tot}\tau_{beam}} A_{pix} \sum_{i,j}^{n_x,n_y} \int_{t=0}^{t=\tau_{beam}} c(T(i,j))dT \tag{3.14}$$

where U_{tot} is the total acceleration voltage (beam energy), τ_{beam} the pulse length with beam on, ρ, V and c the tile mass density, volume and specific heat, respectively, and A_{pix} the area covered by each pixel; $n_x \times n_y$ are the total pixels belonging to each tile [69].

The temperature increase map of each tile at a given acquisition frame is fitted as a sum of bidimensional Gaussians, one for each beamlet impinging on the tile:

$$\Delta T(x,y) = \sum_{i=1}^{n_{beamlets}} A_i e^{-\frac{(x-x_i)^2}{w_{x,i}^2}} e^{-\frac{(y-y_i)^2}{w_{y,i}^2}} \tag{3.15}$$

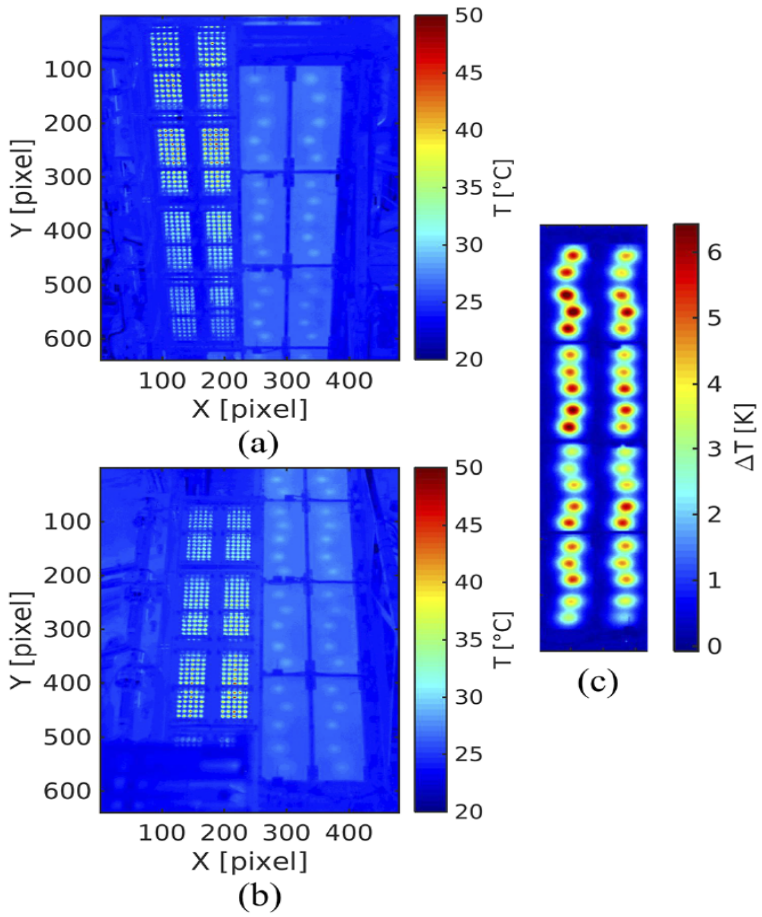

Figure 3.9: *Infrared measurements of SPIDER beam on the STRIKE tiles from the two infrared cameras (a) and b)); in c), the temperature map of the STRIKE panel from the merging of a) and b) is shown. [69]*

From the 1/e widths $w_{x,i}$ and $w_{y,i}$ and the centre coordinates x_i, y_i, both the divergence and deflection of each beamlet can be estimated.
Both the calorimetrical and electrical current measurements, as well as the vertical width of each beamlet estimated by STRIKE, will be compared with the results given by visible cameras.

Chapter 4

Beam emission tomography

In this Chapter, the beam emission tomography is described. Tomographic reconstructions are exploited in very different scientific environments, to reconstruct an object starting from a set of measurements. A brief description of this technique and of its principles is given in Section 4.2. For the first time, the beam emission pattern of a negative ion beam is reconstructed by means of tomographic inversion.
This diagnostic is composed by a set of visible cameras, which measure the light emitted by the interactions of negative ions with the background gas in which they propagate. Being a non invasive diagnostic, which only needs viewports on which to install visible cameras to collect the beam light, it is a very promising tool for characterizing the negative ion beam even in ITER HNB.
Before to describe in detail the analysis performed on the signals measured by visible cameras, the main processes responsible for the visible beam-induced emission are described in Section 4.1. The model developed to directly correlate the visible light emitted by the beam with the beam current density is described, allowing to use the results obtained by the tomographic reconstruction to study the beam homogeneity in terms of equivalent beam current density. The procedure which have allowed to obtain the two-dimensional beam emission pattern, starting from the isolated set of beam profiles measured by different cameras is then presented. Before being applied to the large SPIDER beam, visible cameras are tested to reconstruct NIO1 beam emission pattern, which is a smaller negative ion source; both SPIDER and NIO1 experimental setup are described in Section 4.3. To reconstruct a beam emission pattern, starting from a set of measurements, a robust calibration, both relative and geometrical, of the devices composing the diagnostic is fundamental, which is described in detail in Chapter 4.4. This calibration allows to compare the beam profiles measured by different cameras, which can also be exploited to estimate the beam divergence. In NIO1 and in SPIDER (thanks to the masking of most of the beamlets), it is possible to study the single beamlet divergence, and the technique used to estimate the beamlet width with visible cameras is described in Section 4.5. This analysis is used in Chapter 5 to study the divergence of the beam of SPIDER, also by comparing the results obtained by the other beam diagnostics. In Section 4.6, the tomographic inversion technique developed to reconstruct

both SPIDER and NIO1 negative ion beams is explained and in Section 4.7 the state of the art is presented. In particular, the method used in this work of thesis to study the beam homogeneity is described in detail.
All the methods presented in this chapter will be used in the following to characterize SPIDER negative ion beam, with the support of the other available measurements, described in the previous chapter.

4.1 Interpretation of the beam emission and comparison with the beam current

In this section, the relation between the light measured by the cameras and beam current density is discussed. By taking into account the dependence of the beam emissivity with the background gas density and beam energy, a weighted emissivity directly proportional to the beam current can be estimated. In this way, the reconstructed emissivity can be used to study the beam homogeneity in terms of beamlet current density. First of all, it is necessary that the background gas in which the beam propagates is homogeneous: this is assured, both in the case of SPIDER and NIO1 vessel, by the pumping system; the gas pressure profile along the beam propagation direction in SPIDER is measured in Ref.[70]. The beam energy is varied when the acceleration voltage is changed, ranging from 20 to 70 kV in the case of SPIDER beam, between 2 to 25 kV in the case of NIO1 beam. By assuming that there is no variation along z direction (i.e. the beam propagation direction) in the emitting volume observed by each pixel of the camera sensor, the reconstructed emissivity $\epsilon(x, y)$ is related to the beam current density j_{beam} through

$$\epsilon = n_{beam} n_{bkg} \sigma_{eff} v \frac{A_{32}}{A_{32} + A_{31}} = \frac{j_{beam}}{q} n_{bkg} \sigma_{eff} \frac{A_{32}}{A_{32} + A_{31}} \tag{4.1}$$

where σ_{eff} is

$$\sigma_{eff} = \frac{\sigma_0(E)\Gamma^0 + \sigma_-(E)\Gamma^- + \sigma_+(E)\Gamma^+}{\Gamma^0 + \Gamma^- + \Gamma^+} \tag{4.2}$$

a weighted average of the excitation cross sections of the different species composing the beam, from ground to n=3 (H_α emission) whose fraction is obtained by solving the system of differential equations described in the following; $\frac{A_{32}}{A_{32}+A_{31}}$ determines the emission probability, being A_{pk} the transition probability from level p to level k; n_{beam} and n_{bkg} the beam and background densities, v the beam particles velocity and q the elementary charge. Only variables are the cross section $\sigma_{eff}(E)$, depending on the energy of the beam, E, and the background density n_{bkg}. The sensors mounted on the cameras are sensitive to the entire visible spectrum, as shown in Fig.4.7, so they collect the Balmer series emission and the Fulcher one. The most intense emission line in the visible spectrum is the H_α (or D_α), which corresponds to $\lambda_0 = 656.2793$ nm for H ($\lambda_0 = 656.1032$ nm for D). The H_α (or D_α) is produced through the de-excitation from the n=3 to n=2 energetic level of atoms previously excited. This excited state can be

produced by different reactions:

$$H^-_{beam} + H_2 \rightarrow H^*_{beam} + H_2 + e \tag{4.3}$$

$$H_{beam} + H_2 \rightarrow H^*_{beam} + H_2 \tag{4.4}$$

$$H^+_{beam} + H_2 \rightarrow H^*_{beam} + H^+_2 \tag{4.5}$$

$$H^-_{beam} + H_2 \rightarrow H_{beam} + H + H^* + e \tag{4.6}$$

$$H_{beam} + H_2 \rightarrow H_{beam} + H + H^* \tag{4.7}$$

$$H^+_{beam} + H_2 \rightarrow H^+_{beam} + H + H^* \tag{4.8}$$

where the H^+_{beam} and H_{beam} are produced following the interaction of the H^-_{beam} with the background gas during the beam propagation. To consider the contribution to visible light of different ion species, a simple model is developed. The charge state of a negative ion beam evolves during the propagation due to the interaction with the background particles, constituted by a partially ionized gas. The particle fluxes of different charges are described through a set of equations:

$$\begin{cases} d\Gamma^-/dz = -\Gamma^-(\sigma_{-10} + \sigma_{-11})n_{bkg} \\ d\Gamma^+/dz = \Gamma^-\sigma_{-11}n_{bkg} + \Gamma^0\sigma_{01}n_{bkg} - \Gamma^+\sigma_{10}n_{bkg} \\ d\Gamma^0/dz = \Gamma^-\sigma_{-10}n_{bkg} + \Gamma^+\sigma_{10}n_{bkg} - \Gamma^0\sigma_{01}n_{bkg} \end{cases} \tag{4.9}$$

By assuming *dz=vdt* for non-relativistic particles, these equations describe the variation of the different beam components along the beam propagation path. $\Gamma^-, \Gamma^+, \Gamma^0$ are the H^-, H^+, H^0 fluxes, n_{bkg} is the background H_2 density, estimated from an ideal gas law by assuming a temperature of 300 K. The symbol σ_{mn} denotes the cross section of particles changing the charge state from m to n. The different cross sections are the probability of the various reactions to occur, which are shown in Fig.4.1: σ_{-10} and σ_{-11} are the stripping and double stripping cross sections, producing respectively excited H^0 and H^+, together with the emission of one and two electrons (respectively the green triangles and the red squares in Fig.4.1); the ionization cross section σ_{01} increases the fraction of positive ions, while the charge exchange σ_{10} is responsible of the increase in neutral and reduction of positive ions. All the cross sections are listed in Ref.[20]. The cross sections of stripping σ_{-10} and ionization σ_{01} are very similar at the range of energies explored up to now in SPIDER (between 20 and 60 kV). Once the beam energy is increased, as to 1 MeV (ITER specifications) σ_{01} fast decreases and the main contribution is attributable to the stripping. To estimate the beam composition for a given background pressure and energy at the position seen by the cameras, the system of differential equations is solved, by assuming a beam composed entirely by negative ions at z=0 and a background of H_2. In Fig.4.2 two examples of beam composition with 20 mPa of gas pressure and two different energies, 20 keV on the left and 50 keV on the right, are shown. As the beam propagates, the negative ions neutralize and the fraction of neutrals increases; also the positive ions start to augment, but slowly with respect to the neutrals; the relative composition of the beam changes when the beam energy is

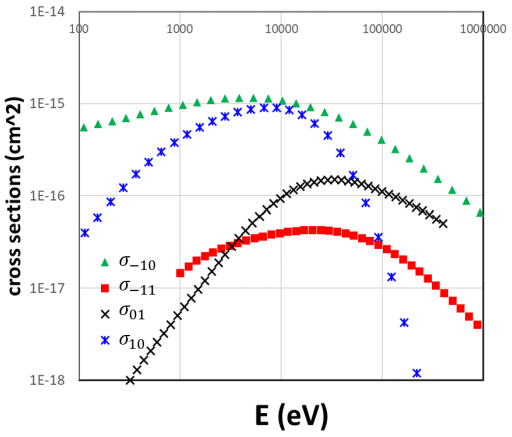

Figure 4.1: *Cross sections of the stripping and double stripping, charge exchange and ionization reactions considered in the model for estimating the composition of the beam along its path [20].*

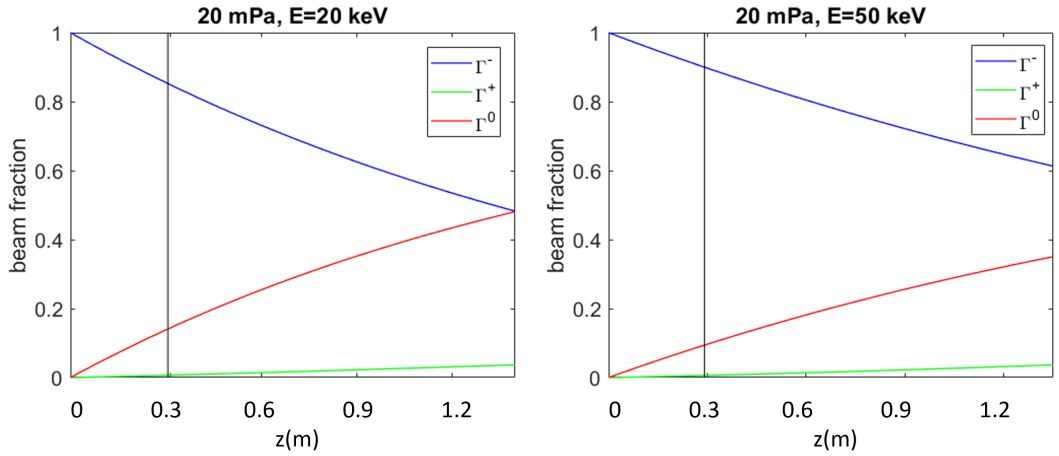

Figure 4.2: *Beam fractional composition along the beam propagation direction for the same background pressure and two beam energies. The black line represents the position seen by the cameras.*

varied. Knowing the composition of the beam, it is possible to take into account the contribution of each species to the emission of visible light, obtaining σ_{eff}, Eq.4.2. The set of included cross sections is shown in Fig.4.3; the strongest contribution is due to the stripping cross sections of the H^- which produces excited H^0 in the level n=3 (black crosses in Fig.4.3). It is thus possible to correct the signal measured by the cameras at different values of pressure and energy and to obtain an estimation of the beam current

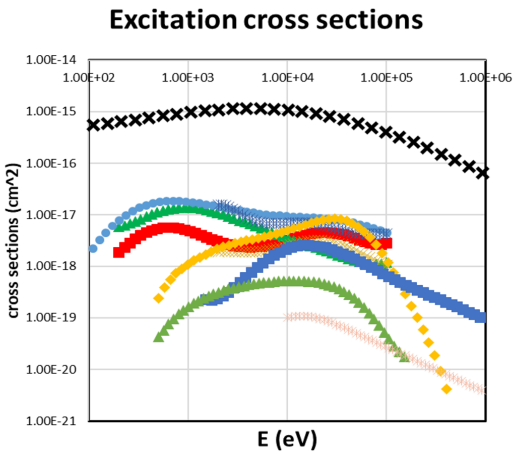

Figure 4.3: *Excitation cross sections to final state n=3 (H_α emission).*

from the beam emissivity. The effect of this correction is shown in Fig.4.4. There, two

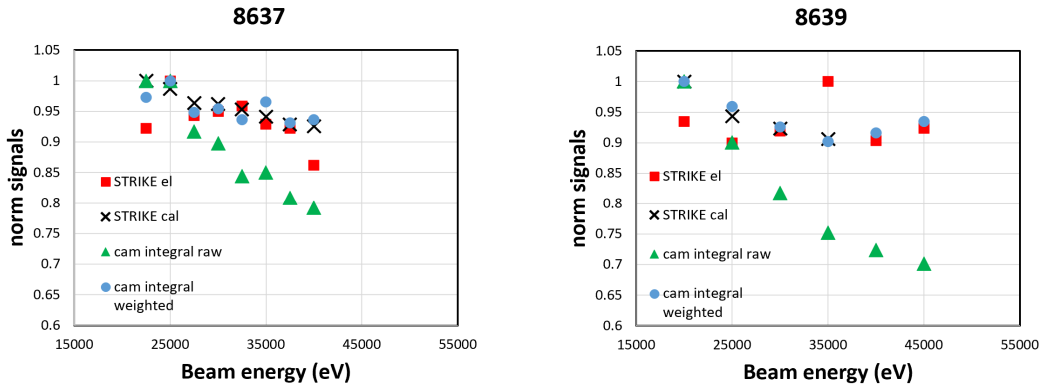

Figure 4.4: *Scans in acceleration voltage (beam energy) at two different radio-frequency powers (4x90 kW on the left, 4x100 kW on the right). The red squares represent the STRIKE electrical current, the black crosses the STRIKE calorimetrical current. The green triangles represent the integral of the beamlets measured by the cameras without the correction, the blue point the weighted integral.*

scans in acceleration voltage, i.e. in beam energy, for two different radio-frequency powers of 4x90 kW on the left and of 4x100 kW on the right, are shown. The signal measured by the cameras is compared with the electrical (red squares) and calorimetrical (black crosses) STRIKE current measurements (this diagnostic is described in Sect.3.2.2). The green triangles represent the camera integral of the beamlets that impinge on the considered STRIKE tile without the correction (raw emissivity); the blue points, instead,

represent the signal of the camera weighed with the excitation cross sections of each species, by considering the different fraction of them when the energy is changed. All measurements are normalized to the highest value. As the beam energy increases, the integral measured by the cameras (green triangles) decreases as the cross sections vary. Considering the different cross sections (Fig.4.3), for the various species composing the beam at a given background density, the light measured by the cameras has the same trend as both electrical and calorimetrical beam current measurements (blue points). With such a correction, the trend of the integral measured by the camera matches the electrical and calorimetrical beam current measured by STRIKE calorimeter, allowing to estimate the beam current density using solely the light measured by the cameras.
In the following, this correction is applied to the experimental data measured by visible cameras, thus allowing to directly estimate the beamlet current density from the reconstructed emissivity.

4.2 Tomography

Tomography derives from the greek words "tomos", which means slice, section, and "grapho", which means to write. Tomographic reconstruction is a multidimensional inverse problem based on the estimation of the profile of a specific system from a finite number of projections. It consists in reconstructing an object, usually an emission or absorption radiation pattern ϵ by starting from a set of measurements (line integral signals). One of the most important properties of this technique, is that it is a non invasive diagnostic while it is intrinsically 2D (or even 3D), allowing at reproducing the object it measures without perturbing it.
The formal solution to the tomographic problem, i.e. the reconstruction of a function from its projections, was found by J. Radon in 1917 who defined an integral transform of a function *f*, whose value at a particular line is equal to the line integral of the function along that line [71].
In 1979, the Nobel Prizes Cormack and Hounsfield devised a practical solution which can be implemented in a computer, opening the path to the modern computer tomography, which is now applied to very different environments: from medicine to mechanics, seismology and many scientific fields. A detailed description of the technique is in Ref.[72] [73]. Each tomographic reconstruction measures a different physical quantity, such as the number of x-ray photons transmitted through the patient along individual projection lines in the computer tomography, the number of photons emitted from a patient in nuclear medicine, the light emitted by the beam particles interacting with the background gas in which they propagate in particle beam framework. In all cases, the goal is to estimate from these measurements the distribution of a particular physical quantity in the object. Under certain conditions, the measurements made in each modality can be converted into samples of the Radon transform of the distribution to be reconstructed, whose inverse provides the mathematical basis for reconstructing tomographic images from measured projection or scattering data.

4.2.1 The Radon Transform

The Radon transform (RT) of a distribution f(x,y) is defined as

$$p(\xi,\phi) = \int f(x,y)\delta(xcos\phi + ysin\phi - \xi)dxdy \tag{4.10}$$

where δ is the Dirac delta function and the coordinates x, y, ξ and ϕ are defined in Fig.4.5; the function $p(\xi,\phi)$ is called sinogram, because the Radon transform of an off-centre point source is a sinusoid. The goal of a tomographic reconstruction is thus to find f(x,y) knowing $p(\xi,\phi)$.
The solution to the inverse Radon transform is based on the central slice theorem (CST), which relates the 2D Fourier transform (FT) $F(\nu_x,\nu_y)$ of $f(x,y)$ to the 1D FT of $p(\xi,\phi)$

$$P(\nu,\phi) = F(\nu cos\phi, \nu sin\phi). \tag{4.11}$$

so that the value of the 2D FT of $f(x,y)$ along a line with the inclination angle ϕ is given by the 1D FT of $p(\xi,\phi)$, which is the projection profile of the sinogram acquired at the angle ϕ (see Fig.4.5) [71]. With enough projections $P(\nu,\phi)$, it is thus possible to

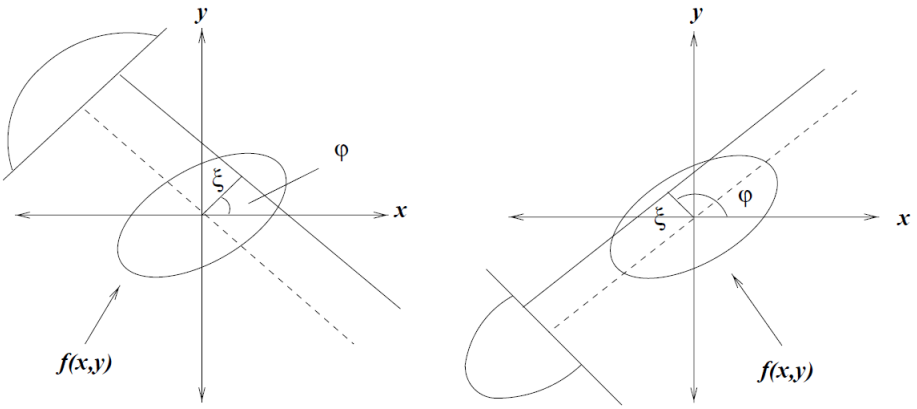

Figure 4.5: *Representation of Radon coordinates and two different projections of the same object, seen from two angles.*

cover the entire space $\nu_x - \nu_y$ and to generate $F(\nu_x,\nu_y)$.
There are many tomographic reconstruction techniques which can be more or less suitable depending on the experimental setup. When the number of lines of sight is limited and not uniformly distributed around the object to be reconstructed, algebraic reconstruction algorithms based on pixel method are preferred, as will be described in the following.

4.3 Negative ion beam emission tomography

Emission tomography is widely used both in plasma physics and in positive ion beams [74] [75], while it is never been used in negative ion beam to completely reconstruct the two dimensional beam pattern. It is based on the measurement of the light emitted during the beam propagation in the background gas by a set of sensors, along a suitable number of lines-of-sight (LoSs) on a plane perpendicular to the beam propagation direction. The brightness f_j, i.e. the radiation measured by the j-th LoS over the emitting area A_j, is related to the beam emissivity pattern $\epsilon(x, y,)$ according to

$$f_j = \int_{A_j} \epsilon(x, y) \cdot dx \cdot dy. \tag{4.12}$$

In the following, SPIDER and NIO1 tomographic systems are described.

4.3.1 SPIDER Experimental setup

A detailed description of SPIDER beam emission tomography can be found in Ref.[76]. It is composed by 15 2D visible cameras mounted all around the beam at the end of the accelerator system (0.3 m from the last grid, the Grounded Grid GG). To guarantee a good tomographic reconstruction, a full coverage of the beam section with LoSs is necessary, to avoid any symmetric arrangement. In Fig.4.6 the SPIDER tomographic system with all the 15 installed cameras is shown. The two camera colours represent the two models used, both CMOS sensors: in blue are indicated the Basler (B) acA1920-40 gm, which uses Sony IMX249 CMOS sensor, composed by 1920x1200 square pixels (5.86 μm side), with 12 bit resolution and maximum acquisition rate 45 frames per second [77]; in red are indicated the PointGrey (PTG) BFS-PGE-27S5M-C, which uses Sony IMX429 CMOS sensor, composed by 1936x1460 square pixels (4.5 μm side), with 16 bit resolution and maximum acquisition rate 43 frames per second [78]. The quantum efficiency of Sony IMX249 CMOS sensor is shown in Fig.4.7. To increase the contrast aiming to better recognize the beamlets, a 200 mm wide strip of aluminium black foil (Metal Velvet coated foil by Acktar [79]) is installed all around the vacuum vessel, in the region observed by the cameras, at 0.3 m from the GG. Furthermore, another black aluminium strip is installed at 1 meter far from the last grid, in order to estimate the beam divergence by taking two different measurements along the beam propagation direction.
In order to have the most complete coverage of the beam, different objectives with various magnifications are mounted on the cameras. Three different focal lengths are used on SPIDER: 8mm, 16mm and 25mm. They have a resolution of 1.5, 0.75 and 0.48 mm/pixel on the CMOS sensors, in the plane at the centre of the beam, respectively. A summary of the cameras currently mounted on SPIDER, with their objectives and location is given in Table 4.1.

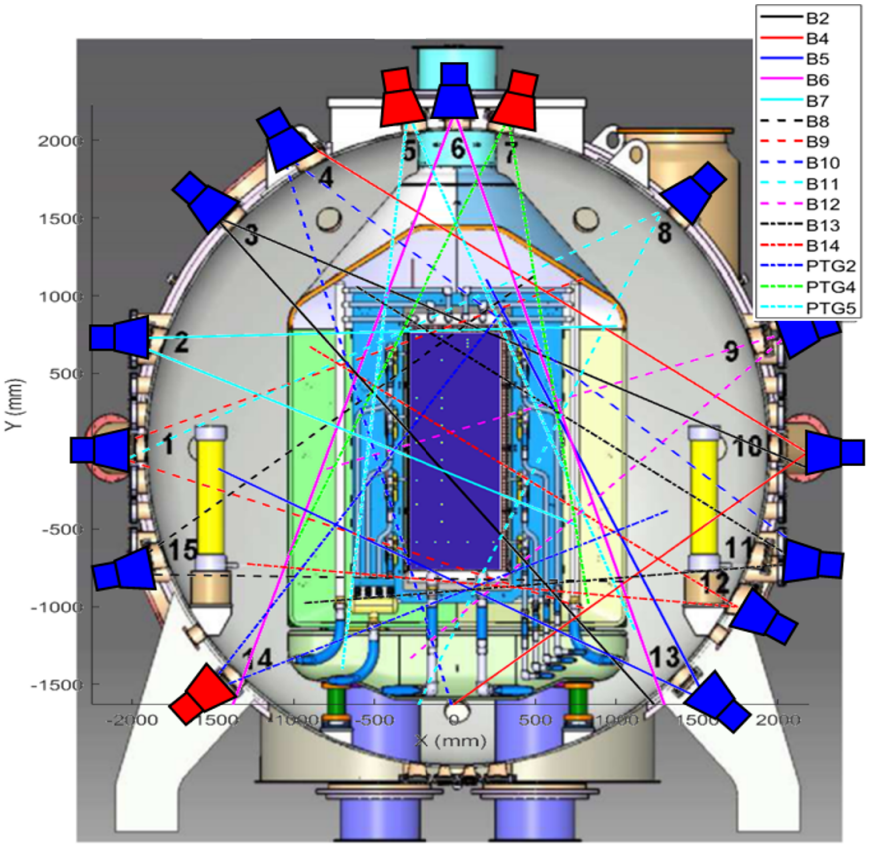

Figure 4.6: *Representation of SPIDER tomographic system; the 15 cameras with their fasn of lines of sight are shown; the two colours represent the two camera models, respectively the Basler in blue and the PointGrey in red. The numbers indicate the tomographic port.*

4.3.2 NIO1 experimental setup

NIO1 tomographic system is simpler than the SPIDER one, since the dimension of NIO1 beam is smaller than SPIDER beam (see Sect.1.5.1). It is composed by two Basler visible cameras, the same model mounted on SPIDER, which are looking at the beam laterally (Lateral Camera LC) and from the bottom (Bottom Camera BC), at the end of the accelerator system, as shown in Fig.4.8, respectively in blue and in green. They mount respectively a 25 mm (0.12 mm per pixel in the beam plane) and 16 mm focal length lens (0.18 mm per pixel in the beam plane). Another camera is installed at 0.7 m from the last grid, and will be used to better estimate the beam divergence. In Fig.4.8 the BES LoSs and the CFC Calorimeter are also shown; the yellow cones represent the 9 beamlets composing NIO1 beam.

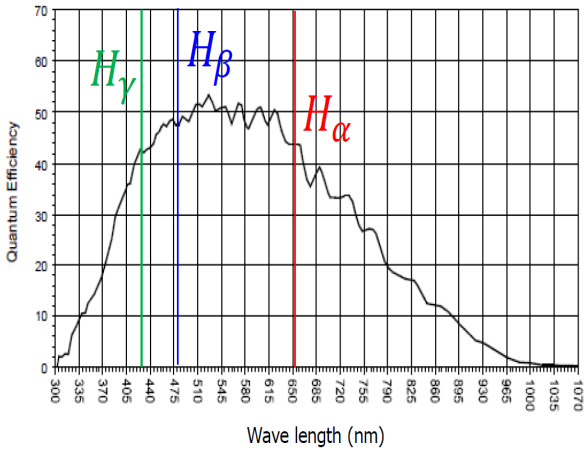

Figure 4.7: *Quantum efficiency of Sony IMX249 CMOS sensor. First three lines of the hydrogen Balmer series are indicated.*

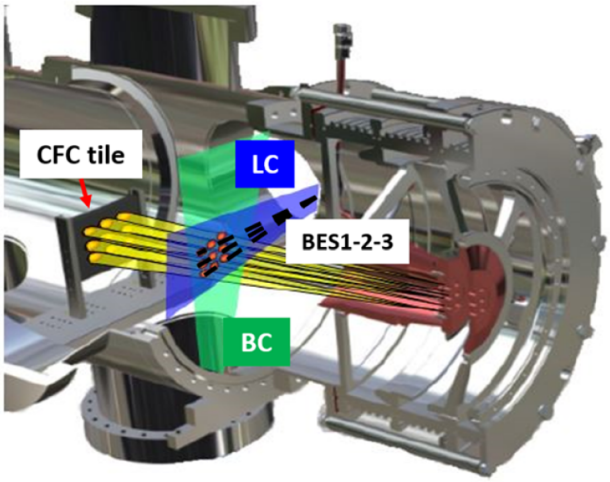

Figure 4.8: *NIO1 diagnostic tube. In blue and in green are shown respectively the fan of LoSs of lateral and bottom camera. The BES LoSs and the CFC calorimeter are also shown; the yellow cones represent the 9 beamlets.*

4.4 Camera calibration

To perform a tomographic reconstruction all cameras must be relatively calibrated, in order to be able to compare the number of photons collected by different sensors composing the tomographic system. Furthermore, it is necessary to know exactly where each

Port number	Name	Model	Obj
01	Basler9	Basler	16 mm
02	Basler7	Basler	25 mm
03	Basler2	Basler	25 mm
04	Basler10	Basler	16 mm
05	PTG5	PointGrey	16 mm
06	Basler6	Basler	16 mm
07	PTG4	PointGrey	16 mm
08	Basler11	Basler	16 mm
09	Basler12	Basler	25 mm
10	Basler4	Basler	8 mm
11	Basler13	Basler	16 mm
12	Basler14	Basler	25 mm
13	Basler5	Basler	16 mm
14	PTG2	PointGrey	16 mm
15	Basler8	Basler	16 mm

Table 4.1: List of camera models and their objectives composing SPIDER tomographic system.

camera is looking at, so a spatially calibration is needed to reconstruct the lines-of-sight of all the cameras. Two different calibrations are thus performed, one in laboratory and the other on site, after the installation of the cameras on SPIDER vessel. The same procedure is applied to calibrate NIO1 cameras.
In the following the two calibrations are described.

4.4.1 Relative calibration

Since two different camera models are used, it is necessary to calibrate them individually, finding the relation that permits to directly compare the light collected by the two sensors. To perform an absolute calibration, however, it is necessary to know the exact composition of the beam, since the cameras measure the entire visible spectrum. The simple numerical model described in 4.1 would be able to convert the number of photons measured by the sensors into beam current, but it only considers the H_α emission line. For this reason, the installation of H_α filters is planned for future SPIDER operation, as well as the improvement of the simple numerical model presented here, taking into account for example also the contribution of secondary electrons or other secondary effects. For the purpose of this thesis work, the relative calibration of the cameras is sufficient, since the proportionality with the beam current is already demonstrated and the relative calibration is mandatory to exactly reconstruct the 2D beam pattern by visible tomography. The two main parameters that are varied during the experimental campaigns are the exposure time and gain. The exposure time determines how long the camera pixels are exposed to light; typical exposure time is between 0.1 and 4

seconds. The gain, instead, determines the slope of the response curve for the camera: by increasing the gain, it results in a higher grey value output from the camera for a given amount of output from the imaging sensors. Usually, the gain is fixed at 100 dB (in a range from 0 to $20log_{10}(x/32)$ dB, with $0 < x < 240$) for Basler cameras and at 5 dB (in a range from 0 to 45 dB) for PointGrey ones.
In the following, dependence on exposure time and gain for the two camera models is described. A LED and a calibrated lamp as fixed light sources are utilized to compose the experimental setup. Cameras are mounted on a support, at a known distance from the light in a dark room, and the background noise is subtracted from all the measurements. For all the analyses, the integrals measured inside the illuminated area of the sensors are reported.

Exposure time dependence

The signal measured by CMOS sensors should increase linearly with the exposure time. This is experimentally verified for the Basler sensor while for the PointGrey, especially for the lowest value of exposure time, this relation fails. The response of both models on the exposure time is shown in Fig.4.9. The same light is monitored by the two camera models, at the same distance and with the same objective. The measurements are shown as a function of the gain and with different exposure times. There was no difference in the results obtained with the LED and calibrated lamp. In Fig.4.9 a), the light measured

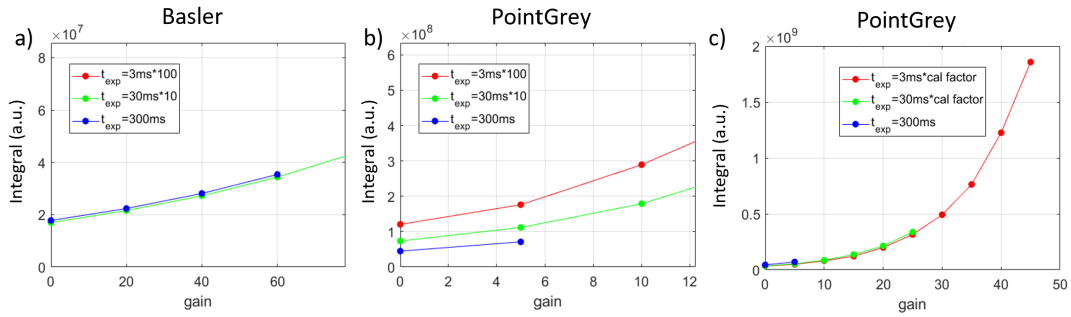

Figure 4.9: *Dependence of the signal measured by the two cameras (Basler on the left, PointGrey on the right) as a function of the gain for three different exposure times. The signals are weighted by the ratio between the three exposure times in the first two charts, in the third the PointGrey data are corrected by the estimated calibration factor.*

by the Basler sensor, for various exposure times, is shown: all signals are normalized to $t_{exp} = 300$ ms, multiplying by 10 the signal measured with $t_{exp} = 30$ ms, by 100 the one with $t_{exp} = 3$ ms. Since the dependence of this sensor on exposure time is linear, the integrals of the image intensity perfectly follow a single curve with respect to the sensor gain. For the PointGrey, instead, the behaviour is different, which means a deviation from the exact linearity of the sensor response on the exposure time, as shown in b). A calibration factor is estimated by taking several measurements as a function of gain and

exposure time, allowing to compare the measured signal as these parameters are varied. The results are shown in c), where the corrected PointGrey sensor measurements with different exposure time are now well overlaid. This calibration factor is used to compare the measured experimental signals for various exposure times from both models.

Gain dependence

To study the dependence on the gain of the sensors response, a set of measurements of the same light source is performed. For both sensors, the dependence on the gain does not vary when the objective is changed and the measured signal increases exponentially with the gain. Since the range in which it is possible to change the gain of the two cameras is different, a conversion between the two is necessary. In Fig.4.10 the range of the PointGrey gain is proportionally converted into the Basler one, and the two curves are fitted as exponential; the results of the fit are shown in each plot. The two cameras are looking at the same light at equal distance; since the two sensor responses are different, the exposure time of the Basler is 500 ms while the PointGrey is 100 ms. Now that the

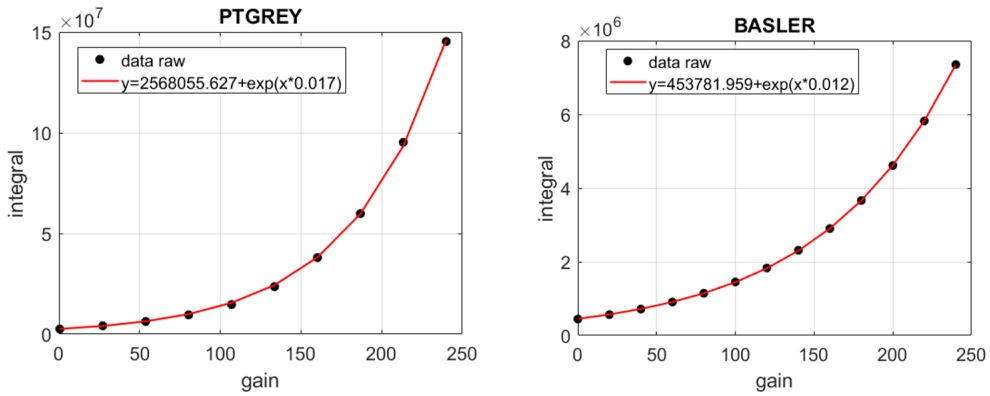

Figure 4.10: *Intensity of the measured signal as a function of the gain for the PointGrey (on the left) and for the Basler (on the right). The range of the PointGrey gain is converted into the Basler one. The two curves are fitted as exponential and the results are reported on each plot.*

dependence on the signal intensity is studied for both the sensors as a function of the gain, with the same source of light, it is possible to find a relation that links the signal of the two cameras. The ratio between the two signals as a function of the gain in the Basler range is shown in Fig.4.11; from the fit of the curve the relation

$$I_{PTG} = 5.789 \cdot exp(0.005192 \cdot I_B) \tag{4.13}$$

allows to directly compare the signal measured by the two different sensors, with I_{PTG} and I_B are respectively the signals measured by the PointGrey and by the Basler. This relation, together with the calibration factor for the exposure time dependence of the

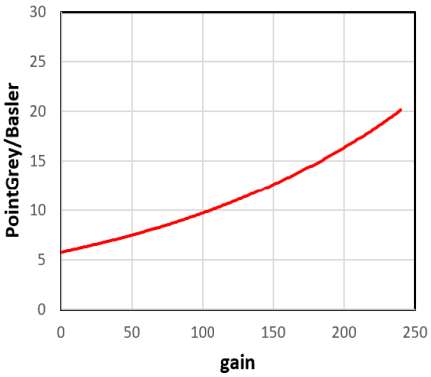

Figure 4.11: *Ratio between the signal measured by the PointGrey and the Basler as a function of the gain in the Basler range.*

PointGrey sensor, allows to directly compare experimental data taken at different conditions for all cameras.

Objective dependence

The last step to complete the relative calibration is to consider the system consisting of sensors and objectives that are mounted on them. The sensors have been calibrated. As next step, the system camera and objective has to be considered. The objectives are commercial devices from different brands, which means that the number of lenses they are made of and the light transmission may depend on the model. Furthermore, a strong dependence on the $F-number$, which defines the open area of each objective, is found. The F-number is defined as the ratio between f, the focal length of the lens, to its effective aperture D. The brightness of the projected image decreases with the square of the F-number and so that the measurements are strongly sensitive to even small changes in it. If the light source and F-number are fixed, the number of photons that is collected by each pixel in the sensor is the same, even if the objective magnification is different (for pixels of the same size). The integral, on the other hand, which is the total light measured by the sensor, assuming the light source is measured entirely, depends on the number of pixels illuminated by the light source itself, which consequently depends on the magnification of the objective. Before installing each camera on SPIDER, for all the objectives the F-number is set to 4, and the system consisting of camera plus objective is calibrated with the same light source. This yields a calibration factor that, together with the exposure time and gain dependence, is used to directly compare all experimental signals collected by the 15 visible cameras mounted on SPIDER.

Background to signal estimation

In Fig.4.12 the ratio of background to signal as a function of the F-number for the two sensors is shown. For these measurements, sensors are lighted with the same light source (signal) and the ratio of background noise to signal is estimated, as the average between the integral of the illuminated and dark pixels, keeping the number of pixels fixed. The two sensors behave similarly especially for low F-numbers, for which the ratio is less than 1%; for F-number=16 instead, the behaviour is different and the ratio is greater than 1%.

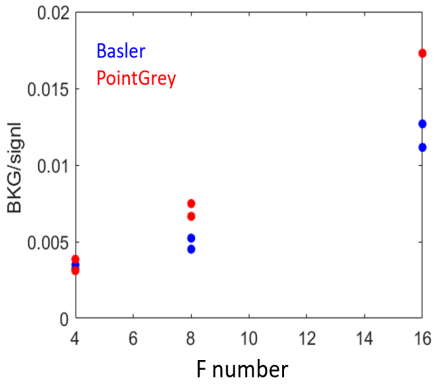

Figure 4.12: *Ratio of background to signal for the Basler sensor in blue and the PointGrey sensor in red, as a function of the F-number.*

4.4.2 On-site calibration

To reconstruct the 2D emissivity pattern of the negative ion beam, it is necessary to know exactly where each camera is looking. For all cameras, a lines-of-sight fan is defined, which is the set of lines along which each detector collects the light emitted by the beam. Each line is uniquely defined by two parameters: the impact parameter p, which is the distance from the centre of the beam, and its tilt angle ϕ, which is the angle between each LoS and the X axis of Fig.4.6. Since the number of windows is limited to 15, the plane (p, ϕ) is not fully covered, but the cameras are installed trying to cover as much as possible the total extent of the beam. The angle of view of each camera, defined as the spatial width of the area enclosed in the fan of LoSs, depends on the magnification of the object mounted on the camera and the number of pixels: as written in Table 4.1, three different magnifications are used on SPIDER, so as to cover the whole beam or just a fraction of it, but with higher resolution. Once the cameras are installed on SPIDER, an on-site calibration is performed, using the technique described in Ref.[80] and the Matlab Camera Calibrator tool [81], allowing the LoS equation to be obtained for each pixel. The technique is based on collecting several images of a planar model, in this case a chessboard pattern, at different orientations. As shown in Fig.4.13, a chessboard

covering the entire extent of the beam is temporarily mounted in the centre of the grids, in the region seen by the cameras; several images of the chessboard at various angles are taken simultaneously from all the cameras and then used to calibrate them. To calibrate

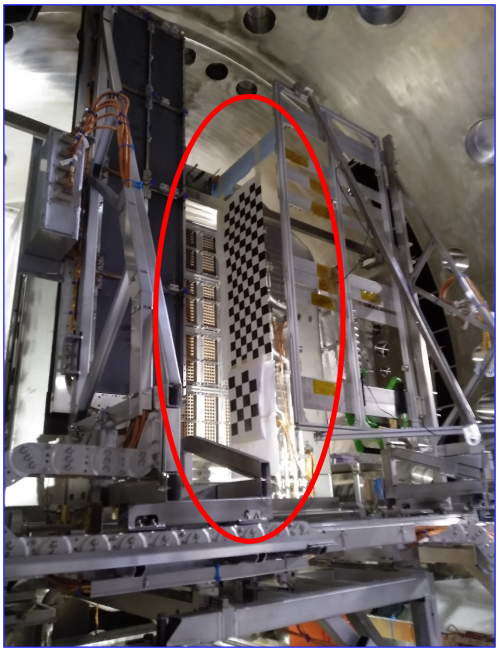

Figure 4.13: *Picture of the chessboard mounted inside SPIDER vacuum vessel to spatially calibrate the cameras.*

a camera it is necessary to estimate both intrinsic and extrinsic parameters: the former represent a projective transformation between the 3D camera coordinate system (scene points) and the 2D image coordinates, while the latter represent a rigid transformation from the 3D world coordinate system to the 3D camera coordinate system. Intrinsic parameters are characteristics of the camera, such as the focal length, the optical centre, also known as the principal point $[z_0, y_0]$, and the skew coefficient s, which is zero when the z and y axes are perpendicular. The cameras intrinsic matrix K is defined as

$$K = \begin{bmatrix} f_z & 0 & 0 \\ s & f_y & 0 \\ z_0 & y_0 & 1 \end{bmatrix} \tag{4.14}$$

where $f_z = f \cdot s_z$ and $f_y = f \cdot s_y$, with f the focal length in mm and $[s_z, s_y]$ the number of pixels per mm along y and z directions, respectively. The extrinsic parameters are a rotation matrix R and a translation vector t connecting the camera coordinates to world coordinates. The equation that provides the transformation that relates a world coordinate in the reference image frame [Z Y X] and the corresponding image point [z

y] is thus

$$s[z\ y\ 1] = [ZYX1] \begin{bmatrix} R \\ t \end{bmatrix} K \tag{4.15}$$

Figure 4.14 shows the relationship between the camera coordinates and the scene point

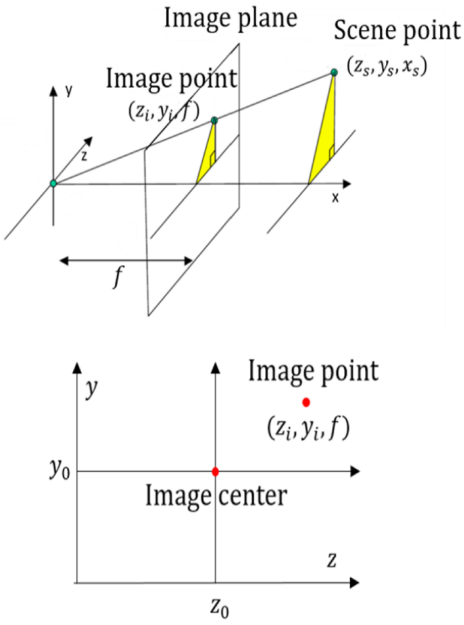

Figure 4.14: *Relation between a scene point (in the beam plane) and a pixel in the camera image.*

just described. Both intrinsic and extrinsic parameters are obtained by analysing the set of chessboard pictures with Matlab Camera Calibrator Tool. It is then possible to write the equation for each LoS, mapping each point in the image scene, which is the real world image observed by the camera, to the corresponding pixel in the camera, using the intrinsic parameters just estimated. The extrinsic parameters then allow the camera coordinates to be transposed to the real-world coordinates. Each LoS is defined as a straight line

$$y_{pix} = f_y \cdot \frac{y_s + z_s y_0}{z_s} \tag{4.16}$$

with y_s and z_s the coordinates of the scene points; then extrinsic parameters allow rotation and translation in the real world. The final coverage in the plane (p, ϕ) of the 15 installed cameras on SPIDER is shown in Fig.4.15: the impact parameter is normalized to half the vertical dimension of SPIDER beam b. The procedure used to write the equation for the LoSs for each camera is described in detail for camera Basler4, which is mounted on port 10, with an 8 mm objective, and observes the entire vertical cross section of the beam almost perpendicularly, with respect to the direction

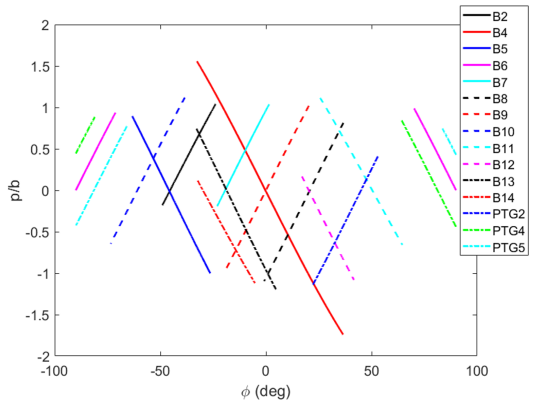

Figure 4.15: *Final coverage in the plane* (p, ϕ) *of SPIDER tomographic system. Line styles and colours are the same of Fig.4.6.*

of beam propagation. The set of chessboard images are used as input into the Matlab tool and the output is shown in Fig.4.16. The tool detects the edges of all black and white squares of the chessboard, thus obtaining its projection onto the camera sensor (as shown in Fig.4.16). Knowing the actual size of the squares, the intrinsic matrix is obtained, through a minimization process. The top right panel shows the average error in pixels between the acquired and reconstructed chessboard images, for the 18 independent chessboard pictures given as inputs. The errors are less than 1 pixel for most of the images, confirming a good estimate of the intrinsic parameters. The bottom panel shows the real-world reconstruction of the chessboard with respect to the fixed camera. The obtained intrinsic parameters are then used to write the LoSs equation. Rotation and translation to connect the scene point to the real world are done by exploiting the CAD drawing of some known points seen by the camera inside SPIDER vessel, such as the positions of the view ports of the tomographic system. Some of the Basler4 reconstructed LoSs are shown in Fig.4.17 (left panel). To have a confirmation of the goodness of the defined LoSs, the experimental beam profile measured by Basler4 is compared with the one obtained by integrating along the LoSs an ideal matrix composed by 2D Gaussian beamlets, one for each aperture, whose positions are the nominal ones of the beamlets. The two profiles are shown in blue and red, respectively, on the right graph in Fig.4.17. They correspond very well, demonstrating that the equations of the LoSs obtained by the spatial calibration procedure described in this section are correct. The discrepancies in the relative amplitude of the two profiles are due to the non-uniformity of the experimental beam.

4.5 1D analysis

A multi-beamlet negative ion beam can be represented as a matrix of bidimensional Gaussians

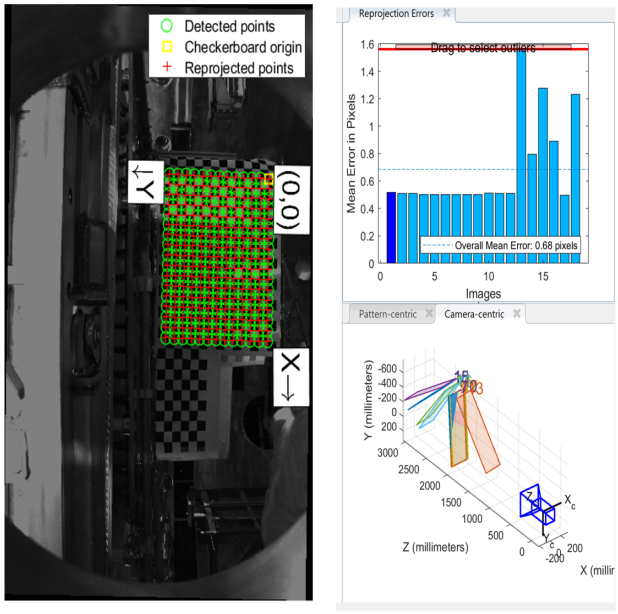

Figure 4.16: *Matlab Camera Calibrator tool [81] output for Basler4. On the left, the detected chessboard; on the top right the mean error for pixel and on the bottom the positions of the reconstructed chessboard in the camera frame of reference.*

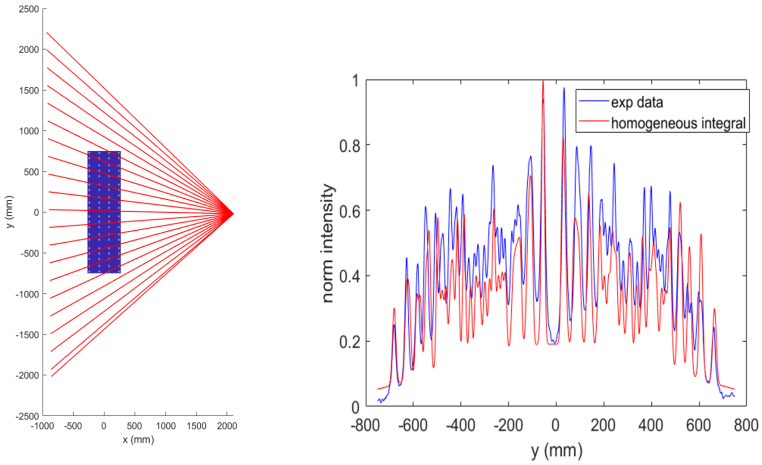

Figure 4.17: *Reconstructed Basler4 LoSs (on the left) and comparison between the 1D experimental profile (in blue) and the integral of an ideal matrix of 2D Gaussians (in red).*

$$\epsilon(y,y) = \sum_{i=1}^{n_{beamlets}} A_i \exp\left(-\left(\frac{(x-x_{0i})^2}{w_{xi}^2} + \frac{(y-y_{0i})^2}{w_{yi}^2}\right)\right) \tag{4.17}$$

with x_{0i} and y_{0i} the beamlet nominal positions and w_{xi} and w_{yi} the beamlet width along x and y directions, being z the direction of the beam propagation; $n_{beamlets}$ is the number of beamlets. This definition is valid because space charge compensation of the beam must occur in order to propagate; otherwise, due to their own charge, the beamlets would repel each other due to Coulomb repulsion during their propagation. At the typical pressure held in the drift region between the accelerator exit and the calorimeter on which the beam is dumped (10-50 mPa), it is demonstrated that the space charge compensation occurs few microseconds after the start of beam extraction [49]: this is accomplished by the creation of positive ions via ionization of the background gas $\underline{H}^- + H_2 \Rightarrow \underline{H}^x + H_2^+ + e^-$. For each camera, a 1D profile of the beam at the blackened area of the vessel is analysed, by taking the average over 5 pixels in the z-direction, i.e., the direction of beam propagation; these profiles represent the integrals of the light emitted by the beam, along the LoSs of the camera, in a plane perpendicular to the beam propagation direction. An example of these profiles is shown in the right-hand graph of Fig.4.17 in blue. Since only few apertures are left open in SPIDER (80 and 28), it is possible to easily distinguish the single beamlet or a line of superimposed and well isolated beamlets, and fit them as 1D Gaussians. An example of experimental data taken with Basler7 (Port 02) in the two configurations with 80 and 28 beamlets are shown in Fig.4.18: at the top there are the two 2D images and at the bottom the 1D profiles between the red lines, with 80 (left) and 28 (right) open beamlets. As it can

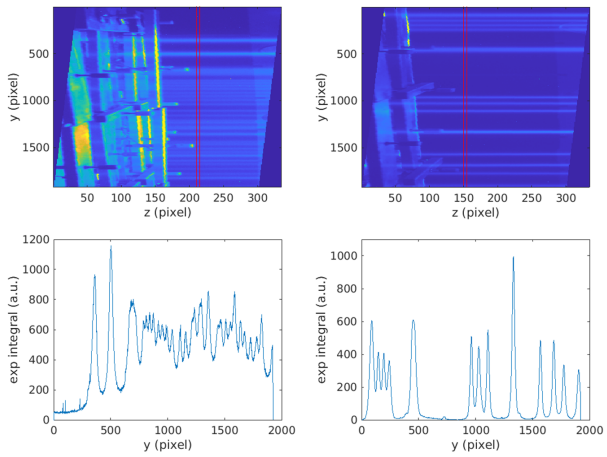

Figure 4.18: *2D images (top) and 1D profiles (bottom) with 80 (on the left) and 28 (on the right) open beamlets seen by Basler7 (Port 02). In the 2D images, the beam propagates from right to left, where it impinges on STRIKE calorimeter. The red lines represent the region in which the 1D profiles shown in the bottom are measured.*

be seen in the 1D profiles, in the case with 80 beamlets the first two rows of beamlets are seen with the smallest inclination angle by the camera and therefore they can be fitted as 1D Gaussian, by assuming that the beamlets belonging to the same row are

well aligned; in the case with 28 beamlets, instead, almost all of them are well isolated and distinguishable, and each beamlet can be fitted individually. From the 1D Gaussian fit, much information about the beamlet is obtained: the position, from which the beam deflection can be estimated; the width, which is proportional to the beamlet divergence; the total integral of each peak, or the product between the width and the amplitude (i.e. the area of fitted Gaussian), which is proportional to the beam current, as discussed in Sect. 4.1.

4.5.1 Beam divergence

By measuring the beam profiles at different positions along the beam propagation direction, it is possible to directly estimate the divergence of the beamlets, by measuring the broadening of the beamlets along their propagation. This method is mainly used on NIO1 where, thanks to the small size of the experimental setup, it is possible to take three different beam profiles in the blackened region (10 cm wide) of the vessel. In Fig.4.19, the experimental images collected by the two cameras mounted on NIO1, i.e., the bottom (on the left) and lateral (on the right) cameras, are shown; in both 2D images, the beam propagates from left to right. At the bottom, the respective 1D profiles of the two cameras, taken at three different positions $z_1 = 210$ mm, $z_2 = 250$ mm and $z_3 = 290$ mm are represented (z=0 at the exit of the last grid of the accelerator). Since no magnetic force acts on the beamlet rows, the three beamlets belonging to the same column are well aligned, and the width of the columns can be assumed to be representative of the width of the single beamlet; the width of the three peaks is therefore a small overestimate of the width of the single beamlet itself. The same approach cannot be applied to the lateral profile, since the alternating residual deflection acts on the beamlet columns, and the three beamlet rows are not easily distinguishable (second plot in Fig.4.19, right). A beamlet exiting from a circular aperture has a divergence δ_x which increases until space charge compensation occurs, usually few centimetres after the last grid, and then stops increasing. The three columns of beamlet measured by the bottom camera at the three different positions are fitted as three Gaussians over a linear background, and an estimate of the divergence is obtained, by linearly fitting the Gaussian widths as a function of the position z:

$$w(z) = w_0 + \delta_x \cdot z \tag{4.18}$$

with w_0 the width of the beamlet at the exit of the last grid of the accelerator, whose apertures have a radius of 4.4 mm. Since the divergence is strictly dependent on the beam current, it is crucial that no current exchange occurs between the three beamlet columns during propagation, to obtain good estimate of the single beamlet divergence. A constraint in then imposed over the integral of each fitted Gaussian: the ratio of the integral of the three Gaussians is kept fixed along the z direction to the value measured at $z = z_1$, after subtraction of the linear background. The same approach can be used on SPIDER: along with the black aluminium foil installed in the region observed by visible tomography, 0.3 m at the end of the accelerator, a second strip of black aluminium foil

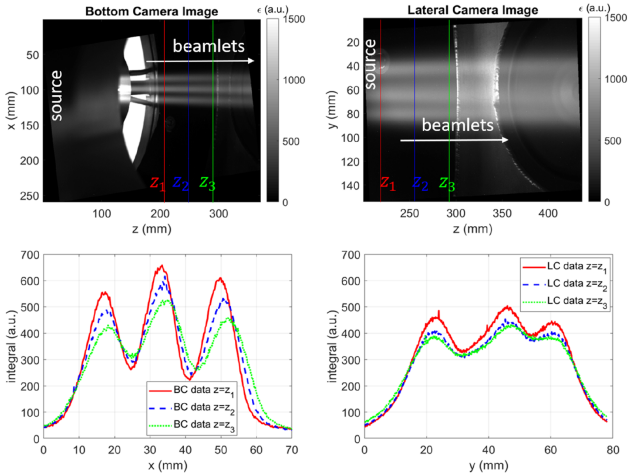

Figure 4.19: *Experimental images of the bottom (left-hand side) and lateral (right-hand side) cameras. At the bottom, horizontal and vertical profiles of the beamlet columns and rows, taken at three different positions along the beam propagation direction, z1, z2, and z3, (indicated in the 2D images), are shown.*

is installed on two sides of SPIDER vessel, 1 meter after the last grid of the accelerator. In this case, since the size is larger, there is also perspective correction to consider.

4.6 2D tomographic reconstruction and SART algorithm

The aim of the beam tomography is the reconstruction of the bidimensional emission profile of the beam, through the measurement of the radiation emitted along several lines-of-sight. From the estimation of $\epsilon(x, y)$ the knowledge of the beam homogeneity is obtained, which is a fundamental property for the beam and a requirement for future ITER NBI. To obtain a tomographic reconstruction different algorithms exist; in this specific case, since the number of LoSs is limited and they are non uniformly distributed around the beam, the algebraic reconstruction algorithms are supposed to give the best performance [82]. They are based on the pixel method, which consists in dividing the target image in a set of finite elements, pixels, in which the emissivity is defined positive and it is equal to an unknown quantity ϵ_i. In this way, the experimental integral I_j, collected by each LoS, is given by the sum of the contribution of each pixel intercepted by the considered LoS:

$$I_j = \sum_{i=1}^{n_{pix}} \epsilon_i \cdot a_{ij} \tag{4.19}$$

where the element of the matrix a_{ij} is equal to the length of the jth LoS inside the ith pixel, and the summation is extended over the total number of pixels n_{pix} in which the

target image is divided. The solution of mathematically ill-posed tomographic problem is the emissivity of each pixel ϵ_i obtained by inverting Eq.4.19. The LoSs are lines with no thickness, $y = a_j x + b_j$: this is a good assumption given the large number of LoSs for each camera (1920 and 1936 respectively for Basler and PointGrey models) and if the distance of the cameras from the beam propagation axis is much larger than the transversal dimension of the matrix of beamlets, as in NIO1 and SPIDER experiments. The iterative algorithm used in this thesis work is the Simultaneous Algebraic Reconstruction Technique (SART), which is based on solving the system of linear equations 4.19 through an error correcting procedure. This algorithm is first tested on NIO1 [83] to prove its capability in reconstructing the experimental signals, and then used on SPIDER. The algorithm is based on the approximation of the emissivity of the ith pixel at the k+1 iteration through the equation

$$\epsilon_i^{k+1} = \epsilon_i^k + \frac{\sum_{j=1}^{n_{los}} \left(a_{ij} \cdot \frac{I_j - \sum_{i=1}^{n_{pix}} \epsilon_i^k \cdot a_{ij}}{\sum_{i=1}^{n_{pix}} a_{ij}} \right)}{\sum_{j=1}^{n_{los}} a_{ij}}. \tag{4.20}$$

where ϵ_i^{k+1} is the reconstructed emissivity of the ith pixel at the k+1 iteration, I_j is the experimental signal measured by the jth LoS, a_{ij} is the matrix element and the sums are extended over the number of pixels n_{pix} and LoSs n_{los}. In this algorithm, developed by Andersen and Kak [84], the emissivity of the ith pixel in the k+1 iteration is estimated by adding to the evaluation of kth step an error correction term weighted with a matrix a, which consists of the normalized difference between the measured integral I_j and the emissivity obtained in the previous step. The simultaneous technique averages this correction for all LoSs in each step, averaging over the contribution of all measurements (the sum is extended to all the LoSs) the emissivity of each pixel. In this way, a good reconstruction is obtained in few iterations. In the following sections,the tomographic techniques used to reconstruct SPIDER and NIO1 bi-dimensional beam emissivity are described.

4.7 SPIDER tomographic reconstruction

Many parameters have to be considered when the inversion is performed using the pixel method. The number of pixels, in fact, determines the resolution of the reconstruction given by the pixel dimension. However, by increasing the number of pixels, also the number of unknowns grows and the reconstruction becomes more challenging. Different approaches are studied using the experimental data collected by the 15 SPIDER visible cameras, upon changing both the number and the dimension of pixels into which the total beam emissivity is split. The number of LoSs is fixed and it is equal to 24060, i.e. equal to the number of pixels of each sensor observing the beam. The pixel number defines also the resolution of the cameras, which corresponds to a few millimetre in the axis of the beam. An estimation of the goodness of the reconstruction is the Root Mean

Square (RMS) between the experimental and the reconstructed profiles

$$rms = \frac{1}{n_{los}} \sqrt{\sum_{i=1}^{n_{los}} (I_{exp} - I_{rec})^2} \tag{4.21}$$

where n_{los} is the number of total lines-of-sight, I_{exp} is the experimental profile and I_{rec} is the reconstructed one. Since SPIDER has so far operated with 80 (from June 2018 to the end of 2020) and with 28 (from the beginning of 2021 to the beginning of the shutdown) extracted beamlets, it is possible to obtain single beamlet information, because they are well isolated during their propagation. When SPIDER will operate with all 1280 apertures, it will be impossible to obtain this resolution because the beamlets will overlap each other and the resolution of this method should be on the order of a fraction of the beamlet group [76]. The profiles of a simulated beam consisting of all 1280 beamlets are shown in Fig.4.20, with various widths w. To meet ITER requirements on beam divergence (less than 7 mrad) at 350 mm along the beam propagation direction, where the cameras are observing the beam, the width of the beamlets must be lower than 7 mm, assuming an initial width of 4 mm at the grounded grid exit. The beamlets depicted in Fig.4.20 therefore have the widths, w, of 5, 10 and 15 mm and they are indicated in blue, green and yellow, respectively. The last one was experimentally measured in the beam operation without caesium evaporation. They show that, as the beamlet width becomes too large, it is no longer possible to distinguish the light produced by different beamlets, making it impossible to achieve resolution on the order of a single beamlet, with the only 15 points of view available on SPIDER vessel.

4.7.1 Number of pixels

Starting from the easier configuration, the one with 28 open beamlets, the algorithm is tested with the aim of reconstructing the 2D pattern of the beam emissivity. The number of pixels into which the matrix to be reconstructed is divided is varied, with different sizes and shapes. The cases studied are described below.

1 pixel per beamlet

One value of emissivity is associated to each beamlet, and the position of the pixel is the nominal position of the extracted beamlet (thus assuming zero deflection). To be sure to collect all the light emitted by the beamlet of unknown width and position, the pixel should be $4 \sim 5\sigma$ larger than the mean width of the beamlets. This information is obtained from the 1D analysis (Gaussian fit of the peaks, described in Sect.4.5). Assuming that SPIDER beam is non-homogeneous and that the actual positions of the beamlets, once extracted, are not known (possible residual magnetic deflections), different pixel sizes were tested, and the RMS of obtained inversions is compared. The pixel size which minimizes the RMS between the experimental and the reconstructed profiles is chosen to perform the beam reconstruction. The evolution of the normalized RMS as a function of the number k of iterations of the SART algorithm is shown in Fig.4.21, for different

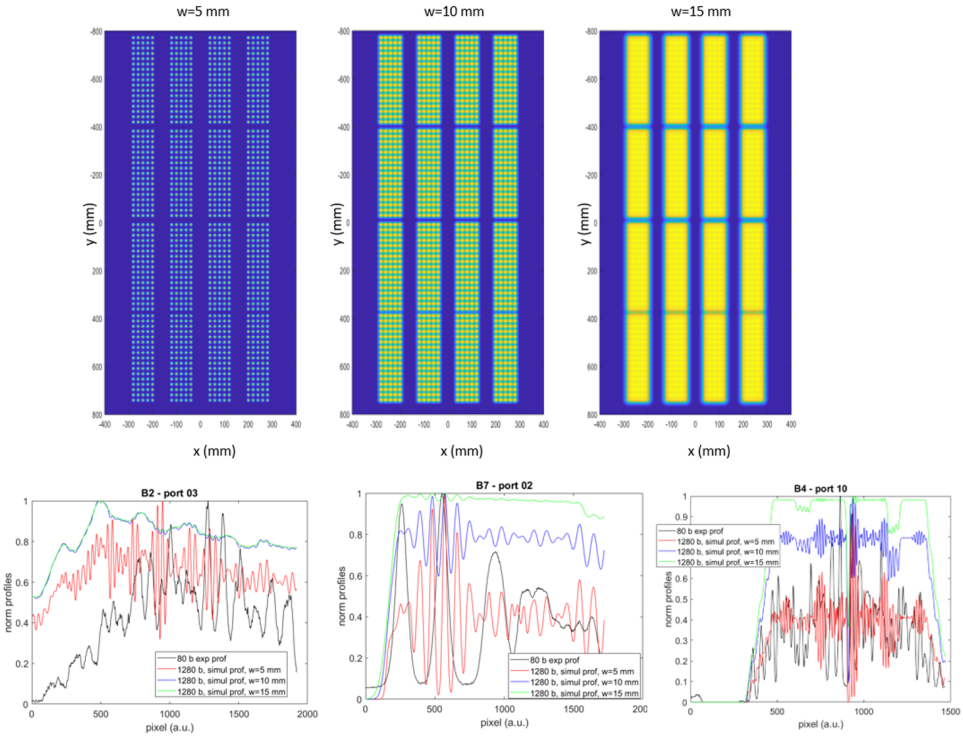

Figure 4.20: *Comparison between the experimental profiles with 80 beamlets measured by three cameras (black curves) and the simulated beam composed by all 1280 beamlets with different widths, respectively w=5 mm (in red), 10 mm (in blue) and 15 mm (in green). On the top, the three simulated matrix of 1280 2D Gaussians for the three widths.*

sizes of square pixels (on the left); all sizes are in millimetres. On the left, square pixels of various sizes are compared. The normalized RMS after six iterations decreases as the pixel dimension increases, from 25 to 40 mm. In fact, if the pixels are too small, some of the signal from the larger beamlets may be missed in the beam profile reconstruction, worsening the RMS between experimental and reconstructed profiles (case 25x25 or 30x30 mm^2). When the pixel size becomes too large, instead, the algorithm is unable to correctly reconstruct the 2D emissivity pattern, as the pixels begin to overlap (pixel size greater than the distance between open beamlets), as it can be seen from the RMS obtained for 45 and 55 mm pixel sides. The pixel size with the lower RMS is the one corresponding to $\sim 5\sigma$ the measured width of the reconstructed beamlets (40x40 mm^2). Since any residual alternate deflection may affect the horizontal position of the extracted beamlets, the largest uncertainty in the position of the beamlets appears along x-direction. In addition, measurements of the beamlet shapes on the STRIKE calorimeter show that beamlets, under certain conditions, are wider in the horizontal direction. For this reason, rectangular pixel, with the long side along x, are preferable. Once the

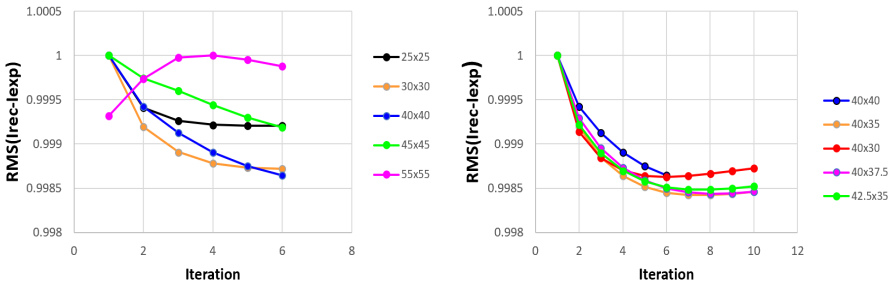

Figure 4.21: *Normalized RMS between the reconstructed and experimental profiles, as a function of the number k of iterations, for different dimensions of the pixels; all the pixel sizes are in millimetres; on the left, square pixels; on the right, rectangular ones.*

optimal square pixel size has been found, the accuracy of the reconstruction can be further increased by slightly changing the y dimension of the pixels. The RMS for different rectangular sizes for the same experimental data is shown in Fig.4.21 (on the right); the best RMS is between 35-37.5 mm along y. For all pixel sizes, the RMS between the reconstructed and experimental profiles decreases rapidly after the first few iterations, and then stabilizes at different values, depending on the goodness of reconstruction. The minimum value of RMS to which the algorithm converges, represents the optimal choice for the pixel size given a fixed number of pixels. The reconstructed 2D emissivity pattern of the 28 beamlets is shown in Fig.4.22, which is obtained with rectangular pixels of 40x35 mm. The colour-map represents the emissivity of each reconstructed pixel. The three adjacent pixels at the top of the third column from the left are extracted, corresponding to three adjacent beamlets of the first group, so they are not well discerned. This indicates that the value of emissivity could be not exactly representative of the single beamlet intensity. The beamlet groups division is highlighted by different colours, from G1 (top) to G4 (bottom). These reconstructions with one value of emissivity per pixel are used in this thesis work to study SPIDER beam homogeneity when the main machine parameters are varied. However, this algorithm allows also to study the beamlets shape and position, using more than one pixel for each beamlet. Some preliminary results are discussed in the following.

More pixels per beamlet

To obtain not only information about single beamlet emissivity, but also about its width and position, it is possible to increase the number of pixels in which the emissivity of each beamlet is subdivided. Many cases have been studied, with various numbers of pixel and sizes of the area to be reconstructed. In Fig.4.23 different reconstructions of the same experimental data shown before are represented. In these images, each area surrounding the extracted beamlets is divided into 11x11 square pixels, whose side dimension is respectively 6.6, 7.6, 8.6, 9.6 and 10.6 mm. As it can be seen, not all the beamlets

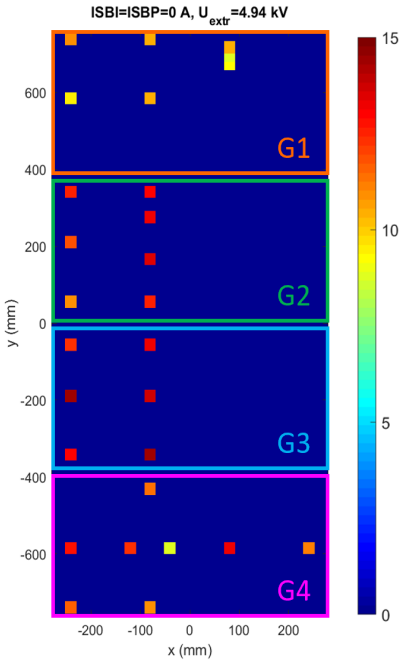

Figure 4.22: *2D reconstructed matrix of beamlets with 28 pixels of 40x35 mm size. Each pixel colour represents the reconstructed beamlet emissivity.*

are well identified, and this is due to the limited number of lines of sight available. As the pixel dimension increases, the reconstructed beamlets are smaller, confirming the capability of the algorithm in actually reconstructing the 28 open beamlets. Moreover, it is evident that many beamlets are not centred in the region selected, indicating that their position is deflected with respect to the nominal one, where each region is centred in.
It is possible to fit with 2D Gaussian the reconstructed beamlets, a shown in Fig.4.24: on the top, the 4 reconstructions of beamlet 9 are shown, which is the central beamlet of the external column of the second group (from the top, G2), increasing the dimension of the region divided in 11x11 pixels (thus also the dimension of each pixel); on the bottom, the 4 patterns fitted as 2D Gaussians. As the region increases, the dimension of the reconstructed beamlet decreases, confirming the soundness of the technique. The 1D profiles corresponding to the summation of the reconstructed beamlet are represented in the chart at the bottom. The resolution of each reconstruction is shown in the legend. From the fitted Gaussians, it is possible to estimate the beamlet widths and positions. In Fig4.25 an estimation of the beam deflection along x direction is shown, with a resolution of 1 pixel=11.6 mm. The two directions of residual magnetic deflection of the open holes is shown by two different colours (on the left). The horizontal deflection is represented by subtracting the mean value of all reconstructed x-positions from that of

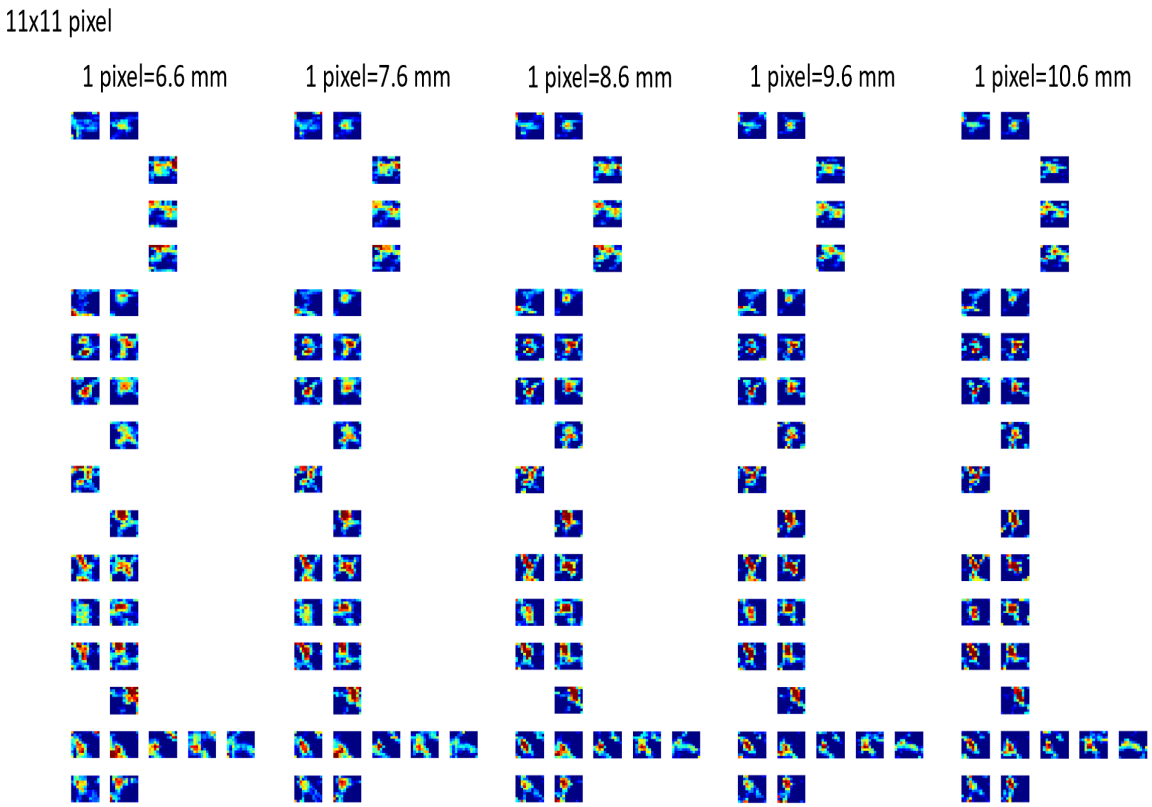

Figure 4.23: *2D reconstructions of the beam emissivity with 28 regions of different dimensions, subdivided in 11x11 pixels each.*

each beamlet. As shown by both STRIKE and tomographic inversion, the two sets of beamlets have opposite displacements from the mean value as a result of the opposite deflection operated by the magnets. Although these are only preliminary results, the agreement between the two diagnostics and the opposite directions in which the deflected beamlets are displaced, are a first confirmation that the beamlet positions can also be reconstructed using this technique.
As the number of pixels is increased, the RMS between experimental and reconstructed profiles with the iterations k is reduced, as shown in the chart on the left of Fig.4.26; the region surrounding each beamlet is 59.4x46.2 mm^2. As discussed previously, the algorithm converges after few iterations even in the number of pixels is increased, to lower values as the reconstruction improves. The dependence of the RMS on the number of pixel in which the total beam emissivity is subdivided is shown in Fig.4.26, on the right; the value of RMS represented is the one achieved after 10 iterations. As the number of pixels grows, the RMS is reduced and the larger decrease ($\sim$ 20%) is in the first 6 points, when the number of pixels per beamlet is increased from 4 (2x2) to 49 (7x7).

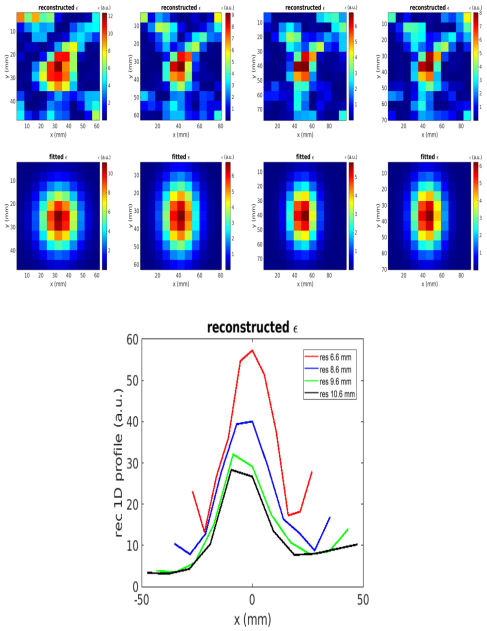

Figure 4.24: *On the top, the 4 reconstructions of beamlet 9 are shown, for different sizes of pixels; on the bottom, the sum along y of the reconstructed matrix of pixels is shown.*

Then it decreases slower with the number of pixels. In Fig.4.27, the comparison between a zoomed part of the experimental profile (coloured in black) and the reconstructed ones for different number of pixels in which the same area is divided, is shown. As the number of pixels increases, the reconstructed profile matches better the experimental one. From the discussed results, an improvement in RMS between the reconstructed and experimental profiles is demonstrated as the number of pixels is increased. However, it is not possible to estimate the goodness of fit of the 2D inversion since a 2D image of the beam emissivity is not available. As predicted by simulations, as the number of pixels increases, the larger number of unknowns into which to subdivide the emissivity matrix to be reconstructed allows for better reproduction of the 1D profiles, as demonstrated by the decrease in RMS. However, since no physical constraint is imposed in the algorithm, this may results in a deterioration of the 2D matrix of the reconstructed beamlets. Further investigation, supported by simulations, along with comparison with different algorithms to perform tomographic inversion is needed.

4.7.2 NIO1 reconstruction

The same technique just described for SPIDER beam was first tested on NIO1. Since the dimension of NIO1 beam is smaller with respect to SPIDER one, it is possible to divide the whole matrix of beamlets in pixels, and to reconstruct the entire pattern of the beam. The representation of the ideal matrix of beamlets, subdivided in 60x60 pixels of

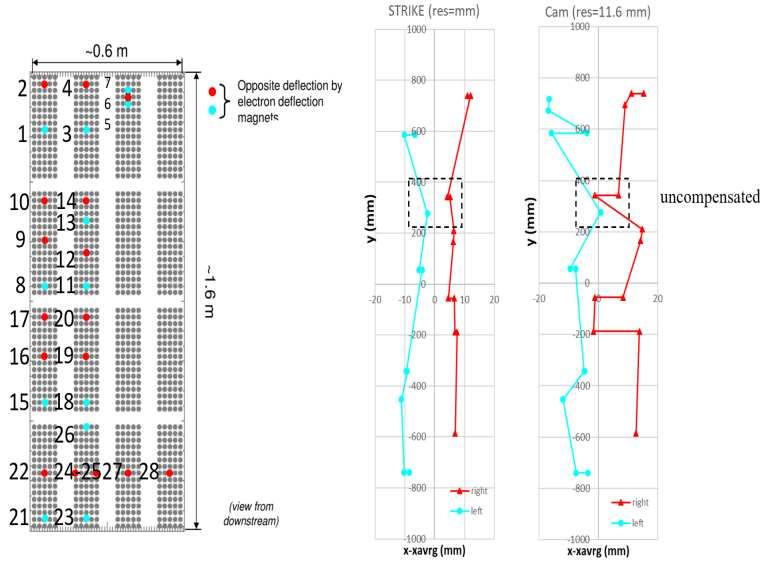

Figure 4.25: *Left: Opposite defection by electron deflection magnet on the open beamlets; the two colours represent the two direction along x. Right: x-x average position of the beamlets measured by STRIKE calorimeter and by tomographic reconstruction.*

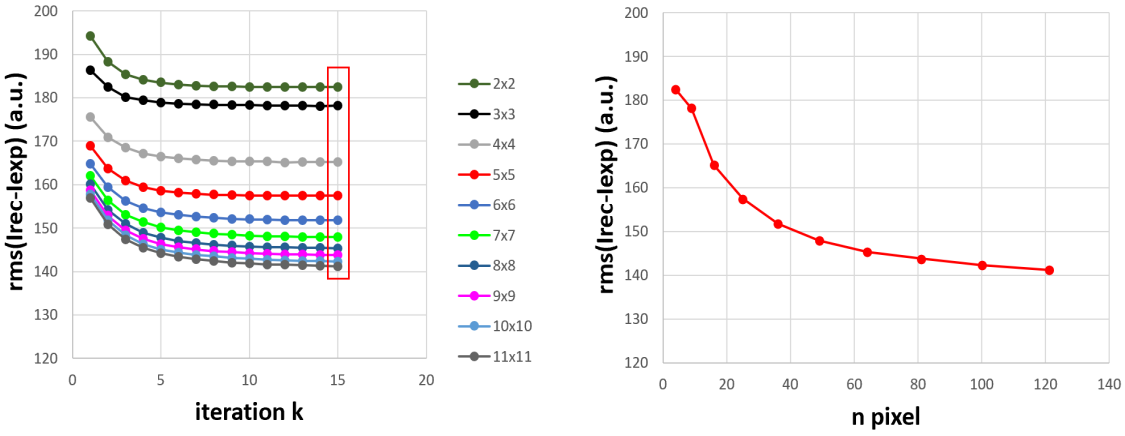

Figure 4.26: *On the left, RMS as a function of the number of iterations for different numbers of pixels per beamlet; on the right, RMS as a function of the number of pixel.*

1 mm side is shown in Fig.4.28; also some of LoSs of the bottom camera are represented with the red dashed lines, while the white points represent the lateral camera LoSs. The numerical reconstructions of the beam emission obtained with the SART algorithm

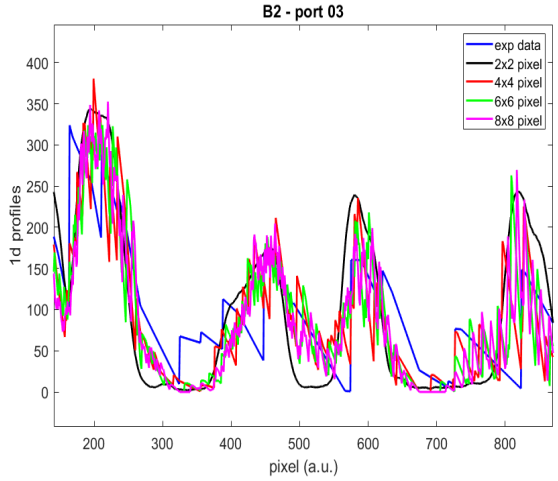

Figure 4.27: *Detail of the comparison between experimental and reconstructed profiles with different numbers of pixels.*

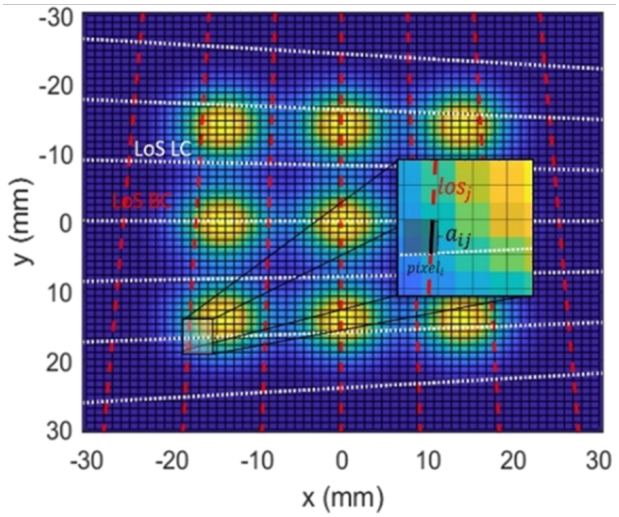

Figure 4.28: *Representation of the ideal matrix of NIO1 beamlets, subdivided in* 60×60 *pixels of 1mm side. The red dashed lines represent some LoSs of the bottom camera (BC), and the white points represent the lateral camera (LC) ones. A pictorial explanation of the evaluation of the* a_{ij} *element of the matrix a is also shown.*

(Eq. 4.20) at three different positions along the beam propagation direction are shown in Fig.4.29 (top images), corresponding to the experimental data shown in Fig.4.19. A direct comparison between the experimental (red solid line) and reconstructed (black dashed lines) profiles represented is shown in Fig.4.30 at the position z = z1. The algorithm well reproduces the experimental data, even if the shape of the LoSs influences

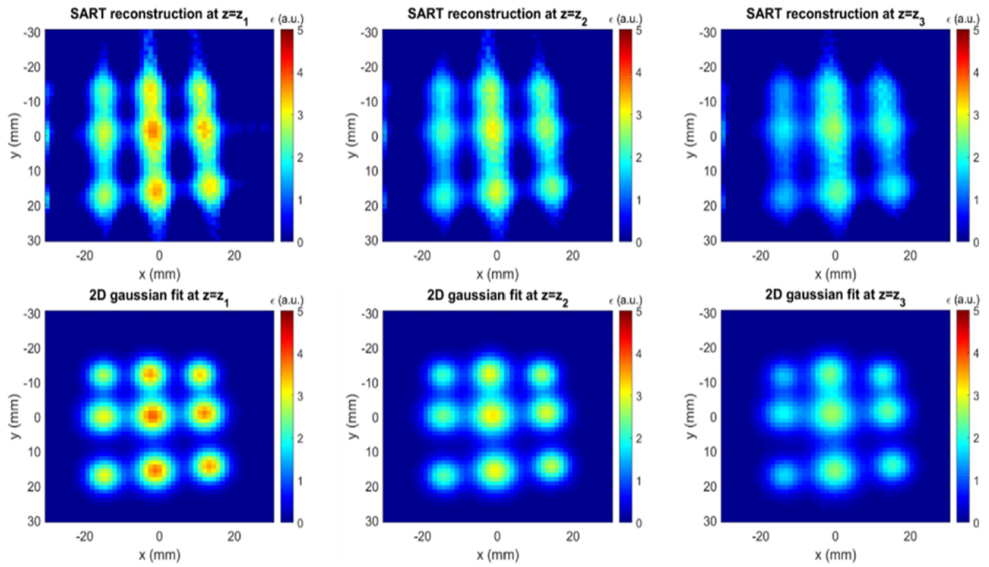

Figure 4.29: *SART reconstructions (top row) and two-dimensional Gaussian fits (bottom row) of the experimental data at the three different positions z1 (left-hand column), z2 (central column), and z3 (right-hand column) along the beam propagation direction.*

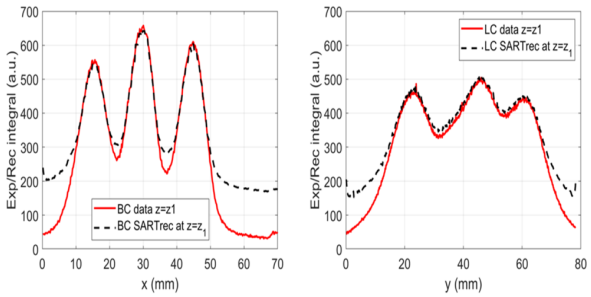

Figure 4.30: *Bottom camera (left-hand side) and lateral camera (right-hand side) experimental and reconstructed profiles at $z = z1$ represented by the red continuous lines and black dashed lines, respectively.*

the reconstruction, due to the only two viewing directions. The beamlet columns and rows obtained by the inversion follow the inclination of the LoSs, and the misalignment of the rows is reconstructed as a deformation of the beamlet shape. However, reliable information about the beam properties can be obtained. The reconstructions are fitted with 9 bidimensional Gaussians (bottom row of Fig.4.29) by assuming that the beamlet width is the same in both the directions $w_x = w_y = w$, while positions and amplitudes are left free. The distances between the reconstructed beamlets are 14 mm, which are

comparable with the size of the matrix of beamlets at the exit of the last grid. Using the

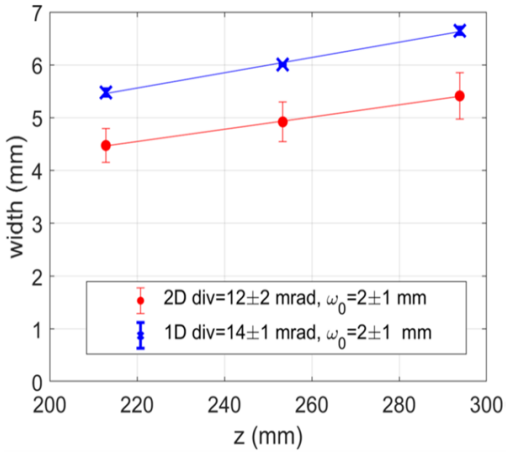

Figure 4.31: *Comparison between the divergence estimated using the widths of the central column obtained with the 1D fit (blue crosses) and using the widths of the central beamlet reconstructed with the tomographic inversion (red points) at the three different positions along the beam propagation direction. The fit is given by Eq.4.18.*

beamlets width obtained both from the 1D fit and the 2D tomographic reconstruction, it is possible to estimate the beam divergence. Fig.4.31 shows the widths of the 1D (blue crosses) and 2D (red points) Gaussian fits of, respectively, the central column of beamlets and the central reconstructed beamlet, along the beam propagation direction z. For both cases, the width increases with z and, by fitting the widths as a function of z with Eq.4.18, the slope of the linear fit gives an estimate of the divergence: the resulting divergence for the optimum optics condition, which corresponds to the most focalized beamlets, is 12 ± 2 mrad for the 2D fit and 14 ± 1 mrad for the 1D fit; the error associated with the 2D reconstruction is in the order of the pixel size of the reconstructed matrix (around 0.4 mm); the error associated with the 1D fitted widths is in the order of the sensor pixel dimension in the plane of the beam (around 0.2 mm). As foreseen, due to the possible non-perfect overlapping of the three beamlets per column, the estimate of the widths obtained with the bi-dimensional fit is smaller than the one obtained with the one-dimensional fit. The fitted $w_{02D} = w_{01D} = 2\ mm$ are in good agreement with half of the radius of the last grid apertures.

Chapter 5

Beam divergence

A beam divergence lower than 7 mrad is one of the constraints that ITER NBI has to satisfy. The width of the beam injection ports together with the width of the neutraliser channels - in turn limited by the acceptable gas throughput from the neutraliser - define the horizontal scraping angle for all beamlets, i.e. the limiting horizontal angle ω_{xlim}. An acceptable beamlet divergence can be defined so that, integrating for all beamlets Eq. 2.12 from $\omega_x = -\omega_{xlim}$ to $+\omega_{xlim}$, a sufficient fraction of the beam power is transmitted through the neutraliser channels (and the other beam-facing components up to the tokamak port). An optimal transmission efficiency allows minimising the heat loads, sputtering damages and secondary emission currents at the mechanical components, along with the requirements of the cooling system.
A description of the physical principles which determine the negative ion beam divergence is given in Section 2.6. Beamlet divergence measured by visible tomography in SPIDER is studied in detail in this chapter, both in surface and volume operation, respectively in Sections 5.1 and 5.2. The dependence on the source and accelerator parameters is discussed, and the minimum of the beamlet divergence in different operational regimes is found. The results are compared with the measurements of the divergence obtained by different diagnostics. The minimum of the divergence measured in SPIDER in volume operation is $\sim$ 20 mrad, which decreases to $\sim$ 12 mrad after caesium evaporation in the source, at the operational conditions explored. The beam divergence depends on the *meniscus* shape, which is the boundary surface between the negative ion beam and the plasma, in the extraction region. All source parameters which modify the shape of the meniscus, i.e. changing the plasma density, along with the extraction voltage, are studied during SPIDER operation with caesium evaporation. The optimum voltage ratio is found to be between 9.5 and 10. Depending on the position of the beamlets along the vertical profile of the beam, different divergences, as well as different dependence on the source and accelerator parameters are estimated. This corresponds to a non-homogeneity of the beam intensity, which will be studied in detail in the following chapters. Furthermore, SPIDER beam performances are compared with the beam divergence measured in BUG and NIO1 experiments in Section 5.3. A similar divergence is measured also on BUG and NIO1 negative ion sources, confirming a larger divergence

with respect to goal for ITER HNB. On the contrary, a beam divergence lower than the desired 7 mrad is measured in arc sources. To understand the reason of this difference, the ion velocity distribution is studied by means of dedicated Retarding Field Energy Analizer RFEA probes in both types of source. The temperature of the negative ions, in fact, plays a role in the beam divergence. The relation between the beamlet divergence and the negative ion temperature measured by the RFEA probes both in SPIDER and in NIFS negative ion sources is discussed in Section 5.4, also by comparing the features of these two different plasma sources (radio-frequency and arc negative ion source). The axial energy distribution of the ions in the two sources demonstrates a wider distribution in radio-frequency source with respect to the arc one, suggesting one possibly explanation for the different experimental results obtained.
The beamlet shape in terms of core and beam halo is also discussed in Section 5.5, starting from the beam profiles measured by visible cameras. At last in Section 5.6, the capability of visible cameras in characterizing an electron beam is demonstrated, by studying the electron beam divergence of the electron gun at the University Paris-Saclay.

5.1 SPIDER beam divergence in surface operation

The H^- current density required to be extracted from the SPIDER ion source is 355 Am^{-2}, in D^- is 285 Am^{-2}. SPIDER is designed to minimize the beam divergence, for all the current densities in the range $70 - 120\%$ of the nominal value. With neglecting the negative ion temperature, the expected minimum from simulations is equal to 2.2 mrad, reached with $U_{extr} = 9.4\ kV$ and $U_{acc} = 100\ kV$, which corresponds to $R = U_{acc}/U_{extr} = 10.6$ and $P/P_0 = 0.26$ [29]. The dependence of the beam divergence on the properties of the first gap (the meniscus) and of the second gap (the $R = U_{acc}/U_{extr}$) of SPIDER accelerator is here studied.

5.1.1 Visible cameras: equivalent perveance and single beamlet width

As explained in section 2.6, the perveance plays a key role in determining the beamlet divergence. Starting from the beamlet emissivity obtained through the tomographic inversion, corrected by taking into account the energy of the negative ions and the background gas density (section 4.1), so to be directly linkable to the beam current, it is possible to define also an equivalent perveance estimated by visible cameras. The beam optics is studied in terms of the beamlet vertical width (y direction), obtained through the Gaussian fit of the 1D beam profiles measured by visible cameras (section 4.5). The divergence of the beamlet is related to its width through

$$w_y(z) = w_y(0) + \delta z, \tag{5.1}$$

where δ is the beamlet divergence along the y direction, $w_y(z)$ is the beamlet width at the position z, $w_y(0)$ the width of the beamlet at $z = 0$ (at the exit of the Grounded Grid GG, assuming that beamlet waist is located at the exit plane of the GG), which can be assumed to be equal to 4 mm, a little smaller than half radius of the apertures of

the GG, which is a well posed assumption, according with beam optics simulations and experimental data [29] [85] [86].
The relation between the estimated beamlet emissivity ϵ, vertical width w_y and the extraction voltage U_{extr} is shown in Fig.5.2. The numbering of the beamlets is shown in Fig.5.1; they are called for simplicity B followed by the number associated with them, i.e. B1 for beamlet 1, B2 for beamlet 2 and so on. It should be noted that beamlets 24, 25, 26 are accelerated from edge apertures (side apertures 24, 25 and top aperture 26), therefore they are extracted from edge position of the plasma volume enclosed within the bias plate window. Differences could be linked to this choice. Beamlets 21 and 23 at the very bottom of the source, instead, have the same position within the beamlet group as other beamlets at the top and bottom of each beamlet group (e.g. 2, 4, 10, 14 and so on). The data discussed in the following were measured with 4×45 kW radio-frequency

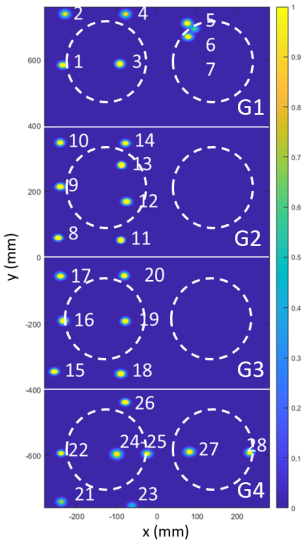

Figure 5.1: *Open beamlets labelling. Also the group division and the drivers position is reported.*

power, 0.9 kA filter current, 0.3 Pa source pressure in hydrogen operation. Current flowing to bias the plasma grid, ISBI, and that to the bias plate, ISBP, has the same value. The extraction and acceleration voltages are increased together with constant ratio R=9.5. For each beamlet group, the central beamlet of the external column is studied; only for group 4 G4 (i.e. the group at the bottom of the beam, numbered from 1 to 4, from the top to the bottom, one group in correspondence of each pairs of drivers), both the open beamlets are shown, i.e. the B22 (the central one) and the B21 (the bottom one). In Fig.5.2 a) and b), respectively, the beamlet vertical width and emissivity as a function of the extraction voltage are shown. Beamlets in different positions along the vertical profile of the beam behave differently, according to the different amount of negative ions available. B1, B9 and B16, which are the central beamlets of G1, G2 and

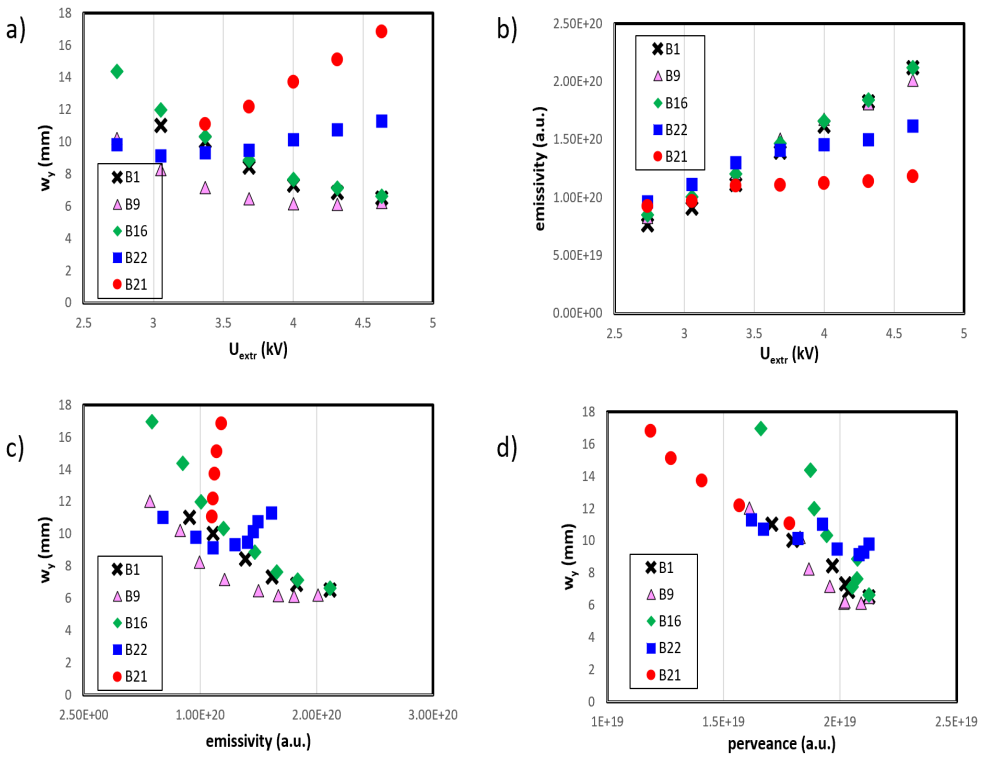

Figure 5.2: *On top, beamlet vertical width (a)) and emissivity (b)) as a function of the extraction voltage, measured by visible cameras (z=0.35 m); on bottom, beamlet width as a function of the beamlet emissivity (c)) and equivalent perveance (d)). Different colours represent various beamlets, called by numbers in the legend. For each beamlet group the central beamlet is shown, except for G4, for which two beamlets are represented (B22-B21). [4×45 radio-frequency power, 0.3 Pa, H, I_{filter}=1.05 kA, ISBI=ISBP=80 A, R=9.5]*

G3, have similar width; B22 and B21, instead, have a larger width, which increases as the extraction voltage grows. The equivalent perveance is defined as $P = \epsilon/U_{extr}^{3/2}$ where ϵ is the corrected beamlet emissivity, and thus it is representative of the beamlet current (this correction is always applied in this thesis work). In this case, the experimental perveance is based on the current of the accelerated beamlet, which might not coincide with the extracted current, if a fraction of the beamlet is intercepted by the extraction grid. To be sure that this experimental perveance is a good estimation of the perveance at the meniscus, only the points with larger experimental perveance estimated from the accelerated current are considered, with the beam transmission closer to unity (i.e at high perveance but low extraction voltage a fraction could be intercepted by the grids). In these conditions the extracted current density is very close to the accelerated current measured by the beam diagnostic. Stripping losses can be neglected, as they are quite

limited thanks to the limited number of apertures. By comparing the measured beamlets width and their perveance, it is possible to improve the results obtained through the tomographic inversion: beamlets with the same width (as for B1, B9 and B16) should have similar perveance (i.e. beamlet current density). For this reason, a self-consistent correction on the reconstructed emissivity of these beamlets can be applied: the mean value of the maximum perveance of beamlets with the same width is used to re-scale the estimated emissivity, thus averaging the error associated to the reconstructed emissivity for each of them. As described, the points at the knee of the current voltage characteristics (Fig.5.2 b)) fulfil the condition that the accelerated beamlet current well represents the beamlet current at the extraction, because they are the points closer to the perveance match and the beamlet does not intercept the extraction grid. At lower extraction voltages, the beamlet transmission is lower than unit, and the points of the accelerated current-extraction voltage characteristics get farther from the power law of limiting perveance; in this sense, since the experimental perveance is defined on the basis of the accelerated beamlet current, the points around the knee are also the ones with the highest experimental perveance, ant they provide our best estimation of the perveance at the extraction. Since the beamlet perveance at the extraction has an absolute validity, this correction allows to reduce the source of error in the estimation of the beamlet emissivity through the tomographic reconstruction. From the analysis of various reconstructed profiles, in fact, it was found that the ratio between the mean value of the maximum values of perveance (estimated through the reconstructed emissivity) of beamlets with the same width, and their maximum perveance is always the same, thus confirming that the differences in the reconstructed values are attributable to limits of the technique (as in the relative calibration of some cameras, for instance). However, this correction is in the order of 8-10 %, thus it does not affect too much the beam profiles obtained through tomographic reconstructions. I have applied this correction to the reconstructed beamlet emissivity every time a good beamlet transmission throughout the accelerator can be assumed. In this way, the optimum of the optics for the beamlets B1, B9 and B16 corresponds to almost the same value of perveance while, the B22 and B21, which behaves differently as shown in Fig.5.2 a) and b), have also a different perveance curve and emissivity. B22 and B21, in fact, have a lower emissivity (and thus beamlet current) and their width increases as the extraction voltage grows, while for the others it decreases (see Fig.5.2 a)). As the extraction voltage is raised, the emissivity of B22 and B21 saturates. This suggests that the negative ions available at the bottom of the beam are less with respect to the ones available for the other groups (the emissivity of the B1, B9 and B16 enlarges continuously with the extraction voltage). The ions availability along the vertical beam profile is discussed in details in chapters 6 and 7. The relation between the beamlet emissivity and vertical width is shown in Fig.5.2 c), in which the different behaviour of various beamlets is more evident. For all beamlets, except the ones of G4, the width reduction corresponds to the increment in the emissivity. In such condition, the accelerated beamlet current is much underestimated with respect to the extracted current, because a fraction of the beam current is intercepted at the extraction grid. The higher the extraction voltage, the closer to perveance match the beamlets get.

The results in Fig.5.2 d) present only the low-perveance side of the "smiling curve" of the divergence, because no points can be placed on the right hand side with respect to the limiting perveance, at which the transmission through the extraction grid starts to decrease below one; this is because the experimental perveance is defined from the accelerated beamlet current, the only one available for measurements. Within this picture of the physical processes occurring at the extraction, we should highlight that the over-perveant side would be limited in experimental perveance, but also in divergence, because of the scraping effect of the EG aperture, which in practice collimates the beamlet. For instance, the pink and the blue points in Fig.5.2 d) (B9 and B22) present this effect.
The results obtained by visible cameras are compared with the beamlet current density and width measured by STRIKE calorimeter and they are shown in Fig.5.3. These

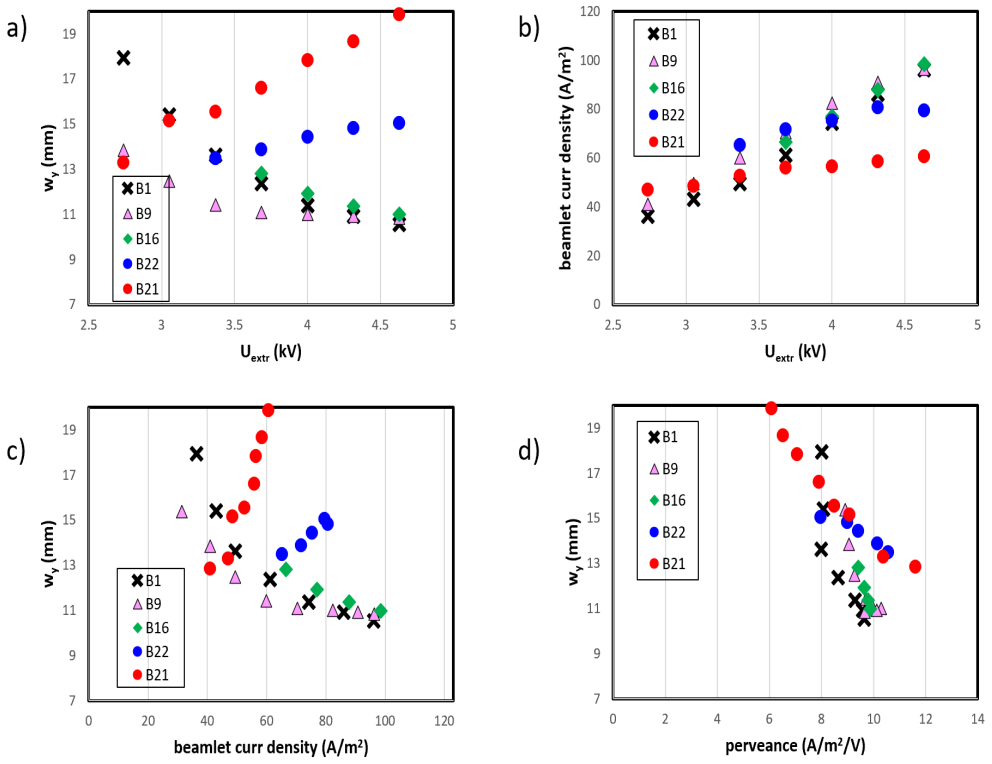

Figure 5.3: *On top, beamlet vertical width (a)) and current density (b)) as a function of the extraction voltage, measured by STRIKE (z=0.5 m); on bottom, beamlet width as a function of the beamlet current density (c)) and perveance (d)). Different colours represent various beamlets, called by numbers in the legend. For each beamlet groups the central beamlet is shown, except for the G4, for which two beamlets are represented (B22-B21). [4×45 radio-frequency power, 0.3 Pa, H, I_{filter}=1.05 kA, ISBI=ISBP=80 A, R=9.5]*

measurements are carried out with STRIKE at $z = 0.5\ m$ from the GG, while visible cameras observe the beam at $z = 0.35\ m$. By comparing the beamlets width measured by STRIKE (Fig.5.3 a)) and by visible cameras (Fig.5.2 a)), both the dependence on extraction voltage and absolute values are consistent; the optimum of divergence is around 12 mrad for STRIKE, 10 mrad for visible cameras (using Eq.5.1), for the central beamlets of G1, G2 and G3. These values are consistent since both diagnostics have a resolution in the order of the millimetre, both in the estimate of the beamlet width and in the position along the beam propagation direction where they are measuring. The B21 and B22 current density (width) is lower (larger) with respect to the one of other beamlets, as already shown by visible cameras (Fig.5.3 and Fig.5.2 b)). The perveance-width curves estimated by the two diagnostics are consistent.
Due to the differences highlighted both in Fig.5.2 and Fig.5.3 between beamlets composing SPIDER beam, and also discussed in details in the chapter dedicated to the beam homogeneity (Chapter 7), a definition of an unique beam divergence for SPIDER beam is not straightforward. For this reason, in this chapter SPIDER beam divergence is studied using both the entire vertical profile of the external column of beamlets, and by analysing the behaviour of the central beamlet of each beamlets group.

5.1.2 SPIDER performances in Cs operation

The two most important effects of Cs evaporation in negative ion sources are a substantial increase in the negative ion current density compared with a Cs-free source, together with a reduction in the electron-to-ion ratio [87].
The main phases of SPIDER campaign with Cs evaporation are summarized in Fig.5.4, in terms of electron-to-ion ratio and negative ion current density measured by Acceleration Grid Power Supply AGPS (on the left) and STRIKE electrical measurements (on the right).

The main features of each phase shown in Fig. 5.4 are:

- Pre Cs. Before to start with Cs evaporation, SPIDER operates with 4x100 kW of radio-frequency power, and maximum acceleration and extraction voltages, respectively, of 50 and 5 kV. The e^-/H^- extracted ratio was between 5-15, with maximum ion current density of 55 A/m^2 measured by the AGPS power supply (40 A/m^2 measured by STRIKE calorimeter). Transition from volume to surface production was immediately seen, with a reduction of the co-extracted electrons current from 2.4 A to 1 A, and an increase in the negative ion current by factor of 2 (4x50 kW of radio-frequency power in Cs operation compared with 4x100 kW in volume operation).

- Phase 1 and 2. Beginning of the operation with Cs evaporation. Good vacuum conditions and caesium effectiveness, but total acceleration voltage available was insufficient: the accelerated current is lower than the extracted one, meaning a bad accelerator transmission. Various Cs evaporation rates and duty cycles were tested, together with the maximum radio-frequency power available (4x100 kW). The e^-/H^- has its minimum of less than 0.1 (according with AGPS electrical

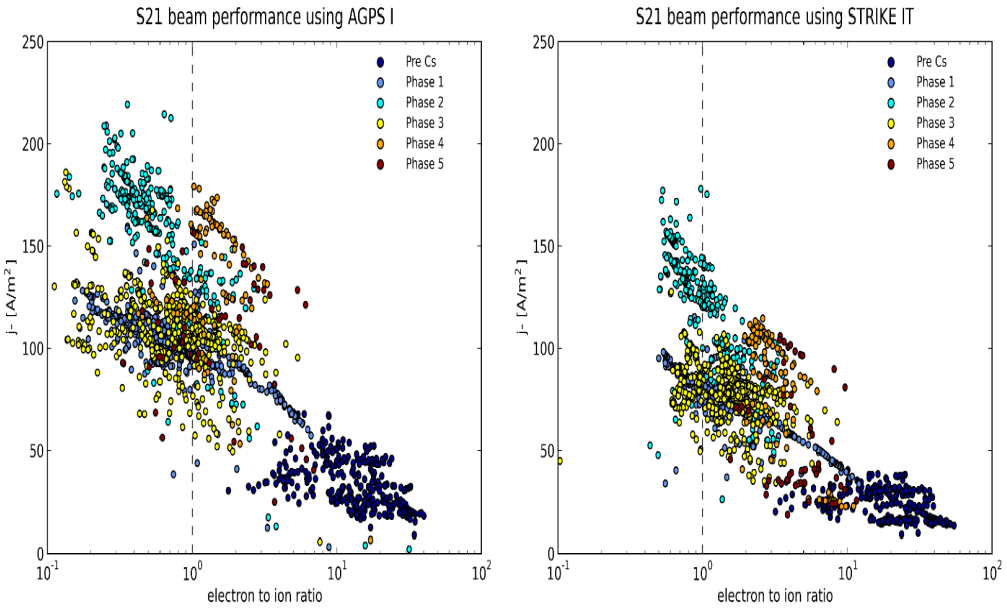

Figure 5.4: *Negative ion density as a function of the electron-to-ion ratio measured by AGPS power supply (on the left) and STRIKE electrical measurements (on the right) during the phases of SPIDER experimental campaign with Cs evaporation.*

measurements) and 0.8 for STRIKE electrical measurements. Maximum extracted current density of 200 A/m^2 and 150-170 A/m^2 respectively for the AGPS power supply and STRIKE electrical measurements.

- Phase 3. Reduction of the total extracted current by reducing the radio-frequency power to perform beamlet optics investigation close to the perveance match. Also a deterioration of the vacuum and caesium effectiveness was found.

- Phase 4. The operation is constrained by the impossibility of raising acceleration voltage above 45 kV and of recovering the caesium effectiveness of phase 2.

- Phase 5. Deuterium operation. Only 2 days of experimental time could be dedicated to the characterization of SPIDER beam in deuterium with Cs evaporation.

During this experimental time, many source and accelerator parameters are varied to characterize the beam performance. The beamlet divergence measured by visible cameras as a function of these parameters is studied in the following, also with a comparison with the other beam diagnostics measurements (BES, STRIKE calorimeter and Allison Emittance Scanner)

5.1.3 Dependence of beamlet divergence on source parameters

As described previously, the shape of the meniscus determines the optics of the extracted beamlets. It depends on the characteristics of the plasma in front of the extraction region (density and composition). Thus, acting on the plasma properties, it is possible to modify the beamlet divergence. The main parameters which can be varied are the radio-frequency power, the source pressure, the filter field strength and the Cs coverage, which depends both on the evaporation rate and on the temperature of the PG. The beamlet divergence (represented by the beamlet width) in SPIDER operation with H beam and Cs evaporation as a function of these parameters is studied.

Dependence on the radio-frequency power

The plasma density depends on the radio-frequency (RF) power applied, as confirmed by spectroscopic measurements [53], thus it can be expected that it influences the density of negative ion for extraction and therefore the shape of the meniscus. In fact, by increasing the radio-frequency power, both the co-extracted electrons and the negative ions currents grow, as shown in Fig.5.5 a). These data refers to 5 kV and 50 kV of extraction and acceleration voltages, ISBI=80 A, ISBP=0 A, 1.5 kA of filter current and 0.4 Pa of source pressure. By applying the same extraction voltage, a higher plasma density means a less concave meniscus, since the current density increases. Thus, this modification affects the divergence of the beam. The increase in the total current (red points in Fig.5.5 a)) and in the total emissivity (blue points in Fig.5.5 b)) results in a modification of the beam homogeneity, as shown by the RMS of the beamlet emissivity in Fig.5.5 b) (red points). It is defined as the RMS divided by the average value of the total beam emissivity. The RMS/average decreases as the radio-frequency power grows. The

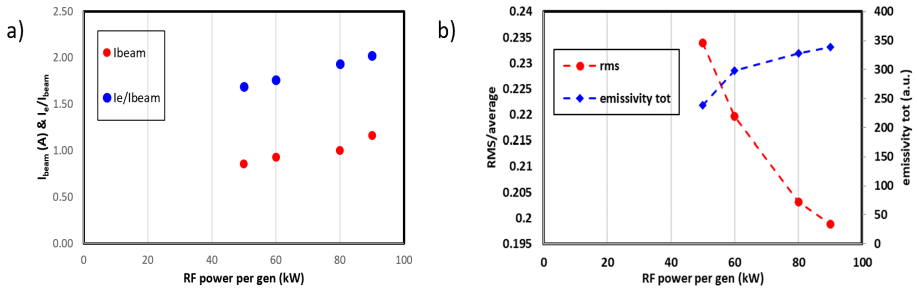

Figure 5.5: *a) negative ions current (in red) and electron-to-ion current ratio (in blue) as a function of the radio-frequency power per generator. b) total reconstructed beam emissivity (in blue) and RMS/average (in red) as a function of the radio-frequency power per generator. [0.4 Pa, H, I_{filter}=1.5 kA, ISBI=80 A, ISBP=0 A, U_{extr} =5 kV, U_{acc} =50 kV]*

vertical profiles of the beam emissivity for the 4 different values of radio-frequency power

are shown in Fig.5.6 (at the bottom): each point represents the reconstructed emissivity of each beamlet composing the external column of open beamlets (from B21 to B2 of Fig.5.1). The correspondent vertical profiles in terms of beamlet width are shown at the top of Fig.5.6. As the radio-frequency power increases, the emissivity of the beamlets grows dis-homogeneously along the vertical profile. In particular, the beamlet with the lowest emissivity is the one at the bottom of the beam (B21). Furthermore, beamlets at the top and bottom of each beamlet group have a lower emissivity than the one at the centre. They are also more sensitive to modification of the radio-frequency power, as confirmed by the wider variation of their widths, which decrease as the radio-frequency power grows. Central beamlets of each beamlet group have a similar width and emissivity. In Fig.5.7, the beamlet vertical width (a)) and emissivity (b) (corrected as described

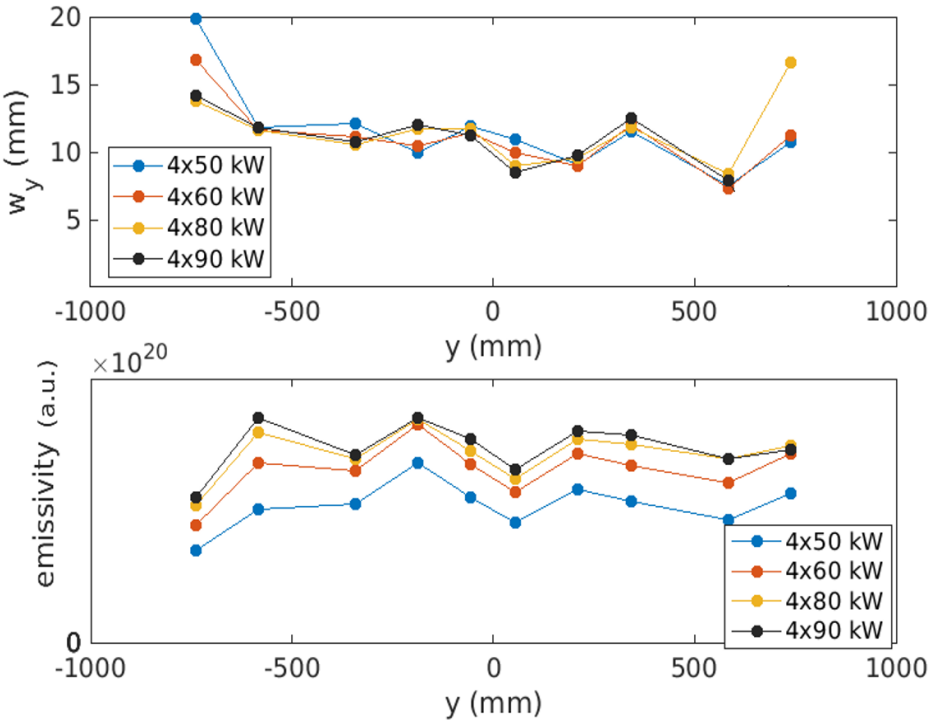

Figure 5.6: *Vertical profile of the beamlet width (on the top) and emissivity (on the bottom) for different radio-frequency power (given in kW per generator/per pair of drivers in the legend). [0.4 Pa, H, I_{filter}=1.5 kA, ISBI=80 A, ISBP=0 A, U_{extr} =5 kV, U_{acc} =50 kV]*

in Sect.5.1.1) of the central beamlet of each group, and of the bottom beamlet of G4, as a function of the radio-frequency power per generator, are shown. In Fig.5.7 a), the width of the B1 (G1), B9 (G2), B16 (G3) and B22 (G4, central beamlet) remains almost the same as radio-frequency power is increased. A little increment is measured when the

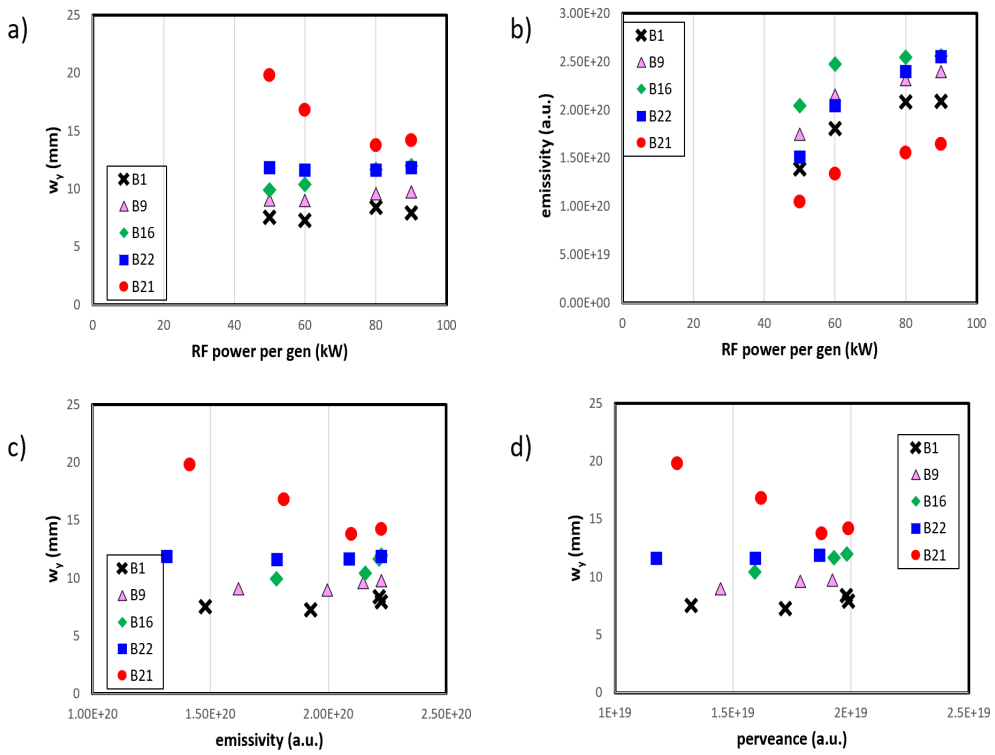

Figure 5.7: *On top, beamlet vertical width (a)) and emissivity (b)) as a function of the radio-frequency power per generator, measured by visible cameras; on bottom, beamlet width as a function of the beamlet emissivity (c)) and perveance (d)). Different colours represent various beamlets, called by numbers in the legend. For each beamlet groups the central beamlet is shown, except for G4, for which two beamlets are represented (B22-B21). [0.4 Pa, H, I_{filter}=1.5 kA, ISBI=80 A, ISBP=0 A, U_{extr} =5 kV, U_{acc} =50 kV]*

radio-frequency power is raised from 60 to 80 kW per generator, which corresponds to the saturation of the total extracted current, as shown in Fig.5.7 b); the highest emissivity is measured in the beamlet 16 (G3). The beamlet width is larger for the beamlet at the bottom of the source (B21-B22), and decreases as moving towards the top of the beam. In Fig.5.7 c), the beamlet width as a function of the its emissivity is represented. For all beamlets, except for the bottom one (B21), the width remains almost constant while the emissivity increases; for B21, instead, a better optics corresponds to the emissivity increment. This different vertical behaviour of the beam divergence can be explained by assuming a non-homogeneous availability of negative ions along the beam vertical profile. In fact, when the radio-frequency power is low, not enough negative ions are available for B21 to be extracted, thus its divergence is larger (too concave meniscus) with respect to the other beamlets; as the plasma density increases, in fact, it optics improves, confirming the larger amount of negative ions available.

To investigate the measured non-homogeneous distribution of negative ions in the extraction region, the plasma in the source can be investigated, using both spectroscopic and electrostatic measurements. A detailed description of the experimental setup of both diagnostics is given in Chapter 3, while the plasma in the source is deeply studied in Chapter 6. Some results are anticipated here: in Fig.5.8 the H_β emission and the H_α/H_β and H_β/H_γ ratios at 35 mm from the PG are shown. The increase in the plasma density inside the source with radio-frequency power is discussed in Ref.[53]. At 35 mm from the PG, as the radio-frequency power increases, the H_β emission grows mostly in the segment 4 (S4). The H_β/H_γ emission ratio remains almost unvaried with the modification of radio-frequency power. The ratio H_α/H_β, instead, has its minimum in S4, suggesting a non uniform distribution of the negative ion density along the vertical profile, with a minimum at the bottom, as confirmed by the peculiar behaviour of the B21 with respect to the others. It should be added that the measurements of Cs density at the bottom segment by the Laser Absorption Spectroscopy generally indicated a lower value with respect to the three segments above, in most operating conditions, throughout the campaign. By increasing the radio-frequency power, both ions and co-extracted

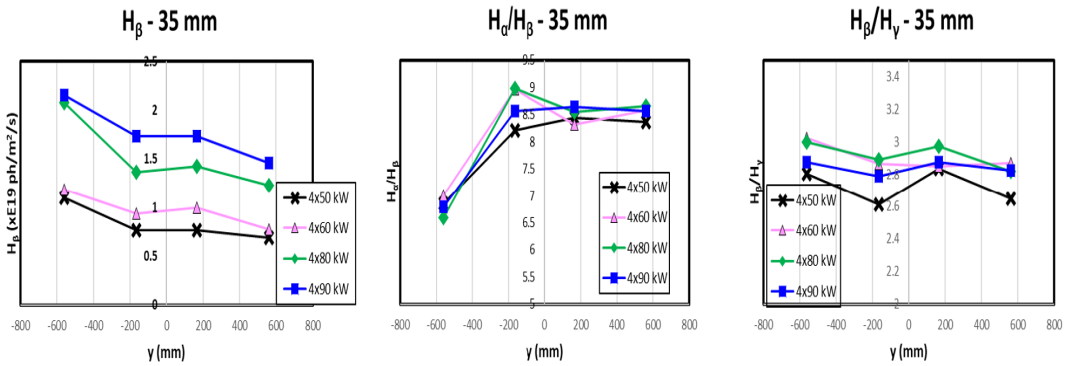

Figure 5.8: *H_β emission, H_α/H_β and H_β/H_γ ratios for various radio-frequency powers, measured at 35 mm from the PG. [0.4 Pa, H, I_{filter}=1.5 kA, ISBI=80 A, ISBP=0 A, U_{extr} =5 kV, U_{acc} =50 kV]*

electrons currents grow. Looking at the beam divergence, the major effect is in the optics of the beamlet at the bottom of the beam, which improves as the radio-frequency power is increased. From vertical profiles of the beamlet width (Fig.5.6), a similar behaviour is found also for external beamlets of G3 and G2. This could be related to the larger plasma density (as confirmed by electrostatic and spectroscopic measurements) which allows to increase the production of negative ions also in the region of the beam where the negative ion density is lower, as suggested by the H_α/H_β ratio. Plasma properties, both in the driver and in the expansion region are deeper investigated in Chapter 6.

PG temperature dependence

Experimental measurements, both in arc and in radio-frequency sources [88] [89] indicate that the performances of caesiated sources depend strongly on the temperature of the PG. In Batman [90], an increase in the calorimetric current density and a reduction of the electron-to-ion ratio when the PG is heated from room temperature to temperatures above 100° C is observed. This effect disappears when the source is well caesiated. The same measurements are performed in SPIDER, where the plasma grid temperature was increased from 80° C to 140° C. In Fig.5.9, the co-extracted electrons (in blue) and

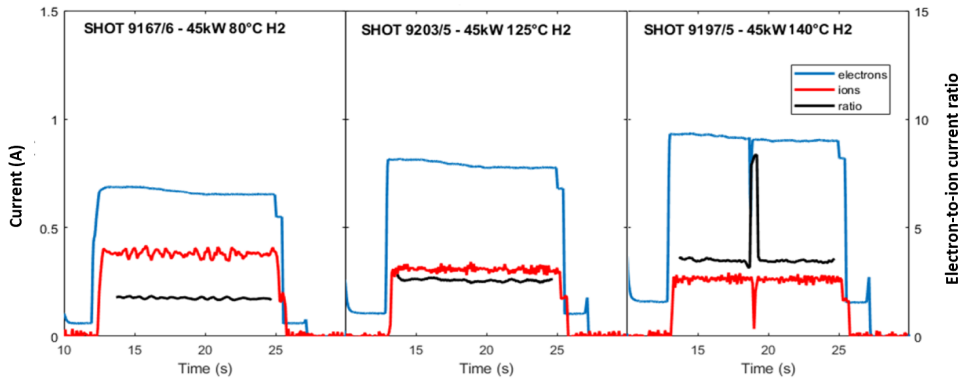

Figure 5.9: *Co-extracted electrons (in red) and accelerated ions (in blue) currents and their ratio (in black) for different PG temperatures. [4×45 kW of radio-frequency power, 0.4 Pa, H, I_{filter}=1.2 kA, ISBI=ISBP=80 A, U_{extr} =5 kV, U_{acc} =40 kV] [91]*

ions (in red) currents as a function of the time, for various PG temperatures are shown; in black, the ratio in between the two currents; from left to right, the temperature is increased from 80° C to 140° C. The negative ion current decreases while the co-extracted electron current grows, with a electron-to-ion ratio magnification from 2 to 4. During the 15 seconds of beam on, both the currents are stationary. These data refer to 45 kW radio-frequency power per generator, 0.4 Pa source pressure ISBI=ISBP=80 A and 1.2 kA of filter field current, 5 kV and 40 kV of extraction and acceleration voltages. A similar dependence of negative ion current on PG temperature is also found in the neutral caesium density measured by the Laser Absorption Spectroscopy diagnostics [91], as shown in Fig.5.10. The caesium density decreases linearly with the PG temperature from 80° C to 140° C. The variation of the amount of available negative ions when changing the temperature of the PG is also confirmed by spectroscopic measurements. The H_α/H_β ratio measured at 5 mm (on the left) and at 35 mm (on the right) from the PG is shown in Fig.5.11. At 5 mm, the line ratio decreases as the PG temperature is increased, except in G4 (bottom). By assuming this ratio indicative of the negative ion amount, this reduction confirms the measurements of the LAS and of the electrical beam current. This decrease is lower at 35 mm from the PG. The only difference is measured when the temperature is decreased to 140° C. This could suggest that negative ion

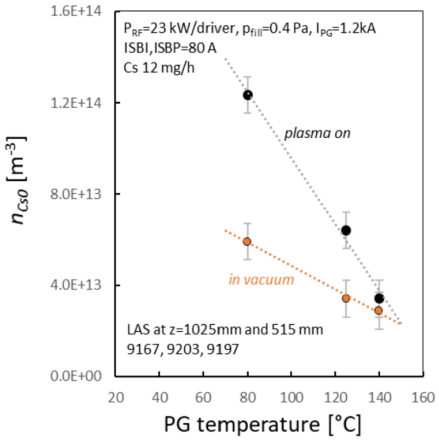

Figure 5.10: *Cs density measured by the LAS diagnostics as a function of the PG temperature with plasma on (in black) and without plasma in the source (in red). [91]*

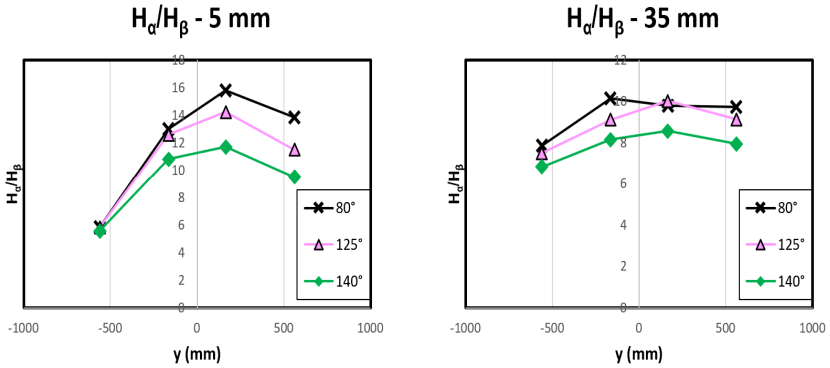

Figure 5.11: *H_α/H_β ratio measured at 5 mm (on the left) and at 35 mm (on the right) from the PG, for different PG temperatures. . [4×45 kW of radio-frequency power, 0.4 Pa, H, I_{filter}=1.2 kA, ISBI=ISBP=80 A, U_{extr} =5 kV, U_{acc} =40 kV].*

production is not large enough that the region of high negative ion density could expand backward in the plasma (i.e. at 35 mm). Figure 5.12 illustrates the dependence of the negative ion current (first panel) and electron-to-ion currents ratio (second panel) on the extraction voltage; different colours represent various PG temperatures. The larger ion current is measured when the PG is heated to 80°C and the pressure is high (0.4 Pa, red points), which corresponds also to the lower electron-to-ion ratio (second panel), equal to 1.6; in these conditions, the extracted negative ion current increases continuously with the extraction voltage without saturation, suggesting that not all the available negative ions are extracted, even at the largest extraction voltage of 5 kV. Once the

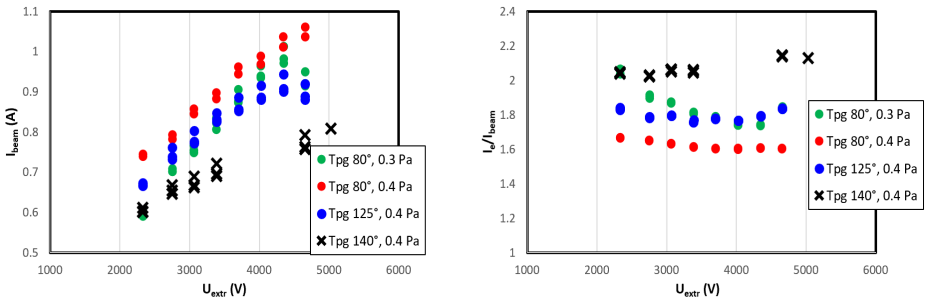

Figure 5.12: *Negative ions (first panel) and electron-to-ion (second panel) currents as a function of the extraction voltage, for various PG temperatures and pressures. [4×45 kW of radio-frequency power, 0.3-0.4 Pa, H, I_{filter}=1.2 kA, ISBI=ISBP=80 A, R=9.5]*

source pressure is reduced to 0.3 Pa, the total extracted current is diminished too (green points, first panel), to a value still larger than at higher PG temperatures and pressure: the ion current decreases continuously as the PG temperature is enhanced. The effect on the electron-to-ion current is the opposite: it increases with the PG temperature, from 1.6 to 2. On the electron-to-ion ratio, the reduction of the source pressure from 0.4 Pa to 0.3 Pa and the increment of the PG temperature from 80° C to 125° C have the same effect.

The total beam emissivity and the RMS/average, as a function of the extraction voltage,

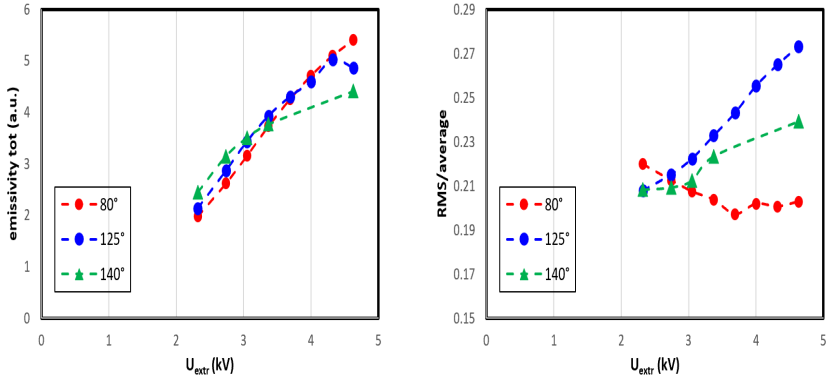

Figure 5.13: *Total reconstructed beamlet emissivity (on the left) and RMS/average (on the right), as a function of the extraction voltage, for different PG temperatures. [4×45 kW of radio-frequency power, 0.4 Pa, H, I_{filter}=1.2 kA, ISBI=ISBP=80 A, R=9.5]*

and for different PG temperatures, are shown in Fig.5.13. The total emissivity well reproduces the electrical measurement of the beam current shown in Fig.5.12. Figure 5.13 on the right illustrates a more homogeneous beam as the PG temperature augments,

for low extraction voltages. As the extraction voltage is increased, the RMS at low PG temperature is reduced while, at larger temperatures, it increase with the extraction voltage. The vertical profiles of the external column of beamlets emissivity at low and high extraction voltages are shown in Fig.5.14 (top panel), together with the vertical profiles of the beamlet width (bottom panel), to explain this observed modification in the beam homogeneity and current. At low extraction voltage (2.32 kV case, solid

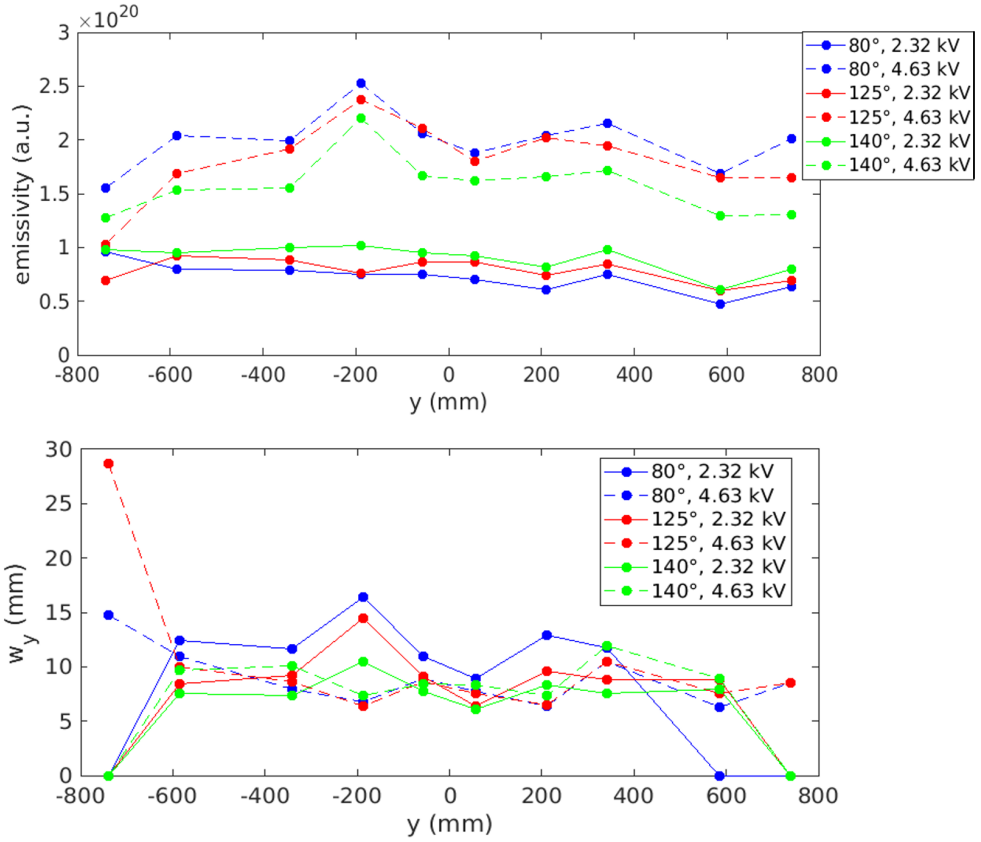

Figure 5.14: *Vertical profiles of the external column of beamlets emissivity (on the top) and width (on the bottom) for two values of extraction voltage, 2.32 kV solid lines, 4.63 kV dashed lines; various colours refer to different PG temperatures [4×45 kW of radio-frequency power, 0.4 Pa, H, I_{filter}=1.2 kA, ISBI=ISBP=80 A, R=9.5].*

lines in Fig.5.14), the total emissivity is larger when the PG temperature is higher, the opposite when the extraction voltage is 4.63 kV. This is easily explained by considering the different amount of Cs at the various PG temperatures (see Fig.5.10). When the negative ion density is larger (low PG temperature case), an elevated extraction voltage is needed to be capable of extracting all negative ions. If the applied voltage is not enough, in fact, the space charge of the beamlet limits its transmission throughout the accelerator (scraping on the extraction grid, too convex meniscus, Fig.2.5), reducing the

total beam current extracted at low extraction voltage and PG temperature. This affects the vertical profile of the beam. This is confirmed also by the beamlet width shown at the bottom of Fig.5.14, which is larger for the low voltage case, especially for central beamlets of each beamlet group, which have the largest current density (as explained in the following). As the extraction voltage is increased, instead, the largest emissivity is measured for the case with the lowest PG temperature, which corresponds to the largest negative ion density available. This reflects in a reduction of beamlet widths along the vertical profile, especially for central beamlets: they are the ones with still enough negative ions to be extracted at high PG temperature at the bottom of the beam; at the top, their space charge is still too large to avoid the scraping on the extraction grid. The effect of space-charge limit appears evident in the comparison of high and low extraction voltage cases: only for sufficiently large extraction voltages, the non-uniformity of the beam profile offers the indication of the available negative ion density at the extraction region, while at low U_{ext} the uniformity is only apparent, and scraping at EG is possibly occurring for many of the beamlets.

In Fig.5.15, the beamlet vertical width (a)) and emissivity (b)) as a function of the extraction voltage, for two different values of PG temperature (open marks 80° C, solid marks 125° C) for central beamlets of each beamlet group are shown; for G4, also the external beamlet is represented (B21, the bottom one). The bottom beamlet (B21), is the one for which the width changes the most when the temperature of the PG is varied. It features the worst optics and the lowest emissivity; as the extraction voltage grows, its emissivity saturates. A similar behaviour is measured for B22, even if its emissivity (width) is larger (lower). For all other beamlets, instead, the emissivity increases with the extraction voltage (Fig.5.15 b)), and, as a consequence, the vertical width is reduced (Fig.5.15 a)). Depending on the position along the vertical beam profile, the total current carried by various beamlets is different: for all central beamlets, except for B16, which is the central beamlet of G3, the emissivity at high PG temperature saturates for the maximum values of applied extraction voltage. In the case with low PG temperature, instead, their emissivity continues to increase. The effect of the beamlet perveance at the meniscus is evident in the different divergence of the beamlets when the same extraction voltage is applied, as presented in Fig.5.15 c) and d) where, respectively, the beamlet width as a function of the beamlet emissivity and perveance is shown. The B16 (G3), B9 (G2) and B1 (G1) behave similarly: they bring almost the same current, which corresponds to the same beamlet width as the extraction voltage is increased enough. This is confirmed by both the relation between beamlet width and emissivity, and the perveance plot, where all curves collapse to the same value of beamlet perveance for the minimum of divergence (width). For G4, instead, both beamlets shown have a different behaviour. The width of both of them (the effect is stronger for B21, which is the bottom one) increases while their emissivity saturates. This effect is related to the different amount of available negative ions at the bottom of the beam (the behaviour changes with the PG temperature). In addition, at saturation (i.e. high extraction voltage) the available negative ion current at the extraction is more uniform for the case at 80°C (including also the bottom beamlet B21 in the overall result), and this is

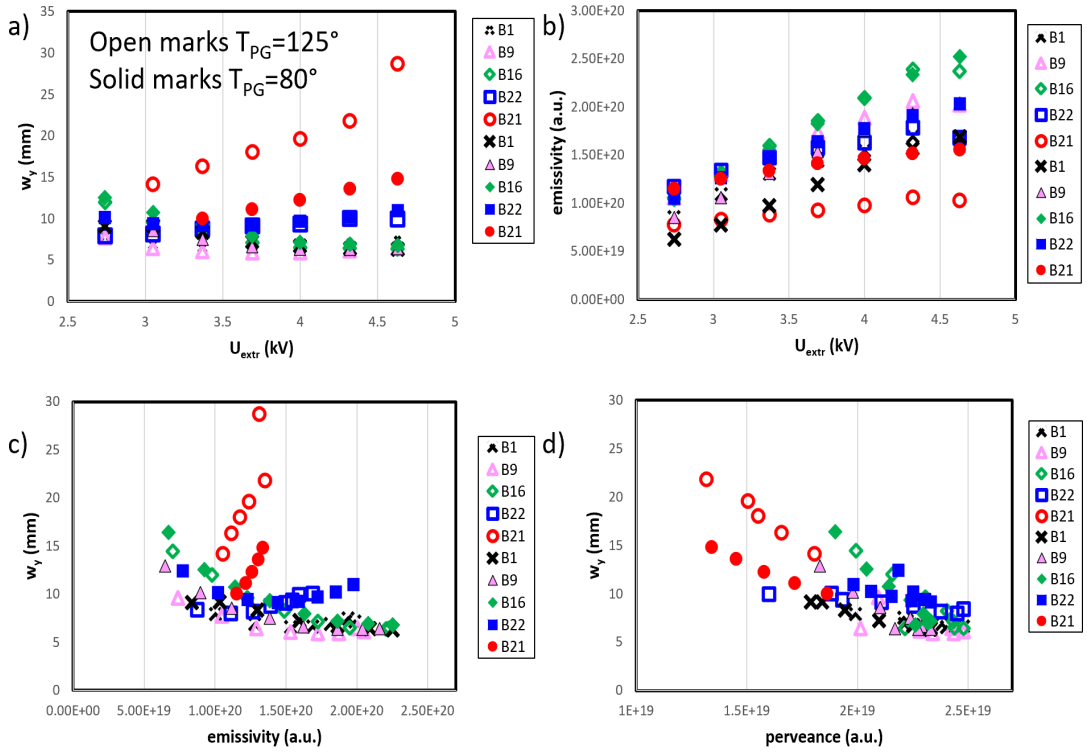

Figure 5.15: *On top, beamlet vertical width (a)) and emissivity (b)) as a function of the extraction voltage, measured by visible cameras; on bottom, beamlet width as a function of the beamlet emissivity (c)) and perveance (d)). Different colours represent various beamlets, called by numbers in the legend; open marks refer to 125° C, solid ones to 80° C. For each beamlet group the central beamlet is shown, except for G4, for which two beamlets are represented (B22-B21). [4×45 kW of radio-frequency power, 0.4 Pa, H, I_{filter}=1.2 kA, ISBI=ISBP=80 A, R=9.5]*

also evident from the beamlet width (Fig.5.15 a)); the lowest current case (B21, 125°C) presented a very large increase of the divergence, bound to culminate with interception by the grounded electrode (largely under-perveance case).
Both electrical and optical beam measurements show an improvement of the beam in terms of total current and divergence, when the temperature of the PG is lowered. The bottom of the beam is the region which suffers the most the worsening of the caesium performances (bad optics and low current density at elevated PG temperatures).

Source pressure dependence

As with the radio-frequency power, the gas pressure plays a key role in determining the plasma density. As shown by electrical current measurements in Fig.5.12, the main effect

of increasing source pressure is to increase the beam current and reduce the electron-to-ion ratio (red and green series). For both values of extraction voltage, the beamlet emissivity is higher when the source pressure is also higher, confirming the agreement between the beamlet emissivity and the electrical measurement of the negative ion current. The evolution of the central beamlet of each beamlet group, for the two values of

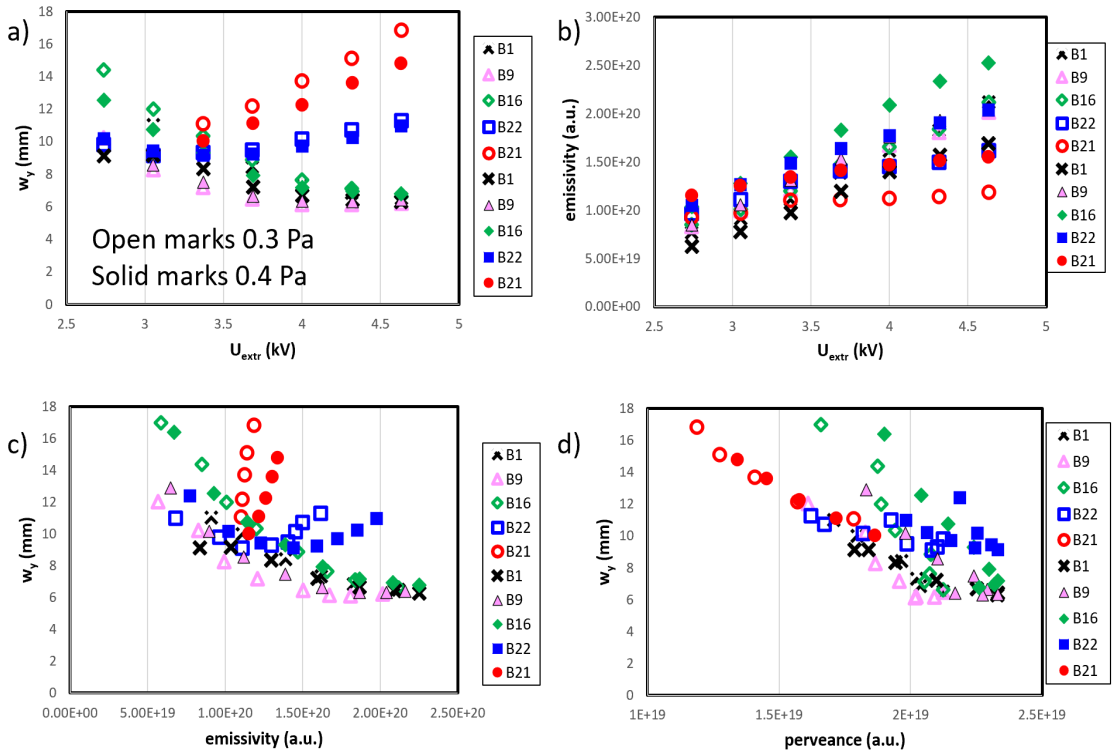

Figure 5.16: *On top, beamlet vertical width (a)) and emissivity (b)) as a function of the extraction voltage, measured by visible cameras; on bottom, beamlet width as a function of the beamlet emissivity (c)) and perveance (d)). Different colours represent various beamlets, called by numbers in the legend; open marks refer to 0.3 Pa, solid ones to 0.4 Pa. For each beamlet group the central beamlet is shown, except for G4, for which two beamlets are represented (B22-B21). [4×45 kW of radio-frequency power, 0.3-0.4 Pa, H, I_{filter}=1.2 kA, ISBI=ISBP=80 A, R=9.5, T_{PG} =80°]*

source pressure (0.3 Pa open marks, 0.4 Pa solid marks), as a function of the extraction voltage is shown in Fig.5.16. The improvement in beam homogeneity as source pressure increases is evident here for G4 beamlets (B21 is the outer, B22 the middle one). The central beamlets of G1, G2 and G3 behave in the same way: their width decreases as the extraction voltage is increased (Fig.5.16, a)), and this corresponds to a growth of their emissivity (Fig.5.16 b)). The higher the source pressure, the greater their emissivity. The different amount of total extractable ions along the vertical profile is evident by ob-

serving the behaviour of B22 and B21 relative to the other beamlets. After a minimum, their width begins to increase as the extraction voltage grows, up to different values, depending on their current density (here represented by their emissivity). As the source pressure increases, so does their current, resulting in less divergence. The difference between G4 beamlets and the others is also highlighted in terms of beamlet perveance (Fig.5.16 d)).
From all measurements, an improvement of the beam in terms of current density and homogeneity is found as the source pressure increases.

Filter field dependence

The effect of the filter field both within the plasma source and on beam homogeneity is discussed in detail in Chapters 6 and 7. It mainly affects the beamlets at the bottom of the source (in the standard direction, the opposite when the filter filed is reversed). This naturally results in a change in beamlet width, as it modifies the shape of the meniscus, changing the beamlet current density. Figure 5.17 shows beamlets emissivity (first panel), width (second panel) and the relationship between beamlets perveance and width (third panel); the open marks refer to B21, the lower one, the solid ones to B22, the central beamlet in the outer column of G4; different colours indicate various filter field values. As expected, the effect of the filter field is stronger on the beamlet at the

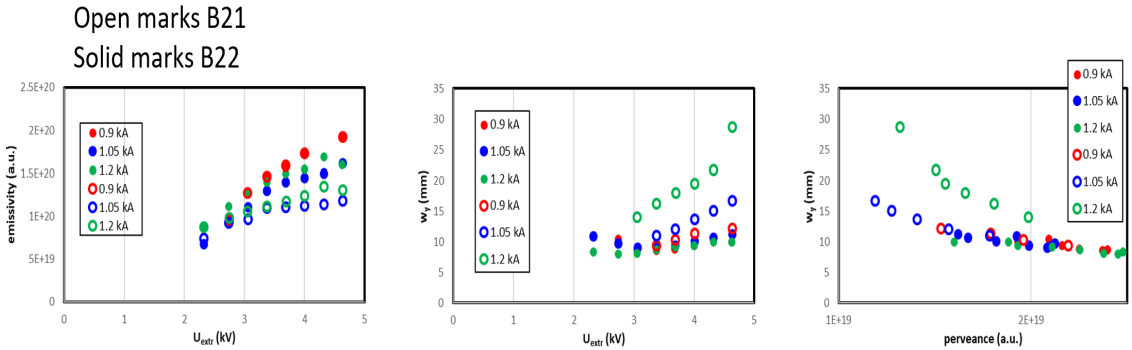

Figure 5.17: *B21 (open marks, bottom beamlet of G4) and B22 (solid marks, central beamlet of G4) emissivity (first panel) and vertical width (second panel), perveance-width curve (third panel) measured by visible cameras as a function of the extraction voltage. Different colours represent various filter field values (standard direction). [4×45 kW of radio-frequency power, 0.3 Pa, H, ISBI=ISBP=80 A, R=9.5, T_{PG} =80°]*

bottom, which has the largest width when the filter field in the standard direction is higher, and it belongs to a different perveance curve. The increase of non-homogeneity inside to the beamlet groups with the filter field is described in Chapter 7, both in volume and surface operations.

5.1.4 Voltage ratio dependence

Most of the data discussed in the previous section are measured with the ratio $R = U_{acc}/U_{extr} = 9.5$, which corresponds to the optimum of beam optics according to simulations [29]. This minimum of beamlet divergence is found experimentally by keeping fixed the acceleration voltage while the extraction voltage is varied. Two examples of the

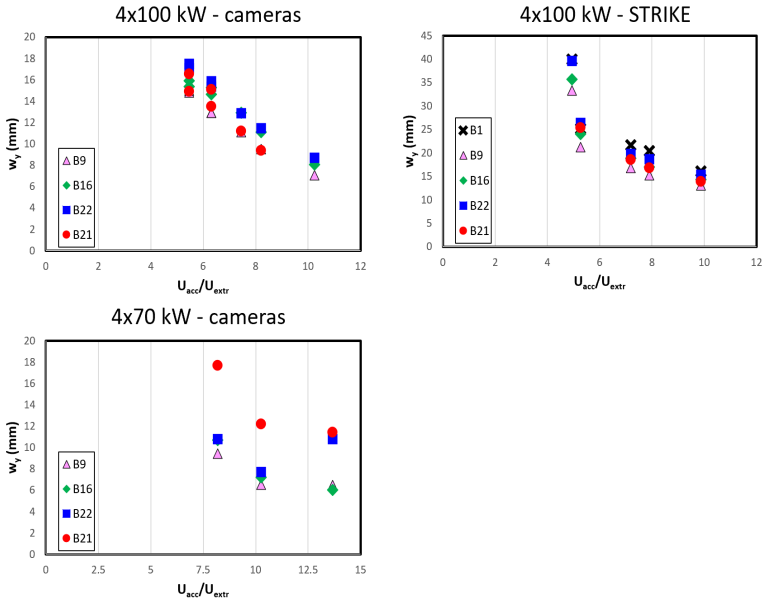

Figure 5.18: *Beamlet width measured by visible cameras (on the left) and by STRIKE (on the right) as a function of the voltage ratio. At the top, data with 4x100 kW, at the bottom ones with 4x70 kW of radio-frequency power. [0.4 Pa, H, ISBI=190 A, ISBP=80 A, I_{filter}=1.5 kA, U_{acc} = 45 kV, T_{PG} =80°]*

dependence of beamlet width measured by visible cameras (on the left) and STRIKE (on the right) as a function of voltage ratio, for two different radio-frequency power values, are shown in Fig.5.18. The width of central beamlets of each group is measured, along with the width of the bottom beamlet (B21): for all of them, the minimum divergence is measured as R approaches to 9.5-10. Both diagnostics show the same results. At 100 kW, data with $R > 10.5$ are missing, so a scan performed at 70 kW is also reported (bottom panel), to show that as the voltage ratio exceeds the optimum, beamlet width begins to increase again, confirming the best value of the voltage ratio between 9 and 10. For both diagnostics, the optimum of beamlet divergence δ at 100 kW per generator, assuming an initial beamlet width $w(0) = 4\ mm$ and considering the two different positions along the beam propagation direction, i.e. $z_{cameras} = 0.35\ m$, $z_{STRIKE} = 0.5\ m$, from the relation $w(z) = w(0) + \delta z$ is equal to 12 mrad.

H vs D beam

SPIDER performances in Cs operation with D gas are described in Chapter 7. Here, the comparison between the beamlet divergence in H and D beam, at the same operational conditions, is performed. As already pointed out, only few data in D during the campaign with Cs are available, due to the limited operational time. Two scans in extraction

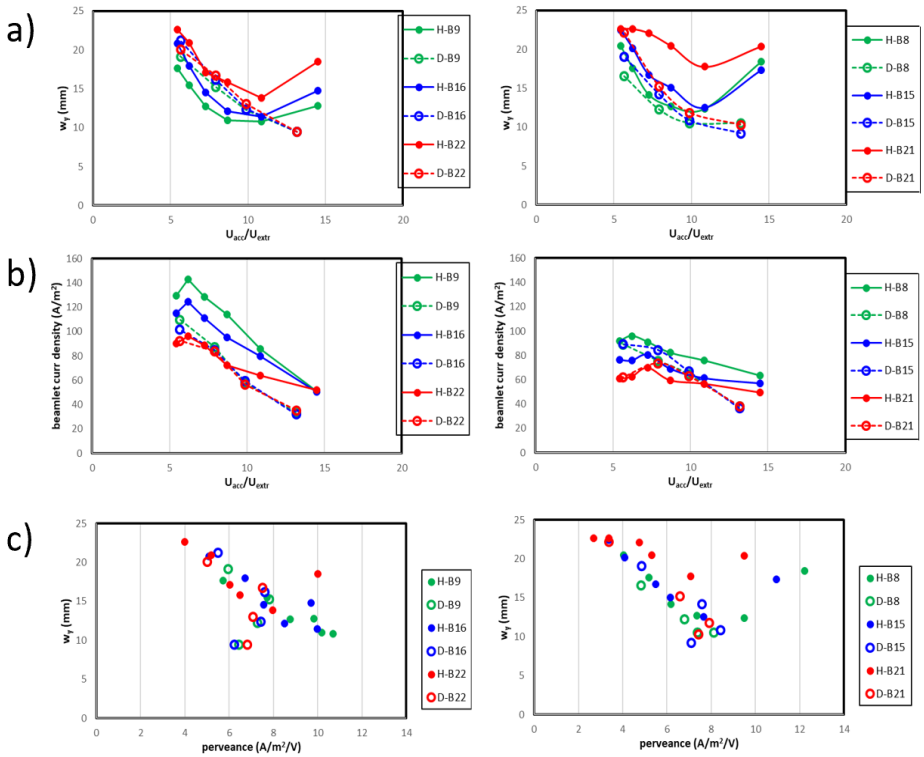

Figure 5.19: *Beamlets width (a)), current density (b)) and width as a function of the perveance measured by STRIKE, as the ratio between extraction and acceleration voltages is varied. Different colours represent various beamlets, as reported in the legend. Open marks refer to D beam, solid ones to H beam. [4×100 kW of radio-frequency power, 0.3 Pa, H and D, ISBI=190 A, ISBP=80 A, I_{filter}=1.5 kA, U_{acc} = 45 kV in H, 40 kV in D, T_{PG} =80°]*

voltage in H and D beams are performed, with 4x100 kW of radio-frequency power, 0.4 Pa of source pressure, 1.5 kA of filter current, ISBP=80 A, ISBI=190 A. The beamlets width (a)) and current density (b)) measured by STRIKE, as a function of the ratio between acceleration and extraction voltages, for central (on the left) and external (on the right) beamlets of G2, G3 and G4 are shown in Fig.5.19, both for H (solid marks) and D beam (open marks); in c) the dependence of beamlets width on the perveance is reported. Differences between the same beamlets but different ions are evident here,

as well as between the central and external beamlets of each group (in both H and D). The width of central beamlets in H has a minimum for R=9.5-10.5, with the lowest divergence corresponding to the beamlet with the largest current density (B9, belonging to G2); similar behaviour is found for external beamlets, although the current density is lower and thus the minimum divergence is greater, especially for the beamlet at the bottom of G4 (B21). The central beamlets of the D beam, on the other hand, have a minimum of divergence for the largest value of R (i.e. the lowest extraction voltage), which corresponds to the smallest value of beamlet current density. This behaviour could be related to the fact that beamlets scrape on the EG, so the measured beamlet width does not correspond to the actual beamlet divergence; at the same time, the emissivity is not representative of the actual beamlet current density, since part of it is lost inside the accelerator. This is also suggested by the perveance-width plot (c), empty points on the left), where at the same value of perveance, the minimum and maximum values of beamlet divergence correspond. This feature is slightly reduced for the external beamlets, although the minimum of divergence still corresponds to the minimum of beamlet current density.
Even if these are only preliminary results, many differences between the H and D beam at the same operational conditions are highlighted. More experiments in D with Cs evaporation are needed to perform a more detailed analysis, as planned for the next operational phase.

5.1.5 Comparison with Allison Emittance Scanner diagnostic

To measure the phase-space profile of the beamlets extracted from SPIDER ion source, an Allison type emittance scanner AES [92] was developed and installed, aiming to provide a complementary and more complete tool to assess the quality of the beam with respect to the other beam diagnostics [93].
The AES observes tree adjacent beamlets of G1, which are seen also by visible cameras. A comparison between the width estimated by visible cameras and the divergence measured by AES is shown in Fig.5.20. The beamlets correspond to B7 (top), B6 (central) and B5 (bottom) referring to the labels in Fig.5.1. These data refer to 4x45 kW of radio-frequency power, 1.05 kA of filter current (SF), ISBI=110 A, ISBP=140 A and 0.4 Pa of source pressure (H beam). In these measurements, both the acceleration and the extraction voltages are varied, by keeping their ratio constant and equal to 9.5.
The results obtained by the two diagnostics are similar: the bottom beamlet (yellow) is the one with the lowest width and divergence, then the central and the top one is the widest. Also the extraction voltage at which the minimum is measured agrees, towards larger value for the beamlet with the lower divergence. The divergence measured by the AES, after reaching the minimum, increases by raising furthermore the extraction voltage since, after reaching the perveance-match, the accelerator is moving to the over-perveance region. This worsening of the beamlet divergence is observed by the visible camera only for the beamlet at the top. This could be related to the superimposition of beamlet tails observed by the cameras, as it can be seen in the experimental 1D profile at the bottom of Fig.5.20, which may make difficult to distinguish the single beamlet

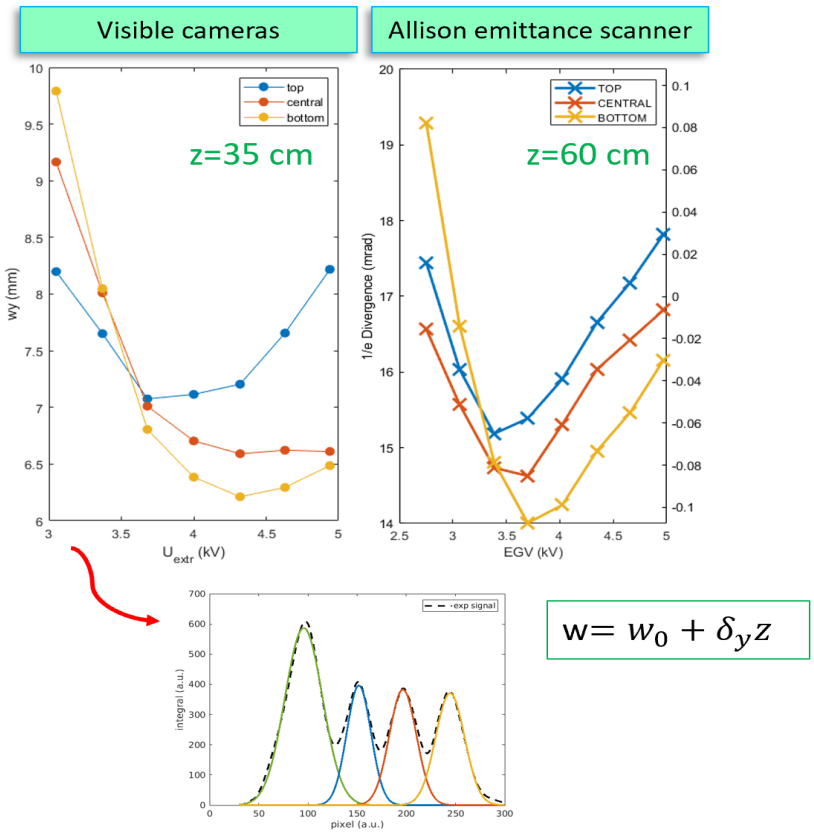

Figure 5.20: *Comparison between the beamlets width measured by visible cameras (on the left) and by AES (on the right); on bottom, an example of the 1D beamlets profile seen by the camera (B7=top, B6=central and B5=bottom, referring to the labels in Fig. 5.1). [4×45 kW of radio-frequency power, 0.4 Pa, H, ISBI=190 A, ISBP=140 A, I_{filter}=1.05 kA, R=9.5, T_{PG} =80°]*

when their optics becomes too bad. On the other hand, it was found that the right hand side of the AES divergence plot exhibits a less steep increase when Gaussian fit of the angular distribution is applied, instead of obtaining it from RMS calculation of the whole acquisition (i.e. a very low current of very large-angle ions causes the rapid divergence increase on the high-voltage side). On the overall, these results confirm the capability of visible cameras in estimating the beamlet divergence even for three adjacent beamlets. The relation which links the beamlet width and the divergence, also reported in Fig.5.20, allows to estimate a minimum beamlet divergence measured by the cameras of 9 mrad, which is lower than the one measured by the AES. The error associated to the divergence calculated by visible cameras, as already discussed, comprises not only the uncertainty on pixel to mm calibration, but also on the exact position along the beam propagation direction where the cameras are looking at and on the initial width of the

beamlets (guess on $w(z = 0)$ in Eq.5.1). The resolution in the estimate of the divergence of the AES is in the order of half mrad, being 0.2 mm the slit width.

5.2 SPIDER beam divergence in volume operation

In the previous section, SPIDER beam optics has been studied for surface operation. Here, volume operations are considered, for both configurations with 80 and 28 open beamlets. The self-correction of equivalent perveance described in Section 5.1.1 is not applied here.

5.2.1 Case 1: 80 beamlets

In the configuration with 80 open beamlets, it is not possible to distinguish the single beamlet from integrate signals measured by visible cameras. However, beamlets seen

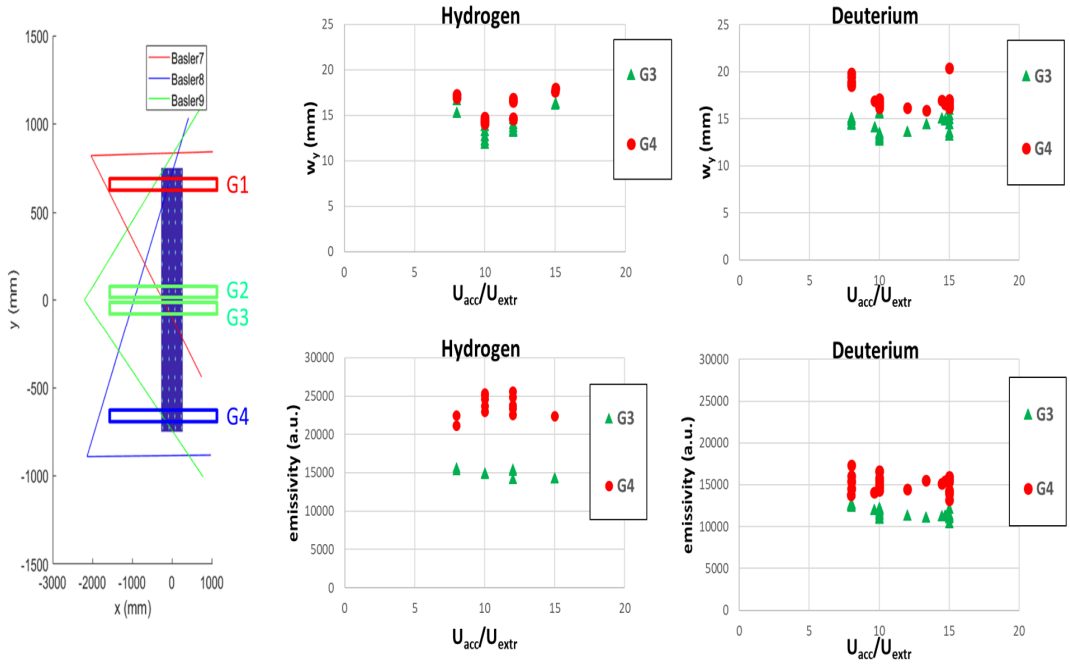

Figure 5.21: *On the left, representation of the beamlet rows fitted by different cameras, indicated by various colours. On the right, the beamlet width (on top) and emissivity (on bottom) for two beamlet rows (in green for the G3, in red for the G4), both in H and D beams, as a function of the acceleration-to-extraction voltages ratio. [3×100 kW of radio-frequency power, 0.36 Pa, H, ISBI=140 A, ISBP=110 A, I_{filter}=1.8 kA]*

with a small angle of view by the cameras produce a single peak, composed by the

sum of the light emitted by the 4 beamlets belonging to the 4 different columns and same row, which are well aligned from the camera point of view (see Fig.5.21, left-hand picture). For this reason, they can be fitted as one-dimensional Gaussian and its width is representative of single beamlet width itself; at most, a small overestimation of the beamlets width due to the eventual non-optimal superimposition of beamlets belonging to the same row has to be considered. The error associated with the different distances of the 4 beamlets belonging to the same row can be neglected (few percentage), since the distance of cameras is much larger than the size of beamlets. As the angle of view increases, the beamlets belonging to different columns start to superimpose each other and the peaks are not clearly distinguishable any more. In Fig.5.21, on the left, the beamlet rows seen with the smallest angle of view by the three cameras Basler7 (port 02), Basler9 (port 01) and Basler8 (port 15) are highlighted. One row per each beamlet group is selected, to study any difference along the beam vertical profile. In Fig.5.21, on the right, beamlets width (on the top) and emissivity (on the bottom), as a function of the acceleration-to-extraction voltages ratio, for a H and D beam are shown. The different colours represent various beamlet rows: the one belonging to G3 in green, to G4 in red. These data refer to 3x100 kW of radio-frequency power per generator, 1.8 kA of filter field current, ISBI=140 A, ISBP=110 A and 0.36 Pa of source pressure (hydrogen). The radio-frequency generator powering G2 was off, for this reason only beamlets belonging to G3 and G4 are shown. By comparing the H and D beams, a different optimum of the beamlet optics is found: for H beam, the minimum corresponds to $R = U_{acc}/U_{extr} = 10$ with $w = 12\ mm$, i.e. 22 mrad of beamlet divergence; this minimum coincides to the maximum extracted current, as shown by the emissivity (bottom panel). For D beam, instead, the minimum of divergence is not clear, towards higher values of R with respect to the H beam and higher (lower beam emissivity, bottom panel). The isotope effect on both beamlets width and current density is the same observed in surface operation (Sect. 5.1.4). By comparing beamlets width, the effect of caesium evaporation in the increment of beamlet current density and thus in reducing beamlet divergence is clear: in volume operation the optimum is ∼22 mrad, with respect to the ∼ 10-12 mrad in Cs operation.

As already discussed in Cs operation results, the beamlet width depends both on the acceleration-to-extraction voltages ratio, and on source properties (plasma density). In Fig.5.22, the beamlet width of the first two rows of beamlets of G1, for three values of filter field, as a function of the $R = U_{acc}/U_{extr}$ is shown. The minimum of divergence corresponds to the lower filter field current (green markers) and to a voltage ratio $R = U_{acc}/U_{extr} \sim 15$. As the filter current is increased, the minimum is shifted towards lower values of R and it is larger, from 12 mm for 1.5 kA to 15 mm for 3 kA of filter field current, which correspond respectively to 22 mrad and 30 mrad of divergence. This dependence on the filter field is related to the different current density of the beamlets, along with the reduction of co-extracted electrons which, in volume operation affect the space charge of the beamlets. These two effects cause a change in the shape of the meniscus, and thus a different optimal voltage ratio for optics optimization.

The beamlet divergence measured through visible cameras is compared with the same

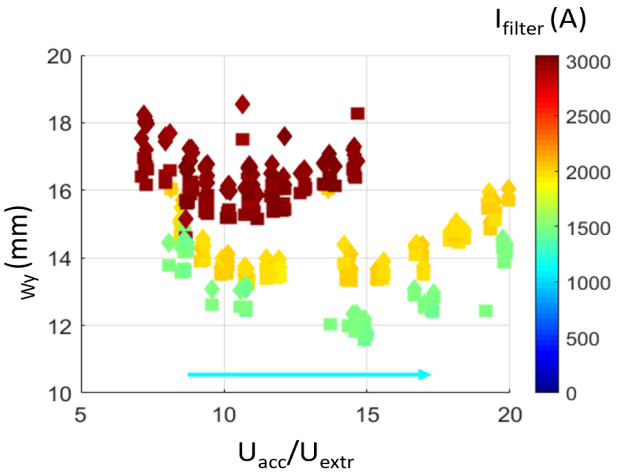

Figure 5.22: *Beamlet width as a function of the acceleration-to-extraction voltages ratio, for different values of filter field. [3×100 kW of radio-frequency power, 0.36 Pa, H, ISBI=140 A, ISBP=110 A]*

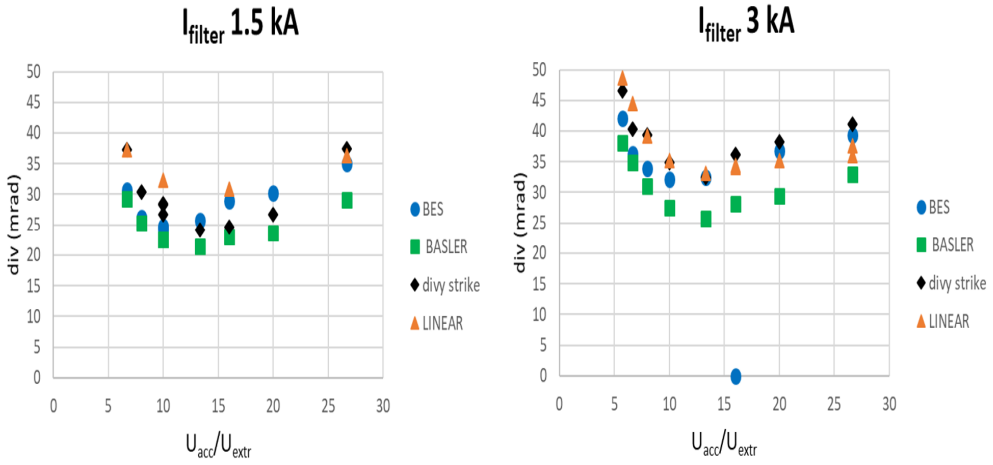

Figure 5.23: *Beamlet divergence estimated by various diagnostics as a function of the $R = U_{acc}/U_{extr}$, for two values of filter field current. [3×100 kW of radio-frequency power, 0.36 Pa, H, ISBI=140 A, ISBP=110 A, I_{filter}=1.8 kA]*

estimate obtained by different diagnostics: its evolution, as a function of $R = U_{acc}/U_{extr}$ for two filter field values (1.5 kA on the left, 3 kA on the right), is shown in Fig.5.23. The different signs represent the divergence measured by the various diagnostics: Beam Emission Spectroscopy (BES), "BASLER" is the divergence estimated from the width measured by visible cameras, "divy strike" the one estimated by STRIKE calorimeter and "LINEAR" is the divergence measured by a 1D visible camera installed on SPIDER

at the beginning of experiments. For all diagnostics, as the filter field increases, the divergence becomes larger and the minimum corresponds to a lower value of R. Both absolute values and the dependence on R of the divergence estimated by the 4 diagnostics, three spectroscopic and one calorimetric, are in good agreement.
The effect of the filter field on beamlet divergence in volume operation is discussed in detail in the next section, where the behaviour of single extracted beamlet in the 28-beamlets open configuration is studied.

5.2.2 Case 2: 28 beamlets. Filter field effect

In volume operation, the space charge of co-extracted electrons plays a role comparable to that of negative ions in the onset of the meniscus shape. In SPIDER, the electron-to-ion ratio is between 20 and 10, respectively for low (0.75 kA) and high (1.8 kA) filter field. When the filter field is varied, the beam optics is modified both because the current density of the beamlets changes and because the contribution to the perveance at the meniscus of co-extracted electrons is modified. In addition, the filter field induces a vertical drift of the plasma, as well as a vertical shift on the position of the beamlets. In Fig.5.24, the width (on top) and emissivity (on bottom) of the central beamlets of each beamlet group, as a function of the filter field current, are shown; on the left, measurements with the standard direction of the filter field (SF), on the right the ones with reversed direction (RF). The other machine parameters are 4×100 kW of radio-frequency power, 0.36 Pa source pressure (hydrogen), ISBI=100 A, ISBP=80 A and 2.4 and 24 kV of extraction and acceleration voltages. Depending on beamlets position along the vertical beam profile and on the current they bring, the beamlet width evolves in a different way both as the filter field is increased and as its direction is reversed. In the SF configuration, all widths are similar for low filter and then they differ when it is increased; the opposite in the RF. Concerning beamlets emissivity, it is larger for all of them in the RF configuration, except for B1 (G1). In the SF configuration, the beamlet width has a minimum when the emissivity is largest, which is between 1-1.2 kA for B9 (G2), B6 (G3) and B22 (G4). The width of B1 (G1) instead, decreases continuously as the filter field grows. The optimum of beam optics corresponds to $w = 7 - 8\ mm$. This value is lower than that measured with 80 open beamlets (see previous section), because the reduced number of beamlets allows the cameras to measure the width of the single beamlets. The widest beamlet is the one at the bottom of the beam profile (B22), whose optics worsen as the filter field grows. When the filter field is inverted, the width of B1 and B9 remains almost unchanged, as does their emissivity. Their emissivity slightly decreases with the filter field, as their width increases. B16 and B22, instead, have an optimum for the largest value of filter field, and they are wider compared to the widths of the other two beamlets. Their emissivity is also higher than both B1 and B9, and than that of the SF configuration. The filter field, therefore, acts differently for the various central beamlets, depending on its direction.
In Fig.5.25, the behaviour of external beamlets of each beamlet group are shown. The effect of filter field strength and direction on external beamlets is different from that on central beamlets. The main difference is between the top beamlet (B2) and the bottom

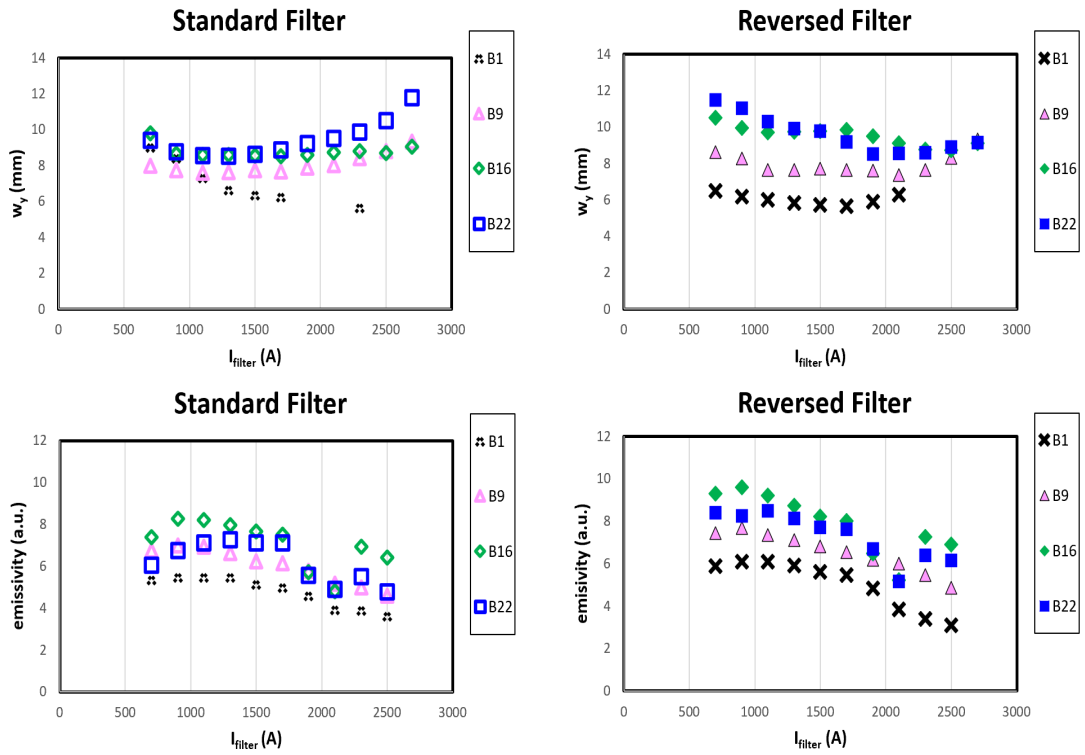

Figure 5.24: *Vertical width (on top) and emissivity (on bottom) of the central beamlets of each group, measured by visible cameras, as a function of the filter current. On the left, measurements in SF configuration, on the right ones in RF configuration. [4×100 kW of radio-frequency power, 0.36 Pa, H, ISBI=100 A, ISBP=80 A, U_{extr}=2.4 kV, U_{acc}=24 kV]*

one (B21) of the entire beam vertical profile. In the standard direction, B21 has the greatest width and its emissivity is the lowest. In RF, on the other hand, B2 is too wide to fit and its emissivity is the lowest. Moreover, in the SF configuration the width of B2 remains unchanged when the filter field varies, the same as the width of B21 in the reverse direction. An inversion of the behaviour of these two extreme beamlets is therefore evident. B8 and B15, on the other hand, behave the same in the two configurations: their width increases, while their emissivity decreases.
The different behaviour of central and external beamlets of each beamlet group, as well as the inversion of beamlet properties at the top and at the bottom of the beam profile when the filter field direction is reversed, highlight the different effect of the filter field along the beam vertical profile. From the one dimensional analysis of beam profiles, it is also possible to estimate the vertical shift of beamlet positions. In Fig.5.26, *delta* y_0 represents the relative displacement of the beamlet vertical position with respect to the average one, for the three beamlets of G2 (on top) and of G3 (on bottom), as a func-

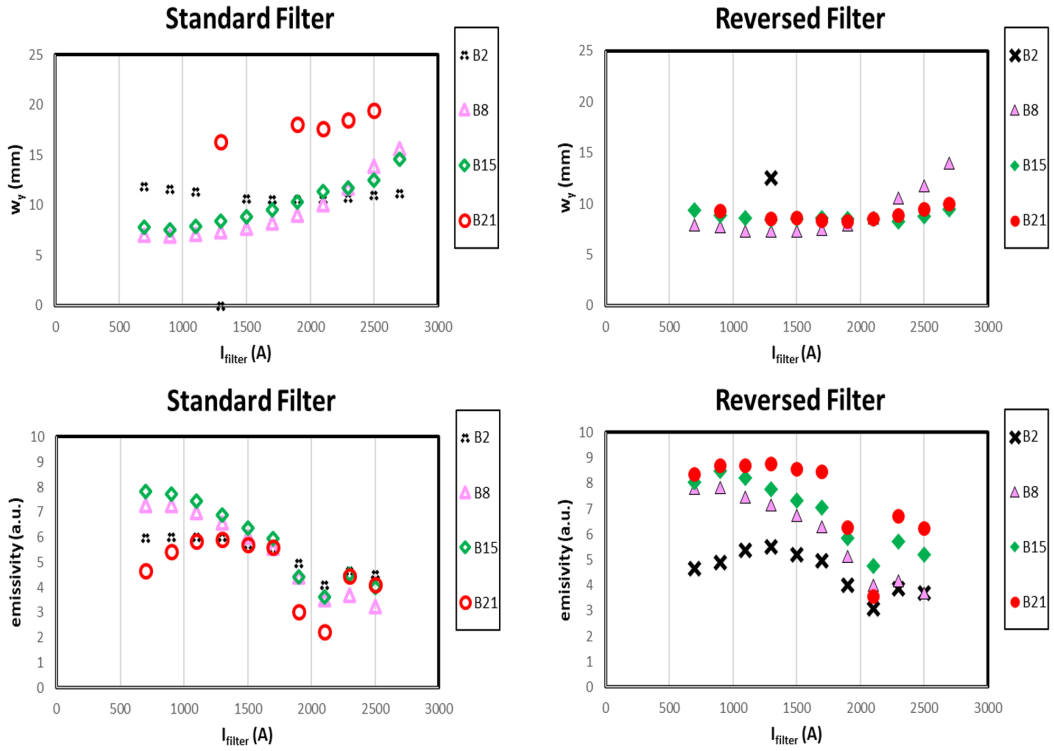

Figure 5.25: *Vertical width (on top) and emissivity (on bottom) of external beamlets of each group, measured by visible cameras as a function of the filter current. On the left, measurements in the standard (SF) configuration, on the right ones in the reverse (RF) configuration. [4×100 kW of radio-frequency power, 0.36 Pa, H, ISBI=100 A, ISBP=80 A, U_{extr}=2.4 kV, U_{acc}=24 kV]*

tion of the filter field current (on the right is the standard configuration, on the left the reverse one). The vertical deflection depends on both the beamlet space charge, which changes as the filter field increases, and the residual magnetic deflection due to the current flowing in the PG. The beam deflection is opposite to that of the plasma, since the direction of the filter magnetic field on either side of the PG is reversed. The non-homogeneity of beamlets belonging to the same beamlet group is most evident here. In the G2-SF, the two external beamlets are deflected in opposite directions as the filter increases, while the vertical position of the central beamlet remains the same. In the RF, instead, they are all deflected in the same direction, which is downwards, as the filter current is larger than 1.5 kA. A similar behaviour is measured in the G3-RF, even if the filter value at which the beamlets start to be deflected in the same direction is different for the three beamlets. In SF, instead, the deflection is less pronounced for all the beamlets.

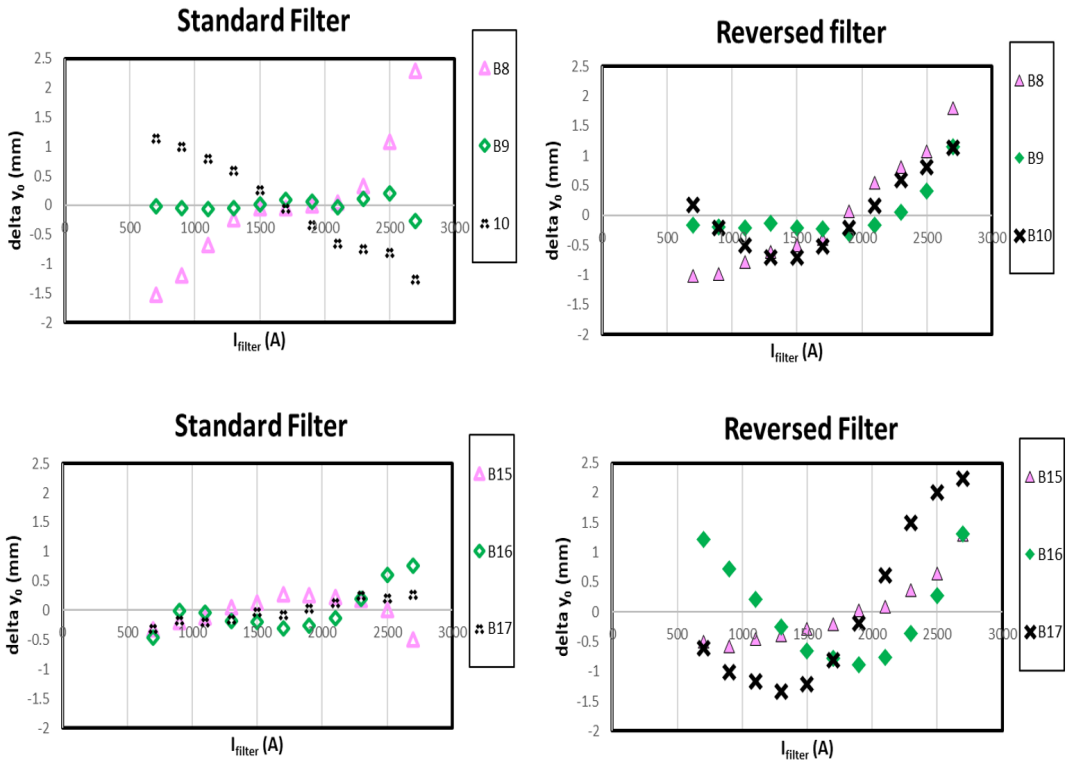

Figure 5.26: *Vertical displacement of beamlet positions, defined as the difference between beamlet position and the average position, for the three beamlets of the G2 (on top) and G3 (on bottom), as a function of the filter field current; on the left the SF configuration, on the right the RF one. [4×100 kW of radio-frequency power, 0.36 Pa, H, ISBI=100 A, ISBP=80 A, U_{extr}=2.4 kV, U_{acc}=24 kV]*

5.3 Comparison with the beamlet divergence measured in other machines: BUG and NIO1

In this thesis work, beamlet divergence is studied also in two different radio-frequency sources: Batman Upgrade (BUG) at IPP Garching and NIO1 at Consorzio RFX (both described in Sect.1.5).
From the BATMAN Upgrade (BUG) ion source, 70 beamlets of H^-/D^- ions are accelerated up to 50 keV by an electrostatic accelerator with an ITER-like grid system [34]. Beam divergence is usually measured through Beam Emission Spectroscopy (BES). BUG features two arrays of lines-of-sight (LoS), which intercept the beam at 0.2 m and at 1.3 m from the Grounded Grid (GG). The beam is usually dumped onto a copper calorimeter (about 2 m downstream the GG). During a dedicated experimental campaign, the beam is stopped by the mini-STRIKE diagnostic calorimeter [94], mounted at 1.34 m from the GG. The divergence measured by these two diagnostics is compared. In order

to measure the divergence of one isolated beamlet, as done in SPIDER, 24 of the 70 apertures of the PG were masked and the single beamlet was expected to be collected by the Carbon-fiber-Composite (CFC) tile. An example of the experimental infra-red (IR) measurement of the heat load on the CFC tile, seen by a thermo-camera, is shown in Fig.5.27, together with the 1D profiles through the beamlet centre; the vertical lines highlight the portion of data used for the fitting. The Gaussian footprint of the isolated beamlet is well distinguishable on the CFC tile, and from its shape the vertical and horizontal width of the beamlet is estimated.

The aim of this campaign was to demonstrate the over-estimation of beamlet diver-

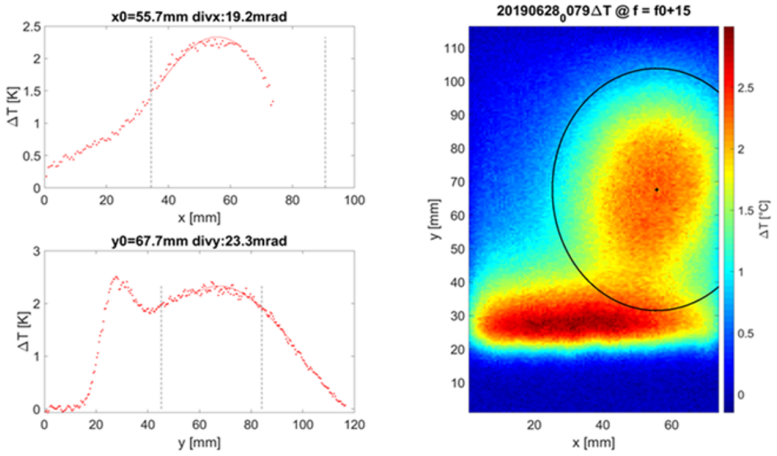

Figure 5.27: *On the left, the 1D profiles along the beamlet centre; on the right, the IR image of the temperature increase on the CFC tile 0.6 seconds after the beam starts, on BUG.*

gence measured by the BES when all beamlets apertures are left open. The BES LoS which intercepts the isolated beamlet gives an estimation which agrees perfectly with the CFC calorimeter measurements. An example of an acceleration scan, performed with $U_{extr} = 3.7\ kV$, 0.6 Pa of source pressure (H beam, with Cs evaporation) and 88.93 A/m^2 of negative ion beam current density is reported in Fig.5.28 (on the left). The agreement between the two diagnostics (MiniStrike and single beamlet BES, BES13) is almost perfect; even if the diagnostics derive divergence from different quantities (heat flux and light emission) they provide the same values. Beamlet divergence measured by the BES LoSs which intercept more than one beamlet (the beam bulk, BES9 and BES7), instead, overestimate the measurement, due to superimpositions of many beamlets and to their residual magnetic deflection. The optimum of beam optics is 12 mrad and $R = U_{acc}/U_{extr}$=8. The minimum divergence at 0.3 Pa in surface operation was measured to be 14 mrad, which is similar to the one measured on SPIDER, as shown before.

The beamlet divergence is measured also on the negative ion source NIO1, by both BES

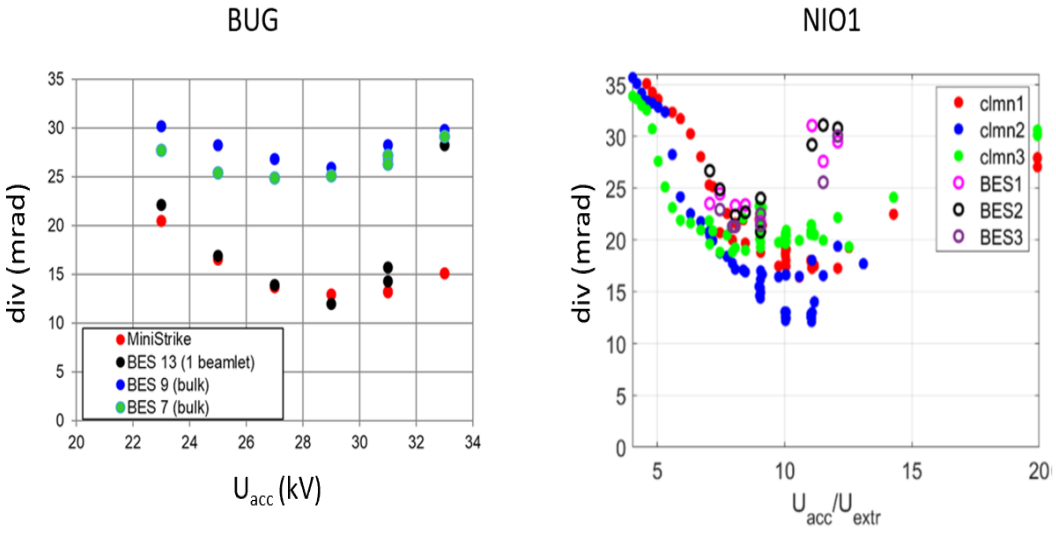

Figure 5.28: *On the left, acceleration scan performed at BUG. The beamlet divergence measured by miniSTRIKE calorimeter and BES is compared. On the right, beamlet divergence measured in NIO1 by visible cameras and BES as a function of the* $R = U_{acc}/U_{extr}$. *In both experiments, the minimum of beam divergence is found to be around 12 mrad.*

and visible cameras; the technique used to estimate the beamlet divergence with visible cameras is described in Sect.4.5.1. In Fig.5.28 on the right, beamlet divergence measured in NIO1 by both the diagnostics, as a function of the $R = U_{acc}/U_{extr}$, is shown; the solid points represent the divergence of the three columns of beamlet estimated by visible cameras (referred as clnm1, clmn2 and clmn3), open points represent the divergences measured by the three LoSs of BES (BES1-2-3). The optimum value for both divergences obtained with the two diagnostics corresponds to a ratio $R = 9.5 - 10$, with a divergence between 12 and 20 mrad; the minimum refers to $U_{acc} = 6.5\ kV$ and $U_{extr} = 0.6 - 0.65\ kV$. The three beamlet columns observed by the bottom camera exhibit a similar behaviour, as expected. The BES (open points) confirms these results, both the relation between beam divergence and R and the absolute values. The difference observed at larger values of R can be due to an overestimation of the BES measurements: when the optics gets worse, different rows of beamlets may superimpose or shift in the space, broadening the Doppler signal seen by each optical head. In Fig.5.29, the divergence of the isolated beamlet on BUG measured by miniSTRIKE calorimeter and BES as a function both of the radio-frequency power (on the left) and source pressure (on the right) is shown. As measured on SPIDER and shown in Fig.5.16 and in Fig.5.7, respectively, the beam optics improves when both the radio-frequency power and the source pressure are increased. A similar behaviour is measured also in NIO1. The divergence of beamlet columns estimated by visible cameras as a function of the source pressure is shown in Fig.5.30 (on

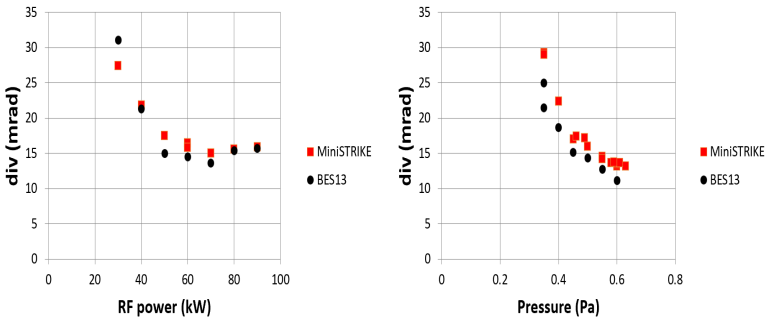

Figure 5.29: *Single beamlet divergence measured on BUG by miniSTRIKE calorimeter and BES as a function of the radio-frequency power (on the left) and of the source pressure (on the right).*

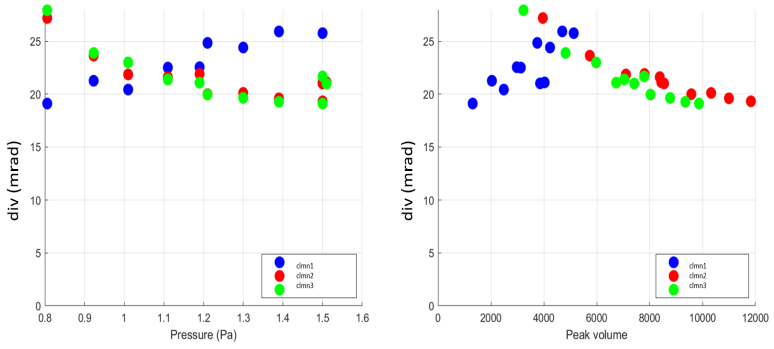

Figure 5.30: *Beamlets divergence measured by visible camera of the three columns of NIO1 beam as a function of the source pressure (on the left) and relation between the beamlet divergence and their volume (on the right).*

the left). These data refer to 1.2 kW of radio-frequency power, 0.8 and 7 kV of extraction and acceleration voltages and 0.3 A of bias plate current polarization, I_{bb}. The divergence of column 2 and 3 decreases as the source pressure grows. In correspondence, their emissivity enlarges, as shown in the right panel, where the beamlet divergence as a function of the column volume is reported (i.e. beamlet emissivity). Both the divergence and integral of the first column of beamlets, instead, have a peculiar behaviour. The beamlet divergence increases with the source pressure while its volume is the lowest with respect to the other two columns. The behaviour of first column of beamlets can be explained studying the effect of bias plate polarization. The experimental 1D profiles measured by the bottom camera (top row, on the left) and by the lateral camera (top row, on the right) as a function of the bias plate polarization current (I_{bb}) are shown in Fig.5.31; on the bottom, beamlet columns divergence (on the left) and its dependence

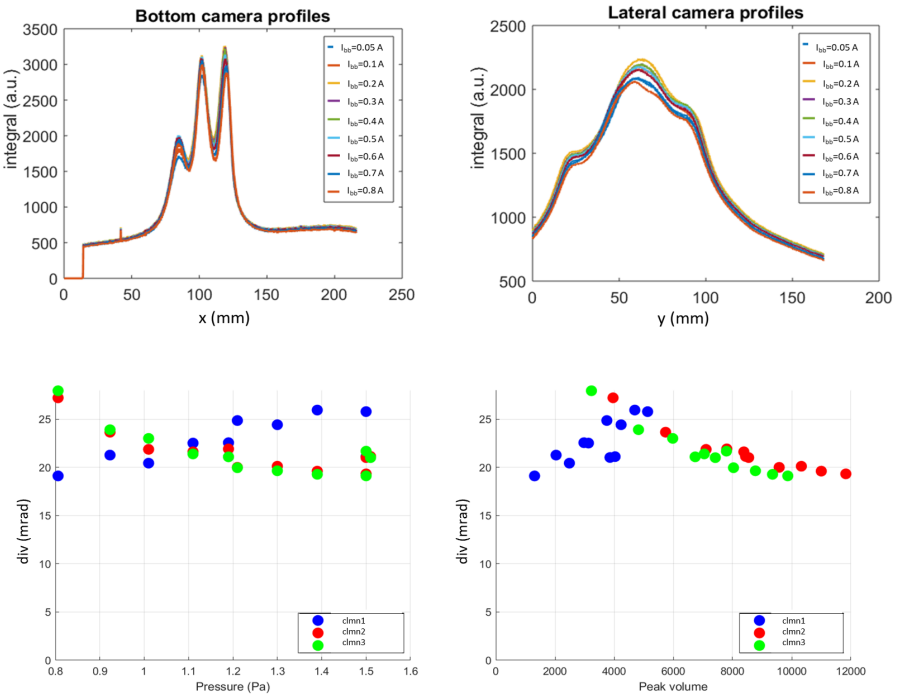

Figure 5.31: *On the top, experimental 1D profiles measured by the bottom camera (on the left) and by the lateral camera (on the right) for different BP polarization currents. On the bottom, the beamlet columns divergence as a function of the BP polarization current (on the left) and its dependence on the columns volume (on the right).*

on the beamlets column volume, as a function of the bias plate polarization current are shown. The divergence of the central beamlet slightly diminishes with the bias current, the opposite for the column 3; for both columns, the emissivity decreases (referred as peak volume in the second panel). The divergence of column of beamlets 1, instead, decreases as the BP polarization current grows and, in correspondence, its volume is slightly reduced. This behaviour can be explained by the impact of the beamlet column on the bias plate, which can be deflected the more the polarization current grows.

5.4 Negative ion temperature role in the beamlet divergence

In all results discussed in the previous sections, the optimum of beam divergence obtained in the three different radio-frequency negative ion sources is around 12 mrad. This value is still larger than the maximum divergence required for ITER NBIs. Many open questions are still without answer about these experimental results. According to numerical simulations, in fact, the expected divergence at the experimental conditions

explored should be lower than the one measured experimentally [29]. In particular, the match with the experimental data is much better in the case of arc sources than in the case of radio-frequency sources: models tend to under-estimate the divergence in the case of radio-frequency sources. The optimum of the divergence measured in arc sources, in fact, is lower than 7 mrad, which is the upper limit of the tolerable beamlet divergence for ITER NBIs [95] [96]. Since a good agreement was found between the numerical simulations and experimental measurements in arc sources, even without taking into account the initial velocity distribution of negative ions, this parameter was not included when the design of SPIDER was defined. However, the temperature of negative ions influences the divergence of the single beamlet. When this effect is included in the codes (IBsimu [97], OPERA [98]) the agreement simulation-experimental measurements improves. The characteristics phenomena of the radio-frequency sources that might affect the transverse energy of extracted negative ions, which are not present in arc sources, are the different plasma potential profile inside radio-frequency sources and the oscillation of the radio-frequency potential.
In the arc sources, the plasma potential Φ is 2-3 V [99]. In radio-frequency sources, instead, is larger than 20 V but, close to the extraction region, it is reduced to few V polarizing the Plasma Grid (PG); experimental measurements of the plasma potential profile from the driver to the PG are shown in chapter 6. In both types of sources, thus, the $\Delta\Phi$ close to the PG is small. However, the major difference between the two types of source is that in arc source the plasma potential is uniform inside the entire source while in the radio-frequency it is not. The larger plasma potential difference (20-30 V) between the driver and the expansion region, measured in the radio-frequency source, is responsible of the acceleration of positive ions. These accelerated ions may transfer their energy to H atoms in the expansion chamber or directly generate fast negative ions at the converter surface. These high energy negative ions may be directly extracted or may exchange charge and momentum with neutrals, as they move towards the PG. In both cases, this results in a higher negative ion temperature, with respect to the arc sources. The influence of the proton energy on the beam divergence is experimentally confirmed by the reduction of the beamlet divergence as the pressure is increased, as shown in Fig. 5.16 on SPIDER, in Fig. 5.29 on BUG and in Fig. 5.30 on NIO1.
To study the positive and negative ions energy distribution, dedicated campaigns are carried out at NIFS (arc source) and on SPIDER (radio-frequency source), using Retarding Field Energy Analyzer diagnostics. In particular, at NIFS, a newly developed Negative Ion NI-RFEA is installed at the upstream surface of the PG, and used to characterize the plasma source with and without caesium, providing a direct estimation of the negative ion energy distribution. Depending on the origin of the negative ion (volume or surface production) and on the processes it underwent before reaching the aperture of the plasma electrode, the energy distribution should be different. In volume, in fact, the ions are distributed around the plasma potential and their energy distribution is spread through charge exchange or Coulomb collisions; the ions produced on the PG surface, instead, are directly extracted and their energy is around the converter potential. The combined effect of these processes on the ion energy distribution is shown in Fig.5.32,

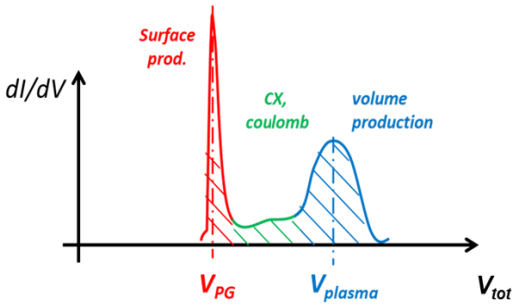

Figure 5.32: *Schematic representation of the negative ion energies at the meniscus, as a function of their origin and of the relevance of the processes responsible of the negative ion transport towards the meniscus itself.*

which represents a schematic energy distribution as a function of the retarding voltage applied to the NI-RFEA (detailed description of the diagnostics in Sect.3.1.3). To properly study the energy distribution of the extracted negative ions, the shape of the plasma facing orifice of the RFEA is designed so as to reproduce the upstream aperture of the PG. Since the RFEA is capable to discriminate only the axial component of the kinetic energy, the dependence on the meniscus shape of the axial energy distribution is measured. The axial energy distribution of extracted negative ions, in fact, depends on the contribution from radial electric fields, i.e. it represents the curvature of the meniscus. The simulated meniscus shape and the expected distribution of the axial energy of negative ions measured by the RFEA is shown in Fig.5.33 [100]; the depth of the meniscus will change the distribution of the measured energy spectra, up to few eV. The measurements of the negative ion energy distribution function (IEDF) through the RFEA can thus provide the perveance; any anomalies in the IEDF, furthermore, can be related to the second-order deformation of the meniscus shape. In the next sections the measurements of positive and negative ion energy distributions obtained by RFEAs in NIFS and SPIDER are discussed, highlighting the difference between the two types of sources.

5.4.1 Ions energy distribution in arc source

To study the energy distribution of negative ions, the polarization of the first grid of the NI-RFEA is varied, which corresponds to a modification of the extraction voltage; the experimental measurements with Cs evaporation are shown in Fig.5.34 a). On the top, the total current measured by the collector (the last grid of the NI-RFEA, which collects negative ions only) as a function of the retarding voltage is shown; different colours refer to various first grid polarizations. When the retarding voltage is negative, no current is measured on the collector, since the diagnostic is designed to repel positive ions to get the

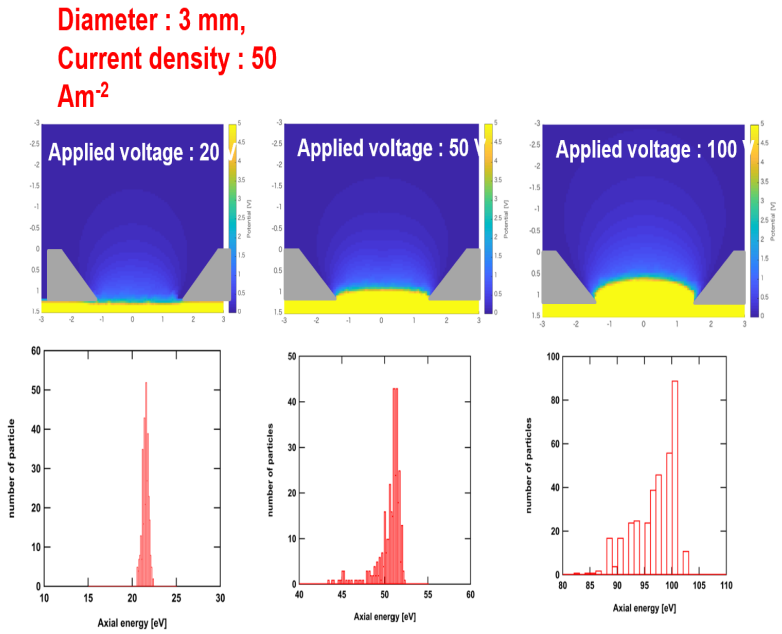

Figure 5.33: *On top, the simulated (OPERA) meniscus shape as a function of the applied first grid voltage; on bottom, the expected negative ions energy distributions.*

collector grid. As the retarding voltage approaches positive values, a current starts to be measured, up to the largest values of the retarding voltage, for which the current collected saturates. This confirms the fact that the probe is measuring negative ions and not electrons. The current measured depends on the first grid polarization V_{G1}: the higher first grid bias, the larger total current collected. The derivative of this V-I characteristic, shown at the bottom of Fig.5.34 a), represents the negative ion velocity distribution. The peak of the derivative, corresponding to the inflection point of the original curve, gives an estimation of the plasma potential with respect to the reference (the plasma grid voltage), while its width is linked with the temperature of incoming particles (and the intensity of magnetic field inside the detector). As the polarization voltage increases, the width of the distribution becomes wider. Its FWHM ranges from 5 to 11 V, while the peak position is fixed between 0 and 1 V, thus confirming that most of negative ions are produced at the PG potential (surface production). The change in shape of the negative ion velocity distribution as a function of the V_{G1} experimentally measured, is also confirmed by SLACCAD simulations, shown in Fig.5.34 b). The modification of the IEDF shape with the first grid voltage is related to the variation of the meniscus shape.

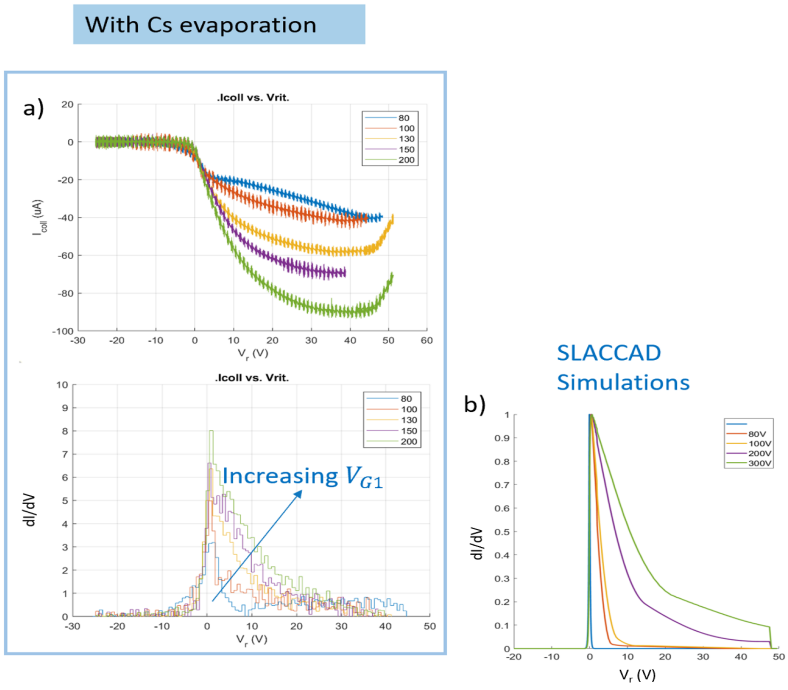

Figure 5.34: *a) Experimental NI-RFEA V-I characteristics for various first grid polarization voltages; on bottom, the ion velocity distribution. b) simulated (SLACCAD) ion velocity distribution.*

Positive and negative ions energy distribution as a function of the Plasma Grid polarization

As explained, the energy of ions close to the extraction region depends on the polarization of the Plasma Grid (PG), i.e. on the potential difference between the region in which they are generated (defined by the plasma potential) and the acceleration they gain as the PG is polarized. To study this effect, the velocity distribution of both positive and negative ions, respectively with PI-RFEA and with NI-RFEA, is studied. In Fig.5.35 a), the derivative of the current measured by the PI-RFEA collector with respect to the retarding voltage applied, when the polarization of the PG, V_{PG}, is varied, is shown; these data are obtained without Cs evaporation. The FWHM of the velocity distribution is almost constant and equal to 2 V while the peak positions move accordingly with the PG polarization. This is reported in Fig.5.35 b), which shows that the peak of positive ions velocity distribution moves towards lower values for positive values of V_{PG}; for negative values of V_{PG}, instead, it moves towards larger values (up to 9 V). In Fig.5.35 c) the positive ion saturation current density measured by the PI-RFEA is shown. For positive values of V_{PG} it decreases as the polarization grows; for negative V_{PG}, instead, it remains almost constant. This behaviour could be explained by considering that

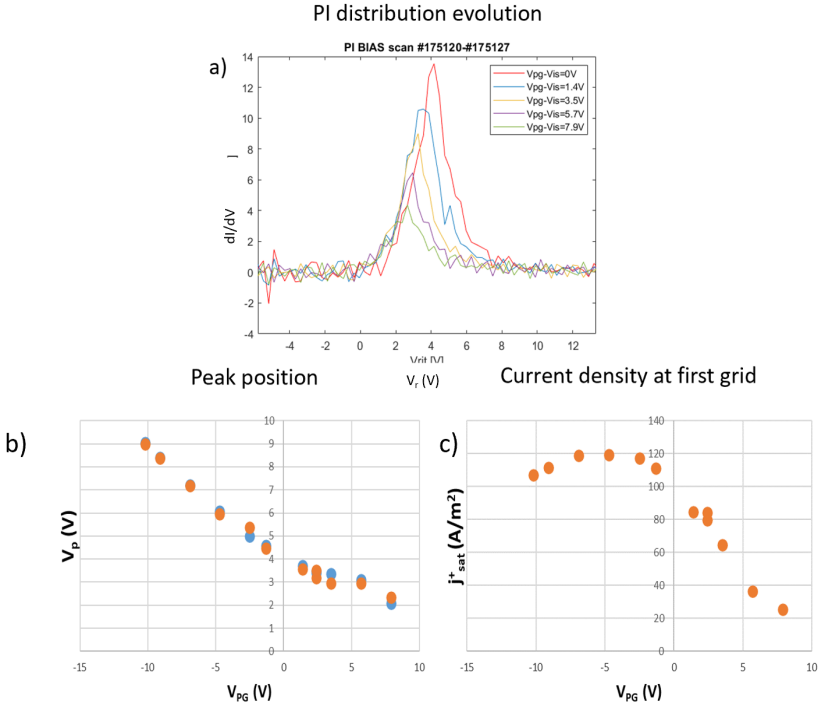

Figure 5.35: *a) Derivative of the positive ion current measured by the PI-RFEA with respect to the retarding potential, for various V_{PG}; b) peak of the distribution position as a function of the V_{PG}; c) positive ion saturation current density as a function of V_{PG}, at NIFS laboratory.*

positive values of V_{PG} cut part of the positive ions distribution, resulting in a reduction of the total current measured. These results are confirmed by the LP measurements [63]. The modification of negative ions velocity distribution when the V_{PG} is changed is reported in Fig.5.36. The dependence of negative ions is opposite to that of positive ones: as the V_{PG} grows, the peak of distribution moves towards larger values; furthermore, the shape of distribution is deformed as the potential is increased (black curve). This could be related to the appearance of high energy components or to a larger spreading of the axial energies, following a meniscus deformation. Measurements with negative values of PG polarization are not available, thus all negative ions measured have an energy larger or equal to the plasma potential (asymptote at $V_{RET} - V_{PG}$=0 V). In all measurements carried out at the NIFS arc source, the velocity distribution of negative ions gives a negative ions temperature in the order of 1-2 eV, which is compatible with an ion temperature lower than 0.3 eV, as measured by other diagnostics at NIFS [42] [101].

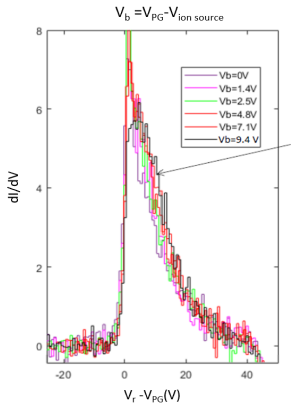

Figure 5.36: *Derivative of the negative ion current measured by the NI-RFEA with respect to the retarding potential, for various V_{PG}.*

5.4.2 Ions energy distribution in radio-frequency source

A large ion energy spread is expected in radio-frequency plasma due to the modulation in the time varying sheath potential. The crucial parameter is the ion transit time across the sheath τ_i and the sheath radio-frequency period τ_{RF} [60]:

$$\tau_i = 3\bar{s}\sqrt{\frac{m_i}{2e\bar{V}_s}}, \tag{5.2}$$

where $\bar{s}$ is the time averaged sheath width, m_i the ion mass and $\bar{V}_s$ the dc sheath voltage drop. When $\frac{\tau_i}{\tau_{RF}} << 1$, ions cross the sheath in a small fraction of the radio-frequency cycle and the final ion energy strongly depends on the phase of the radio-frequency cycle in which they enter the sheath. A broad bimodal distribution is thus obtained, with $\Delta E \sim$ the maximum sheath drop. By assuming a constant sheath width, a uniform sheath electric field, a sinusoidal sheath voltage $V_s(t) = \bar{V}_s + \tilde{V}_s sin(\omega t)$ and zero ion velocity at the plasma-sheath boundary, the resulting expressions for ΔE and ion energy distribution IED are

$$\Delta E = \frac{4e\tilde{V}_s}{\pi}(\frac{\tau_{RF}}{\tau_i}) \tag{5.3}$$

and

$$f(E) = \frac{2n_t}{\omega\Delta E}[1 - \frac{4}{\Delta E^2}(E - e\tilde{V}_s)^2]^{-1/2}, \tag{5.4}$$

where n_t is the number of ions entering the sheath and $\tilde{V}_s$ the amplitude of the radio-frequency component of the sheath voltage. The result of the calculation is a bimodal distribution centred at $e\tilde{V}_s$, with a peak separation ΔE proportional to τ_{RF}/τ_i.
On SPIDER, two PI-RFEAs were used during the campaign dedicated to the movable probes to study the axial energy distribution of positive ions. Due to the phenomena just described, characteristics of a radio-frequency source, the IEDF is expected to be wider

with respect to the one measured in the NIFS arc source. Furthermore, the ion energy distribution depends on source parameters such as the pressure and the filter field. The pressure, in fact, determines the number of collisions which positive ions undergo as they travel from the driver to the RFEA (close to the grids), thus modifying the ions energy distribution. The same holds for the increase in the radio-frequency power. The filter field, instead, as it increases the plasma potential inside the drivers (see Chapter 6), augments the difference of potential between the plasma in the drivers and close to the PG, where the RFEA is measuring, resulting in a wider energy distribution. The experimental results of the dI/dV characteristics measured by the PI-RFEA on SPIDER when these parameters are varied are discussed in the following. No measurement of negative ions energy distribution is available in SPIDER, but the energy of negative ions strongly depends on the one of positive ions.

Pressure dependence

In Fig.5.37, the positive ions saturation current (top) and the derivative dI/dV (bottom), as a function of the retarding voltage, for various source pressures are shown. On the left, the voltage applied to polarize the bias plate (V_{BP}) and plasma grid (V_{PG}) was the same and equal to 20 V, on the right was 40 V; in both cases 100 kW of radio-frequency power, 2 kA of filter current. As expected, the first consequence of the increase in source pressure, is a larger positive ion saturation current; when the bias plate (BP) and Plasma Grid (PG) polarizations are lower, also, the total measured current is higher than the case with high polarizations. This effect could be related to the reduction in plasma density in this region when PG and BP biases are increased, as shown by spectroscopic and electrostatic measurements in chapter 6. Furthermore, by increasing these potentials, the difference between the V_p within the drivers and near the PG is reduced, so the acceleration of positive ions towards the PG is as well. The width of the IEDF is reduced as the pressure is increased, as expected: the ions undergo more collisions before to reach the probe, so their energy is reduced. At the same pressure, the IEDF is wider in the case with low bias of PG and BP than in the case with high bias. This could be explained by the increment in the difference between the V_p and the PG potential. In the case with higher pressure and biases, also the bimodal distribution becomes evident, as expected [60].
The reduction of the width of positive ions IEDF with the source pressure may explain the reduction in beam divergence observed in previous sections, in all the radio-frequency sources.

Radio-frequency power dependence

The effect of the increase in the radio-frequency power on positive ions energy distribution is illustrated in Fig.5.38: on top, the positive ion saturation current, on bottom the derivative dI/dV as a function of the retarding potential; on the left the measurements are carried out with $V_{PG} = V_{BP}$=20 V, on the right V_{PG}=36 V, V_{BP}=20 V. All the measurements are made at 10 mm from the PG. As the radio-frequency power augments,

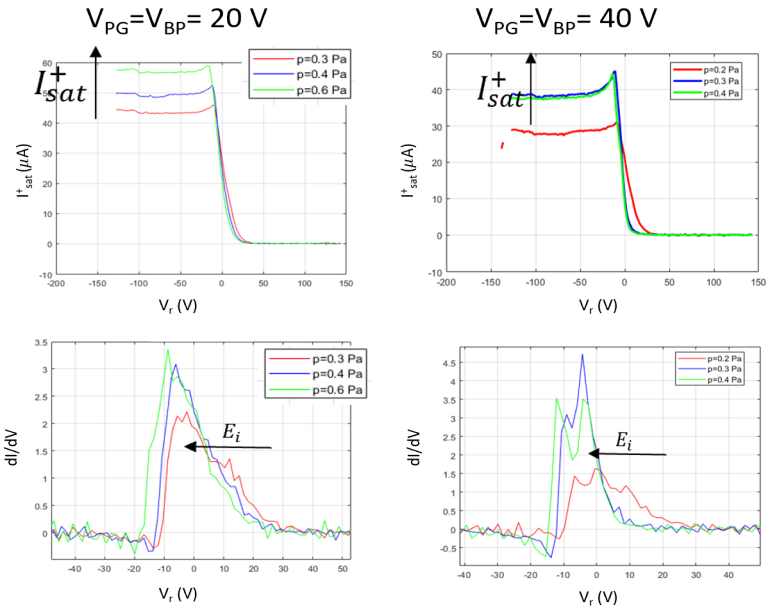

Figure 5.37: *On top, positive ion saturation current, on bottom the derivative dI/dV as a function of the retarding potential, for various source pressures. On the left, the voltage applied to polarize the bias plate and plasma grid was the same and equal to 20 V, on the right was 40 V. The measurements are carried out at 10 mm from the PG, 100 kW of radio-frequency power, 2 kA of filter current.*

the saturation current grows too, as it happens with the source pressure increment. In the case with low biases, a high energy component is evident, which almost disappears when the PG bias is brought to 36 V (closer to the plasma potential in the driver). This affects the IEDFs, which are wider in the case with low biases. They have a bimodal distribution, due to the high energy component of ions reaching the probe, which are accelerated from the driver region to the PG. As radio-frequency power grows, the energy of the ion increases too. All these contributions disappear when the PG potential is higher. While the radio-frequency power modifies the high energy components, the PG bias changes the lowest limit of the distribution (low retarding voltage values), which increases with the bias. These results suggest that, by operating at large radio-frequency power and low biases, the high energy ions component is larger and it may affect the beam divergence.

Filter field dependence

The filter field is responsible of the plasma density and potential increment inside the drivers, as will be discussed in detail in next chapter. This results in a growth of the potential difference between the plasma inside the driver and in the expansion region.

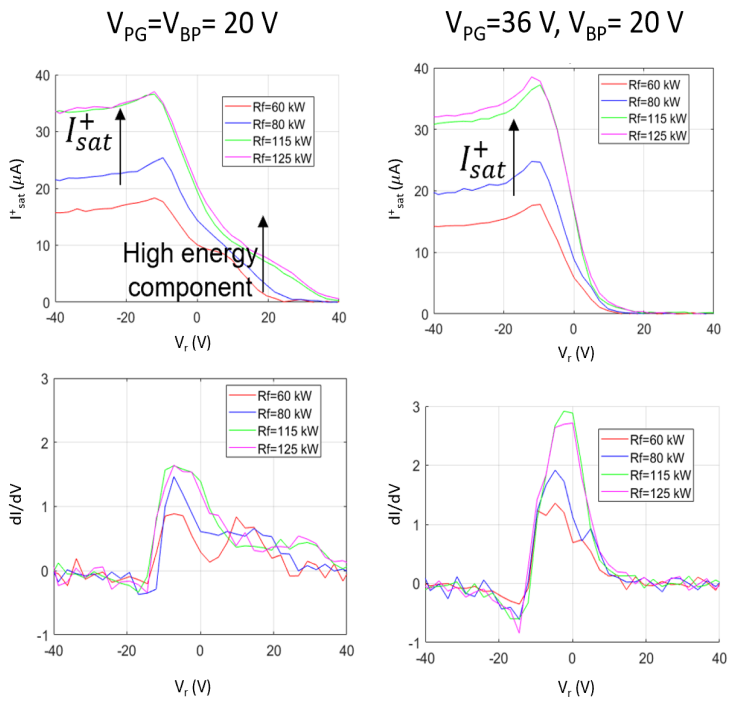

Figure 5.38: *On top, positive ion saturation current, on bottom the derivative dI/dV as a function of the retarding potential, for various radio-frequency power; on the left with $V_{PG} = V_{BP}$=20 V, on the right V_{PG} =36 V, V_{BP}=20 V. The measurements are carried out at 10 mm from the PG, 3 kA of filter current.*

A wider positive ions energy distribution is measured by the PI-RFEA as filter field is increased, as shown in Fig.5.39. At the same time, the positive ions saturation current measured is reduced (top panel Fig.5.39)) and their IEDF becomes wider (bottom panel Fig.5.39). Furthermore, the low energy peak of the distributions moves towards higher values.
Summarizing the results discussed in this section, a wider ion energy distribution in the radio-frequency source than in the arc source is found (20-40 V versus 1-2 V). This could explain the larger beamlet divergence measured in all the radio-frequency sources studied, compared to that measured on the arc source, although further analysis is needed and more phenomena need to be considered. However, both numerical simulations and experimental measurements show a correlation between ion energy distribution and the beam divergence.

5.5 Preliminary studies on the beam halo

In several experiments, the measured heat loads on the acceleration grids is larger of $2-3\%$ and it is not predicted by the existing beam analyses [102]. This unexpected heat

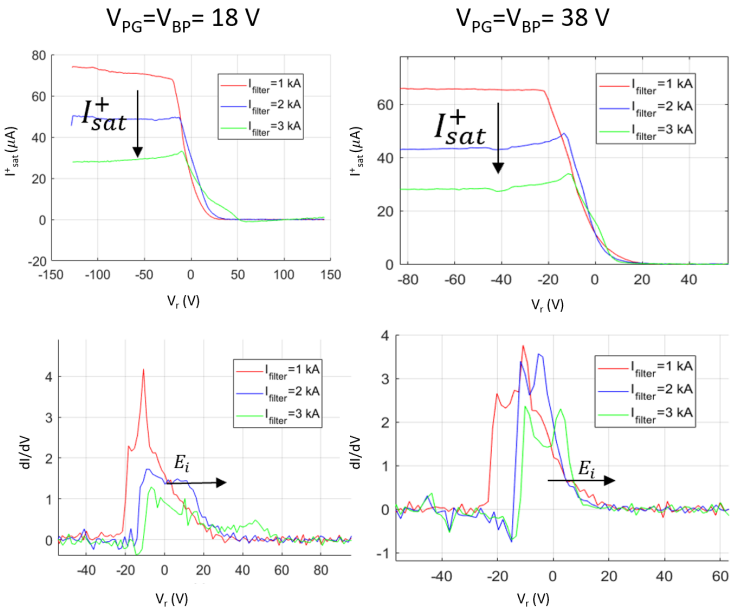

Figure 5.39: *On top, positive ion saturation current, on bottom the derivative dI/dV as a function of the retarding potential, for various filer field currents; on the left with $V_{PG} = V_{BP}$=18 V, on the right $V_{PG} = V_{BP}$=38 V. The measurements are carried out at 30 mm from the PG, 100 kW of radio-frequency power.*

load is one of the essential issues in designing the negative ion beam sources for ITER, because it could be a serious problem on the design of cooling capability of acceleration grids in a case of 1 MeV, 40 A beams. The unexpected heat load was considered to be caused by relatively wide profile in edge region of the beam, the so called "beam halo". This beam halo was considered to have large divergence angles in comparison with the beam core region. The mechanism of the formation of the beam halo is being studied experimentally [103] and theoretically [104]. Particle-in-cell (PIC) simulations suggested that beam halo is originated from the negative ions produced in the periphery near the PG apertures [105]. Due to this halo component, the meniscus is distorted and the actual meniscus is different from that calculated in conventional 2D beamlet analyses. In the volume production case, the distribution of negative ion density on meniscus is considered to be uniform. On the other hand, in the surface production case, because negative ions are produced on the PG surface, some of them are directly extracted from the PG itself. Due to these surface produced ions, the current density might be increased at the peripheral region of the meniscus. Moreover, this direct extraction from the PG surface can cause the deformation of meniscus shape and particles trajectory. There are indications that this deformation produces beam halo and becomes origin of the unexpected heat load on electrodes.
In SPIDER, from the 1D beam profiles measured by visible cameras, it is possible to

study any anomalies in the beamlet shape. Some qualitative results are presented in the following.
In Fig.5.40, 1D profiles measured by different cameras observing the same beamlets are shown. On top, the three beamlets of G2, B10, B13 and B14, seen by Basler7 (on the left) and by Basler9 (on the right) are illustrated; on bottom, beamlet 17 (group 3) observed by Basler14 (on the left) and by Basler12 (on the right). The fan of LoSs of each camera is shown near 1D profiles. These data refer to the extraction voltage scan in Cs operation discussed in Fig.5.18 (case 4x100 kW of radio-frequency power); the acceleration voltage is 45 kV. As the extraction voltage is increased, a wide component at the bottom of

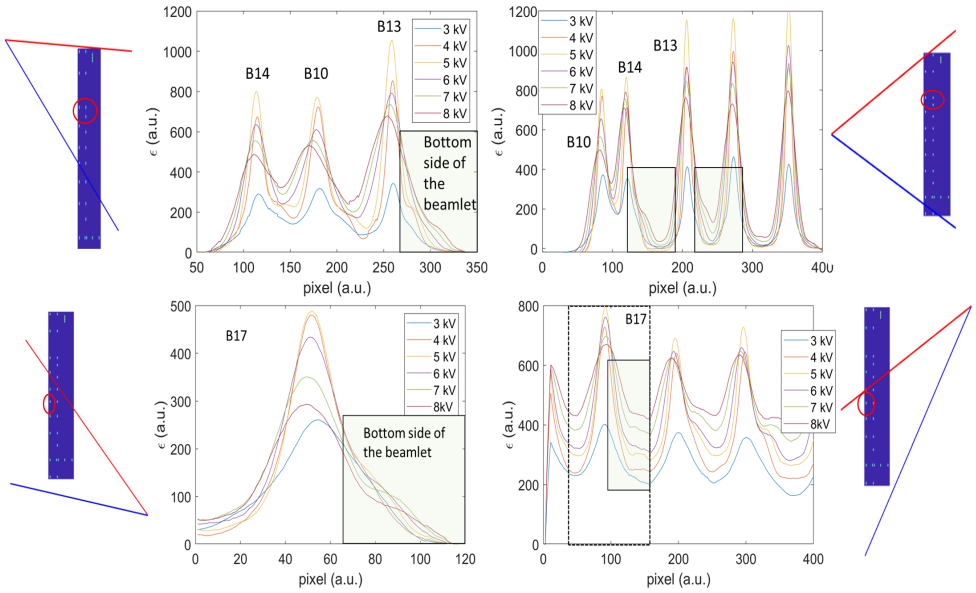

Figure 5.40: *1D beam profiles measured by visible cameras in Cs operation as the extraction voltage increases. On top, beamlets 10-13-14 seen by Basler7 (port 01, on the left) and Basler9 (port 01, on te right). On bottom, beamlet 17 seen by Basler 12 (port 09, on the left) and by Basler14 (port 12, on the right).*

the beamlets appear, and it is observed by all cameras. The usual Gaussian shape of the beamlets almost disappear. The same operational conditions are not explored in volume operation, because of the limit on extraction grid heat load due to the larger amount of co-extracted electrons. The same beamlet observed with Cs evaporation (on top) are compared with an extraction voltage scan in volume operation (on bottom) in Fig.5.41. The main difference between the two beamlet profiles is, of course, in the beamlet emissivity, which is almost 3 times lower in volume operation with respect to the operation with Cs. The data in volume are taken with 4x100 kW and $U_{acc} = 35kV$. As the extraction voltage is changed, the beamlet shape is modified but there is not the particular increase at the bottom of beamlets observed in Cs operation (as reported on

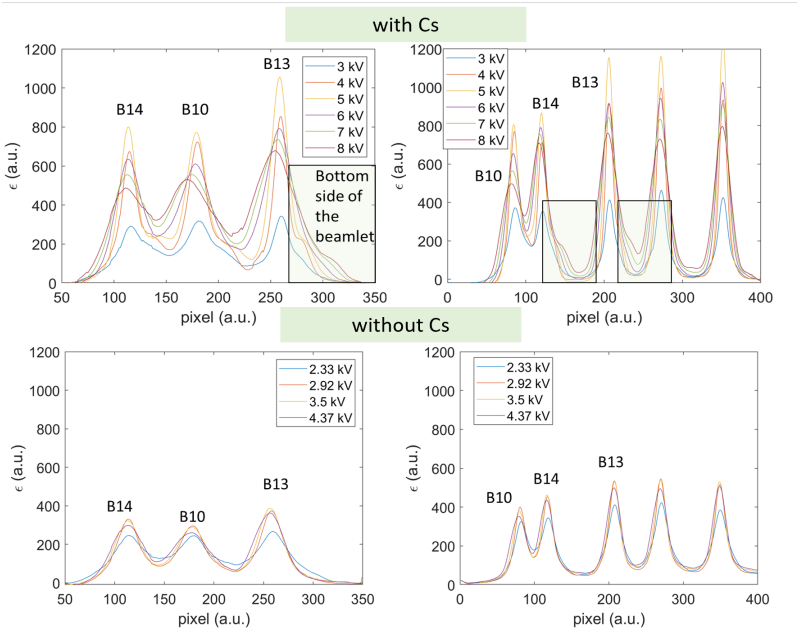

Figure 5.41: *Comparison between the 1D beam profiles measured by visible cameras in Cs operation (on top) and in volume operation (on bottom) as the extraction voltage increases; beamlets 10-13-14 seen by Basler7 (port 01, on the left) and Basler9 (port 01, on the right).*

top of Fig.5.41), and the beamlets profile remains Gaussian in shape.
As explained, this difference in the beamlets shape in volume and surface operation could be related to negative ions produced on the PG and directly extracted after the Cs evaporation, causing a modification in meniscus shape and direction.

5.6 Visible cameras as a tool to study electron-beam shape

The characterization of the space distribution of particle trajectories, or the respective current distribution, in powerful electron beams is an important scientific and practical task, necessary to improve the quality of the electron beam technologies, which are employed in several scientific and technological environments. For various application a small divergence is required, in order to transport the electron beam over long distances and to focus it onto a small spot. Several approaches exist for electron beam characterization, which are generally divided into two groups, whether they do assume or do not a Gaussian distribution of the beam current density. To characterize an electron-beam, the simultaneous knowledge of accelerating voltage, beam current, focus coil current and vacuum level provides little insight into the properties of the beam itself. A schematic representation of the experimental setup studied at the University Paris-Saclay Laboratoire de Physique des Gaz et des Plasmas is shown in Fig.5.42. The plasma (gas argon)

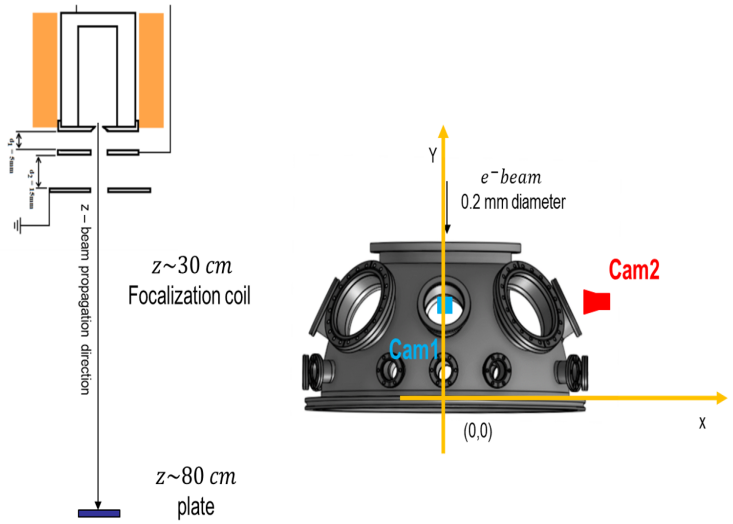

Figure 5.42: *Left: schematic representation of the source and electron beam. Right: vessel and position of the two cameras installed.*

from which the electron beam is extracted is generated in an Electron Cyclotron Resonance (ECR) source, whose deliverable power was limited to few W (1-5 W) due to the absence of an appropriate cooling system. The beam is extracted through a two-grids system, the so called *puller* and the Grounded Grid (GG); the high voltage HV was limited to 15 kV, to avoid large x-rays production; at $z \sim 30$ cm from the GG, a *focalization coil* further focalizes the beam. The pumping system is composed by two rotary pumps, which allow to operate at a pressure ranging from $10^{-3} - 10^{-4}$ mbar in the vessel where the beam propagates. The beam current was measured by the HV power supply and, for few days of operation, by polarizing the plate where the beam impinges ($z \sim 80$ cm from the GG). Even if the accelerator system was not optimized for the extraction of an electron beam, visible cameras were for the first time tested, to verify their suitability as diagnostic to characterize the shape of the beam. Two cameras were installed on the available viewports in the vacuum vessel, as shown in Fig.5.42. "Cam1" is a ImagingSource DMK37BUX226, which uses Sony IMX226CLJ-C CMOS sensor, composed by 1080x1090 pixels, with 8 bit resolution and maximum acquisition rate 30 frames per second; "Cam2" is a Basler, the same installed on SPIDER and described in Section 4.3.1. Both cameras are looking perpendicularly to the beam, with a relative angle of 90 degrees between each other: Cam1 mounts 16 mm focal length objective, Cam2 a 25 mm one. The beam is studied by varying the extraction and acceleration voltages, together with focalization coil current, the ECR power and both the source and vessel pressure. In Fig.5.43, images of the beam collected by the two cameras are shown: on top the pictures measured by Cam1, on bottom by Cam2. The ratio between extraction and acceleration voltages was varied, by keeping the total energy fixed and equal to 8

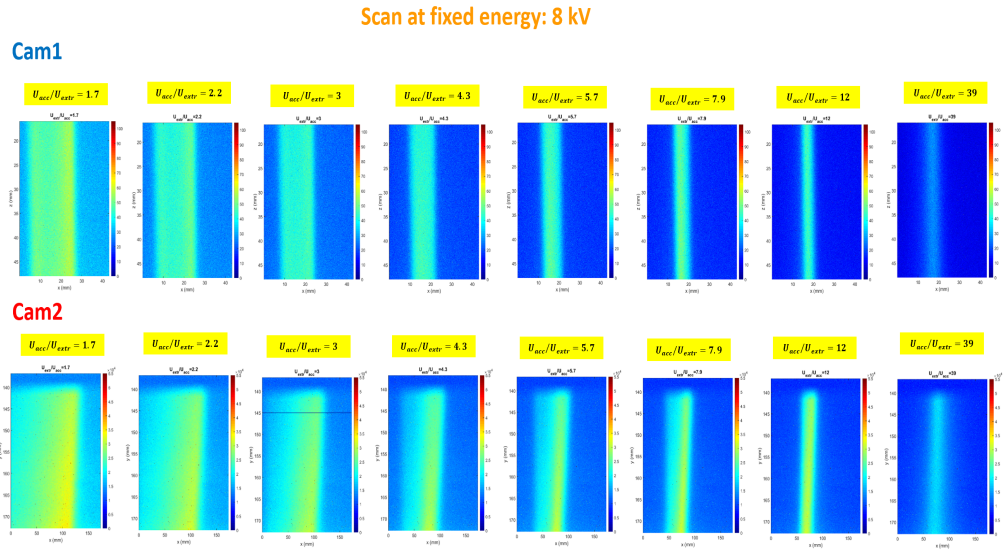

Figure 5.43: *Scan at fixed total energy (8 keV) - 2D images.*

keV; the current of focalization coil was 0.87 A. The 1D profiles are shown in Fig.5.44: on the left the profiles of Cam1, on the right of Cam2. From both 2D and 1D profiles, it

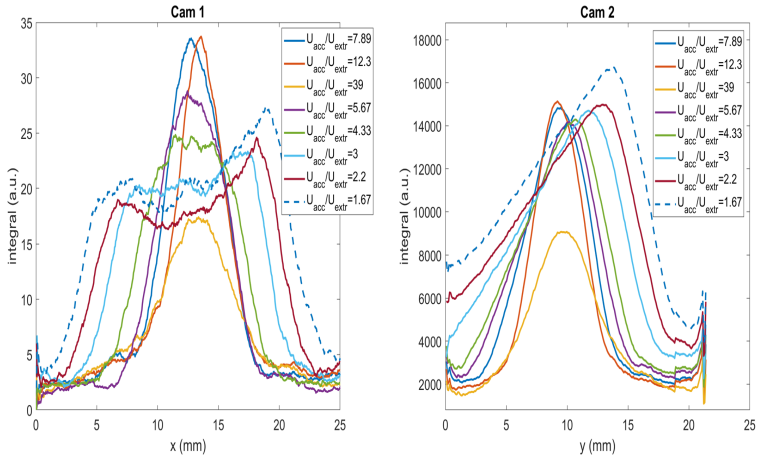

Figure 5.44: *Scan at fixed total energy (8 keV) - 1D profiles.*

is evident that the electron beam has a peculiar shape: especially from the first images in Fig.5.43, i.e. when the ratio between acceleration and extraction voltage is 1.7, it appears that most of the electrons are extracted from the edges of the *puller*, resulting in a larger charge density at the border of the beam than at the centre (see Cam1); this results in an asymmetric beam shape seen by Cam2, from the side. As the ratio of

voltages gets closer to the optimum, the beam becomes Gaussian in shape and its width is reduced. A first attempt of the 2D reconstruction through tomographic inversion is shown in Fig.5.45. The technique is the same used to reconstruct NIO1 and SPIDER

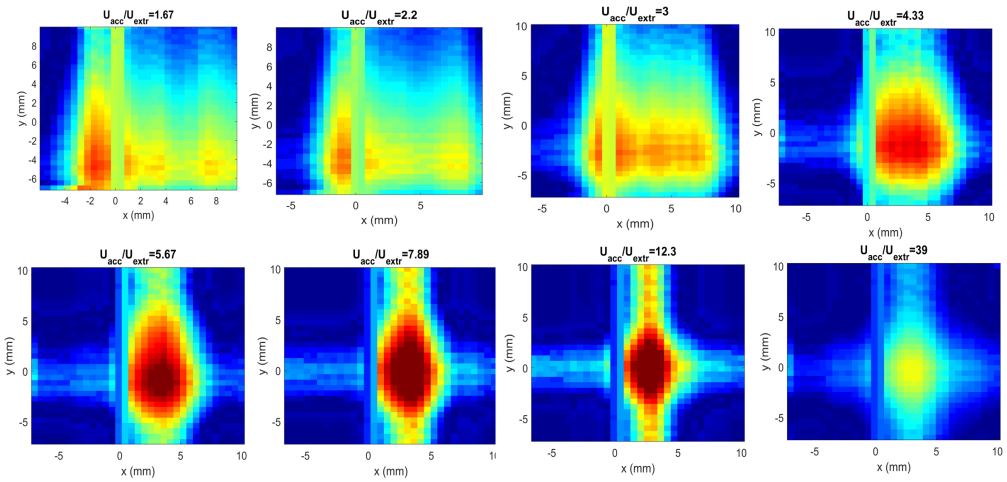

Figure 5.45: *Scan at fixed total energy (8 keV) - Tomographic reconstructions.*

negative ion beams, described in Chapter 4. Since only two points of view are available to observe the electron beam, only a preliminary reconstruction can be performed. The reconstructed emissivity patterns well reproduce the experimental ones, and the shape of 2D patterns show the evolution of the beam as the ratio of extraction and acceleration voltages is varied. When the focalization coil is used properly, by modifying it every time the beam current changes and by increasing the ECR power, the optimum of beam optics was found to be around 3 mm, evaluated as the width of the Gaussian fit of the 1D profile, in both directions.
These results demonstrate the ability of visible cameras and visible tomography to characterise even an electron-beam.

Chapter 6

Plasma homogeneity in the beam source

One of the requirements of heating and current drive neutral beam injectors (NBI) for ITER is a beam homogeneity better than 90%, to achieve a good beam transmission and a homogeneous heat load on the acceleration system. The dimension of the source is $1.9 \times 0.9\ m^2$ and the extraction area is $0.2\ m^2$. The beam homogeneity is related to the plasma source behaviour, through the uniformity of both negative species at the extraction region (negative ions and electrons). The uniformity of the former is mandatory to achieve identical beamlet optics at all apertures, the latter is mandatory to avoid localised heating of the extraction grid onto which the co-extracted electrons are deflected. Diagnosing the plasma electronegativity $\alpha_- = n_-/n_e$ is not trivial, being n_- the negative ion density, n_e the electron density. In the present setup of SPIDER with isolated beamlets, the best measurements of the local n_- is provided by the beamlets themselves. In addition to the local variation of electronegativity, the uniformity of the plasma density $n = n_- + n_e$ is clearly necessary. Since future NBIs are based on caesiated negative ion sources producing negative ions through surface production, the beam homogeneity is related also to a good and stable caesium coverage on the PG grid. The magnetic filter field is necessary to reduce the electron temperature and density close to the extraction region. As a result, the destruction probability of negative ions and the co-extracted electron current decrease. Nevertheless, the main source of plasma inhomogeneity could be attributed to the drift of ion-source plasma caused by the presence of the filter field. Moreover, the complexity of the source and the coupling between the drivers composing the source itself, can be an additional cause of plasma inhomogeneity, in turn influencing the uniformity of the beam.
As described, given the difficulties in diagnosing a large electronegative plasma, in the present SPIDER setup with reduced number of extracted beamlets, the beam diagnostics can provide a substantial contribution to the characterization of the plasma properties at the extraction region, and complement the spectroscopic measurements close to the grid system, together with the electrostatic probes data, and the spectroscopic measurements in the drivers. The interpretation of such combined measurements, as presented in this

chapter and in the following one, will provide key results for the understanding of the beam source behaviour, fundamental for the future operation at full performance. In fact, at full performance with all 1280 beamlets, the measurement of the extracted current uniformity from independent beamlet current will be extremely challenging.
Starting from the analysis of the plasma light measured inside each driver, both a top-bottom and a left-right dis-homogeneity is found. Both of them depend on the strength and direction of the filter field: a less dense plasma is measured in the drivers at the bottom of the source when the filter field is in the standard direction, the opposite when the filter is reversed. This top-bottom asymmetry depends also on the polarization of the Bias Plate (BP) and of the Plasma Grid (PG). The increase of these polarizations results in a larger plasma light, especially in the drivers where a stronger dependence on the filter field is measured. The plasma vertical profile is then studied in the expansion region, where the plasma produced inside each driver spreads and mixes. The spectroscopic measurements are compared with the electrostatic data collected by the set of Langmuir probes installed on the grids. The interpretation of the plasma optical emission in this region, in fact, is more challenging: while with the electron density and temperature found inside the driver, the stronger contribution to the atomic emission is attributable to direct electron excitation, and thus the plasma light is directly related to the plasma density, at the lower electron density and temperature in the expansion region, the recombinant processes play an important role. The plasma properties are not the same in front of the BP and in front of the PG, thus confirming the relevance of the first in modifying the plasma profile, as well as the different composition of the plasma closer to the extraction region.
The various operational regimes explored during SPIDER experimental campaign are studied, both with and without Cs evaporation, to study how the plasma reacts when the principal source parameters are varied. All these results will be exploited in the next chapter to interpret the beam behaviour. The beam, is studied starting from the results obtained by the visible tomography, together with the electrical current measurements (power supplies and STRIKE electrical data). The sources of beam inhomogeneity are highlighted and explained in order to optimize SPIDER in view of MITICA and ITER HNB.
More in detail, in Section 6.1 the plasma profile, from the Plasma Grid to the driver is measured by the movable Langmuir probes. In section 6.2, the measurements of the plasma light in the drivers are used to characterize the whole plasma (vertically and horizontally), as a function of the filter field and of the BP and PG polarization. Then, in Section 6.3 spectroscopic measurements are used to study the plasma on top and bottom of the drivers, along the beam direction. The horizontal spectroscopic measurements, together with the data obtained by the Langmuir probes, are used to study the vertical profile on the plasma close to the BP and PG, in Section 6.4; a comparison with the plasma during Cs evaporation is also given.

6.1 Electrostatic measurements: plasma profile along beam direction

The combined effects of both magnetic filter field and BP and PG polarization on the plasma behaviour is deeply studied in many existing negative ion sources and by simulation codes [44] [106] [107]. The novelty in SPIDER experiment is that it is one of the biggest radio-frequency sources in the world, so plasma dynamics is very complex, even if the physics behind it is the same. The combined effect of the filter field and of the BP and PG biases just described is measured experimentally on SPIDER. In a dedicated campaign [59], a set of movable Langmuir probes measured the plasma profile from the driver to the extraction region, in terms of plasma potential V_p, electron temperature T_e and electron density n_e. The plasma properties for different values of filter field and polarization voltages are shown in Fig.6.1; in these charts $z = 0\ m$ refers to the position of the PG while $z = 0.4\ m$ is inside the driver. All these measurements are collected with only a pair of drivers on, 2×50 kW each, 0.36 Pa of pressure, in hydrogen without caesium.

As described in Ref. [108], without magnetic filter, the plasma potential continuously increases with the bias voltage (first panel, top row). When the filter field is applied, the potential has a peak inside the driver and then it decreases towards the PG. Outside that peak, the plasma potential decreases towards the grids, and it is lower when also the bias voltage is (red points in first panel, second and third rows). The PG bias modifies mainly the plasma close to the PG itself, where the gradient of the plasma potential is reduced as the bias enlarges, bringing the PG potential closer to the plasma potential in the driver. Regarding the electron temperature, instead, a flat profile almost independent of the bias voltage is measured from the driver to the PG, with a high electron temperature between 8 and 10 eV, when no filter field is applied; as the filter field is turned on, the electron temperature close to the grid decreases from 10 to few eV, confirming the effectiveness of the magnetic filter field in reducing the electron temperature in the expansion region. This diminution is almost independent of the bias voltage and, the lower value of filter field (second row) is enough to reduce to few eV the electron temperature (no difference in the T_e between 1.8 and 2.6 kA of filter current is measured). The same behaviour holds for the electron density, which increases towards the driver when the filter field is applied, due to the better confinement of the plasma. When there is no filter field, the density in the drivers is lower by $50 - 55\%$.

6.2 Plasma profile in the drivers: plasma light measurements

As described in Chapter 3, spectroscopic measurements are available on the back of SPIDER source: one photodiodes with H_α filter is installed behind each driver (referred to as plasma light PL), collecting the light emitted by the plasma. The plasma light measured for each driver allows to characterize the plasma in the source, and the first

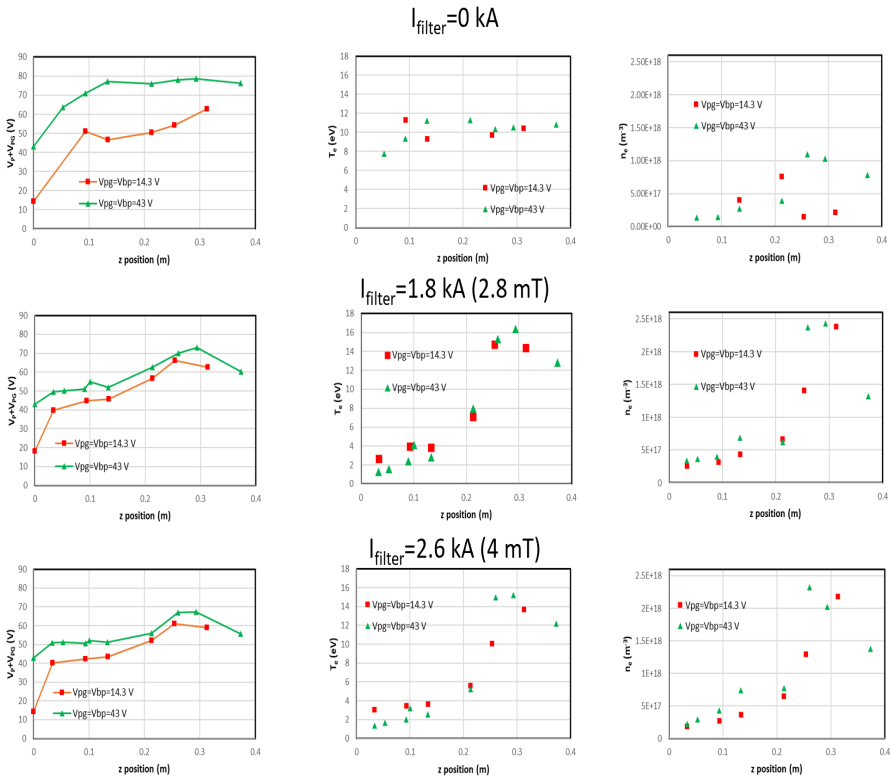

Figure 6.1: *Plasma potential, electron temperature and electron density from the PG (0 m) to the driver (0.4 m) measured with three different values of filter field (from top to bottom, respectively 0, 2.8 and 4 mT); the two colours refer to two polarizations of the PG, 14.3 V in red and 43 V in green.*

results are published in Ref. [53]. At the electron temperature and density inside the drivers (around 10 eV and 10^{18} m^{-3}), the H_α emission is dominated by H excitations, so the PL in the drivers can be assumed to be indicative of the gas dissociation.
To better understand the effect of both the filter and the PG and BP biases on the plasma in the drivers, the measurements of the PL for the two directions of magnetic filter field and for different values of the PG and of the BP polarization voltages, respectively V_{PG} and V_{BP}, are shown in Fig.6.2. The solid lines represent the emissivity (photon flux in 10^{21} $m^{-2}s^{-1}$) for the left drivers, $I_{PL}(L)$ while the dashed lines are used for the right drivers, $I_{PL}(R)$, seen from the back of the source; the different rows refer to the position of the drivers, from the top (segment 1, S1) to the bottom (segment 4, S4) of the source. The red box on the left delimits the measurements carried out with the standard direction of the filter field current onto the PG (from top to bottom, SF) and the green box on the right with the reverse direction (from bottom to top, RF). The columns, instead, represent the variation of both the PG and BP biases, raised together from 0-0 A to 140-110 A respectively. All these data are taken with 100 kW

of radio-frequency power per generator and 0.36 Pa of source pressure (gas hydrogen, without Cs).

The PLs exhibit different behaviour both between drivers powered by the same gener-

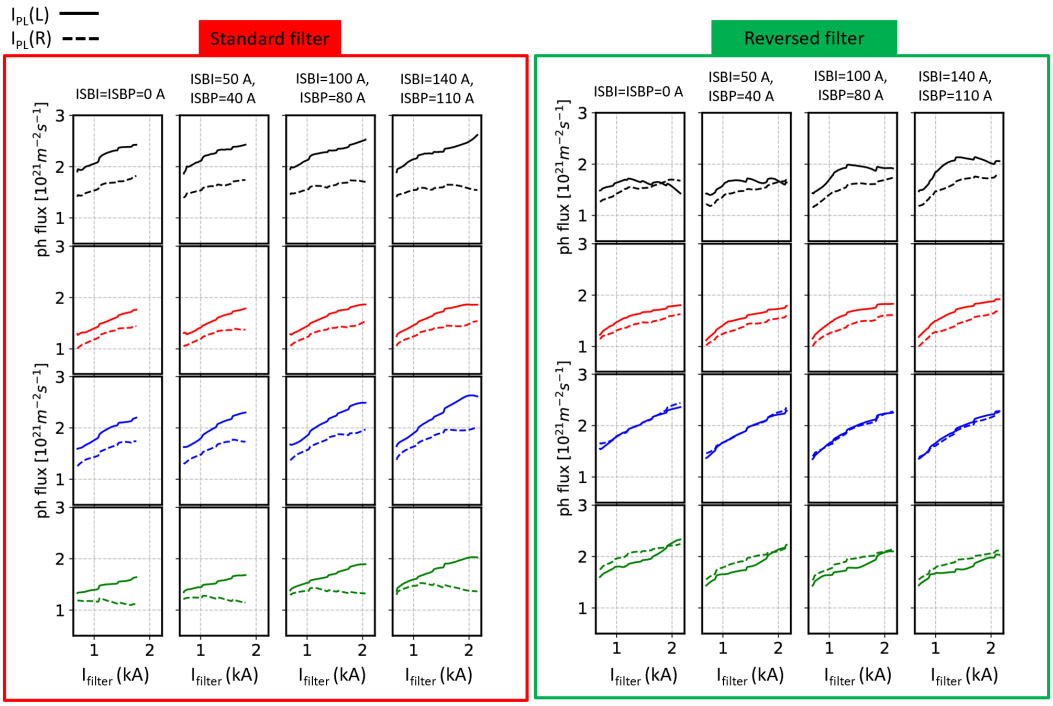

Figure 6.2: *Plasma light measured in each driver (solid line left drivers, dashed line right drivers, seen from the back of the source, from the top to the bottom) as a function of the filter field current, for different pairs of plasma grid and bias plate polarization currents (increased together). In the red box (left) the measurements with the standard direction of filter current (top to bottom of the PG), in the green ones (right) with the reversed direction (bottom to top of the PG).*

ator and between drivers located in different segments. Focusing on the SF (red box), even for the lowest value of filter field (0.7 kA is the minimum value necessary to ignite the plasma, while the plasma starts to become unstable over 2.7 kA), the light measured in the left drivers is always larger than the light collected in the right ones. For all the drivers, except the S4 (and the S1 for the highest bias) right driver, the PL increases with the PG current, demonstrating the better confinement of the plasma inside the drivers (higher density) with the magnetic filter field. As the biases enlarge, the plasma confinement improves too, in particular for the left drivers of all the segments. The PL in the right driver of S1, above a certain filter current and biases, saturates, as it can be seen in Fig.6.3, where the ratios between the PL measured in the left (L) and right (R) drivers are shown, for the same data as Fig.6.2. The largest difference between the L-R drivers in the SF configuration is in the S4, where the ratio increases from 1.1 to

1.5 with the filter current, for all values of bias; the L-R ratio is reduced only when the filter is minimum. The asymmetry in S1, instead, grows with the biases, up to 1.5 for the 140-110 A polarization currents and large filter field. The sum of the emissivity of each pair of drivers for segment is shown in Fig.6.4; it confirms the increase in the total PL both with the filter and the BP and PG biases. These data show a vertical asymmetry in the total emissivity which depends both on the filter field and on the BP and PG polarization currents. The PL of the S4 is the lowest without PG and BP polarization, then it increases reaching the PL of the S2 for the highest values of bias. Also the PL in the S3 shows the same dependence on the biases, becoming the one with the highest emissivity for the strongest bias and filter field case. The PL vertical profile in the drivers depends thus on the intensity of the filter field, and it changes when the biases are increased: for no bias and maximum filter current, in fact, the strongest is the PL in S1, and, decreasing, there are the S3, S2 and S4; when the biases are the highest, instead, the PL is higher is S3, and then in S1, while S2 and S4 are very similar.

When the direction of the filter field is reversed, the behaviour of all the PL measure-

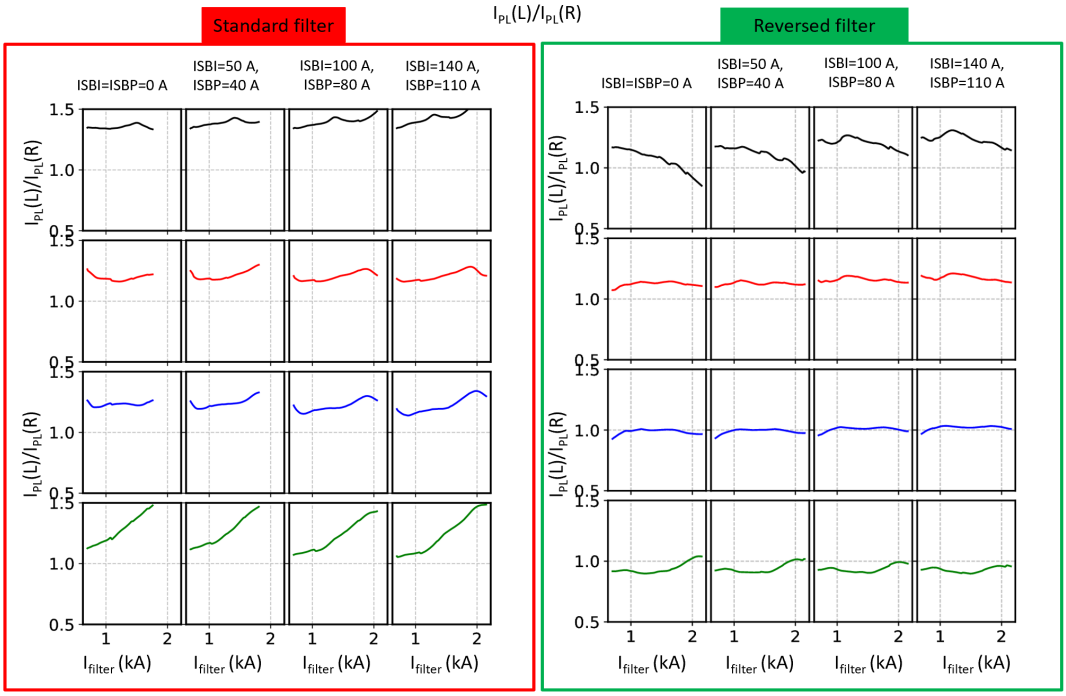

Figure 6.3: *Left to right ratio of the plasma light measured in each driver as a function of the filter field current, for different pairs of plasma grid and bias plate polarization currents (raised together). In the red box the measurements with the standard direction of filter current, in the green ones with the reversed direction.*

ments, both vertically and in between the pairs of driver, changes. These results are shown for the same experimental conditions in the green box of Fig.6.2, 6.3 and 6.4.

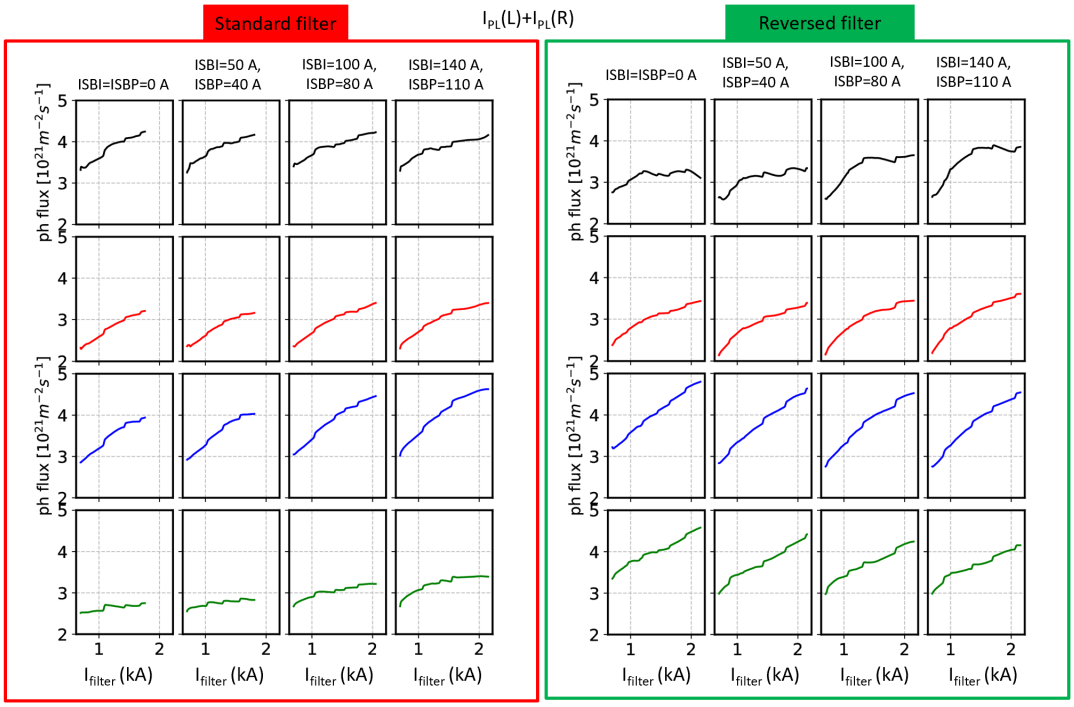

Figure 6.4: *Sum of the left and right plasma light measured in each driver as a function of the filter field current, for different pairs of plasma grid and bias plate currents (increased together). In the red box the measurements with the standard direction of filter current, in the green ones with the reversed direction are shown.*

Fig.6.2 and 6.3 show that the left to right symmetry is highly enhanced in the RF configuration: the L/R is closer to 1 for all the pairs of driver and, except for the S1, where a dependence on the filter field, which modifies with the biases, is measured, the ratio in all the other segments is independent on both the filter field and biases. The sum of the emissivity of the pairs of drivers (shown in Fig.6.4) increases in all the segments with the filter field (in S1 saturates for $I_{filter} \sim 1 - 1.5$ kA, depending on the bias applied), resulting in a larger PL everywhere with respect to the SF, for maximum values of filter field and biases. Looking only at the dependence on the biases, instead, S3 and the S4 behave almost in the same way: the total emissivity slightly decreases as the biases grow, and the final value is larger for the S3 with respect to S4. The PL in S2 and S1, instead, increases as the biases get larger.
In general, when the filter field is reversed, the decrease in the L-R to 1 allows to obtain higher H_α signal for all the drivers, for all the biases and filter field currents, going towards a more homogeneous plasma vertical profile for the maximum values of both of them. This means that, with the same experimental conditions (radio-frequency power and pressure) a better confined and denser plasma is produced inside the drivers. The reason why a more left-right symmetric plasma in the driver couples with the change

of the direction of the current flowing through the PG is still unclear: ideally no left to right asymmetry should be present. One explanation can be related to the different combination between the magnetic field of the permanent magnets installed on the source and the filter field lines, which can lead to a diverse topology of the resulting B: when the filter field is reversed, in fact, the two fields can be in the same or opposite direction, thus resulting in a final different magnetic field. The diverse behaviour of the bottom and top segments with respect to the central ones, instead, can be attributed to the vertical profile of the magnetic filter field inside the driver (right panel in Fig.1.12), which is more intense at the top and at the bottom with respect to the central region. Furthermore, not all the drivers behave in the same way. In particular, the movable electrostatic probes measured a peculiar behaviour of the electron temperature in the S4, not observed in the other drivers, as reported in Fig.6.5: the temperature for the right driver is larger than in the left one, as it approaches to the grids; as a consequence, the density in the driver is reduced, as shown by the PL data (Fig.6.4 left). Unfortunately, similar Langmuir probe measurements with the RF configuration are not available.

All these data were obtained during the experimental campaign without Cs evapora-

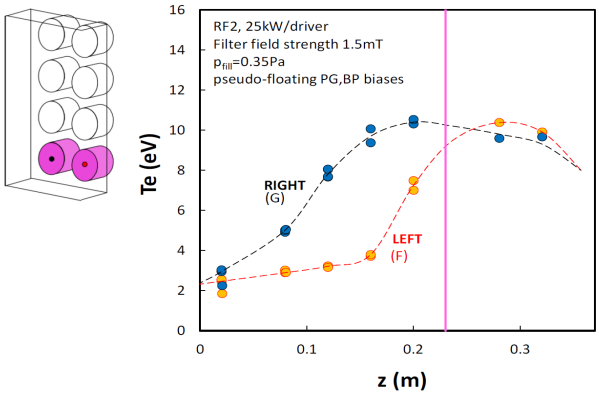

Figure 6.5: *Electron temperature profiles from the PG (0 m) towards the drivers (red line represents the exit of the driver), for the left and right drivers of S4, in the SF configuration [109].*

tion. It was shown Ref.[110] that the H_α emissivity in the drivers, during the campaign with Cs does not vary too much, so these results hold both for the volume and surface negative ion production campaigns.

6.3 From the drivers to the expansion region

As shown by numerical simulations in Ref.[44] and also measured on SPIDER with the movable probes [111], in the SF configuration, when a magnetic field is applied, a cold and dense plasma flows out from the top part of the driver while, at the bottom, a hot and low density plasma comes out. The opposite happens when the filter field is

reversed [112]. Since on SPIDER, 4 pairs of drivers generate the plasma together, the resulting plasma profile in the expansion region is affected by the different behaviour of the various drivers (as described in the previous section).
Two spectroscopic LoSs on the back of the source, along the beam direction just at the top and at the bottom of the S1 and S4, are available. The plasma exiting from the drivers into the expansion region is observed by these LoSs, whose position is indicated on the right-side of Fig.6.6, whereas the H_β dependence on the filter field current for the same pulses discussed in the previous section are shown; the circles refer to the measurements of "top" LoS, the triangles of the "bottom" one; different colours indicate the diverse values of PG and BP polarization currents. The results with the SF are shown in the left panel, the right one displays the measurements with the RF. For the same pulses, in Fig.6.7 the H_β/H_γ line ratio is shown. The H_β emission for the "up"

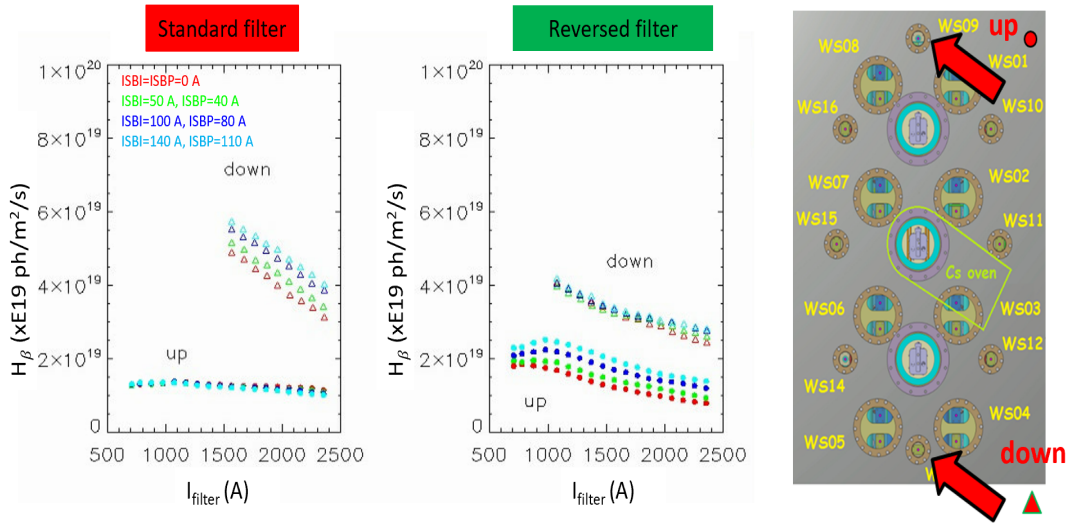

Figure 6.6: *H_β emission as a function of the filter field current, for different biases, for the two LoSs indicated by the red arrows in the picture on the right (seen from the back of the source). Different colours refer to diverse biases; the circles are the measurements of the "up" and the triangles of the "down" LoS.*

LoS in the SF configuration shows no dependence either on the magnetic filter field or on the biases; when the current direction is reversed, instead, the H_β emissivity is slightly increased, depending both on the filter current (after a peak at $I_{filter} = 1.1$ kA, it reduces as the current grows) and on the biases (higher biases result in larger emissivity). This can be related to the PL behaviour shown before: for the S1, in the SF configuration the PL depends slightly on the filter field and it is independent on biases modifications, whereas in the RF, it enlarges up to $I_{filter} = 1 - 1.5$ kA, depending on the biases applied (top rows of Fig.6.4). The H_β emission reduction measured by the LoS "up" could be a consequence of a better plasma confinement inside the drivers thanks to the magnetic

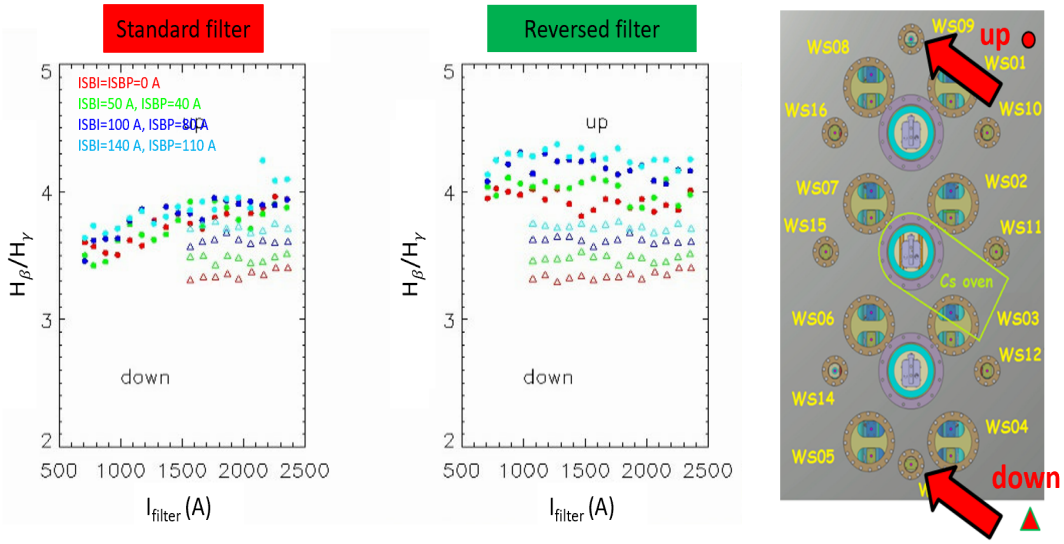

Figure 6.7: *H_β/H_γ ratio as a function of the filter field current, for different biases (same shots discussed previously) for the two lines of sight indicated in the picture on the right (seen from the back of the source). Different colours refer to diverse biases; the circles are the measurements of "up" and the triangles of the "down" LoS.*

field, which is accompanied by larger plasma light detected through the drivers. The same behaviour holds for the LoS "down", even if the signal is always larger than the top one, in particular in the SF; this may be due to a worse confinement of the plasma in the S4, also confirmed by the lower PL measured in the SF configuration (bottom rows of Fig.6.4); the dependence on the biases is evident in the SF configuration, as it is for the PL in the drivers, while in the RF it is stronger for the LoS "up", again in opposite way with respect to the PL in the drivers.
The line ratio shown in Fig.6.7 does not change in both configurations for the LoS "down", even if the emissivity varies. For the LoS "up", instead, it increases when the filter field current is reversed. None of them depends on the filter field current, except for the LoS "up" in the SF configuration. The PG and BP polarizations act in the same way in all measurements: as the biases increase, the line ratio grows too. The decrease in the H_β emissivity without the variation of the line ratio suggests that the electron temperature does not change, and its reduction can be related to a shift of the plasma in the expansion region, due to the electron drift, as a result of the combination of the bias and of the magnetic field. These measurements confirm an asymmetry in the plasma vertical profile in the expansion region, as it is observed inside the drivers.

6.4 Plasma profile on the grids: spectroscopic and electrostatic measurements

As described in Chapter 3, on SPIDER both electrostatic and spectroscopic measurements are available close to the PG and to the BP. The data collected with the two directions of filter field and for different PG and BP polarizations are here discussed.

6.4.1 Plasma characterization without caesium

In the following, the plasma profile close to the BP and to the PG is characterized, using both spectroscopic and electrostatic measurements, in the same conditions discussed previously (4x100 kW, 0.36 pA, H gas).

In front of the Bias Plate

As presented in Chapter 3, a set of windows allows to measure the vertical emission profile of the plasma at 35 mm from the PG, which is in front of the BP (BP is 20 mm away from the PG, towards the drivers). To characterize the plasma vertical profile, only the LoSs centred on the axis of the drivers are chosen, in order to avoid any local effect of the bias plate components.

In the two panels on the top row of Fig.6.8, the effect of the filter field on the plasma emission (H_β) close to the BP is represented. The measurements refer to 0 A of polarization current both for the PG and for the BP. The blue marks (squares for SF, triangles for RF) represent the H_β emission at the minimum value of filter which can be used to operate in volume with beam extraction, without biasing the grids; the red ones the maximum value of filter applicable without quenching the plasma in the drivers. At lower filter field, the H_β emission is larger in the RF, with a maximum in the S3. As expected, when the filter field is increased the plasma emissivity reduces, for both directions; the two vertical profiles become similar to each other, with the minimum H_β emission measured in the S1. This is different from what collected inside the drivers, where the lowest PL is in the S4 for the SF configuration. For low magnetic field, the H_β emission is dominated by ionizing processes due to the large electron density and temperature (like the plasma inside the driver, expanding towards the extraction region). When the magnetic field increases, the electron temperature in this region is reduced to few eV and the emission is dominated by recombinant processes [46] [55]; in particular, by the H_2^+ dissociative and mutual (with negative ions) recombinations. The H_β emission is thus related to electron collisions and heavy particles processes, and not only to the gas dissociation. Since these measurements are carried out at 35 mm from the PG without caesium (low negative ion density), as the filter field increases, the principal contribution is attributable to the channel $H_2^+ + e^- \rightarrow H + H(p)$ [55].
The effect of biasing grids, is shown in the two charts at the bottom of Fig.6.8. As the biases are increased, the two profiles become more inhomogeneous, respectively showing a large emissivity at the top with the SF and at the bottom with the RF. This is observed also in ELISE spectroscopic data [113].

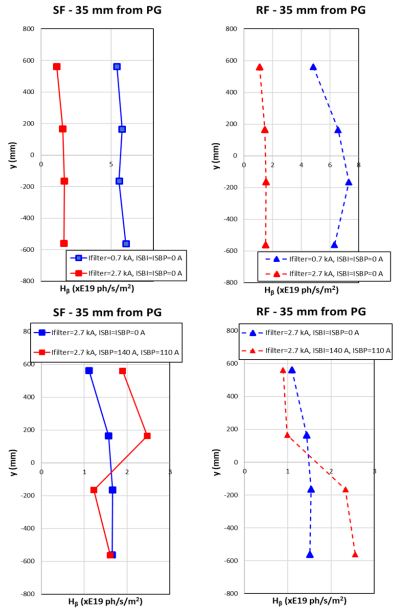

Figure 6.8: *H_β emission at 35 mm from the PG. Only the LoSs which are looking perpendicularly to the plane of each driver are plotted, from the S1 to S4. On the left there are the measurements taken with the SF, on the right with the RF. On the top, the effect of the filter field and on the bottom the effect of the PG and BP bias are shown.*

To better characterize the dependence on the filter field and on the biases of each segment, the H_β emissivity as a function of the filter current for two values of biases (0 and the maximum current) is shown in Fig.6.9; the filled marks represent the SF measurements, the empty ones the RF. For almost all segments, the larger decrease in the emissivity is between 0.7 and 1 kA of filter current, which corresponds to 1.1-1.6 mT of magnetic field. All these data can be compared with the positive ion saturation current I_{SAT} measured by Langmuir probes, even if the plasma seen by the two diagnostics is not exactly the same: the spectroscopic LoS are looking at 15 mm from the BP, while the probes are installed on the BP itself. Since the major effect of the filter field direction is found to be in the top and in the bottom segments (see PL in Fig.6.2, 6.3 and 6.4), the average ion saturation currents measured by the three probes installed on these two segments of the BP are shown in Fig.6.10. The first two charts show the I_{SAT} in the S1 and in the S4, solid lines with the SF and dashed ones with the RF; different colours represent various biases; the third chart, instead, shows the ratio between the segment with the largest I_{SAT} (S1 for SF and S4 for the RF) and the mean between S1 and S4. The behaviour of each segment is described in detail in the following, also by comparing the H_β emission with the I_{SAT} measured by the LP.

- Segment 1 (S1). In the SF (filled marks) the H_β emission decreases up to 1.7 kA of filter current; after this value, the effect of the BP and PG biases becomes

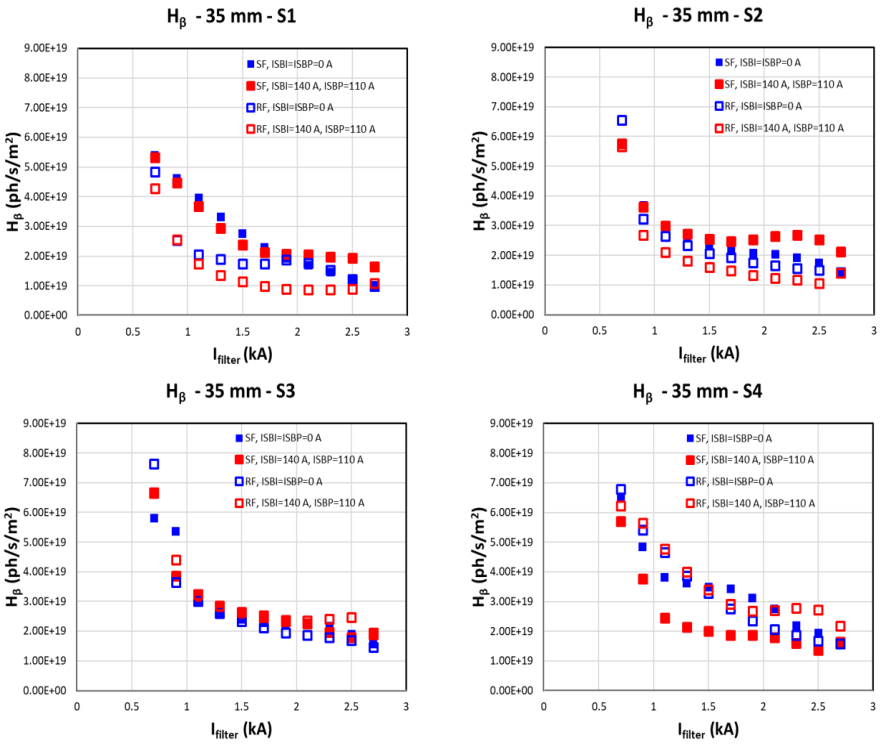

Figure 6.9: *H_β emissivity for each segment as a function of the magnetic filter field, for the two directions of magnetic field (filled marks the SF, empty marks the RF), for two values of bias at 35 mm from the PG.*

relevant: for high biases, H_β emission saturates to a larger value with respect to the one with zero biases; in the low bias case it continues to decrease, although less steeply than with the lower value of filter current. In the RF, instead, the H_β emission decreases up to 1 kA and then it remains constant, to a lower value for high biases (the opposite with respect to the SF configuration). This is similar to what is measured by the LP (Fig.6.10, first panel). For all the values of biases, the increment of the filter field reduces I_{SAT} by 50 %, to a largest value in the SF configuration. In the RF, the I_{SAT} dependence on the BP and PG polarizations is stronger: larger biases mean lower I_{SAT}, especially at high filter field; no effect of the biases is obsrved in the SF configuration.

- Segment 2-3 (S2 and S3). For both these segments, after an initial strong reduction of the H_β emission between 0.7 to 1 kA of filter current, the signal remains almost constant, independently on the filter field direction. The biases modifies the H_β emission only in the S2, where the behaviour is opposite as the filter direction is reversed (similar to the observations in the S1): higher emissivity in the SF, lower

in the RF for high biases.

- Segment 4 (S4). The behaviour of S4 is almost the opposite as S1. In the RF configuration, in fact, the H_β emission decreases continuously with the filter field current, and it stabilizes to high values when the biases are polarized with the maximum current. In the SF, instead, the H_β emission reduces between 0.7 to 1 kA of filter current, and then it saturates to a lower value for large BP and PG biases. This is similar to what measured by the LP, as shown in the second chart of Fig.6.10. In both configurations, I_{SAT} is sensitive to the grid polarization as the filter field is increased, but in an opposite way: I_{SAT} is lower (larger) as the bias currents grows (reduces) in the SF (RF) configuration. The absolute values of both the H_β emission and of I_{SAT} in these two segments invert with the filter field direction, suggesting an inversion of the vertical plasma profile (as confirmed by the PL in the drivers Fig.6.4).

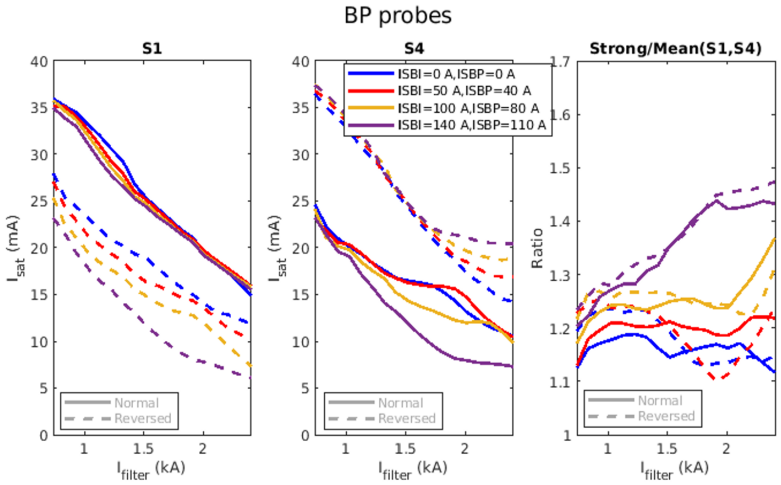

Figure 6.10: *Ion saturation current as a function ot the filter field current, measured by the Langmuir probes installed on the S1 (first chart) and S4 (second chart) of the BP; solid lines refer to the SF, dashed ones to the RF; different colours represent diverse BP and PG polarization currents.*

To summarize, with both the diagnostics an increase in the plasma dis-homogeneity is observed as the biases augment and the top-bottom segments behave in the opposite way when the magnetic filter is reversed (see in particular third panel of Fig.6.10). A good agreement between the H_β emission and I_{SAT} is found, suggesting the capability of estimating the positive ions density by this measurement. Both for S2 and S3, the effect of the filter direction and bias is negligible. This behaviour could be explained by the fact that S2 and S3, being the central segments, are sensitive to the plasma drifting from the top and bottom segments, so any local drift is compensated by the plasma coming from the neighbour pairs of driver. S1 and S4, instead, are close to the source wall, so

they are sensitive both to the plasma-wall processes and, being in the extreme region of the source, they are not compensated by the plasma coming from the nearby drivers. For this reason, the plasma displacement due to the combination of the magnetic and electric fields is more relevant. The fact that the vertical profile inverts when the filter field is reversed, confirms the hypothesis that the magnetic filter field is one of the main responsible of the plasma drift, also in this region in front of the BP (35 mm from the PG). The PG and BP biases play a role too in determining the plasma properties in this region and the outcome is related to the filter field direction.

In front of the Plasma Grid

The same analysis can be performed in front of the plasma grid: LoSs of the emission spectroscopy are available at 5 mm from the PG, together with a set of Langmuir probes installed on the grid itself (described in Chapt. 3). In Fig.6.11 the vertical profiles of

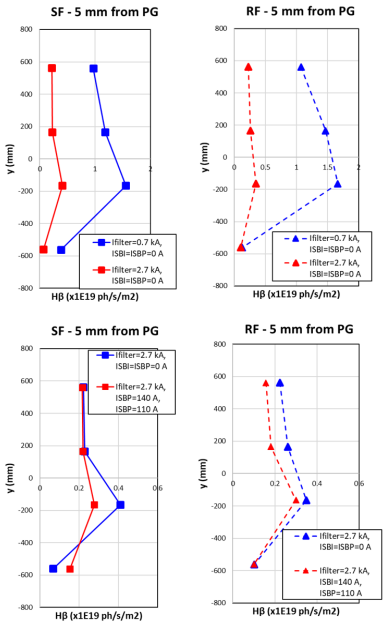

Figure 6.11: *H_β emission at 5 mm from the PG. Only the LoSs which are looking perpendicularly to the plane of each driver are plotted, from the S1 to S4. On the left there are the measurements taken with the SF, on the right with the RF. On top, the effect of the filter field and on bottom the effect of the bias is shown.*

the H_β emission for two values of filter field (top row) and for two biases (bottom row) are shown, on the left for the SF configuration, on the right for the RF one. For both directions of the filter field, the H_β in the bottom segment is lower with respect to the other segments. Moreover, it does not change when the filter is increased, unlike the other segments, which exhibit a strong reduction of the H_β emission (by $\sim 65 - 70\%$).

The H_β emission is 80% lower with respect in front of the BP, when the filter is the higher.
Polarizing BP and PG, instead, reduces the H_β emission only in the S3 in the SF configuration, everywhere except in the S4 in the RF one (see Fig.6.11, bottom panels). This is different from what measured in front of the BP, where the BP and PG biases increase the H_β emission at the top (bottom) in the SF (RF) configuration. Moreover, at 5 mm from the PG, the effect of the bias is lower than in front of the BP, even if the polarization of the PG is the same as for BP.
The plasma in this region, i.e. in between the BP and the PG, is sensitive to the biasing of both grids. In particular, when the grids are polarized with $ISBI = ISBP = 0\ A$, both of them are measuring a negative current (~ -45 A) and their potential is $\sim 38-40$ V. This value is determined by the plasma facing the grids: the potential drop at the plasma grid depends in fact by the relation $U_{bias} - V_p$. From the measurements shown in previous sections, the vertical profile of the plasma is non-homogenous neither in the drivers and in front of the BP, resulting in a diverse plasma sheath (different plasma potential): the bias of the PG is the same for the entire grid whereas the plasma potential depends on the vertical position. Then, the effect on the plasma of the polarization of these grids locally changes according to the plasma potential of the plasma which faces the grids.
To better highlight the dependence on the magnetic filter field and BP and PG polarization, the evolution of the H_β emissivity in each segment, as a function of the filter field current, for two values of bias current, is shown in Fig.6.12. The spectroscopic measurements are compared with the ion saturation currents measured by the LP installed on the PG, and shown in Fig. 6.13, for the S1 and S4.

- Segment 1 (S1). In this segment, the effect of the magnetic filter field direction on the H_β emission is evident up to 2 kA of current; then, the signal becomes equal almost for all the values of biases and filter current. The emissivity in the SF configuration is larger and independent from the biases, and it steadily decreases with the filter field current. This is the same behaviour measured by the LP and shown in Fig.6.13, first panel, solid lines. With the RF, instead, the H_β emission is strongly reduced in between 0.7 and 1 kA, like at 35 mm from the PG (Fig.6.9), and then stabilizes and remains almost constant up to the maximum filter current; the dependence on biases here is stronger, and both the H_β emission and the ion saturation current are lower for the highest biases. For high filter current and low polarization, both the H_β emission and I_{SAT} in the two directions of the magnetic filter field coincide, while for low filter they do not.

- Segment 2-3 (S2 and S3). These two segments depend on the filter field current in the two configurations in the same way. The final value of H_β emission is larger in S3 than in S2; furthermore, it is minimal in S2 (S3) in the RF (SF) configuration, for high biases.

- Segment 4 (S4). The H_β emission measured in this segment differs both from the one observed in other segments and from the comparison with the I_{SAT} of

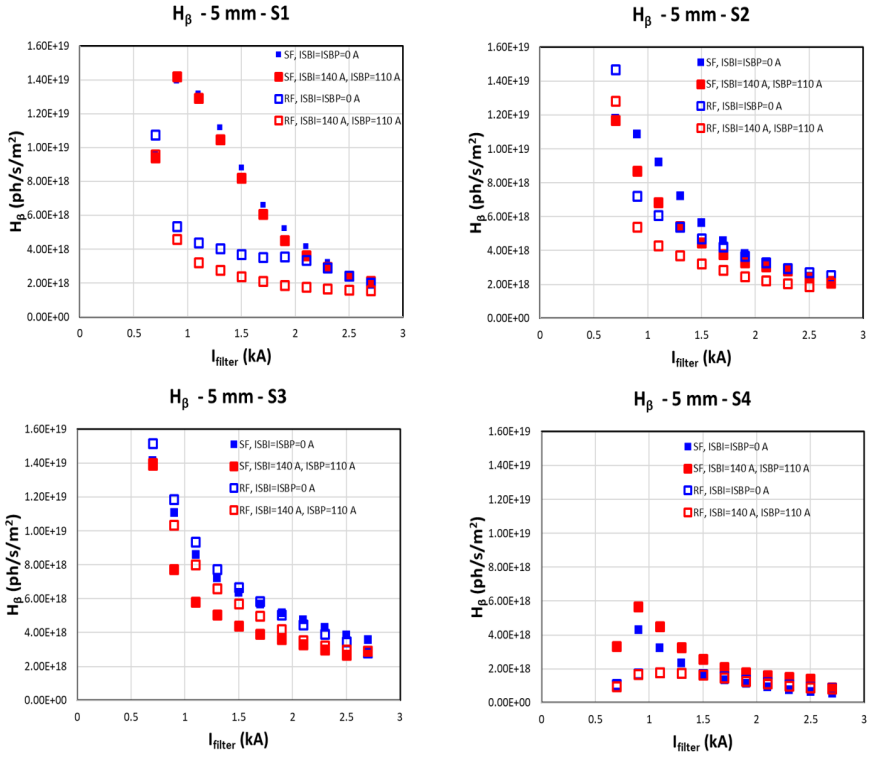

Figure 6.12: *H_β emission for each segment as a function of the magnetic filter field (filled marks the SF, empty marks the RF), for two values of bias current at 5 mm from the PG.*

the LP. In fact, the H_β has its minimum for both directions of filter field, and for $I_{filter} > 1.5$ kA, it is almost independent both on the value of biases and of the filter field. This is different from what is measured by the LP, in which the inversion of the behaviour of the S1 and S4 when the filter field is reversed, as observed on the BP, is confirmed. Also in this case, the bias increases dis-homogeneity, as shown in the third chart of Fig.6.13.

The discrepancy between the LP and spectroscopic measurements close to the PG in the segment 4 can be explained in several ways. The H_β emission is lower by almost 50% with respect to the nearby S3, in both magnetic configurations. This could be related to the peculiar behaviour of the electron temperature in the extraction region highlighted in Fig.6.4, which may play a major role in the emission cross sections in this range of energies. Furthermore, it has to be considered that these measurements are taken in the region in which the drift of the plasma related to the combined effect of the magnetic filter field and of the PG biasing is stronger. Qualitative information on the different composition of the plasma in front of the PG can be obtained also by studying the $H_\gamma/H_{Fulcher}$ ratio, which is almost independent of T_e and is only slightly dependent

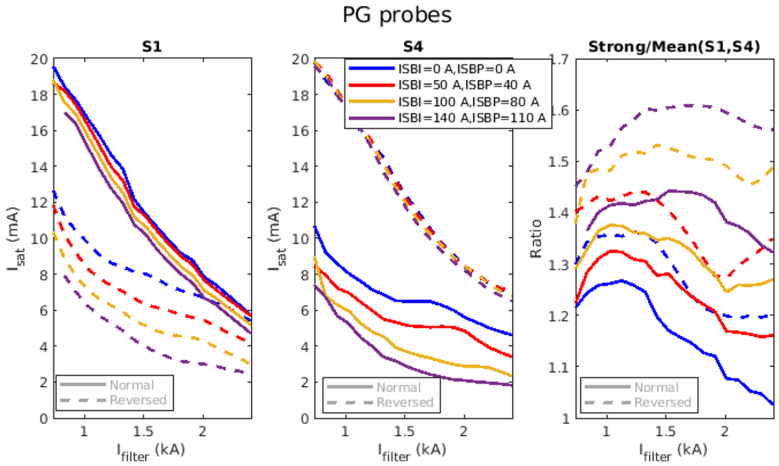

Figure 6.13: *Ion saturation current as a function ot the filter field current, measured by the Langmuir probes installed on the S1 (first chart) and S4 (second chart) of the PG; solid lines refer to the SF, dashed to the RF; different colours represent diverse values of BP and PG polarization.*

on n_e for $5 \times 10^{16} m^{-3} < n_e < 5 \times 10^{18} m^{-3}$ [51]; thus it can be used to evaluate the dissociation degree, i.e. the density ratio between atoms and molecules. The $H_\gamma / H_{Fulcher}$ ratios for the segments 1-2 and 4 at 5 mm from the PG are shown in Fig.6.14, for the same source parameters just discussed. The data for S3 are not available. The dissociation changes vertically and it depends both on the strength and on the direction of the magnetic filter field. In the S1-SF, the dissociation decreases with the filter current, suggesting a reduction in the electron temperature and, as a consequence, a decrease in the ionization degree (recombinant plasma). When the filter is reversed, instead, the ratio slightly increases with the filter current for low biases, while it is lower and almost independent of the magnetic filter field when the biases are higher, showing a different plasma with respect to the SF one. A similar behaviour is measured in the neighbouring S2, both the strong reduction of the ratio with the filter current in the SF configuration and the minor dependence on the filter field current in the RF configuration; however in the SF, especially for low filter current, the ratio is larger for low biases while the difference measured at large filter current in S1 in RF configuration between the two biases is here reduced. The behaviour of S4, instead, is completely different. In the SF, $H_\gamma / H_{Fulcher}$ is independent both of the biases and the filter field strength: it is constant to a lower value with respect to all the other segments. When the filter is reversed, instead, it increases with the filter current up to 1.3-1.5 kA, and then it decreases, for both values of bias. A quantitative interpretation of these measurements is not straightforward because many processes involve the plasma at these densities and temperatures. However, they suggest a different vertical plasma composition and behaviour, as confirmed by the previous data: the top and bottom behaviour of the plasma inverts when

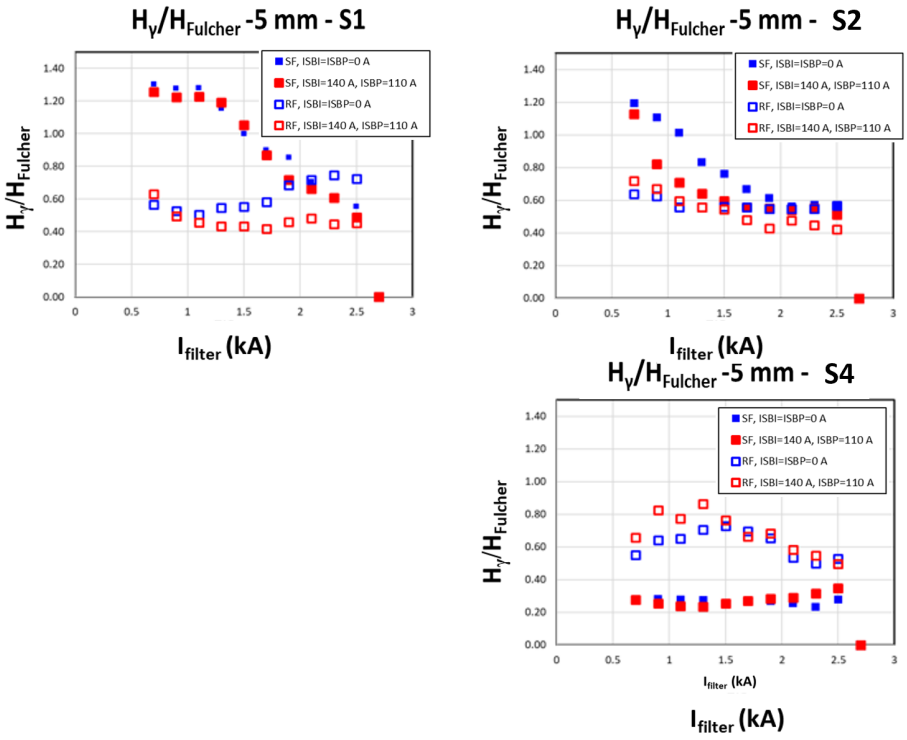

Figure 6.14: *$H_\gamma/H_{Fulcher}$ emission ratio for each segment as a function of the magnetic filter field (filled marks the SF, empty marks the RF), for two values of bias at 5 mm from the PG.*

the filter field direction is reversed. A Collisional Radiative (CR) model coupled with a study of the plasma dynamics is needed to have a complete understanding of the plasma composition and evolution, and it is under development.
Together with the electrostatic probes and the spectroscopic data, some information on the plasma is also given by the ISBI and ISBP power supplies, which measure the potential reached by the grids when the polarization current is varied. They are shown as a functions of the polarization currents (sum of the ISBI and ISBP currents, they are varied together) in Fig.6.15. The potentials reached by both grids are lower when the filter field is reversed, and this is representative of the different properties of the plasma in the two configurations. In both cases, the current measured by the two power supplies is the same and positive when the BP and PG polarization currents are high, meaning that they are attracting the same amount of electrons. The differences in the potential, instead, could be related the diverse vertical profile of the plasma facing the grids, as it is suggested by all the other measurements discussed previously. The modification of the plasma profile when the filter field is reversed, is confirmed also by the measurements of the Langmuir probes installed on the BP. In Fig.6.16, the floating potential V_f and

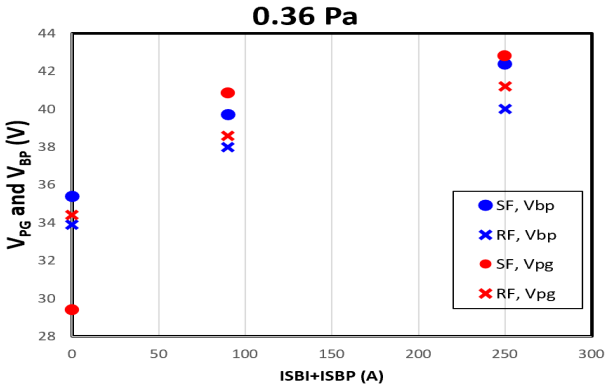

Figure 6.15: *V_{PG} and V_{BP} as a function of the sum of the the polarization currents (they are varied together) for the two directions of the filter field.*

the ion saturation current vertical profiles on the BP are shown, for the two directions of filter field (full circles SF, crosses RF) and 250 A of total current of bias; the floating potential is measured with respect to the source body. A reduction of the floating potential along the entire vertical profile in the RF is measured, as by the grids power supplies shown before. This corresponds to a larger ion saturation current everywhere but at S1.
The vertical profile of the plasma in front of the PG (without Cs evaporation) is characterized, as a function of the BP and PG biases and of the filter field strength and direction, using spectroscopic and electrostatic measurements. Even without a model to completely interpret the information collected by the different diagnostics, a picture of a non-homogeneous plasma profile is conceivable. In particular, the plasma properties dependence on the filter field direction are highlighted, and they are relevant also in this region. As the direction of the filter is reversed, the BP and PG biases modify the plasma in a different way, confirming not only the vertical asymmetry of the plasma profile, but also consistent overall differences. The agreement found in front of the BP between the H_β emission and the I_{SAT} measured by the Langmuir probes, in this region does not hold everywhere along the vertical profile of the plasma, thus suggesting a different composition of the plasma. All these plasma properties will be compared with the beam behaviour in next chapter.

6.4.2 Spectroscopic measurements in surface operation

During the Cs campaign, the beam optics and homogeneity characterization is performed at reduced radio-frequency power (Phase 3 in Sect. 5.1.2), 0.35 Pa of source pressure, 1.05 kA of filter current in SF configuration and different biases. To study the correlation between the beam and the plasma shape, plasma properties at these source conditions and different biases are studied, to integrate the information collected up to there.

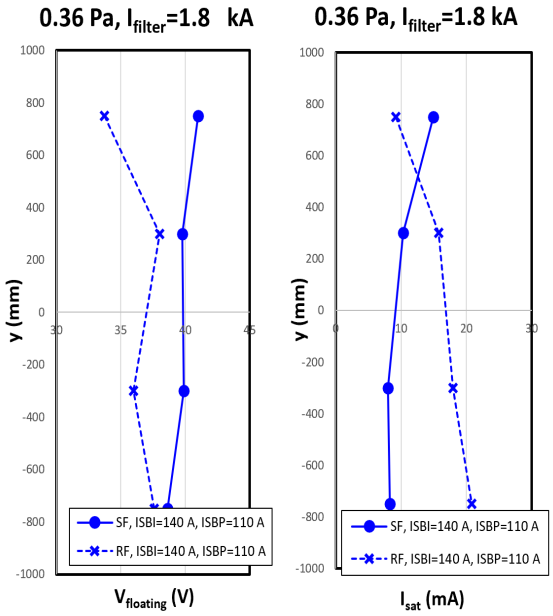

Figure 6.16: *Vertical profiles of the $V_{floating}$ and the ion saturation current measured by the LP on th BP, for 250 A of total bias current and 1.8 kA of filter field current, for the two directions of the filter field.*

Bias effect

Experimental measurements on SPIDER show that the H_α emission in the driver remains unvaried after the Cs injection (if the Cs coverage is optimal), so only the measurements close to the PG grid are shown, since this is the most interesting region for the production of H^- in surface operation. The dependence of spectroscopic measurements on the PG and BP biases, respectively at (0-0) A, (80-80) A and (190-140) A of PG and BP polarization current are shown in Fig.6.17 (SF filter field direction); from left to right the H_β, $H_{Fulcher}$, H_β/H_γ and $H_\gamma/H_{Fulcher}$ spectral lines are shown. The H_β emission has a maximum for the intermediate value of bias, and then it decreases everywhere, except in the S4 (where H_β emission increases with the biases); for all the polarization currents, the maximum of the emission is in the S3. Even if the absolute value is different, the shape of the vertical profile is similar to the profiles measured without caesium evaporation, and shown in Fig.6.11. The molecular emission, instead, decreases everywhere with the biases except for the S4, where it is slightly increased; also for the molecular emission, the maximum is measured in the S3. This could be explained by simply considering that one of the effect of the biases is in reducing the plasma density close to the PG, resulting in a decrease also of the molecular excitation. Since these measurements are carried out at lower radio-frequency power with respect the ones discussed in previous sections, the effect of the biases is stronger, as a consequence of the overall lower plasma density. H_β/H_γ increases everywhere with the biases except in S4, where the value is

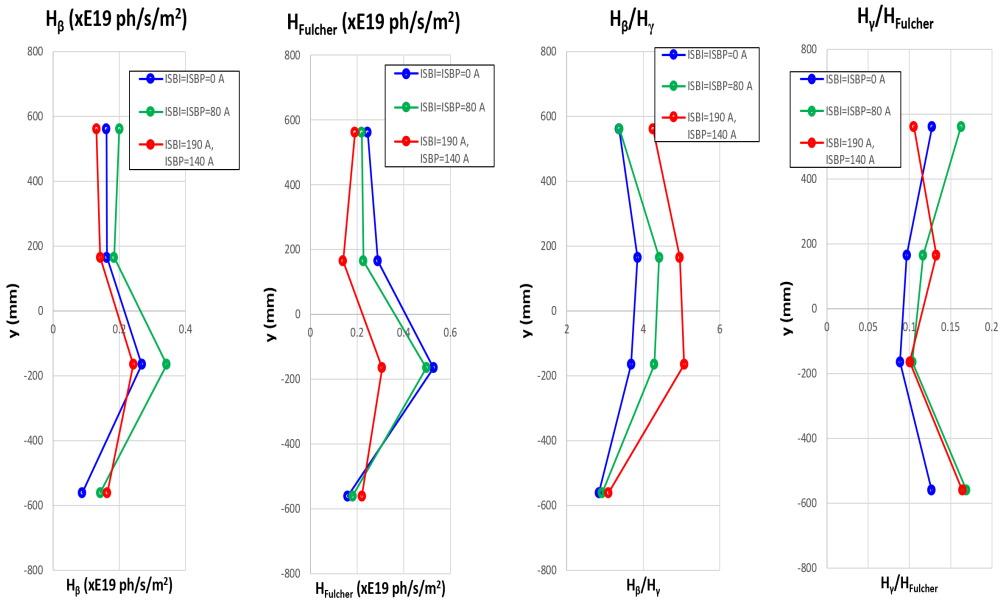

Figure 6.17: *Spectroscopic measurements at 5 mm from the PG. Only the LoSs which are looking perpendicularly to the plane of each driver are plotted, from the S1 to S4. From the left to right there are H_β and $H_{Fulcher}$ emission, H_β/H_γ and $H_\gamma/H_{Fulcher}$. Different colours refer to various bias currents (PG and BP are moved together).*

lower with respect to the other measurements. The $H_\gamma/H_{Fulcher}$ ratio, instead, increases with the biases everywhere except in S1, where it has a maximum for ISBI=ISBP=80 A and then decreases for higher currents. As for the $H_{Fulcher}$ vertical profiles, this could be related to a decrement in the dissociation, due to the lower plasma density close to the grids when their polarizations are increased.
As shown by the previous results without Cs evaporation, the PG and BP biases do not modify the overall vertical profile of the plasma at 5 mm from the PG. The reduction of both the H_β and $H_{Fulcher}$ emission lines, as well as the decrement in the ratio H_β/H_γ, may suggest a decrease in the plasma density as the biases grow, as confirmed also by the I_{SAT} measured by the LPs (Fig.6.13). This results will be compared to the modification of the beam in surface production, as these parameters are varied.

Independent polarization of BP and of PG

In this section, the plasma profile when only one of these two grids is polarized is analysed. To study how these polarizations affect the plasma close to the BP and to the PG, the spectroscopic measurements of H_β emission and of the ratios H_α/H_β and H_β/H_γ are shown in Fig. 6.18: on the left, the vertical profiles at 35 mm from the PG (15 mm from the BP), on the right at 5 mm from the PG. Since H_α is most affected by

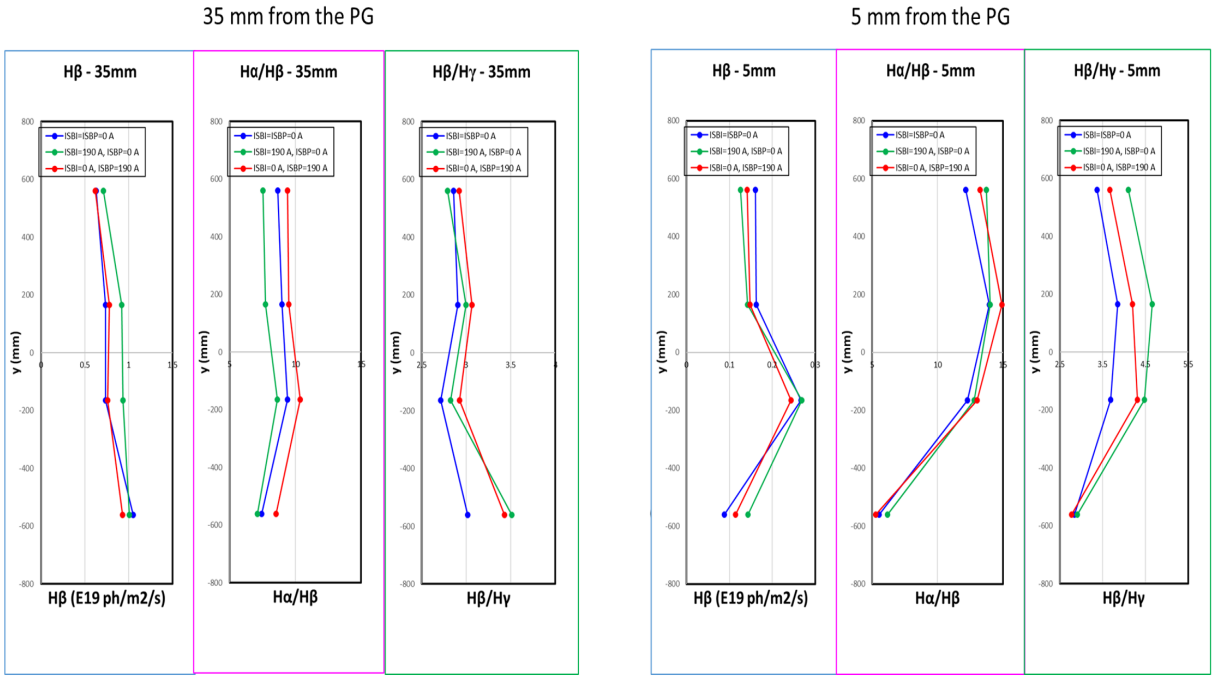

Figure 6.18: *H_β, H_α/H_β and H_β/H_γ vertical profiles at 35 mm (on the left) and at 5 mm (on the right) from the PG, for different values of PG and BP polarization currents.*

mutual neutralization and since all Balmer lines depend on n_e and T_e, an estimation of the negative ion densities can be obtained from the line ratios H_α/H_β. In Ref.[51], the line ratios obtained from the collisional radiative model YACORA as a function of the ratio of negative ion density to atomic density, for different electron density and electron temperature of 3 eV is shown. The H_α/H_β can be used to estimate the negative ion density while the H_β/H_γ is proportional to the plasma parameters, mainly to the n_e.

- ISBI=0 A, ISBP=140 A. Looking at the plasma profile at 35 mm from the PG (Fig.6.18, on the left), the H_β remains unvaried when the bias plate is polarized from 0 to 140 A, with no current on the PG (red and blue profiles), except in the S4, where the H_β emission slightly decreases. Both the line ratios, instead, increase everywhere. The H_α/H_β is lower in the S4; the H_β/H_γ increases mostly in the S4, where it has the maximum value, while it remains almost unvaried in the S1, confirming the different effect of the bias of the BP in the vertical direction at 35 mm from the PG.
  At 5 mm from the PG (Fig.6.18, on the right), the polarization of the BP reduces (increases) the H_β (H_α/H_β and H_β/H_γ ratios) emission everywhere except for the S4. Both the ratios have the minimum in the S4.

- ISBI=190 A, ISBP=0 A. The polarization of the PG with 0 A on the BP acts

differently to the plasma at 35 mm from the PG, with respect to the case with the polarization of the BP only. In fact, the H_β emission increases everywhere, except for the S4. The H_α/H_β, instead, decreases everywhere with respect to the case without polarization of the grids; the smallest effect is measured in the S4. H_β/H_γ increases everywhere except in the S1. At 5 mm from the PG, instead, the polarization of the PG acts similarly to the case in which the BP is polarized, just described.

By comparing these profiles in which the bias of the BP and on the PG are modified separately with the ones in which they are changed together, shown in Fig.6.17, it is evident that no difference in the plasma vertical profile at 5 mm from the PG is found. The shape of H_β and H_β/H_γ vertical profiles is the same when both the biases are changed together, as well as when they are modified separately. This suggests that the plasma close to the PG is influenced in the same way by the biasing of the two grids, thus confirming the influence on the plasma of both of them, also when they are polarized at 0 A. In fact, they collect anyway a current due to the plasma facing the grids, by possibly unbalancing the plasma vertical profile, as discussed previously in detail. Measurements with zero current collected by the two grids are not available in the currently SPIDER configuration. This will be considered in future operation, by modifying the power supply, allowing to polarize the grids negatively with respect to the source body.

Filter field direction

Also during the campaign with Cs, the filter current direction was reversed, to study the effect both on the plasma and on the beam. The measurements obtained at the same conditions for the two directions of magnetic field correspond to 4x45 kW of radio-frequency power, 0.35 Pa of source pressure, ISBI=190 A, ISBP=0 A and $I_{filter} = 1.05$ kA. The spectroscopic measurements from the driver to the PG are shown in Fig. 6.19 as indicated by the arrows; in the drivers only the H_α emission is measured, while closer to the grids both H_β and H_β/H_γ are shown.

As already described in Section 6.2, the H_α emission vertical profile in the drivers is inverted when the direction of the filter field is changed: from SF to RF configuration, it decreases in S1 while increasing in S4; no modification in the two central segments is observed at these values of filter and bias. Moving towards the grids, at 35 mm, the H_β vertical profile is different with respect to the light in the drivers: the H_β emission in the S3 and S4 grows in the RF, resulting in a more inhomogeneous profile with respect to the SF one. This top-bottom unbalancing is found also in the H_β/H_γ ratio: when the filter is reversed, the line ratio increases mostly at the top. Since the H_β emission is unvaried, H_γ is reduced at the top of the source when the filter field is inverted. In the bottom half of the source, instead, the line ratio remains constant while H_β enlarges in the RF configuration; this means that the H_β increment is compensated by the same augment in the H_γ emission. This confirms an asymmetry in the plasma composition in front of the BP, not depending only on the direction of the filter field.

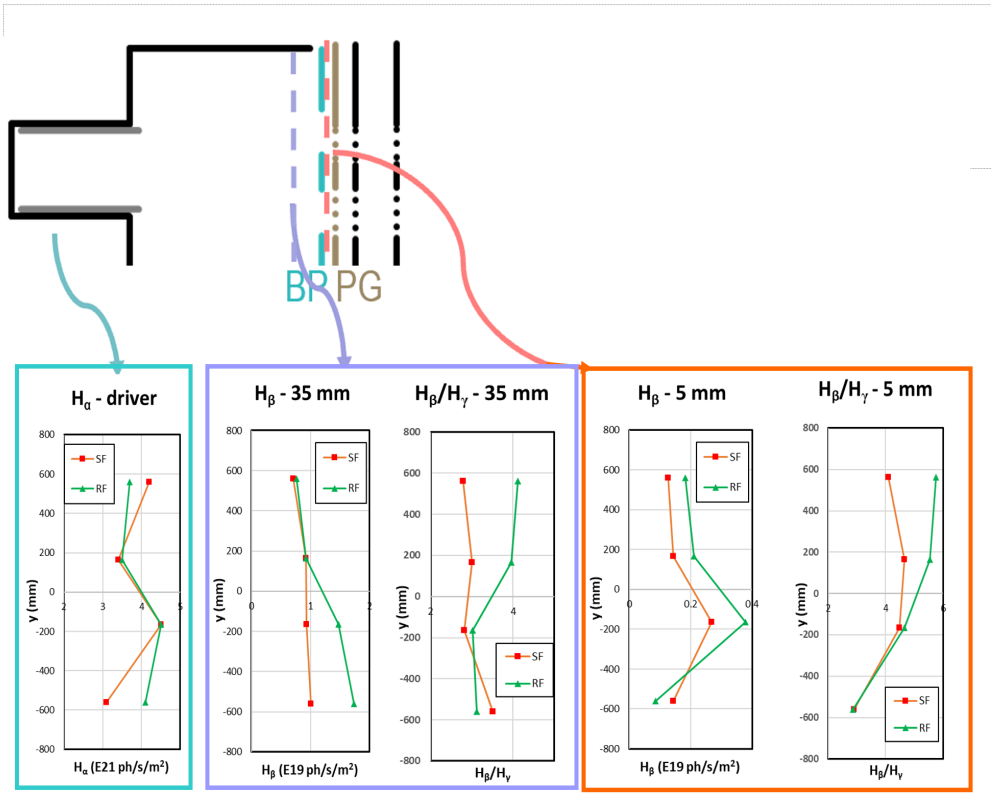

Figure 6.19: *Spectroscopic measurements at different positions from the driver to the PG for two directions of filter field current (in red the standard direction, in green the reversed one).*

The behaviour changes again at 5 mm from the PG, where both the H_β and the H_β/H_γ ratio are larger everywhere with the RF, except for the S4; the H_β emission has a maximum in the S3, the H_β/H_γ ratio in the S1. Even if a quantitative interpretation of the H_β/H_γ is not possible without a model taking into account the densities of the different species composing the plasma, the modification of the profiles in the two positions is representative of a different plasma in the two regions. The profiles in the two configurations are not inverted, suggesting the effectiveness of the BP and PG polarization in modifying the plasma vertical profile. In fact in these pulses, even if the bias plate was not polarized ($I_{set} = 0$ A), it measured in both cases a negative current of $\simeq -45$ A, due uniquely to the plasma (electrons and ions) which are collected onto the BP.
To better understand how the plasma profile is modified when the filter field is reversed in Cs operation, the plasma parameters measured by the LP installed on the PG, i.e. the electron density, electron temperature and plasma potential, for the two directions of the filter field, are shown in Fig.6.20. As already observed, at 5 mm from the PG the H_β emission line is not correlated with the plasma density: the n_e measured by the LP is lower everywhere except in the S4, in the RF configuration, while the H_β is larger. The

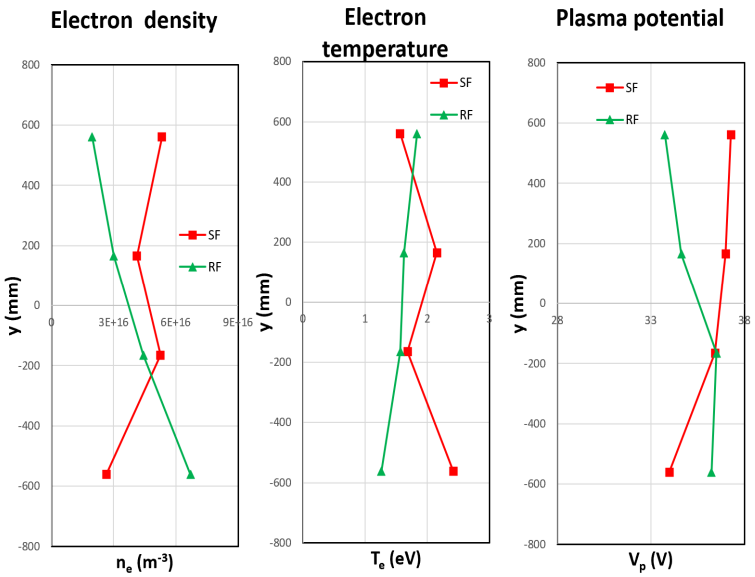

Figure 6.20: *Electron density, electron temperature and plasma potential vertical profile for the two directions of the filter field measured by the LP installed on the PG.*

largest decrease in the T_e profile with the inversion of the filter field is observed in the S4, which corresponds to the increase in both the n_e and V_p. This matches very well the PL measurements inside the driver. The plasma potential follows the inversion of the filter field direction as well: it is higher at the top in the SF, and the opposite in the RF. This is related both to the modification of the T_e and of n_e, which decrease everywhere, except the T_e (n_e) in the S1 (S4), when the filter field is reversed. The lowest electron temperature, together with the largest density at the bottom, will be related with the modification in the beam vertical profiles.

The same measurements made by the probes installed on the BP are shown in Fig.6.21. Here, the electron density vertical profiles behave very similarly to the H_β emission shown in Fig.6.19: higher emission and electron density everywhere, except in the S1, when the filter field is reversed. This confirms the correlation already discussed in Section 6.4.1 between the H_β emission and I_{SAT} also in a caesiated source. A decrease in the electron temperature in the RF is measured also by the Langmuir probes installed on the BP, but with a different vertical profile: on the BP the electron temperature is lower everywhere except in the S4. Again, by comparing the spectroscopic data measured at 35 and 5 mm from the PG, as well from the LPs results shown in Fig.6.20 and 6.21, the strong modification in the plasma vertical profile before and after the BP is evinced. The electrostatic measurements can be compared with the H_α/H_β vertical profiles close to the BP and to the PG; Fig.6.22 illustrates the H_α/H_β vertical profiles measured at 35 mm (on the left) and at 5 mm (on the right) from the PG. By assuming the H_α/H_β ratio to be mainly proportional to the negative ion density, the effect of the inversion

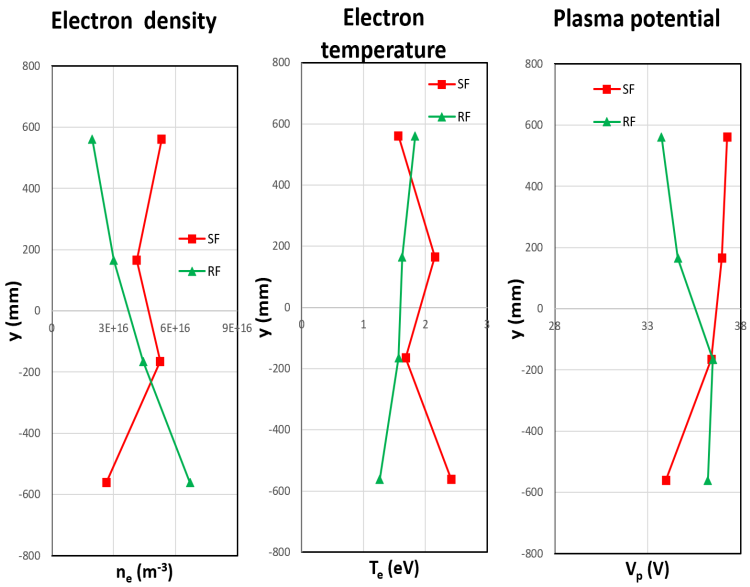

Figure 6.21: *Electron density, electron temperature and plasma potential vertical profile for the two directions of the filter field measured by the LP installed on the BP.*

of the magnetic filter field is evident. As seen by comparing the LP measurements on the BP (Fig.6.21) and on the PG (Fig.6.20), the plasma profile in these two positions is different. Close to the BP, in fact, as the direction of the filter field is reversed, the H_α/H_β ratio increases at the top (S1 and S2) while it remains almost unvaried at the bottom. Close to the PG, instead, the H_α/H_β ratio is higher at the top with the SF, the opposite at the bottom. The behaviour of H_α/H_β shown in the right panel of Fig.6.22 reflects very well the inversion of the beam emissivity vertical profile, since the production of the negative ions is mostly concentrated close to the PG. All these dependences of the plasma vertical profiles on the magnetic filter field strength and direction and on the BP and PG polarization will be compared with the beam properties in the following chapter.

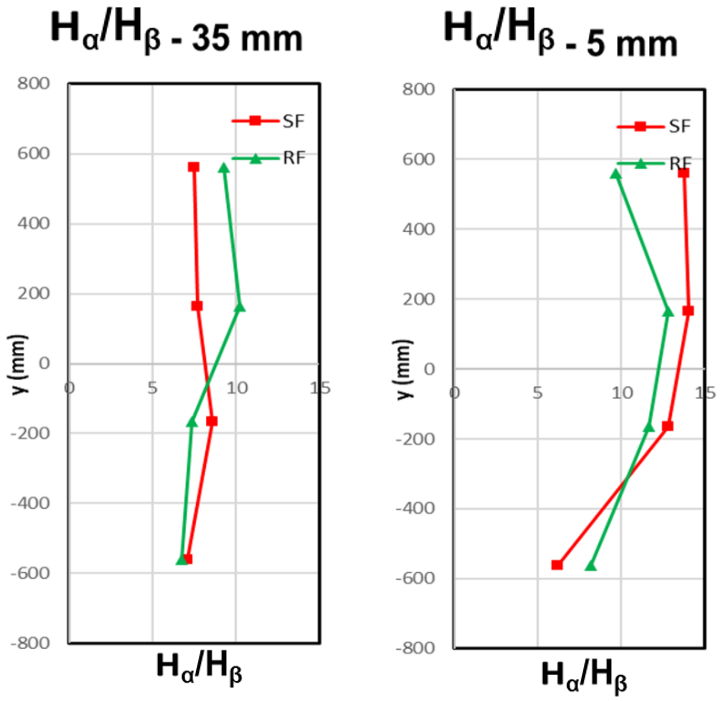

Figure 6.22: *H_α/H_β vertical profiles at 35 mm (on the left) and at 5 mm (on the right) from the PG.*

Chapter 7

Beam homogeneity

Due to the physics peculiarity governing the production of negative ions in volume and surface operation (described in detail in Section 2.1), the beam homogeneity in these two different regimes is studied separately in this chapter. Regarding the volume production, at first the characterization of the beam composed by 80 beamlets was performed, as a function of the filter field and for different extraction voltages. The beam composed by 28 beamlets is then studied in detail. The effects of the filter field direction and of the PG and BP biases on the beam shape are analysed, and the beam behaviour is correlated with the plasma source physics. Then, the results obtained with surface production are discussed. Most of the data in caesium were measured with low power (4x45 kW per generator) but few data are available also at higher power (4x100 kW), and the beam homogeneity in these two regimes is compared. The data collected with the hydrogen and deuterium negative ions are analysed and the dependence of the beam homogeneity on the different isotopes is discussed. By varying the main source parameters, such as the PG and BP biases, the magnetic filter field, the radio-frequency power as well as the Cs coverage, the beam homogeneity is increased as much as possible. At the operational conditions in which SPIDER operated up to now, the best beam uniformity and its dependence on the source parameters is presented, together with the limitations related to the plasma non-uniformity discussed in Chapter 6.
Both without and with Cs evaporation, a correlation between the beam behaviour and the plasma in the source is found. In volume operation, at the bottom (top) the beam current density, here described in term of beamlet emissivity reconstructed through visible tomography, is lower with respect to the top (bottom), when the filter field is in the standard direction (reverse direction). This is directly related to the plasma light vertical profile shown in Fig.6.4. When the Bias Plate and Plasma Grid polarizations are increased, the beam current density grows at the bottom (top) with the biases in the SF (RF), as it happens in the plasma light measurements in the correspondent pair of drivers. The total beam emissivity in the reversed direction is lightly larger than the one measured in the standard direction configuration, again reflecting what observed in the plasma light in the drivers. A similar behaviour is observed when the direction of the filter field is reversed in surface operation. In this case, due to the lower radio-

frequency power applied, the influence of the bias is stronger, reducing the beam current density especially at the bottom of the beam. This can be explained upon assuming a non-homogeneous vertical negative ion density, as suggested by the vertical profile of the H_α/H_β emission on the grids shown in Fig.6.22, which can be assumed as indicative of the negative ion density. Another source of beam non-homogeneity in surface operation is linkable to the limit on the available acceleration voltage which was fixed to 45 kV, due to technical issues. To maintain the optimum of the beam optics, found in Chapter 5 for $R = U_{acc}/U_{extr} = 9.5 - 10$, the maximum extraction voltage applicable was 5 kV, which is too low to compensate the large beamlet space charge at the top of the source (in SF), where the negative ion density is larger. This results in a bad transmission of the beamlets through the accelerator (scraping on the extraction grid), which reduces the beam current density at the top for low values of extraction voltage.
Furthermore, in both regimes, a bell-shaped profile of the beamlet emissivity inside each beamlet group is found, which is increased when the filter field grows. This may be related to the more peaked plasma density profile inside the drivers as the filter field increases.
A comparison between D and H beam in surface operation is then performed. No strong differences in terms of beam homogeneity are found. The typical decrease in the extracted current density, together with the growth of the co-extracted electrons is however measured, as observed in the other existing negative ion sources.
The beam homogeneity in volume operation is discussed in Section 7.1; in Section 7.2 in surface operation.

Beam homogeneity definition

In this chapter, the homogeneity of SPIDER beam is discussed. As a figure of merit, the average Root Mean Square (RMS) divided by the mean value of total emissivity will be used:

$$\frac{RMS}{avrg} = \frac{(\sqrt{\frac{1}{n_{beamlet}} \sum_{i=1}^{n_{beamlet}} (\epsilon_i - \epsilon_{avrg})^2})}{\epsilon_{avrg}} \tag{7.1}$$

where $n_{beamlet}$ is the total number of beamlets whose homogeneity is studied, ϵ_{avrg} is the mean value of the reconstructed beam emissivity and ϵ_i is the emissivity of the ith beamlet. ITER requires a maximum beam non-homogeneity of 10%, between each beamlet and the average [18]. Even if only few beamlets are left open during SPIDER experimental campaign (80 and then 28), the beam homogeneity in term of average RMS can be studied using the tomographic reconstructions described before and by exploiting the careful distribution of the few beamlets over the beam cross-section. For each beamlet, one value of emissivity is obtained through tomographic inversion, directly proportional to the beam current density by applying the correction described in Section 4.1.

7.1 SPIDER Beam homogeneity in volume production

The formation of H^- negative ions in low-pressure hydrogen discharges is primarily due to the dissociative electron attachment to vibrationally excited molecules, as explained in section 2.1. For this reason, high molecular and electron densities are desirable. The plasma profile from the drivers to the grids was been described in the previous chapter. Here, the shape of SPIDER beam in volume operation is studied starting from the results obtained by visible tomography and compared with the plasma source properties.

7.1.1 Case 1: 80 beamlets

During SPIDER experimental campaign in volume operation with 80 beamlets, the tomographic system composed by 11 cameras is used to study beam homogeneity. The tomographic inversion is performed using one pixel for each beamlet, thus obtaining one value of emissivity ϵ, proportional to the beamlet current density, for each of them. This technique is thoroughly described in Section 4.7. In Fig.7.1 two 2D beam emissivity patterns at two different filter currents obtained with the tomographic inversion are shown, respectively at 0.75 and 2 kA (standard filter SF configuration) [114]. These measurements are carried out at 1 kV of extraction voltage, 22 kV of acceleration voltage and 90 kW of radio-frequency power per generator. Since all pixels have the same size, the only information given by these preliminary reconstructions is the emissivity of each beamlet. For these two reconstructed patterns, the difference between the experimental and the inverted profiles, is equal to 8% and 6% respectively for 0.75 kA and 2 kA of filter current. The reconstructed 2D patterns are useful to characterize the beam homogeneity. Although at this low extraction voltage the non-uniformity is not so relevant, in Fig.7.1 the modification of the beam shape due to the filter field is visible. The beam intensity is lower in the fourth beamlet group (G4, at the bottom), where the filter field is stronger (see Fig.1.12); while, for both the values of filter current, the beam is more intense in the second group (G2, from the top). The beam inhomogeneity, re-defined as the ratio between the RMS of the reconstructed pixel emissivity divided by its mean value (Eq.7.1), is 18% at low filter and 19% at high filter. To better highlight the dependence on the filter field, Fig.7.2 shows the sum of the emissivity of the 4 reconstructed beamlets of each row, from the bottom (row 1) to the top (row 20), for the two different values of filter field. When the filter field increases, a slight reduction of the emissivity especially of the bottom group is measured. This can be related to the different behaviour of the PL in S4 with respect to the other segments (Fig.6.4): in S4, in fact, the PL does not increase when the filter field grows, while in the other segments it does. This corresponds to a decrement of the plasma density in the bottom part of the source with respect to the others, which could explain the reduction in the extracted current at the bottom part of the beam when the filter field is raised. Beam homogeneity depends also on the extraction voltage. To show how this affects the beam shape, the 1D profiles of camera Basler4 (Basler4, port 10) are used to evaluate the top/bottom beam asymmetry, since it observes the entire vertical beam profile. The raw experimental 1D vertical profiles seen by the Basler4 are shown in Fig.7.3; different colours represent various extraction

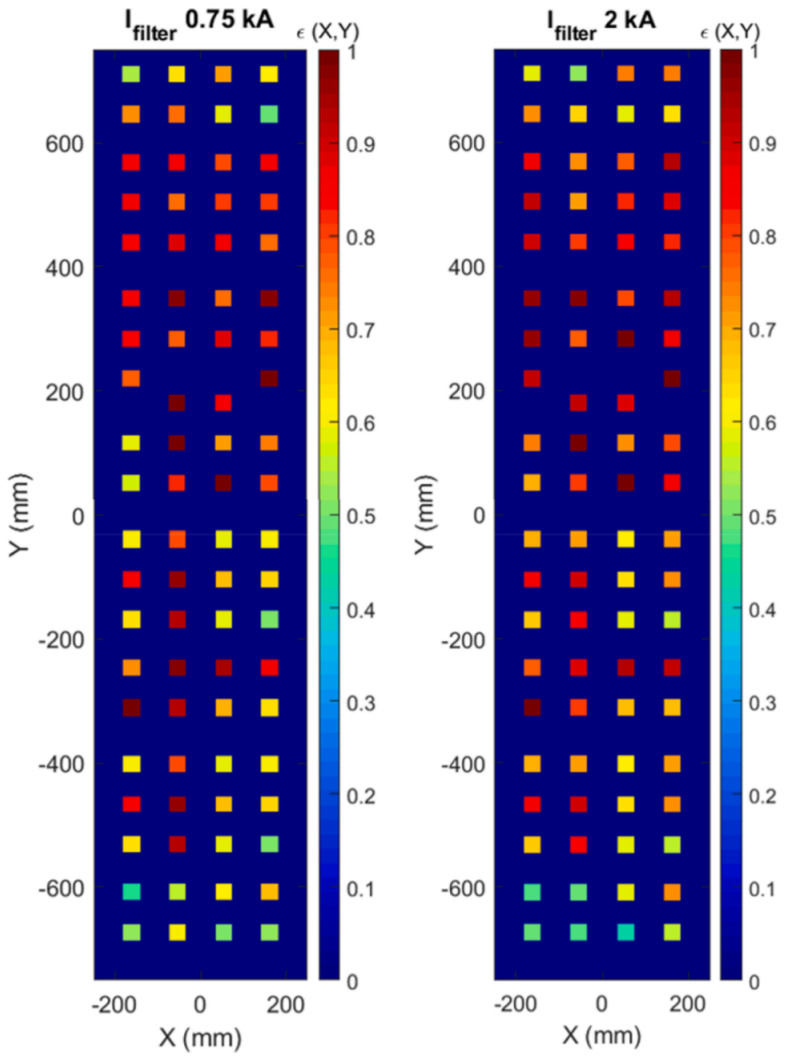

Figure 7.1: *2D beam emissivity reconstructions at two different filter currents (I_{filter}=0.75 kA on the left and I_{filter}=2 kA on the right, standard direction). The colormaps are normalized to the maximum of each reconstructed matrix; each square corresponds to a beamlet [114].*

voltages while the filter current is 2 kA. When increasing the extraction voltage, more ions are extracted where the plasma is sufficiently dense while, in the regions where there are less negative ions available, the current of the beam cannot increase any more. This means that the top/bottom asymmetry in SPIDER beam shown before augments with the extraction voltage. To better show this modification, the ratios between the top ($Y > 0$) and the bottom ($Y < 0$) integral of 1D profiles measured by Basler4 (Fig.7.3) as a function of the extraction voltage, for different values of filter field, are shown in

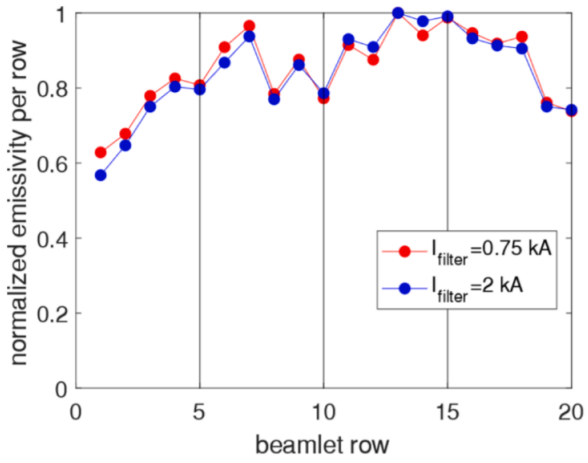

Figure 7.2: *Sum of the emissivity of the 4 beamlets belonging to each row, from the bottom (row 1) to the top (row 20) for two different values of filter current.*

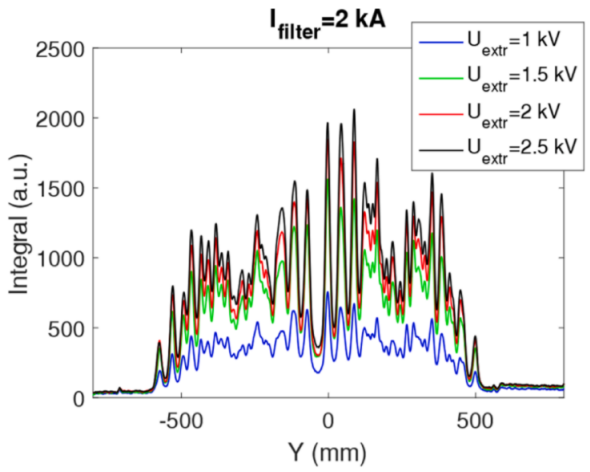

Figure 7.3: *Basler4 (port 10) experimental profiles. Each colour represents an extraction voltage value.*

Fig.7.4. For all the values of filter field, the top/bottom beam asymmetry increases as the extraction voltage is augmented. It is more pronounced when the filter field is higher, since it contributes to increase the top/bottom asymmetry (as shown in Fig.7.2). In fact, when the filter field is stronger, this unbalance starts at lower value of extraction voltage. Fig.7.4 shows that for U_{extr}= 1.5 kV, when the filter field is low (red and blue points) the beam is more symmetric than for the highest value of filter field (2 kA, green point), for which the bottom part is 10% less intense than the top one, confirming the

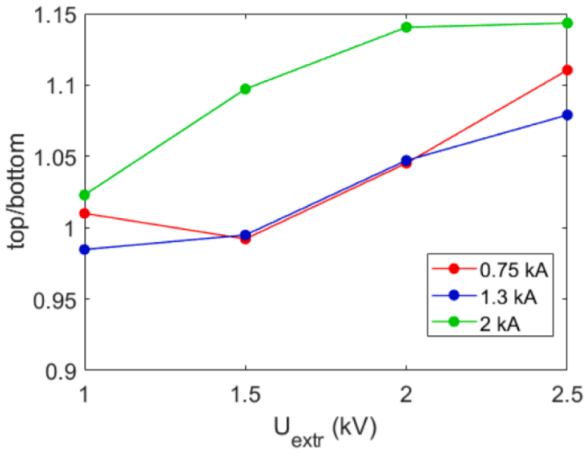

Figure 7.4: *Top/bottom ratio of the Basler4 (port 10) line-integrated signals, as a function of the extraction voltage for different filter field values. The asymmetry is maximum at* $I_{filter} = 2\ kA$ *and increases with the* U_{extr}.

decrease of the beam emissivity (as observed for the plasma intensity) at the bottom part of the source as the filter field is augmented. So, in this operational regime, the beam top-bottom asymmetry grows both as the extraction voltage and as the filter field increase.
Besides the top-bottom asymmetry, also the right-left homogeneity was investigated. In Fig.7.5, the left-right ratio of the emissivity of the reconstructed beamlets for each

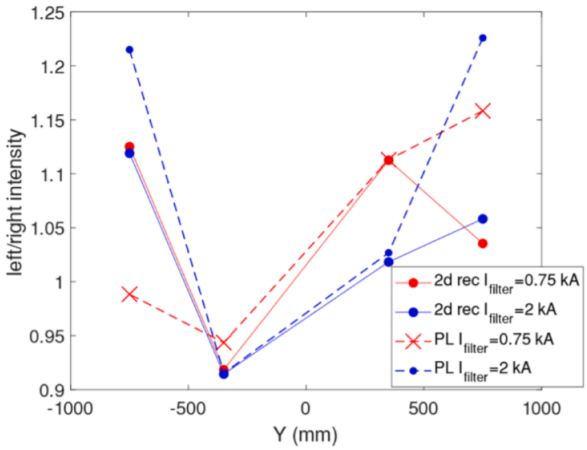

Figure 7.5: *Comparison between the left/right plasma light signals PL (dashed lines) in the 4 drivers with the 2D reconstructed beam emissivity (solid lines), for the two different values of filter current.*

beamlet group (from the bottom to the top), for the two values of filter field, is shown (solid lines); each point represents one beamlet group. In the bottom part of the beam ($Y < 0$, group 3 G3 and group 4 G4, which correspond to segment 3 S3 and segment 4 S4 in the source), there is no dependence on the filter field. In the top part of the beam ($Y > 0$, group 1 G1 and group 2 G2, which correspond to segment 1 S1 and segment 2 S2), instead, the left/right ratio depends in the opposite way to the filter field. These signals can be compared with the H_α measurements of the 8 photodiodes in the drivers which collect the plasma light (PL); they show a left/right asymmetry which depends also on the filter field. In Fig.7.5 the dashed lines represent the left/right ratio of the plasma light. Except for the segment (beamlet group) at the top, the PL and the beam emissivity have the same trend for the two values of filter field (low filter in red and high filter in blue). This figure shows that the behaviour of the intensity of the beam reflects the one of the plasma in the source. In fact, when the filter field changes, the asymmetry of the beam emissivity (and of the plasma light) varies as well. The relation between the beamlet current density and the plasma properties in volume operation is studied in details with the 28 beamlets configuration in the next section. No further investigations on the left to right beam symmetry was carried out, since the open beamlets in the 28 configuration belong all to the right part of the source.

7.1.2 Case 2: 28 beamlets

A more detailed study of the SPIDER beam shape dependence on the magnetic filter field strength and on the PG and BP biases is carried out, based on the data collected during the experimental campaign in volume operation with 28 beamlets. For two different values of source pressure (0.36 and 0.5 Pa) in hydrogen, 4x100 kW of radio-frequency power, and three values of filter field current I_{filter}=0.75, 1.2 and 1.8 kA, the total current polarizing both the BP and the PG is increased from zero to 280 A, and the beam shape is studied. The same pulses are repeated with the inversion of the magnetic filter field direction. The ratio between the extraction and the acceleration voltages is fixed to 10, with U_{extr}=2.4 kV and U_{acc}=24 kV, which corresponds to the optimum ratio for the beam optics (see Chapter 5). The main effect of both the filter field and of the BP and PG biases is to reduce the amount of co-extracted electrons, which in volume operation are the dominant species. Since the electrons are deflected on the EG by the permanent magnets installed within the grid itself, the current measured by the EG power supply is assumed to consist only of electrons. Due to their larger mass, the negative ions are not dumped on the EG by the magnetic field and they are measured by the acceleration power supply. The effect of the filter field as a function of the total bias current on the ratio I_e/I_{beam} is shown in Fig.7.6. I_e is the electron current, I_{beam} the beam current. The different colours represent various values of filter field current, while the markers represent the direction of the current flowing onto the PG (full circles for the SF, crosses for the RF); on the left, the ratio measured at 0.36 Pa, on the right at 0.5 Pa. As expected, the higher the filter field, the lower the electron to ion ratio, which decreases by 65-70 % when the filter current is varied from 0.75 to 1.8 kA. It depends also on the source pressure: higher pressure (chart on the right of Fig.7.6) means lower

I_e/I_{beam} ratio. A slight dependence on the filter field direction is evinced for all the values of filter current: the ratio is lower in the RF configuration. The I_e/I_{beam} ratio decreases also when the bias currents grow, reducing from 10 to 5 for the high filter case. To better understand how these two parameters affect the electron and the negative ion currents, the behaviour of these two measurements is studied separately. The I_{beam} (on

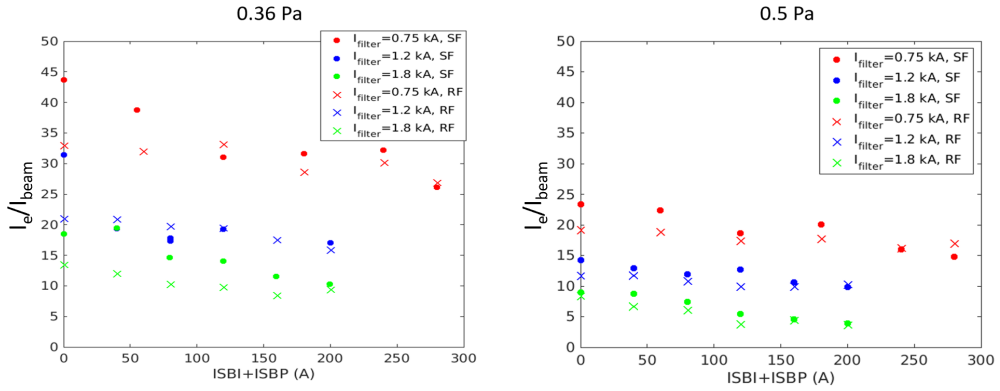

Figure 7.6: *I_e/I_{beam} at two different source pressures (0.36 Pa on the left, 0.5 Pa on the right) for different values of filter field current and directions, as a function of the BP+PG bias current.*

top) and I_e (on bottom) measured by the two power supplies are shown in Fig.7.7. The data represented in these panels correspond to the same measurements as Fig.7.6. In all configurations studied (various filter field currents in the two directions), the negative ion current does not depend on the total polarization of the bias plate and plasma grid. The main effect is related to the different source pressure: the higher the pressure, the higher the extracted beam current (~ 0.14 A for 0.36 Pa and ~ 0.2 A for 0.5 Pa). Furthermore, for both pressures, a larger H^- current is measured in the RF configuration and $I_{filter} = 1.2$ (blue crosses); the minimum corresponds to 1.8 kA and SF magnetic filter field.
As expected, the magnetic filter field mostly affects the amount of co-extracted electrons, which decreases by $40 - 50\%$ from 0.75 to 1.8 kA, for both configurations; moreover, the co-extracted electron current is lower for high pressure. A reduction of the electronic current as the polarization of the grids is increased is also measured, while the H^- current remains almost stable. These measurements give information regarding the collective behaviour of SPIDER beam when the filter field strength and the BP and PG polarization are varied. The dependence of the beam homogeneity on these parameters is now discussed in detail. The beam is characterized using the beamlet emissivity reconstructed through the tomographic inversion, with one pixel for each beamlet (28 unknown ϵ_i). The total beam emissivity (shown in Fig.7.8, as a function of the sum of the BP and PG bias currents, for different values and direction of filter field, on the left for 0.36 Pa and on the right for 0.5 Pa of source pressure.) is thus related to the accel-

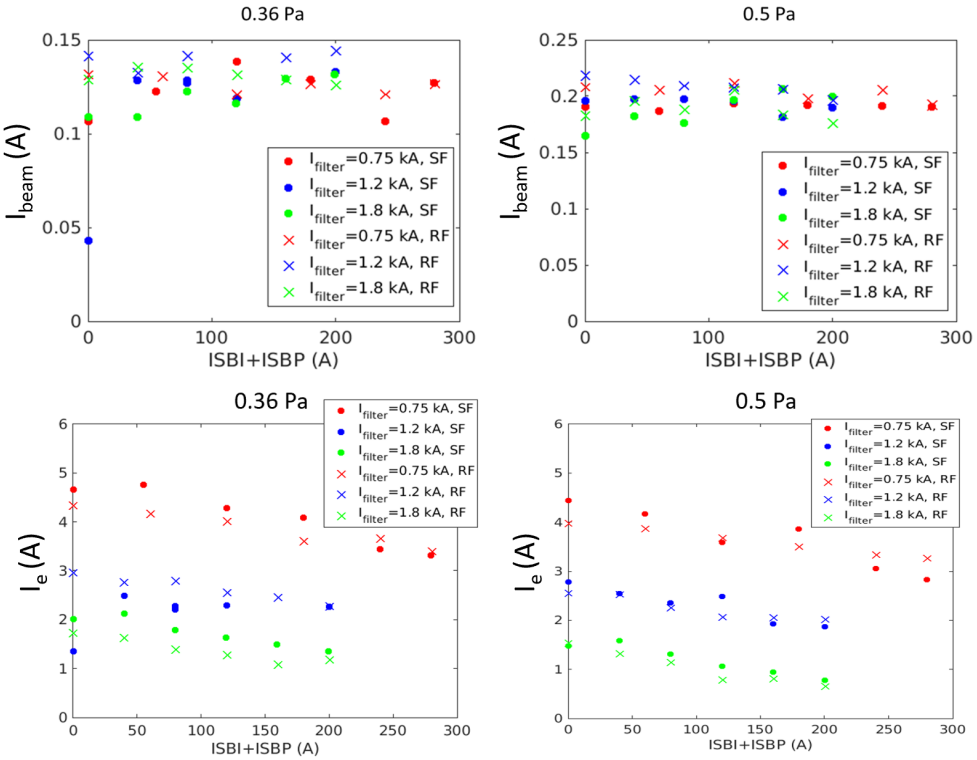

Figure 7.7: *I_{beam} (on the top) and I_e (on the bottom) at two different source pressures (0.36 Pa on the left, 0.5 Pa on the right) for different values of filter field current and directions, as a function of the BP+PG bias current.*

erated beam current, and it can be compared with the current measured by the AGPS power supply. In Fig.7.8, the full circles represent the total beam emissivity in the SF, the crosses in the RF configuration. For both values of pressure, the reconstructed emissivity is higher when the filter field is reversed, and it shows almost no dependence on the bias currents. This is the same behaviour measured by the accelerator power supply shown in Fig.7.7, thus confirming the capability of the beam emissivity in representing the beam current. The BP and PG biases modify more the total beam emissivity (and thus current) at low pressure and 1.8 kA of filter current, especially in the SF configuration. At low pressure, the maximum of the beam emissivity is with I_{filter} =1.2 kA for both the directions, which is also confirmed by the cavity ring down spectroscopy (CRDS) and by the AGPS current measurements. The negative ion density in volume operation at 0.36 Pa has a maximum for I_{filter} =1-1.2 kA and then it starts to decrease again [115]. This effect is less prominent when the pressure is larger. The reconstructed emissivity is almost the same for all the values of filter field in the SF configuration. It is confirmed to be larger when the direction of the filter is reversed and it decreases for I_{filter}=1.8 kA. The larger difference between SF and RF configurations of the total beam

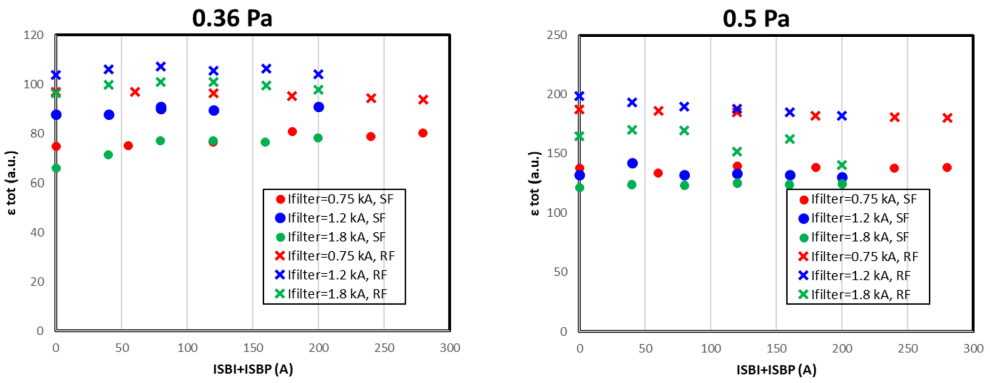

Figure 7.8: ϵ_{tot} *of the beam at two different source pressures (0.36 Pa on the left, 0.5 Pa on the right) for different values of filter field current and directions, as a function of the BP+PG bias current.*

reconstructed emissivity, with respect to the one shown by the AGPS electrical data, could be related to the fact that tomographic diagnostics is more sensitive in measuring the beam current with respect to the AGPS power supply, at such low values of current. The observed reduction of the filter field effectiveness in reducing the total beam current at larger pressures, instead, can be explained in terms of plasma density. When the filter field is too high with respect to the plasma density in the source, the reduction in the n_e with the filter field decreases also the probability of the negative ions to be produced by volume processes. Of course this is related to the source pressure (and the radio-frequency power), which has a key role in the plasma density.
The tomographic reconstruction allows to study how these source parameters modify the beam shape. It is possible to characterize in terms of single beamlet current density the entire beam pattern, thanks to the masking of the majority of SPIDER beamlets (only 28 are extracted, of the total 1280). In this way, the vertical profile, as well as the dynamics inside each beamlet group can be studied, allowing to detect the dependence of the beam shape on the source and accelerator settings.
Both from the electrical measurements (Fig.7.7 on top) and from the total beam emissivity (Fig.7.8), the larger modification of the beam is measured at low pressure and I_{filter}=1.8 kA, in both the directions. The vertical beam profiles in these conditions are shown in Fig.7.9: each point represents the mean value of the reconstructed emissivity of the beamlets belonging to the same row, from bottom to top; different colours represent various currents of BP and PG polarization, at the top in the SF, at the bottom in the RF. From these vertical profiles, the different action of the BP and PG polarization along the beam is highlighted, as well as the modification of its shape when the filter field is reversed. Looking at the profiles with the SF (top panel of Fig.7.9), the beam in the G4 grows together with the biases; this increment slightly affects also the G3. G2 and G1, instead, show almost no dependence on the bias currents. In the RF configuration,

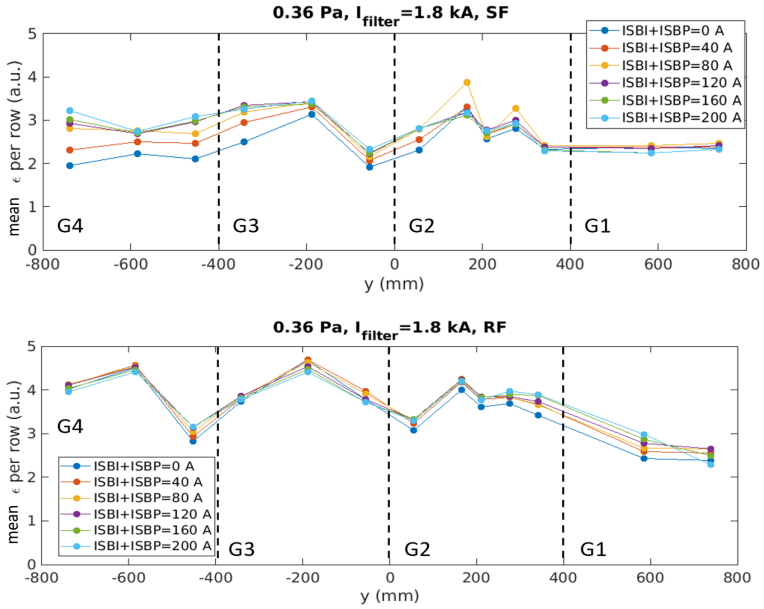

Figure 7.9: *Mean of the reconstructed emissivity ϵ of the vertical beam profile per each row, for the two directions of the filter field current (top panel SF, bottom panel RF), as a function of the sum of ISBP and ISBI polarization currents.*

the effect of the bias currents is reduced almost everywhere along the vertical profile. However, G1 and G2 emissivities increase with the biases, as observed for the G4 and G3 ones in the SF configuration.
A direct comparison between the beam vertical profiles in the two configurations of filter field, for three values of bias, is shown in Fig.7.10. As seen in Fig.7.8, the reconstructed

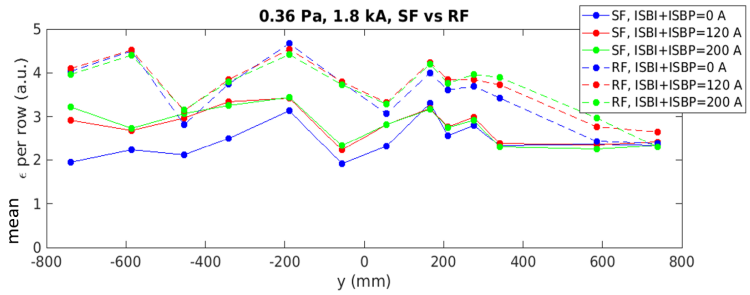

Figure 7.10: *Mean of the reconstructed ϵ of the vertical beam profile per each row, for the two directions of the filter field current (solid lines SF, dashed lines RF), as a function of the sum of ISBP and ISBI polarization currents.*

total beam emissivity is overall larger in the RF configuration. This growth affects mostly G4 and G3, while it is less pronounced in the G2 until the G1, where the difference between the two configurations is minimal. This behaviour could be compared with the plasma light data shown in Fig.6.4, both in terms of the inversion of the filter field direction and of the bias currents. In the SF configuration, in fact, the PL is larger at the top and lower at the bottom, where it increases with the biases. This is the same effect observed on the beam vertical profiles. In volume operation this could be explained in terms of plasma density growth and, thus, in the probability of negative ions to be produced. The opposite happens when the filter field direction is inverted. For all bias currents, the PL is larger in all segments in the RF configuration except for S1, where the effect of the bias currents is stronger: the plasma light grows in S1 as the bias currents are increased, as it is for the beam emissivity in G1. Since the plasma density in the SF (RF) is lower at the bottom of the source (at the top), the effectiveness of the BP and PG polarization is stronger especially in this region; this explains the observed modification of the beam emissivity.
The total increase in the beam emissivity with the inversion of the filter field could also be correlated to the different properties of the plasma close to the extraction region in these two cases. The I_{SAT} vertical profile measured by Langmuir probes (Fig.6.16), in fact, shows a larger plasma density in the RF configuration everywhere except in the S1, which reproduces perfectly the increase in the extracted current density when the filter is reversed (see Fig.7.10) along the vertical beam profile; this could be explained by the larger probability of negative ions production by volume processes.
This correlation between the plasma density and the beam emissivity can be studied in detail by increasing step-by-step the filter field which, as observed, plays a key role in determining the plasma density along the vertical profile of the source. The dependence of the beamlet emissivity in various vertical positions gives information regarding the plasma density modification both in the vertical direction as well as inside each beamlet group. In Fig.7.11 the electron current (on the left) and the total reconstructed beam emissivity (on the right), for the two directions of the filter field (in red the SF, in blue the RF), as a function of the filter field current are shown. The other machine parameters are 0.36 Pa of source pressure, 4x100 kW of radio-frequency power, I_{ISBI}=100 A, I_{ISBP}=80 A, 2.4 kV of extraction voltage and 24 kV of acceleration voltage. As the magnetic field increases from 0.7 to 2.7 kA, the co-extracted electron current is reduced from 3.6 to 0.35 A. The beam current instead, estimated by the reconstructed beam emissivity, increases for low values of filter current and then it starts to decrease too, by $\sim$ 37%. To study how the filter field current acts locally, the vertical profiles of reconstructed beam emissivity are shown in Fig.7.12. The vertical beam profiles of the external column are shown at the top, those of the internal one at the bottom; different colours represent various filter field currents; on the left there are the profiles in the SF, on the right the ones in the RF. For all the cases represented, a reduction in the total beam emissivity is measured when the filter field current grows. As already observed in Fig.7.9 and 7.10, the inversion of the filter field current reverses the beam vertical profile too: higher total emissivity at the top in the SF, at the bottom in the RF.

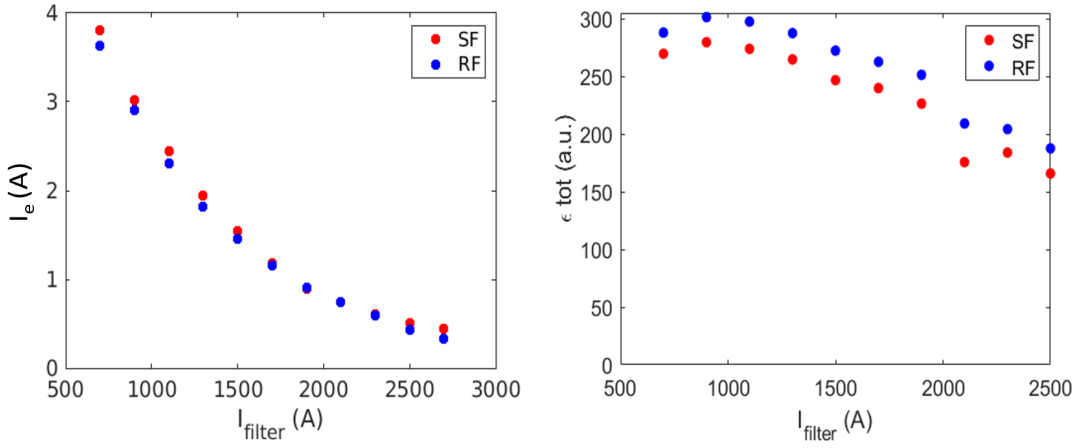

Figure 7.11: *Electron current (on the left) and total reconstructed beam emissivity (on the right) for the two directions of the filter field (in red the SF, in blue the RF) as a function of the filter field current.*

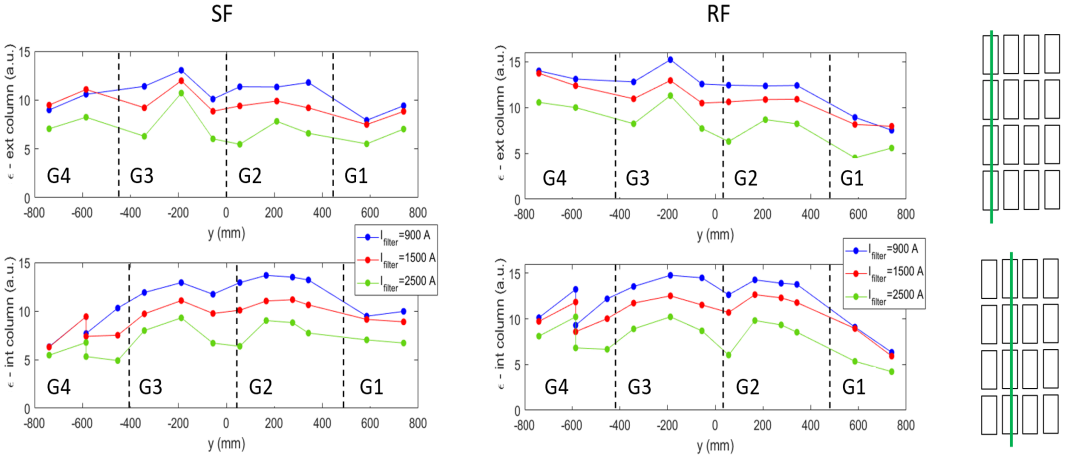

Figure 7.12: *Reconstructed vertical beam profiles as a function of the magnetic filter field, for the two directions of filter current (on the left SF, on the right RF). The profiles on top correspond to the external column of beamlets, at the bottom to the internal ones (as indicated by the scheme on the right).*

The filter field modifies also the shape of the beam emissivity inside the beamlet group: as already observed in SPIDER [116], the difference between the central and the external beamlets current density, for each groups, augments with the filter field strength. This peaking inside the beamlet groups is clearly evident by comparing the shape of the blue profiles ($I_{filter} = 0.9\ kA$) with the one of the green profiles ($I_{filter} = 2.5\ kA$) in

Fig.7.12; with only 28 extracted beamlets, it is clear especially in the G3 and G2 (three open beamlets per column). This could be explained by the projection in the expansion region of the more peaked shape of the plasma inside the drivers with the increase in the filter current, which hinders the sideways expansion of the plasma. This behaviour will be also discussed in surface operation.

As just explained, the filter field direction and strength modify the beamlets emissivity

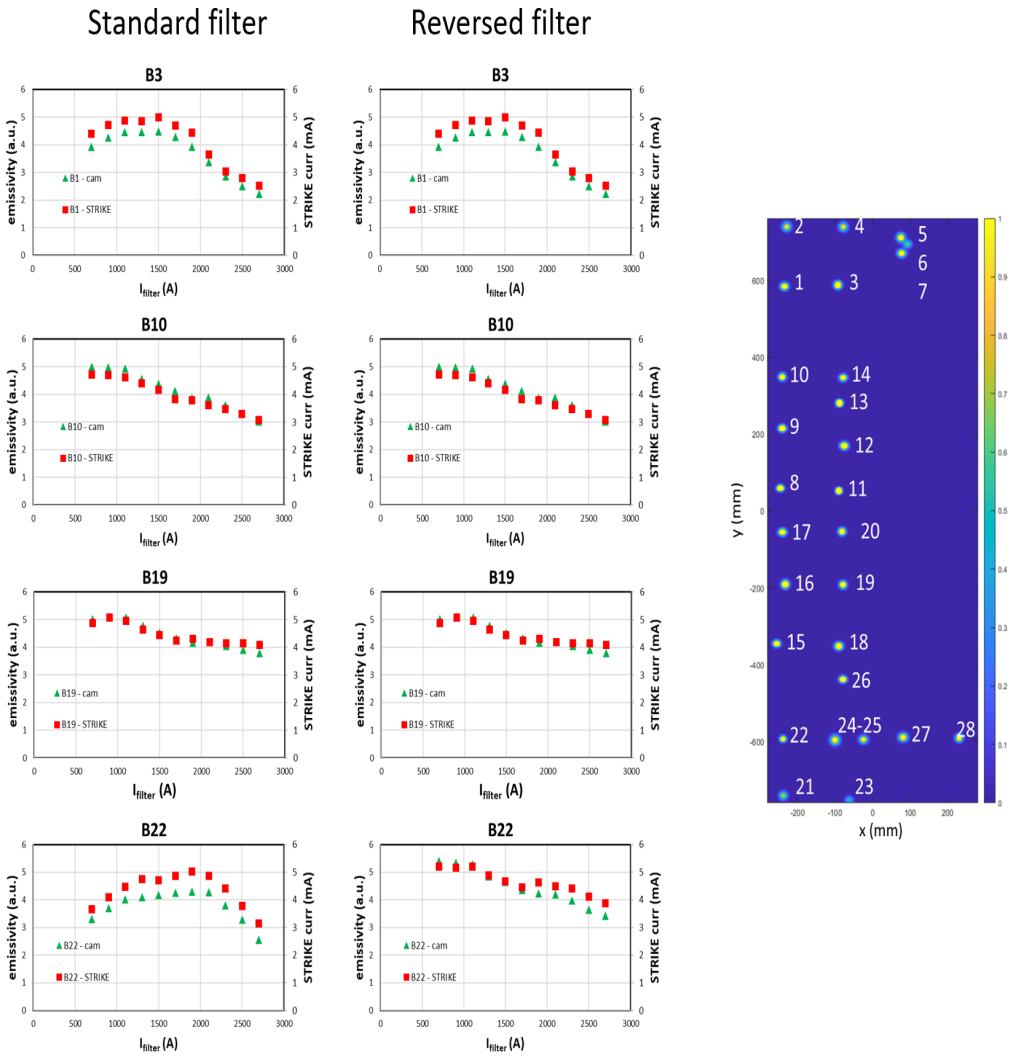

Figure 7.13: *Comparison between the emissivity measured by the cameras (green triangles) and the STRIKE calorimetrical current (red squares) for selected beamlets as a function of the filter field current.*

in a different way, depending respectively on their vertical position and on their relative

location with respect to the centre of the beamlet groups. Figure 7.13 shows the evolution of both the emissivity (green triangles) and the calorimetrical current measured by STRIKE (red squares) of selected beamlets in various positions along the SPIDER beam. The measurements obtained by the two diagnostics have the same trend, confirming the possibility to estimate the beamlet current density from the beamlet induced emission measured by visible cameras. The dependence of the beamlet current density on the filter magnetic field changes along the beam vertical profile. Beamlets B3 and B22, which are respectively located at the centre of G1 and G4, shows the inversion of the vertical profile of the beam current density when the filter field is reversed. For both of them, the emissivity has a maximum and then it decreases with the filter current; the reduction of B3 emissivity (B22) is lower than the one of B22 (B3) in the SF (RF) configuration. The effect of the filter field on the beamlet current is thus stronger in the beamlet group at the bottom in the SF, at the top in the RF. By comparing B19 (central beamlet G3) and B10 (external beamlet G2), the internal dynamics of the beamlet group is highlighted (Fig.7.12) whereas, being both at the centre of the beam vertical profile, no dependence on the filter field direction is found. The reduction in the B10 current density is larger than the one of B19 (central beamlet of S3) with the filter field current as it exceeds 1 kA; this is a consequence of the bell-shaped beamlet profile inside each group, as shown in Fig.7.12.
By summarizing the results in the explored operational regime, the increasing of the filter field reduced not only the co-extracted electron current, but also the beam current (especially in low pressure regimes), although to a lesser extent. The electron current, instead, decreases continuously with the increase of the filter field current, as expected. The optimal value in average is found to be 0.9-1.1 kA: the negative ion current increases while the electron current is reduced. The vertical profile of the SPIDER beam in volume operation is strongly related to the plasma density. This is shown by the inversion of the beam vertical profile when reversing the direction of the filter field, which is the main responsible for the total drift of electrons in the plasma, as well as responsible of the different density of the plasma in the drivers (both in absolute value as well as in the vertical profile), as confirmed by the spectroscopic measurements in the drivers. The effect of the bias currents becomes relevant only when the filter is large (I_{filter}=1.8 kA in the case studied) and it acts differently along the vertical beam profile: at the bottom for the SF, at the top for the RF (see Fig.7.9). The other main effect related to the increase of the filter field is in the emissivity profile of the beamlets belonging to the same beamlet groups, with a larger beamlet current density for the beamlets at the centre with respect to the top and bottom ones (peaking inside the beamlet groups).

7.2 SPIDER beam homogeneity in surface production

In surface production, the negative ions are generated when hydrogen (or deuterium) atoms bounce off walls coated with caesium, which is exploited as a source of electrons. This process is described in detail in Sect. 2.1 . Experimentally, when a small amount of Cs vapour is evaporated into the source, a fast decrease of the co-extracted electron

current occurs, accompanied by a growth of the negative ion current [87]. As described in

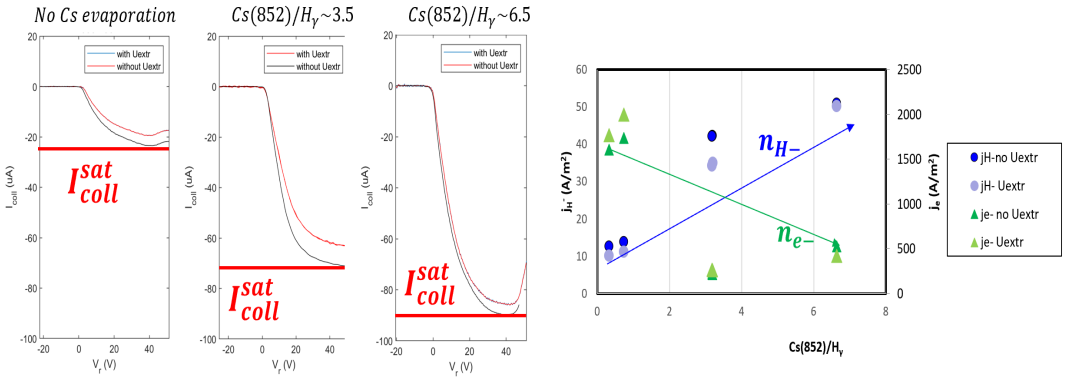

Figure 7.14: *Effect of the caesium evaporation on the negative ion current measured by the dedicated RFEA diagnostic. On the right, the comparison between the negative ion (blue points) and electron currents (green points) as a function of the ratio* $Cs852/H_\gamma$.

Chapter 3, at the negative ion source RNIS (NIFS laboratory) a Retarding Field Energy Analyser diagnostic designed to collect the negative ion current was tested for the first time. The increase in the saturation current, i.e. the negative ions collected by the probe, with the evaporation of caesium is shown in Fig.7.14. The left three panels show that the negative ion current grows as the evaporation of Cs in the source is increased. The current measured by this diagnostic is zero when negative polarization is applied, since it is designed to repel positive ions and, a system of grids, allows to measure only the contribution of the negative ions, capable to reach the last grid, for positive values of polarization. The current grows from less than 20 μA in Cs-free operation to 90 μA, once the caesium coverage is optimized. As an index of the atomic ratio of caesium to hydrogen, the ratio between Cs emission line at 852 nm and the H_γ emission is used. As shown in the panel on the right, as this ratio increases, the negative ion current augments and, in correspondence, the co-extracted electron current is reduced.
The effect of the Cs evaporation on the total beam current and on the beam homogeneity in surface operation in SPIDER are discussed in the following. The dependence on the filter field strength and direction, as well as on the radio-frequency power is analysed. The beam properties in hydrogen are compared with the ones in deuterium, to investigate the isotope effect on the beam homogeneity. The best homogeneity in the explored operational conditions is shown, and the outlook for the future is discussed. All the data refer to the 28 beamlets configuration.

7.2.1 BP and PG biases dependence

Before discussing the beam homogeneity in surface operation when the BP and PG biases are varied, the dependence of the negative ions and of the co-extracted electron currents on these parameters are studied. In Fig.7.15 the negative ion current and the

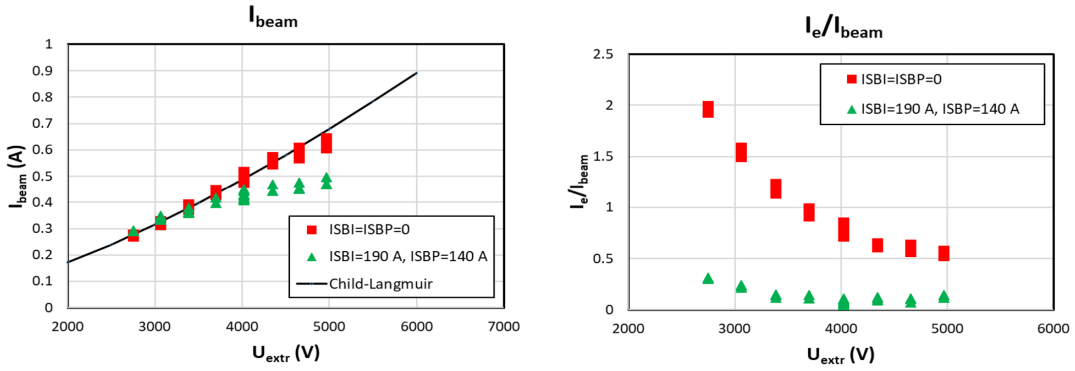

Figure 7.15: *Negative ion (on the left) and electron to ion current ratio as a function of the extraction voltage for two different currents of BP and PG polarization, measured by the power supplies.*

ratio I_{e^-}/I_{H^-} as a function of the extraction voltage, for two different polarization currents of both PG and BP, are shown. These beam currents are obtained with measuring the electric current flowing in the acceleration and extraction gaps. For low extraction voltages, the extracted current is limited by the Child-Langmuir law (black line in the first panel). For the high biases case (green triangles) the current starts to saturate for $U_{extr} > 4\ kV$, to a lower value with respect to the case with no polarization (red squares), where the extracted current starts to saturate for the maximum values of extraction voltage currently available on SPIDER. These data, in fact, are obtained with the optimum value of U_{acc}/U_{extr} voltages ratio, which is found to be between 9.5-10. Since the AGPS power supply is currently limited to 45 kV, the maximum extraction voltage used is 5 kV. The effect of the Cs evaporation is clear by comparing these currents to the ones shown in volume operation in Fig.7.7: the negative ion current measured by the AGPS power supply is three times larger, even if these data were measured at lower radio-frequency power (4x45 kW with respect to 4x100 kW in volume operation). At the same time, the I_{e^-}/I_{H^-} ratio is reduced from 10-5 to less than 1, as shown in the right panel of Fig.7.15. The effect of the biasing of the BP and PG is here more evident. The electron-to-ion ratio is reduced from 0.5 to less than 0.2 by increasing the polarization. These data refer to 1.05 kA of filter current (SF), hydrogen gas and 4x45 kW of radio-frequency power per generator. The reduction of the beam current as well as the co-extracted electrons can be related to the too high BP and PG polarization applied in the low radio-frequency power regime at which these measurements are carried out. The reduction of the electron density in the extraction region, in fact, results in a decrease of the positive ion density, necessary close to the extraction region both to compensate for the large negative charge due to the negative ion production (virtual cathode), and also to contribute to the negative ion generation itself. This is confirmed by the H_β emission shown in Fig.6.17, where the total emissivity decreases when the biases are increased from zero to the maximum polarization current. This effect would

be reduced when SPIDER will operate with the nominal radio-frequency power (4x200 kW).
To understand how the polarization of the BP and PG acts along the vertical profile of the beam, the tomographic reconstruction of the entire beam in these two cases (ISBI=ISBP=0 A on the left, ISBI=190 A ISBP=140 A on the right), together with the beamlet current densities measured by STRIKE calorimeter, are shown in Fig.7.16. All

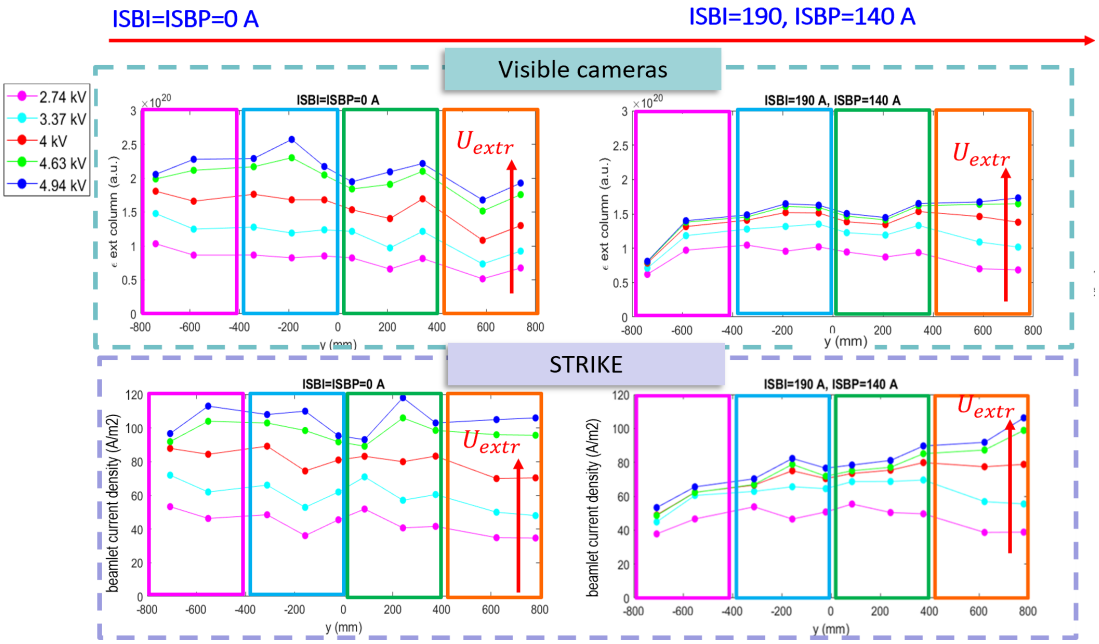

Figure 7.16: *Vertical profiles of the reconstructed beam emissivity of the external column of beamlets (top row) for different extraction voltages and two values of BP and PG polarization: 0 A on the left, 140-190 A on the right. On the bottom, the same vertical profiles in terms of beamlet current density measured by STRIKE calorimeter.*

vertical profiles correspond to the external column of beamlets, which is preferred since the open beamlets in different groups are in the same position with respect to the group itself, allowing to discuss also the internal dynamics of the beamlet groups.
The beam profiles obtained through tomographic inversion (on top) are very similar to the one measured by STRIKE calorimeter (on bottom), both as a function of the extraction voltage (various colours) and of the BP and PG biases. The discrepancies between the two measurements, evident especially in the larger increase of the beamlet current density measured by STRIKE at the top of the beam in the high biases case, can be in part attributable to the error associated to the calibration procedure of the two diagnostics. The STRIKE calorimeter, in fact, is composed by 16 tiles which may have a non-homogeneous heat transmission; the error associated to the tomographic reconstruction, instead, is related both to the relative calibration of the cameras and to the inversion procedure.

As already shown by the beam electrical measurements, when the bias is zero and the extraction voltage increases, the beamlet total emissivity (and thus the beamlet current density) grows continuously; Fig.7.16 (on the left) shows how this increment is homogeneous along the whole vertical beam profile. This is not the case when the biases are higher: the total emissivity saturates at lower U_{extr} (as the electrical current); different saturation extraction voltages are found for beamlets at different vertical coordinates. At the top, the beam emissivity continues to increase with the extraction voltage while, at the bottom, the current does not grow. In particular, the beamlet at the bottom of G4 is the one with the lowest emissivity. This is representative of a non-homogeneous distribution of the negative ion availability along the beam vertical profile, which enhances as the biases are increased. This is confirmed also by the spectroscopic and electrostatic measurements shown in Fig.6.12 and 6.13. With the SF, in fact, both the H_β and the ion saturation current in the S4 is lower with respect to the other segments, and they decrease with the BP and PG polarization. A lower plasma density results in a lower probability of producing negative ions, thus it can explain the smaller amount of extracted current at the bottom of the beam. This is also confirmed by the H_α/H_β vertical profiles shown in Fig.6.18: this ratio can be used to estimate the negative ion density and, for all values of bias, it is minimal at the bottom of the source (S4, at 5 mm from the PG).
Another dynamics between the beamlet groups is evinced from these profiles: depending on their vertical position, the central and top-bottom beamlets of each group behave differently. By looking at the profiles with low biases (the ones with the larger beamlet current density) the emissivity of the central beamlet of the G1 (y=585 mm) is always lower with respect the one of the external beamlet (y=739 mm). The opposite happens between the two beamlets of the G4, for large extraction voltages. This can be explained in terms of the different availability of negative ions and of the Gaussian profile of the beamlet group emissivity. In fact, if the beamlet space charge is too large, a fraction of the beamlet can be lost inside the accelerator (beamlet scraping) if the extraction voltage applied is not enough. This is described in details in Chapter 5 and shown in Fig.2.5 (too convex meniscus case). Where the negative ion density is lower (at the bottom of the beam) all the current is transmitted through the accelerator. This process can explain the different behaviour of central beamlets in different vertical positions. The external beamlets, instead, due to the Gaussian shape of the beamlet groups shown previously (in volume operation, Fig.7.12), have a lower current density and they are fully transmitted through the accelerator. These two effects explain the different behaviour observed for the central and external beamlets of the G1. The same happens in the G2, especially for the lower values of extraction voltage. As the voltage is increased enough, all the current starts to be transmitted also in the central beamlet and the difference between the central and external beamlet current densities decreases for the highest voltage. This effect is reduced moving towards the bottom of the beam, as it can be seen from the behaviour of central and lateral beamlets of the G3 and G4: all the current is extracted from all the beamlets as the voltage is increased, resulting in a larger total emissivity for the beamlet at the bottom with respect to the ones at the top.

This highlights the different distribution of the negative ion density along the vertical profile of the source in the extraction region: higher density at the top with respect to the bottom. This unbalance becomes larger when the biases are increased. Since in these conditions the availability of negative ion is reduced everywhere along the vertical profile (as a consequence of the reduction in plasma density close to the extraction region described before), in the region where the negative ion density is larger (at the top), the beamlet emissivity grows as the extraction voltage is increased. Where the negative ions density is lower, instead, the extractable current cannot increase any more with the voltage, resulting in a more asymmetric vertical beam profile.
This behaviour can be described also in terms of RMS/average of the 28 reconstructed beamlet emissivity (Eq.7.1), as an estimate of the non-uniformity of the beam. The dependence of this parameter on the extraction voltage for the two different values of BP and PG biases is shown in Fig.7.17. In these curves, the two behaviours just described

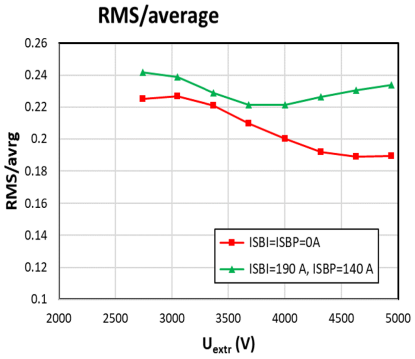

Figure 7.17: *RMS/average for the 28 reconstructed beamlets as a function of the extraction voltage for two different values of BP and PG polarization.*

are evident: for low extraction voltages, especially in the low bias case (red squares, larger beamlet current density) the beam homogeneity is affected by the not optimal transmission of all the extracted beamlet throughout the accelerator system (scraping on the EG). In the high bias case, instead, after an optimum the RMS starts to increase again with the voltage growth, due to the vertical non-homogeneous distribution of the negative ions density along the source. The lowest RMS is measured at low biases, corresponding to $\sim 19\%$. To quantitatively represents the different growth of the total beam emissivity inside each beamlet group with the extraction voltage, in Fig.7.18 the ratio between the total emissivity of the each group with respect to G1 is shown. The dynamics between the groups is more evident. The squares represent the ratio between the beamlet groups with 0 A, the triangles with 140-190 A of BP and PG polarization currents. In the low polarization case, the higher emissivity is measured in G4 with respect to G1, the opposite happens when the bias currents are high. Here, in fact, the total extracted current is reduced everywhere and there is no beamlet scraping due to the too large space charge, even at the top of the beam. This results in a larger emissiv-

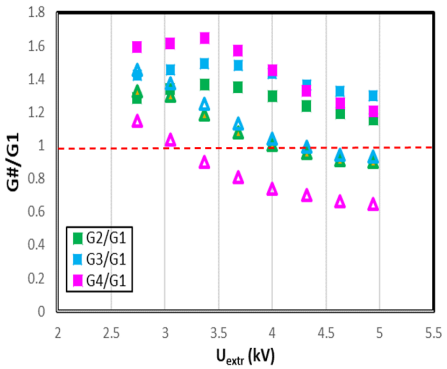

Figure 7.18: *Ratio between the total emissivity of each group with respect to G1, as a function of the extraction voltage. The squares corresponds to 0 A, the triangles to 140-190 A of BP and PG polarization currents; the colours represent the different groups (same as Fig.7.16) .*

ity in the G1. Furthermore, G4 becomes the one with the lowest emissivity, confirming the non-homogeneous availability of negative ions along the vertical profile.

The beam homogeneity can be discussed also in terms of beamlet width, which is proportional to beamlet divergence. As explained in Chapters 3 and 4, both with visible cameras and with STRIKE calorimeter it is possible to measure the vertical width of the extracted beamlets. The vertical profiles of the beamlets width w_y measured by visible cameras (top row) and by STRIKE calorimeter (bottom row) as a function of the extraction voltage and for two different values of BP and PG polarization currents are shown in Fig.7.19; on the left with 0 A, on the right with 140-190 A of BP and PG polarization currents. The shape of the profiles measured by the two diagnostics is very similar. The difference in the absolute value is related to the fact that visible cameras are looking at 35 cm along the beam propagation direction, from the grounded grid, while STRIKE is measuring at 50 cm; furthermore, the beamlet footprint on STRIKE is measured on the back of the tiles, resulting in an additional enlargement of the beamlet width. The relation between the beamlet width and the beamlet current density is discussed in details in Chapter 5. However, it is evident that, when the beam emissivity profile becomes more homogeneous, the beamlet width is more homogeneous too. With low bias currents, the homogeneity of the vertical profile improves with the extraction voltage. The opposite happens when the polarization of the BP and PG is higher, in particular at the bottom of the beam, where also the beamlet current is minimal.

The effect of the BP and PG polarization were also investigated separately. In Fig.7.20 the vertical profiles of the beam emissivity of the external column of beamlets are shown for different polarization currents of PG and BP. The larger effect on the beam profile is given by the polarization of the PG: this can be seen by comparing the green profile with the blue one, respectively with ISBI=140 A, ISBP=0 A and ISBI=ISBP=0 A. When

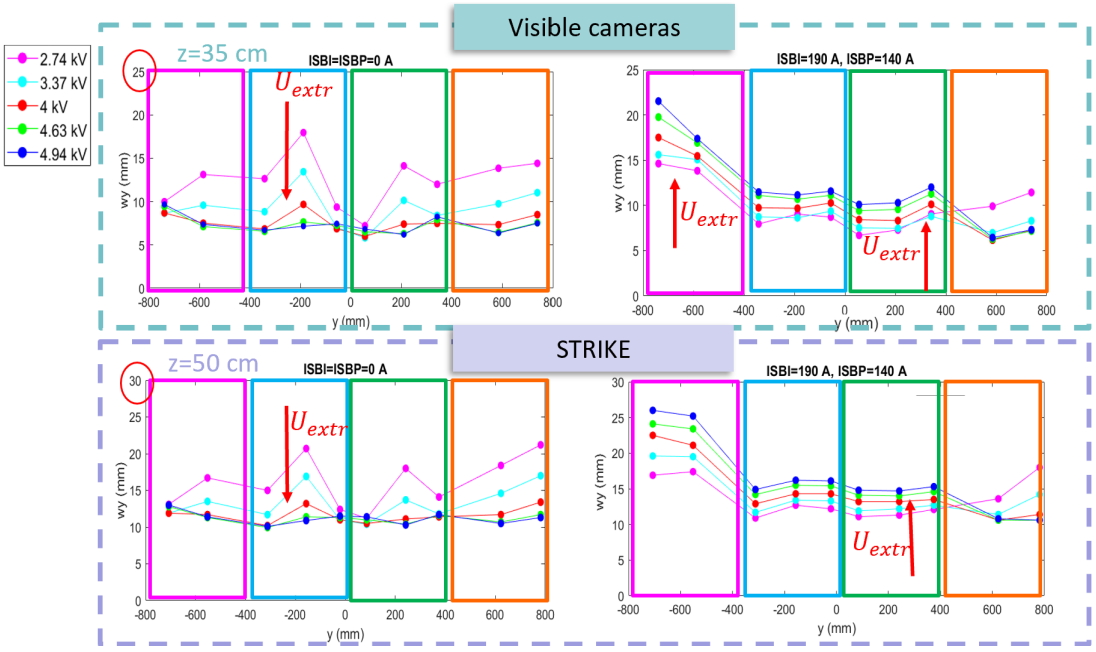

Figure 7.19: *Vertical profiles of the beamlets width measured by visible cameras (top row) and by STRIKE calorimeter (bottom row) of the external column of beamlets for different extraction voltages and two values of BP and PG polarization: 0 A on the left, 140-190 A on the right.*

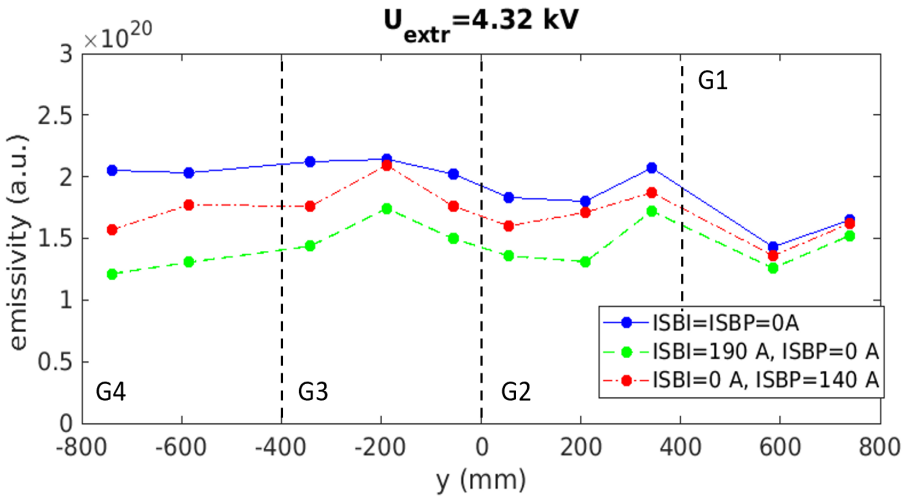

Figure 7.20: *Vertical profiles of the beam emissivity of the external column of beamlets for different polarization currents of ISBI and ISBP.*

the PG polarization is zero and the BP is polarized with the maximum current (140 A, red data in Fig.7.20), the decrease of the beam current is lower with respect to the case with high current on the PG and zero on the BP. Also in these cases, the major effect of the bias is at the bottom of the beam (G3-G4), while the G2 and G1 remain almost unvaried. No modifications of the beamlet group internal dynamics is seen when only one of the two bias currents is changed. The effect of biasing only the BP or PG

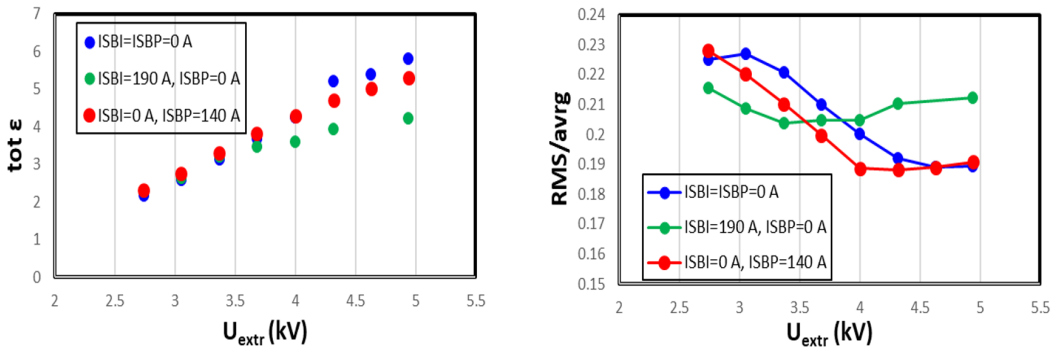

Figure 7.21: *Total beam emissivity (on the left) and RMS/average (on the right) as a function of the extraction voltage for different biases of the BP and PG.*

on the total emissivity of the beam (thus on the total beam current) and on the RMS is shown in Fig.7.21. As seen with the vertical profiles, the lower beam current is extracted when the bias of the PG is maximum and BP is not polarized (green points). When only the BP is polarized and the PG bias is zero (red marks), the beam total current decreases with respect to the case with no polarization of either grids, but only by 10% with respect to 30% with the ISBI=190 A, for the highest extraction voltage. This reflects the evolution of the beam RMS with the extraction voltage and different bias currents. The RMS is larger when the bias of the plasma grid is maximum. It slightly decreases as the extraction voltage grows, and then it increases again. Without grid bias, the RMS is higher than the other two cases for low extraction voltages, due to the space charge limit on the extracted current (negative ion density too large relative to the applied extraction voltage). It decreases continuously as the extraction voltage increases. Similar is the behaviour when only the bias plate is polarized, although the RMS reaches a minimum and then it starts to rise again with the extraction voltage. The RMS has its minimum for the case with ISBI=190 A and ISBP=0 A equal 20.5%, confirming the strongest effect of the polarization of the PG. This value is larger with respect to the minimum measured in the other two cases (around 19%). This is related to the fact that negative ions are produced through atoms bouncing off the PG surface coated with caesium, so the plasma in front of the PG dominates the beam profile shape. However, also the polarization of only the BP modifies the beam profile mostly in the bottom part. The reduction in the H_α/H_β shown in Fig.6.18 may explain the larger

reduction in the total beam current extracted when the PG is polarized (see Fig.7.20 and 7.21, in terms of beam emissivity).

7.2.2 Dependence on the magnetic filter field strength and direction

As already shown in Cs-free operation, both the filter field strength and direction affect the shape of the beam. Firstly, the effect of the filter current increase in the SF configuration is studied. The vertical profiles of the beam emissivity for two values of extraction voltage (4.63 kV solid lines, 3.05 kV dashed lines) and three values of filter field current are shown in Fig.7.22; in both cases, the acceleration voltage is varied to keep the ratio R constant and equal to 9.5 (optimum of the beam optics). Depending on

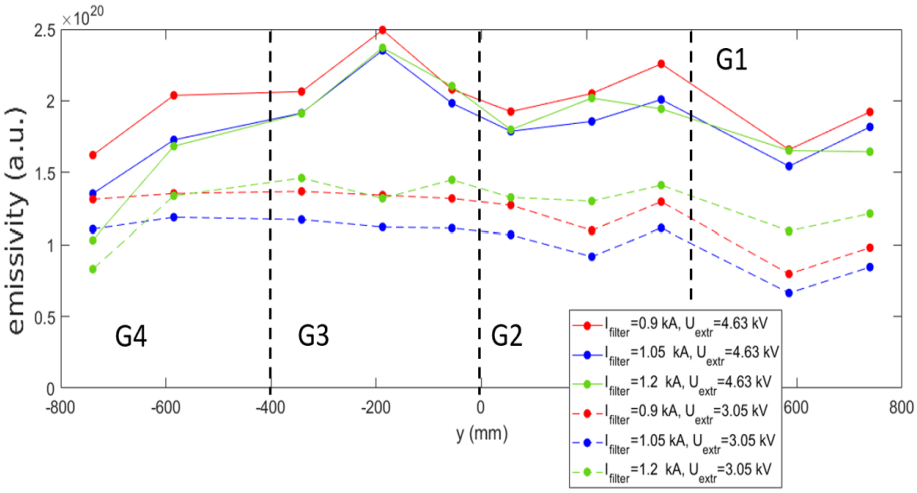

Figure 7.22: *Beam emissivity vertical profiles of the external column of beamlets for filter field currents (different colours) and extraction voltages (solid and dashed lines).*

the extraction voltage, the total beam emissivity is larger at different filter fields. When the voltage is lower (case with 3.05 kV, dashed lines), the largest emissivity is measured with the highest filter, the opposite for $U_{extr} = 4.63$ kV. This can be explained in terms of total negative ion availability. By increasing the filter, in fact, the electron density is reduced in the extraction region. As observed in the previous section, the reduction in the plasma density affects also the extractable negative ion current. If the space charge is too large, at low extraction voltage the beamlet scraping on the EG occurs, thus reducing the total accelerated beam current. This explains the larger emissivity at high filter and low extraction voltage. Only for the beamlet at the bottom (y=-739 mm) the emissivity reduces with the filter field, confirming the stronger effect of the filter field on the bottom of the beam in the SF configuration, as well the lower negative ion density at the bottom. When the extraction voltage is larger, the extractable negative ions with high filter saturate while, for the cases with lower filter current, more ions are extracted.

This behaviour explains the dependence of the total emissivity on the extraction voltage for the three values of filter field current shown in Fig.7.23 (on the left), and also the behaviour of the vertical profiles. The Gaussian shape of the beamlet groups seen in volume operation (in Fig.7.12) here is evident only in G4 and $U_{extr} = 3.05$ kV, which is the region where the density of negative ions is lower, as confirmed by H_α/H_β profiles in Fig.6.22. As the filter current increases, for both values of extraction voltage, the difference between the central beamlet (y=-585 mm) and the external beamlet (y=-739 mm) increases. With the highest extraction voltage, instead, the Gaussian shape is evident in both G4 and G3, in G2 for the maximum filter current, confirming the reduction of the negative ion density along the whole vertical profile of the beam. The dependence of the

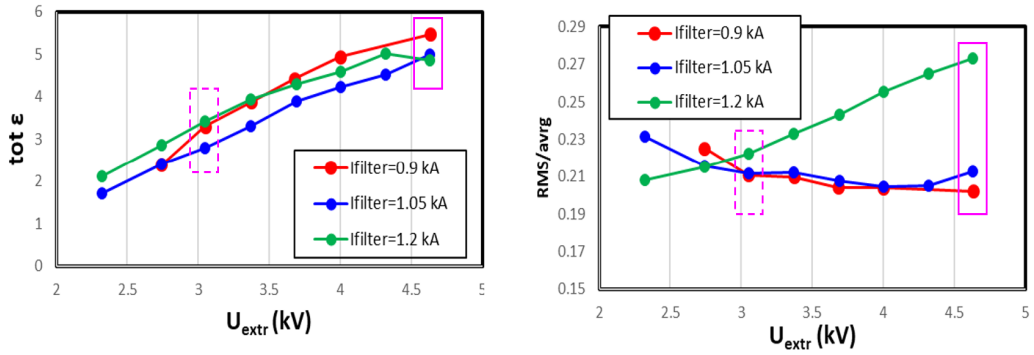

Figure 7.23: *Total beam emissivity (on the left) and average RMS (on the right) as a function of the extraction voltage for three different filter field currents (SF) The extraction voltages corresponding to the profiles shown in Fig.7.22 are highlighted by the pink boxes.*

RMS on the extraction voltages for different values of filter field (Fig.7.23 on the right) is a combination of these two effects, the accelerator transmission and the availability of negative ions to be extracted along the vertical beam profile.
The effect of inversion of the magnetic field on the vertical profiles of the beamlet emissivity (at top) and beamlets width (at the bottom) is shown in Fig.7.24. These data refer to 4-40 kV of extraction and acceleration voltages, ISBI=0 A, ISBP= 140 A, 0.36 Pa of source pressure and 4x45k W of radio-frequency power; the red profiles are in the SF and the green ones in the RF configuration; the filter current is 1.05 kA. As seen in volume operation (Fig.7.12), when the direction of the filter field is reversed, the vertical beam profile (both the emissivity and the w_y) inverts too. The plasma evolution from the drivers to the PG is shown in Fig.6.19. The inversion of the filter field affects mainly the profile of the plasma light in the drivers, which inverts when the filter field is reversed: larger H_α signal at the top with the SF, the opposite with the RF. The vertical profile of the electron temperature at the PG, shown in Fig.6.21, behaves exactly as the beam emissivity: the temperature is lower everywhere when the filter field is reversed

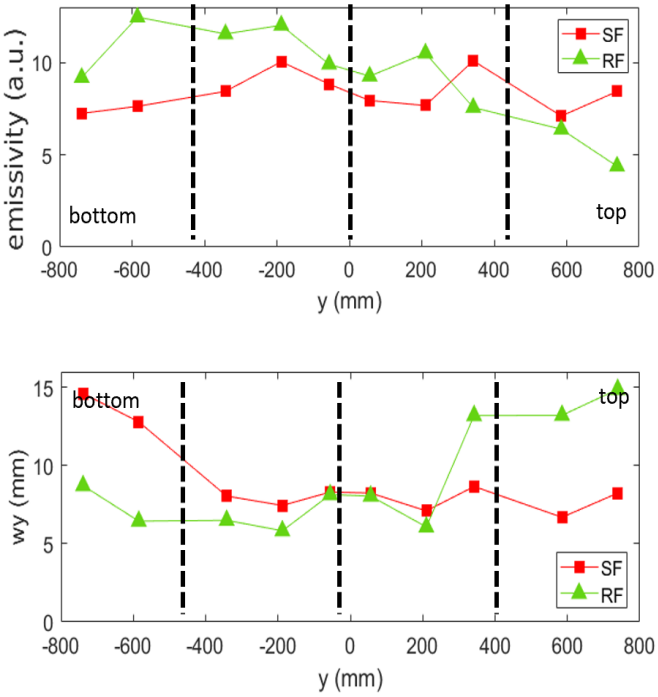

Figure 7.24: *Vertical profiles of the beamlets emissivity (at the top) and width (at the bottom) of the external column of beamlets for the two directions of the filter field.*

except in S1. Lower electron temperature close to the extraction region means lower negative ions destruction probability, which could explain the increase in the extracted current everywhere except in S1, as shown in Fig.7.24. When the direction of the filter field is reversed, the concentration of negative io inverts too: larger at the top with the SF, the opposite with the RF. This behaviour is confirmed by all measurements (both electrostatic and spectroscopic).

7.2.3 Unbalancing the radio-frequency power

All measurements shown above, demonstrate that the vertical beam current density profile is unbalanced: it is lower at the bottom than at the top in the SF configuration, the opposite in the RF. To compensate for that in the standard configuration, the radio-frequency power delivered by the 4 generators is unbalanced, trying to compensate the lower amount of negative ions by increasing the radio-frequency power of the generator at the bottom with respect to the others. The vertical profiles of the reconstructed beam emissivity for two values of extraction voltage and with all generators supplying the same power (solid lines) and unbalanced radio-frequency power (dashed lines) are shown in Fig.7.25 at the top; at the bottom, the vertical width in the two configurations

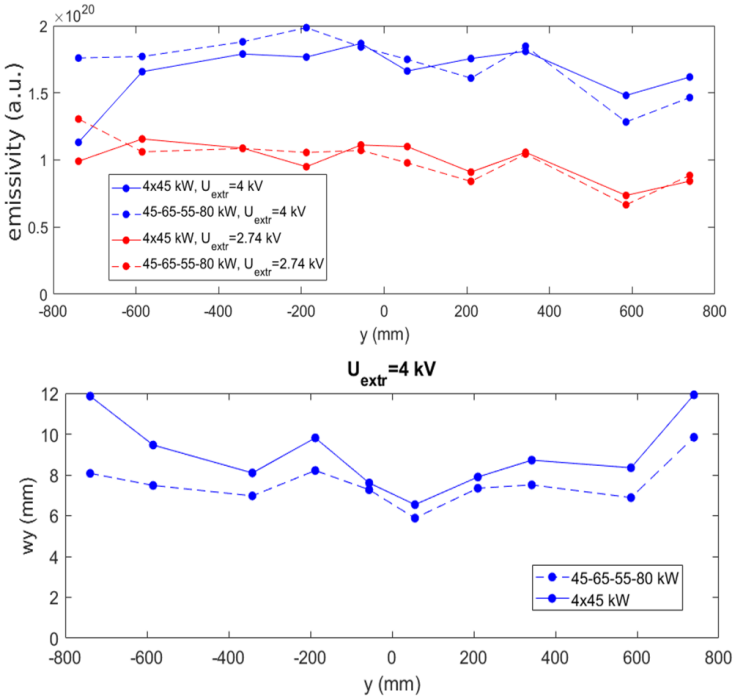

Figure 7.25: *Vertical profiles of the beamlets emissivity (at the top) and width (at the bottom) of the external column of beamlets for two values of extraction voltages and different radio-frequency powers applied to the 4 generators.*

and $U_{extr} = 4kV$. From the top to the bottom of the plasma source, the applied power in the unbalanced configuration is 45-65-55-70 kW per generator. The effect of such unbalancing is evident in the beam vertical profile, especially in the case with high voltage applied. The beam emissivity at the bottom increases with respect to the case with uniform input power. The same holds for the vertical width of the beamlets, resulting in a more homogeneous profile and in a decrease of the width especially at the bottom of the beam, due to the increase in the extracted negative ion current. This is just a preliminary results and it is tested only at low power. However, the unbalancing of the power applied to the generators could be a way to improve the beam homogeneity. It is not straightforward that this behaviour will be repeatable also at higher power. If it is related to an unbalancing in the total drift of the plasma, in opposition to the drift due to the filter field (here in SF configuration), it could work also with higher power.

7.2.4 PG temperature

The beam divergence and homogeneity when the temperature of the PG is varied is described in details in Section 5.1.3

7.2.5 Isotope effect: D vs H

The experimental time dedicated to the deuterium beam with caesium injection was limited to two experimental days, thus only a preliminary study on the isotopic effect was performed. In Fig.7.26 the comparison between the current of the ions (in red), the

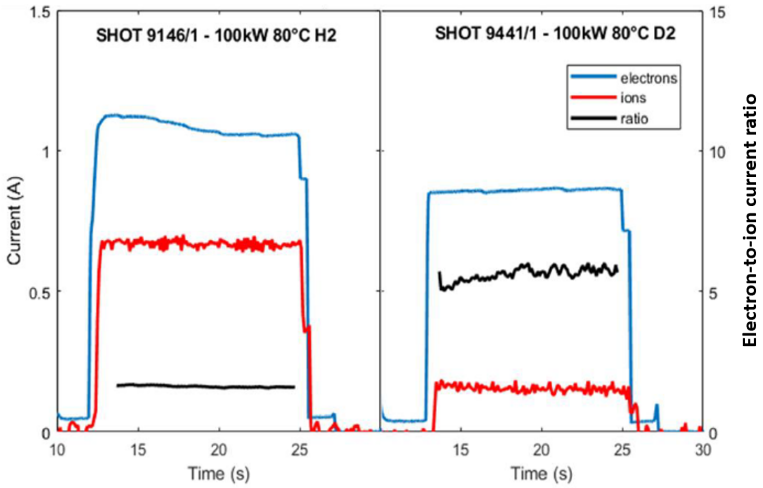

Figure 7.26: *Comparison between H (on the left) and D (on the right) beam operation in terms of extracted ions, electrons and ratio electron to ions currents.*

co-extracted electrons (in blue) and the ratio between electron-to-ion current (in black) in hydrogen and deuterium beam are shown. As already seen in other negative ion sources [117], the most important difference between hydrogen and deuterium operation is in the amount of co-extracted electrons with respect to the negative ions current, which is larger in D beam, together with the lower negative ion beam current. It has also to be taken into account the fact that, due to the limited operational time, the conditioning of the source was not optimal. A study on the effect of the biasing of both PG and BP is performed also with D beam. The data are obtained with 4x100 kW, 7 kV and 45 kV of extraction and acceleration voltages, thus not in perveance match (R=6.4 instead of 9.5-10), and 2.5 kA of filter current, due to the higher co-extracted electron current. The vertical profiles of the reconstructed emissivity are shown in Fig.7.27. The D beam behaves similarly to the H beam shown in Fig.7.16. As the biases are increased, the total beam emissivity is reduced: from 0 A to 140-190 A of BP and PG polarization currents, the total emissivity is reduced by 40%. By looking at the vertical profile, the G4 emissivity is reduced by 50%, while G1 one by 28 %, confirming the non-homogeneous distribution of available negative ions along the beam vertical profile, already detected in H beam. This results in an increase of the average RMS, as indicated in Fig.7.27. The Gaussian shape of the beamlet is evident in all the beamlet groups except G1, for all biases: the emissivity of the central beamlet is always larger than the one of the external beamlets. The dependence on the extraction voltage of both the beamlet current density

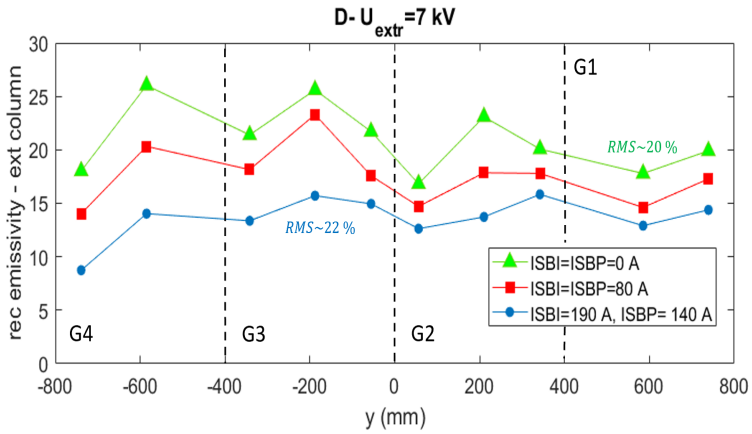

Figure 7.27: *Vertical profiles of the beam emissivity vertical profiles for different BP and PG currents for D beam.*

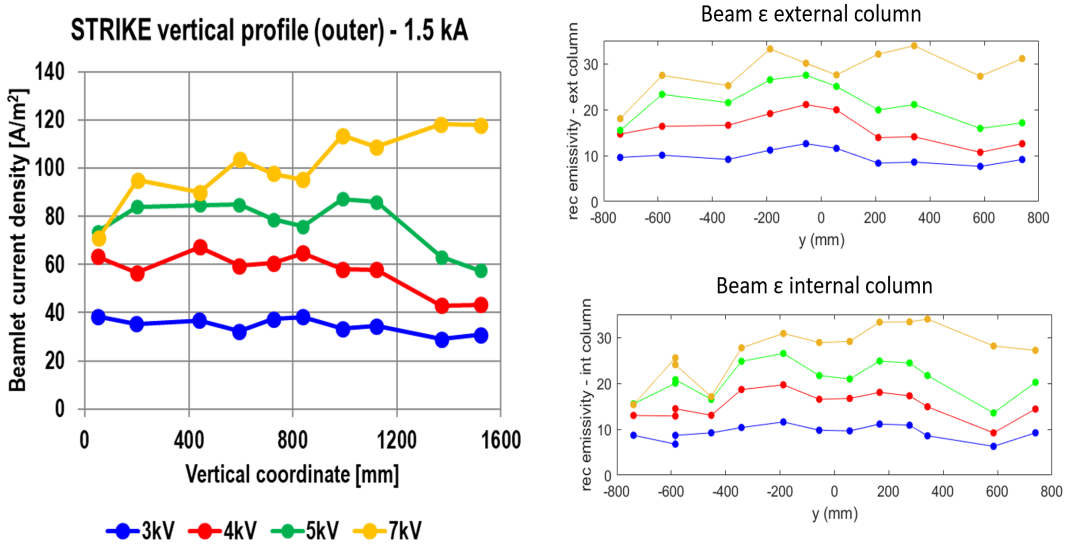

Figure 7.28: *Beamlet current density (on the left) and beamlet emissivity (on the right) vertical profiles for different extraction voltages. The beam emissivity vertical profiles for both the column of beamlet are shown: the external at the top, the internal at the bottom.*

measured by STRIKE (on the left) and the reconstructed beam emissivity (on the right) vertical profiles are shown in Fig.7.28. For the beam emissivity both the columns of beamlet are represented. As expected, as the extraction voltage is increased, the top-bottom non-homogeneity grows; this behaviour holds for both the columns of beamlets, as shown by the reconstructed emissivity. A good agreement between the STRIKE

beamlet current densities and the reconstructed beam emissivity is found. For both diagnostics, as the extraction voltage increases, the already discussed Gaussian shape of the beamlet groups grows too.
Regarding the beam vertical profile, no strong modification with respect the H beam is found: the dependence on the biases and on the extraction voltage is the same. The only strong difference is in the co-extracted electrons, which is larger with respect to the H beam, and in the total beam current, which is lower.

Conclusions and perspectives

In this thesis work, a characterization as complete as possible of the negative ion source and beam of SPIDER experiment is proposed. I analysed the large size negative ion beam divergence and homogeneity, starting from the results obtained through the visible tomography, and I correlated them with the plasma properties.
SPIDER is the full-size prototype of the negative ion source for ITER Heating Neutral Beam Injector (HNB). Its goal is the optimization of the production and extraction of negative ions, in view of MITICA operation, the one-to-one prototype of the entire HNB for ITER. Among the various requirements to be satisfied, SPIDER aims to obtain the required negative ion current, electron-to-ion ratio and pulse duration, as well as the beam divergence and homogeneity needed. During summer 2021, SPIDER operation with caesium evaporation was performed for the first time. Despite several technological limits, a first study of the source and beam performances during surface production was carried out, which is of major interest for the future HNB. Herein also the results of volume operation are described, as their knowledge proved important for the successful operation with caesium. SPIDER aims also at demonstrating the capability of diagnosing both the plasma and the beam using a complete set of diagnostic system. In MITICA and in future HNB, in fact, only a limited amount of diagnostics will be available, so in SPIDER as much information as possible both on the plasma and the beam needs to be acquired. It is also a test-bed to improve the data analysis techniques for all the diagnostic systems.

In particular I have developed the visible tomography as a new non-invasive and complete diagnostic to characterize the large negative ion beam. I first installed this diagnostic system on the small negative ion source NIO1, proving its capability in studying the divergence and homogeneity of a small negative ion beam. Then, I took care of the installation of a large set of visible cameras on SPIDER. The method I developed to calibrate all of them, both relatively and geometrically (i.e. to write the correct equations of their lines-of-sight) was for the first time applied, proving its capability of reconstructing the entire two dimensional pattern of the beam emission. I performed the tomographic inversion by developing the Simultaneous Algebraic Reconstruction Technique (SART) algorithm, and the results obtained are compared with the ones given with STRIKE calorimeter, demonstrating a good agreement between such completely different diagnostics. The algorithm is based on an error correcting procedure and on

the pixel method: the beam emission pattern is subdivided in pixels, in which the emissivity of each pixel is unknown. Different number and sizes of the pixels were tested, and the limit and the resolution of the technique were assessed. From the comparison between the experimental and reconstructed profiles, a good agreement was found both on NIO1 and on SPIDER beam. I used the reconstructed 2D beam emission patterns to characterize the homogeneity of SPIDER beam, giving one value of emissivity for each open beamlet. Furthermore, I developed a model that takes into account the beam composition during its propagation, its energy and the background gas density, which are the main parameters in determining the visible light emission, allowing to directly estimate the beamlet current density. Thanks to the single beamlet configuration in which most of the 1280 apertures are closed due to the pumping system limitations, I also exploited visible cameras to estimate the beam divergence. In these beam conditions, I demonstrated the capability of visible cameras in studying the beamlet shape, and their results are confirmed by the other measurements available. The estimations obtained are then used to study SPIDER beam divergence.

Starting from the light emitted by the beam, I demonstrated that it is possible to study the negative ion beam in terms of homogeneity and divergence, the latter in the specific configuration in which most of the apertures are masked. For the first time the 2D pattern of the beam emissivity was reconstructed. The main source of error of this technique is attributable to the relative calibration of the cameras composing the diagnostics. Another uncertainty is intrinsic to ill-posed mathematical problems like the tomographic inversion technique, which can be further improved to better reproduce the experimental data by ameliorating the algorithm presented and by comparing the results obtained by different algorithms. The method developed to characterize the negative ion beam will be exploited also when all 1280 beamlets will be extracted. Even if it will be not possible to study the single beamlet behaviour any more, an estimation of the beam homogeneity inside each beamlet group is expected to be achievable. Furthermore, the larger total beam emission will allow to install H_α filter on the cameras, in order to decrease eventual sources of error of the measurement, by reducing the background noise. All these results are very important because this diagnostic system will be used also in MITICA, and it can be exploited also in future HNB, since it does not perturb the beam and it only needs viewports through which the beam light can be observed.

The main results achieved from the analyses of the experimental data are here summarized. I estimated the divergence of the beam of SPIDER, and I compared the results with the ones of other existing sources. Moving from volume to surface production, the optimum of divergence decreased from 20 mrad to 12 mrad, at perveance match. This value is similar to the one measured in BUG and NIO1, the other two radio-frequency driven negative ion sources studied in this thesis. This beam divergence is still larger with respect the 7 mrad required for the beam of ITER HNB, which has never been reached by the existing radio-frequency driven negative ion sources. In the arc source type, instead, an even lower divergence is measured. The ion temperature plays a key

role in determining the beam divergence, as high energetic positive ions could transfer their energy to hydrogen atoms in the expansion chamber, fostering the generation of fast negative ions, or directly generate negative ions at the converter. To demonstrate the role of the ion temperature in the beam divergence, a dedicated NI-RFEA, capable of measuring the negative ion axial velocity distribution, was tested for the first time in the NIFS-RNIS arc source, together with another RFEA probe to simultaneously study also the positive ion velocity distribution. The latter was then installed on SPIDER, to correlate the positive ions temperature with the beam performance in these two types of source. From the analysis of the experimental results, I estimated a wider positive ion velocity distribution in the radio-frequency source (20-30 eV) with respect to the arc one (few eV). I studied its shape in many operational regimes, by varying the source pressure, the radio-frequency power and the biasing of the grids, and correlated them with the beam optics, since all of these parameters modify the plasma density in front of the extraction region.

From the analysis of the vertical profile of the beam divergence I obtained another important result: beamlets in different positions, both with respect to the whole beam and inside each beamlet group, have a diverse divergence and behave differently when the source parameters are varied. This reflects the beam dis-homogeneity in terms of beamlet current density. In particular, both in surface and in volume operation, the beamlets at the bottom of the beam always exhibit a larger divergence with respect to the others. When the plasma density is increased, by raising the source pressure and the radio-frequency power, an improvement in the optics is found, especially for these beamlets. To increase the survival probability of negative ions, a magnetic filter field is generated through a current flowing in the Plasma Grid, which reduces the electron temperature close to the extraction region. It induces cross-B drifts on the magnetized electrons in the plasma, both on vertical and horizontal direction, modifying the profile of the plasma in the expansion region. To understand the role of the filter field in the top/bottom beam dis-homogeneity, I studied the dependence of the plasma on its modification, both in strength and direction, from the drivers up to the extraction region. As the filter field is increased, the plasma light measured in the drivers grows, resulting in a better confined plasma with a peaked density profile at the centre of the driver, but it acts differently on the various pairs of drivers: a lower emission is measured at the bottom of the source in the standard direction of the filter field, at the top in the reversed one. Such a dependence on the filter field of the measured top/bottom dis-homogeneity is confirmed by the fact that also the beam profile inverts when the direction of the filter field is reversed. This is observed also in other existing negative ion sources, thus confirming that the filter field is one of the principal sources of beam dis-homogeneity. The filter field does not only modify the overall beam vertical profile, but it also affects the beamlet density profile inside the beamlet groups. As the filter grows, the difference between the current density of the central beamlets with respect to the top and bottom ones increases, both in surface and volume operation. This (piece of evidence) could be a direct consequence of the more peaked plasma profile measured inside the drivers.

From the analysis of plasma emission, another peculiar behaviour is found inside the SPIDER source: when the filter field is reversed, the difference between the plasma light measured in the pairs of driver is reduced, resulting in a denser plasma with the same radio-frequency power and source pressure. This means also a larger beam current density, in both volume and surface production. The increase in the left-right symmetry of the plasma density in the driver is still unclear, since no source of horizontal unbalancing should be present. This is probably related to the design of the filter field and of the source itself.

Together with the filter field strength and direction, I also analysed both the plasma and beam homogeneity when the polarization of the Bias Plate and of the Plasma Grid are varied. When their polarizations change, both the plasma in the drivers and in the expansion region modifies, in the same way with and without caesium evaporation. In particular, two different plasma profiles are found in front of the Bias Plate and in front of the Plasma Grid, both from the spectroscopic and electrostatic measurements, thus confirming the relevance of the first in modifying the plasma vertical profile and the diverse properties of the plasma as it approaches the extraction region. The behaviour of the beam, instead, is different in surface operation with respect to volume operation. The increase of the bias slightly reduces the beam top-bottom dis-homogeneity in volume operation, by increasing the beamlet current density at the bottom of the beam in the standard direction, at the top in the reverse direction. This reflects the behaviour of the plasma light inside the drivers, which enhances with the biases respectively at the bottom and at the top of the source, in the two configurations. The local increase of the beam current density can thus be related to the larger plasma density and, as a consequence, a higher probability of negative ion production in the whole plasma volume. With Cs evaporation, instead, the biases are studied only in the standard magnetic filter field configuration and at low power regime. In these conditions, the increase of the polarization both of the Bias Plate and of the Plasma Grid reduces the amount of negative ions extracted, especially at the bottom of the beam, where the availability of negative ions is always lower with respect to the top, as suggested by spectroscopic measurements of H_α/H_β emission ratio in the extraction region. The beam dis-homogeneity is thus increased by the BP and PG polarizations. The different beam behaviour in volume and surface production can be explained by the fact that in the latter, the negative ions are produced mainly on the plasma grid, thus it is the plasma in this region which plays the main role in determining the beam shape.

A solution found and tested experimentally for reducing the top/bottom dis-homogeneity is the unbalance of the radio-frequency power applied to the 4 pairs of drivers: the beam vertical profile becomes more homogeneous when a larger radio-frequency power is applied to the drivers at the bottom with respect to the ones at the top. This method works for radio-frequency power comprised between 45 and 80 kW per generator. Further experiments have to be carried out at larger radio-frequency power, to see if this solution is applicable also to these radio-frequency power regimes.

This is the first comprehensive analysis of the experimental data measured during the experimental campaigns of SPIDER experiment, both in volume and surface operation, focusing on the beam divergence and homogeneity. All the investigations I performed demonstrated how strongly the beam properties are correlated with the plasma features, moving the attention to the source control parameters for the improvement of the negative ion beam performances. As I have demonstrated in this thesis, the increase of the plasma density results in a more homogenous beam, in particular in the region of the source affected the most by the magnetic filter field. In parallel, a more complete understanding of the coupling of the radio-frequency power to the plasma is need, to obtain a more homogeneous plasma in the source.

The set of available diagnostics demonstrated capable of describing the behaviour of the beam and the plasma, but a complete understanding of the entire dynamics governing the plasma in the source is still not achieved. To fully understand the experimental results, the support of numerical simulations taking into account the entire plasma dynamics is necessary and they are under development. To have a complete picture of the physics of the plasma and of the beam, as well as to increase the plasma density, modifications of the experimental setup are needed, to widen the explorable experimental scenario. For instance, a more flexible design of the power supplies which polarize the Bias Plate as well as the Plasma Grid could be useful, in order to study the plasma properties also in the regimes not achievable with the current system. Moreover, since the Bias Plate is subdivided into 5 segments, the separate polarization of each of them would allow to better control the plasma vertical profile. A further tool to study the properties of the electronegative plasma at the extraction region could be the measurement of the co-extracted electron current in each beamlet group. With the estimation of the beamlet current obtained through visible tomography, this measurement will allow to evaluate the electron-to-ion ratio along the entire vertical beam profile. If a more homogeneous plasma profile will not be achieved, another solution could be the modification of the design of the extraction apertures, to reduce the scraping of the beamlets on the grid itself, when their space charge is too large to be properly focused by the electrostatic lens of the grids. To increase the plasma density, however, it is necessary to modify the confinement of the plasma inside the source, for example by adding additional magnets.

Since the shutdown of SPIDER has just started, some modifications of both the source and of the accelerator systems can be upgraded, to ameliorate the beam features and to fully understand the physics behind them, towards the achievement of the requirements for future ITER HNB.

Bibliography

[1] *The United Nation Human Development Report*, 2020 http://hdr.undp.org/en/content/latest-human-development-index-ranking.

[2] *2021 United Nations Framework Convention on Climate Change*, url:unfccc.int.

[3] M. Spurio, *Particles and Astrophysics. A Multi-Messenger Approach*, Springer; https://doi.org/10.1007/978-3-319-08051-2 (2014).

[4] K.O. Hintermann and R. Wideröe, *Tritium Production and Cycling in a Fusion Reactor with Lithium Blanket*, A/CONF.15/P/1471, IAEA (1959).

[5] R. Rhodes, *The Making of the Atomic Bomb*, New York: Simon & Schuster. ISBN 0-671-44133-7. OCLC 137943436 (1986).

[6] *ITER Organization*, https://www.iter.org/.

[7] K.S. Krane, *Introductory Nuclear Physics*, John Wiley & Sons, 2nd Edition (1955).

[8] J.D. Lawson, *Some Criteria for a Useful Thermonuclear Reactor*, A.E.R.E. report GP/R 1807 (1955).

[9] ITER Ita Newsletter, *International Atomic Energy Agency, Vienna, Austria*, ISSN 1727-9852 (2006).

[10] V.P. Smirnov, *Tokamak foundation in USSR/Russia 1950-1990*, IOP Publishing and International Atomic Energy Agency, Nucl. Fusion **50** 01 4003, doi:10.1088/0029-5515/50/1/014003 (2010).

[11] R. Aymar *et al.*, *The ITER design*, Plasma Phys. Control Fusion **44** 519 (2002).

[12] C. Gormenzano *et al.*, *Hybrid advanced scenarios: perspectives for ITER and new experiments with dominant RF heating*, Plasma Phys. Control Fusion **46** B435-B447 (2004).

[13] A.C. Riviere, *Penetrations of fast Hydrogen atoms into a fusion reactor plasma*, Nucl. Fusion **11** 363 (1971).

[14] M. Kikuchi *et al.*, *Fusion Physics*, International Atomic Energy Agency, Vienna, STI/PUB–1562; ISBN 978-92-0-130410-0, (2012).

[15] K.H. Berkner *et al.*, *Intense, mixed-energy hydrogen beams for CTR injection*, Nucl. Fusion **15** 249 (1975).

[16] J. Maglica, *Plasma heating with neutral beam injection*, University of Ljubljana, Seminar (2005).

[17] S. Denizeau, *Numerical and experimental study of high voltage negative ion accelerator for ITER NBI*, PhD Thesis (2020).

[18] R. S. Hemsworth *et al.*, *Overview of the design of the ITER heating neutral beam injectors*, New. J. Phys. **19** 025005, https://doi.org/10.1088/1367-2630/19/2/025005 (2017).

[19] R.K. Janev *et al.*, *Collision Processes in Low-Temperature Hydrogen Plasmas*, FZ-Juelich Report **4105** (2003).

[20] C.F. Barnett *et al.*, *Atomic data for Controlled fusion Research*, (1977).

[21] P. McNeely *et al.*, *Neutral depletion in an H^- source operated at high RF power and low input gas flow*, Plasma Source Sci. Techol., **30** (4), 045005; https://doi.org/10.1088/0963-0252/20/4/045005 (2011).

[22] P. Sonato *et al.*, *Conceptual design of the beam source for the DEMO Neutral Beam Injectors*, New. J. Phys. **18** (12), 125002; https://doi.org/10.1088/1367-2630/18/12/125002 (2016).

[23] G: Chitarin *et al.*, *Optimization of the electrostatic and magnetic field configuration in the MITICA accelerator*, Fus. Eng. and Des., **88** (6-8), 507-511; https://doi.org/10.1016/j.fusengdes.2013.02.052 (2013).

[24] H. P. L. de Esch *et al.*, *Updated physics design ITER-SINGAP accelerator*, Fus. Eng. and Des., **73** (2), 329-341; https://doi.org/10.1016/j.fusengdes.2005.07.003 (2005).

[25] T. Inoue *et al.*, *1 MeV, ampere class accelerator r&D for ITER*, Nucl. Fusion **46** S379; https://doi.org/10.1088/0029-5515/46/6/S20 (2006).

[26] R. Pasqualotto *et al.*, *Progress on development of SPIDER diagnostics*, AIP Conference Proceedings **1869**, 030020; https://doi.org/10.1063/1.4995740 (2017).

[27] P. Agostinetti *et al.*, *Detailed design optimization of the MITICA negative ion accelerator in view of the ITER NBI*, Nucl. Fusion **56** 016015; https://doi.org/:10.1088/0029-5515/56/1/016015 (2016).

[28] D. Marcuzzi *et al.*, *Detail design of the beam source for the SPIDER experiment*, Fus. Eng. and Des., **85** (10-12), 1792-1797; https://doi.org/10.1016/j.fusengdes.2010.05.039 (2010).

[29] P. Agostinetti *et al.*, *Physics and engineering design of the accelerator and electron dump for SPIDER*, Nucl. Fusion **51**, 063004; https://doi.org/10.1088/0029-5515/51/6/063004 (2011).

[30] B. Heinemann *et al.*, *Design of the "half-size" ITER neutral beam source for the test facility ELISE*, Fus. Eng. and Des., **84** 2, 915-922; https://doi.org/10.1016/j.fusengdes.2008.11.076 (2009).

[31] N. Marconato *et al.*, *An optimized and flexible configuration for the magnetic filter in the SPIDER experiment*, Fus. Eng. and Des. **166** 112281; https://doi.org/10.1016/j.fusengdes.2021.112281 (2021).

[32] M. Pavei *et al.*, *SPIDER plasma grid masking for reducing gas conductance and pressure in the vacuum vessel*, Fus. Eng. and Des., **161**, 112036; https://doi.org/10.1016/j.fusengdes.2020.112036 (2020).

[33] M. Cavenago *et al.*, *Development of a versatile multiaperture negative ion source*, Rev. Sci. Instrum. **83**, 02A707; https://doi.org/10.1063/1.3670350 (2012).

[34] B. Heinemann *et al.*, *Upgrade of the BATMAN test facility for H^- source development*, AIP Conference Proceedings **1655**, 060003; https://doi.org/10.1063/1.4916472 (2015).

[35] K. Tsumori *et al.*, *Spatial distribution of the charged particles and potentials during beam extraction in a negative-ion source*, Rev. Sci. Instrum. **83**, 02B116; https://doi.org/10.1063/1.3672116 (2012).

[36] K. Tsumori *et al.*, *High power beam injection using an improved negative ion source for the large helical device*, Rev. Sci. Instrum. **75**, 1847; https://doi.org/10.1063/1.1702107 (2004).

[37] M. Bacal, *Physics aspects of negative ion sources*, Nucl. Fusion **46** S250; https://doi.org/10.1088/0029-5515/46/6/S05 (2006).

[38] P. W. van Amersfoort, *Formation of negative hydrogen ions on a cesiated W(110) surface; the influence of hydrogen implantation*, Journal of Applied Physics **58**, 3566; https://doi.org/10.1063/1.335732 (1985).

[39] W.M. Haynes, *CRC Handbook of Chemistry and Physics*, CRC Press (2014).

[40] A. Rizzolo *et al.*, *Characterization of the SPIDER Cs oven prototype in the CAesium Test Stand for the ITER HNB negative ion sources*, Fus. Eng. and Des., **146**; https://doi.org/10.1016/j.fusengdes.2019.01.0538 (2019).

[41] U. Fantz *et al.*, *Fundamental experiments on evaporation of cesium in ion sources*, Rev. Sci. Instrum. **81** (2), 02B102; https://doi.org/10.1063/1.3258428 (2010).

[42] H. Nakano *et al.*, *Cavity Ringdown Technique for negative hydrogen- ion measurement in ion source for neutral beam injector*, Journal of Instrumentation, **11** (03), C03018-C03018; https://doi.org/10.1088/1748-0221/11/03/c03018 (2016).

[43] S. Lishev *et al.*, *Fluid-model analysis on discharge structuring in the RF-driven prototype ion-source for ITER NBI*, Plasma Sources Sci. Technol. **27**, 125008; https://doi.org/10.1088/1361-6595/aaf536 (2018).

[44] G. Fubiani *et al.*, *Modeling of plasma transport and negative ion extraction in a magnetized radio-frequency plasma source*, New J. Phys. **19**, 015002; https://doi.org/10.1088/1367-2630/19/1/015002 (2017).

[45] J.E. Allen, *The plasma-sheath boundary: its history and Langmuir's definition of the sheath edge*, Plasma Sources Sci. Technol. **18**, 014004; https://doi.org/10.1088/0963-0252/18/1/014004 (2008).

[46] I. Mario, *Correlation between plasma and beam properties at the ELISE test facility*, PhD Thesis (2020).

[47] R. McAdams*et al.*, *Transport of negative ions across a double sheath with a virtual cathode*, Plasma Sources Sci. Technol. **20**, 035023; https://doi.org/10.1088/0963-0252/20/3/035023 (2011).

[48] G. Serianni *et al.*, *Neutralisation and transport of negative ion beams: physics and diagnostics*, New. J. Phys. **19**, 045003; https://doi.org/10.1088/1367-2630/aa64bd (2017).

[49] E. Sartori *et al.*, *Simulation of space charge compensation in a multibeamlet negative ion beam*, Rev. Sci. Instrum. **87**, 02B917; https://doi.org/10.1063/1.4933252 (2016).

[50] S.R. Lawrie *et al.*, *Detailed beam and plasma measurements on the vessel for extraction and source plasma analyses (VESPA) Penning H- ion source*, Rev. Sci. Instrum. **87**, 02B122; https://doi.org/10.1063/1.4934580 (2016).

[51] U. Fantz *et al.*, *Spectroscopy a powerful diagnostic tool in source development*, Nucl. Fusion. **46** S297-S306; https://doi.org/10.1088/0029-5515/46/6/S10 (2006).

[52] R. Pasqualotto *et al.*, *Plasma light detection in the SPIDER beam source*, Fus. Eng. and Des., **146**; https://doi.org/10.1016/j.fusengdes.2019.01.061(2019).

[53] B. Zaniol *et al.*, *First measurements of optical emission spectroscopy on SPIDER negative ion source*, Rev. Sci. Instrum. **91**, 013103; https://doi.org/10.1063/1.5128900 (2020).

[54] $http://www.princetoninstruments.com/userfiles/files/assetLibrary/Datasheets/Princeton\_Instruments\_IsoPlane\_SCT\_320\_Rev\_N4\_1\_11-10-14.pdf$ for information on IsoPlane spectrometers.

[55] D. Wunderlich *et al.*, *Yacora on the Web: Online Collisional Radiative Models for plasmas containing H, H2 or He* , Journal of Quantitative Spectroscopy and Radiative transfer, **240**, 106695; https://doi.org/10.1016/j.jqsrt.2019.106695 (2019).

[56] M. Brombin *et al.*, *Electrostatic sensors for SPIDER experiment: Design, manufacture of prototypes, and first tests*, Rev. Sci. Instrum. **85** (2), 02A715; https://doi.org/10.1063/1.4831746 (2014).

[57] M. Spolaore *et al.*, *Design of a system of electrostatic probes for the RF negative ion source of the SPIDER experiment*, J. Phys. D: Appl. Phys. **43**, 124018; https://doi.org/10.1088/0022-3727/43/12/124018 (2010).

[58] H. M. Mott-Smith *et al.*, *The Theory of Collectors in Gaseous Discharges*, Phys. Rev. **28**, 727; https://doi.org/10.1103/PhysRev.28.727 (1926).

[59] E. Sartori *et al.*, *Development of a set of movable electrostatic probes to characterize the plasma in the ITER neutral beam negative-ion source prototype*, Fus. Eng. and Des. **169** (8), 112424; https://doi.org/10.1016/j.fusengdes.2021.112424 (2021).

[60] D. Gahan *et al.*, *Retarding field analyzer for ion energy distribution measurements at a radio-frequency biased electrode*, Rev. Sci. Instrum. **79** (2), 033502; https://doi.org/10.1063/1.2890100 (2008).

[61] E. Sartori *et al.*, *Report on joint experiments in NIFS-RNIS in 2019-Negative ion source plasma investigation by Compact Retarding Field Energy Analysers.*, Technical Note, RFX (2019).

[62] E. Sartori *et al.*, *Development of an energy analyzer as diagnostic of beam-generated plasma in negative ion beam systems*, AIP Conference Proceedings **1869**, 060005; https://doi.org/10.1063/1.4995792 (2017).

[63] M. Kisaki *et al.*, *Characteristics of plasma grid bias in large-scaled negative ion source*, Rev. Sci. Instrum. **85**, 02B131; https://doi.org/10.1063/1.4854295 (2014).

[64] J. Bredin *et al.*, *Langmuir probe analysis in electronegative plasmas*, Phys. Plasma **21**, 123502; https://doi.org/10.1063/1.4903328 (2014).

[65] B. Zaniol *et al.*, *Design of a beam emission spectroscopy diagnostic for negative ions radio frequency source SPIDER*, Rev. Sci. Instrum. **83**, 043117; https://doi.org/10.1063/1.4705739 (2012).

[66] M. Barbisan *et al.*, *First results from beam emission spectroscopy in SPIDER negative ion source*, Plasma Phys. Control. Fusion **63** 125009, 043117; https://doi.org/10.1088/1361-6587/ac2eb2 (2021).

[67] M. De Muri *et al.*, *Design and specifications of the diagnostics for the instrumented calorimeter of Source for the Production of Ions of Deuterium Extracted from Radio frequency plasma*, Rev. Sci. Instrum. **83**, 02B724; https://doi.org/10.1063/1.3678212 (2012).

[68] A. Rizzolo *et al.*, *Final design of the diagnostic calorimeter for the negative ion source SPIDER*, Fus. Eng. and Des. **123**, 768-772; https://doi.org/10.1016/j.fusengdes.2017.05.003 (2017).

[69] A. Pimazzoni *et al.*, *Assessment of the SPIDER beam features by diagnostic calorimetry and thermography*, Rev. Sci. Instrum. **91**, 033301; https://doi.org/10.1063/1.5128562 (2020).

[70] E. Sartori *et al.*, *Simulation and measurement of rarefied gas flow and neutral density profiles through a large multi aperture multigrid negative ion accelerator*, Fus. Eng. and Des., **151**, 111398; https://doi.org/10.1016/j.fusengdes.2019.111398 (2020).

[71] J. Radon, *On the determination of functions from their integral values along certain manifolds*, IEEE Transactions on Medical Imaging, **5**, 4; https://doi.org/10.1109/TMI.1986.4307775(1986).

[72] M. Cormack, *Representation of a Function by Its Line Integrals, with Some Radiological Applications*, Journal of Applied Physics **34**, 2722; https://doi.org/10.1063/1.1729798 (1963).

[73] G. N. Hounsfield, *Computerized transverse axial scanning (tomography). 1. Description of system*, The British Journal of Radiology **46**, 551; https://doi.org/10.1259/0007-1285-46-552-1016 (1963).

[74] G. A. Cottrell *et al.*, *Tomography of neutral beams*, Rev. Sci. Instrum. **55**, 1401; https://doi.org/10.1063/1.1137949 (1984).

[75] F. Bonomo *et al.*, *Tomography feasibility study on the optical emission spectroscopy diagnostic for the negative ion source of the ELISE test facility*, Plasma Phys. Control. Fusion **56**, 015006; https://doi.org/10.1088/0741-3335/56/1/015006 (2014).

[76] M. Agostini *et al.*, *Tomographic diagnostic of the hydrogen beam from a negative ion source*, Phys. Rev. ST Accel. Beams **14**, 102801; https://doi.org/10.1103/PhysRevSTAB.14.102801 (2011).

[77] https://www.baslerweb.com/en/products/cameras/area-scan-cameras/ace/aca1920-40gm.

[78] https://visionlink.it/product/blackfly-s-28-mp-color-gige-vision-sony-imx429/.

[79] https://www.acktar.com.

[80] Z. Zhang, *A flexible new technique for camera calibration*, Anal. Mach. Intell. **22** (11), 1330-1334; https://doi.org/10.1109/34.888718 (2000).

[81] *https://it.mathworks.com/help/vision/ref/cameracalibrator-app.html.*

[82] N. Fonnesu *et al.*, *Tomographic reconstruction of the beam emissivity profile in the negative ion source NIO1*, Nucl. Fusion **56**, 126018; https://doi.org/10.1088/0029-5515/56/12/126018 (2016).

[83] M. Ugoletti *et al.*, *Visible cameras as a non-invasive diagnostic to study negative ion beam properties*, Rev. Sci. Instrum. **92**, 043302; https://doi.org/10.1063/5.0038911 (2021).

[84] A. H. Andersen *et al.*, *Simultaneous Algebraic Reconstruction Technique (SART): A superior implementation of the ART algorithm*, Ultrasonic Imaging, **6**, 81-94 https://doi.org/10.1016/0161-7346(84)90008-7 (1984).

[85] P. Veltri *et al.*, *Effects of Negative Ion Source Characteristics on Beam Optics: The Case of SPIDER*, IEE. Trans. Plasma Sci. **40** (9), 2279-2284; https://doi.org/10.1109/TPS.2012.2207742 (2012).

[86] A. Hurlbatt *et al.*, *First direct comparison of whole beam and single beamlet divergences in a negative ion source with simultaneous BES and CFC tile calorimetry measurements*, AIP Advances **11**, 025330; https://doi.org/10.1063/5.0039080 (20121).

[87] M. Bacal *et al.*, *Basic processes of negative hydrogen ion production and destruction in sources and beams*, Rev. Sci. Instrum. **67**, 1138; https://doi.org/10.1063/1.1146770 (1996).

[88] R. Trainham *et al.*, *Negative ion sources for neutral beam injection into fusion machines*, Rev. Sci. Instrum. **69**, 926; https://doi.org/10.1063/1.1148545 (1998).

[89] M. Hanada *et al.*, *Development of negative ion sources for the ITER neutral beam injector*, Fus. Eng. and Des., **56-57**, 505-509; https://doi.org/10.1016/s0920-3796(01)00335-0 (2001).

[90] E. Speth *et al.*, *Overview of the RF source development programme at IPP Garching*, Nucl. Fusion **46** S220; https://doi.org/10.1088/0029-5515/46/6/S03 (2006).

[91] E. Sartori *et al.*, *First operation with caesium of the negative ion source SPIDER*, Oral contribution, ICIS 2021.

[92] P.W. Allison *et al.*, *An Emittance Scanner for Intense Low-Energy Ion Beams*, IEEE Transactions on Nuclear Science, **30**, 4, pp. 2204-2206; https://doi.org/10.1109/TNS.1983.4332762 (1983).

[93] C. Poggi *et al.*, *Design and development of an Allison type emittance scanner for the SPIDER ion source*, Rev. Sci. Instrum. **91**, 013328; https://doi.org/10.1063/1.5129650 (2020).

[94] C. Wimmer *et al.*, *Beamlet scraping and its influence on the beam divergence at the BATMAN Upgrade test facility*, Rev. Sci. Instrum. **91**, 013509; https://doi.org/10.1063/1.5129336 (2020).

[95] K. Tsumori *et al.*, *Neutral beam injection with an improved accelerator for LHD*, Rev. Sci. Instrum. **79**, 02C107; https://doi.org/10.1063/1.2822111 (2008).

[96] P. Veltri *et al.*, *Optics of the NIFS negative ion source test stand by infrared calorimetry and numerical modelling*, Rev. Sci. Instrum. **87** (2), 02B908; https://doi.org/10.1063/1.4932982 (2016).

[97] *IBSimu, Ion Beam Simulator*, http://ibsimu.sourceforge.net/.

[98] *OPERA, Electromagnetic and Electromechanical Simulation*, url: www.3ds.com/products-services/simulia/products/opera.

[99] S. Geng *et al.*, *Spatial Distributions of Charged Particles and Plasma Potential before and during Beam Extraction in a Negative Hydrogen Ion Source for NBI*, Plasma and Fusion Research, **10** (0), 3405016-3405016; https://doi.org/10.1585/pfr.10.3405016 (2015).

[100] E. Sartori *et al.*, *Investigation of negative ion energy distribution and extraction mechanism with a compact retarding field energy analyser in a large filament-arc source for neutral beam injectors*, SOFE Conference 2021 (submitted).

[101] S. Geng *et al.*, *Charged particle flows in the beam extraction region of a negative ion source for NBI* , Rev. Sci. Instrum. **87**, 02B103; https://doi.org/10.1063/1.4931796 (2016).

[102] T. Inoue *et al.*, *1 Me V, ampere class accelerator RD for ITER*, Nucl. Fusion. **46** S379; https://doi.org/10.1088/0029-5515/46/6/S20 (2006).

[103] H.P.L. de Esch *et al.*, *Negative ion beam halo mitigation at the 1 MV testbed at IRFM*, Fus. Eng. and Des. **86** 363-368; https://doi.org/10.1016/j.fusengdes.2011.02.098 (2011).

[104] S. Nishioka *et al.*, *Study of plasma meniscus and beam halo in negative ion sources using three dimension in real space and three dimension in velocity space particle in cell model*, Rev. Sci. Instrum. **85**, 02A737; https://doi.org/10.1063/1.4854976 (2014).

[105] K. Miyamoto *et al.*, *Study of negative hydrogen ion beam optics using the 2D PIC method*, AIP Conference Proceedings **1515**, 22; https://doi.org/10.1063/1.4792766 (2013).

[106] P. Franzen *et al.*, *Beam Homogeneity Dependence on the Magnetic Filter Field at the IPP Test Facility MANITU*, AIP Conference Proceedings **1390**, 310; https://doi.org/10.1063/1.3637401 (2011).

[107] U. Fantz *et al.*, *Plasma expansion across a transverse magnetic field in a negative hydrogen ion source for fusion*, Plasma Sources Sci. Technol., **23** (4), 044002; https://doi.org/ 10.1088/0963-0252/23/4/044002 (2014).

[108] J. P. Boef *et al.*, *Physics of a magnetic filter for negative ion sources. I. Collisional transport across the filter in an ideal, 1D filter*, Physics of Plasmas **19**, 113509; https://doi.org/10.1063/1.4768676 (2012).

[109] E. Sartori *et al.*, *Movable electrostatic probes in SPIDER (end of second phase)*, EAC meeting, 2 August 2020.

[110] G. Serianni *et al.*, *Caesium operation in SPIDER*, NAC5, 19-22 October 2021.

[111] C. Poggi, *Numerical and experimental study of the physics of negative ion beams*, PhD Thesis (2021).

[112] L. Schiesko *et al.*, *Magnetic field dependence of the plasma properties in a negative hydrogen ion source for fusion*, Plasma Phys. Control. Fusion **54**, 105002; https://doi.org/10.1063/1.3637401 (2011).

[113] U. Fantz *et al.*, *Negative Hydrogen Ion Sources for Fusion: From Plasma Generation to Beam Properties*, Front. Phys., 29 September 2021; https://doi.org/10.3389/fphy.2021.709651 (2021).

[114] M. Ugoletti *et al.*, *First results of SPIDER beam characterization through the visible tomography*, Fus. Eng. and Des. **169**, 112667; https://doi.org/10.1016/j.fusengdes.2021.112667 (2021).

[115] M. Barbisan *et al.*, *Development and first operation of a cavity ring down spectroscopy diagnostic in the negative ion source SPIDER*, Rev. Sci. Instrum. **92**, 053507; https://doi.org/10.1063/5.0043226 (2021).

[116] A. Pimazzoni *et al.*, *Co-extracted electrons and beam inhomogeneity in the large negative ion source SPIDER*, Fus. Eng. and Des. **168**, 112440; https://doi.org/10.1016/j.fusengdes.2021.112440 (2021).

[117] B. Heinemann *et al.*,, *Towards large and powerful radio frequency driven negative ion sources for fusion*,New J. Phys. **19**, 015001; https://doi.org/10.1088/1367-2630/aa520c (2017).